

UNIVERSIDADE DE SÃO PAULO
INSTITUTO DE QUÍMICA
Graduate Program in Chemistry

THENNER SILVA RODRIGUES

**Hollow metal nanostructures as the active phase in
supported and unsupported catalysts: optimizing
performances by controlled synthesis**

Original version of the dissertation defended

São Paulo

Deposit date at SPG:
February 20th 2017

THENNER SILVA RODRIGUES

**Hollow metal nanostructures as the active phase in
supported and unsupported catalysts: optimizing
performances by controlled synthesis**

*Dissertation presented to the Institute of
Chemistry of the University of São Paulo to obtain
the Doctor's Degree in Chemistry.*

Academic advisor: Prof. Dr. Pedro Henrique Cury Camargo

São Paulo
2017

To all my family and friends

ACKNOWLEDGMENTS

First of all, I would like to thank my partner Anderson for being by my side throughout all these years, for the unconditional support he has always given me, for love, and dedication. We are together on this walk and the certainty that you are always on my side makes it all easier. Thanks also to my academic advisor Prof. Pedro Camargo for everything he did for me. His immense dedication and passion for science made this work a reality. Thank you for the great attention you have given me these years, which made me a much better person and professional than I was when I joined your group. Surely you knew how to extract what was best in me, and I am eternally grateful to you for it. I thank my beloved undergraduate students Bruna, Rafael Silva, Mariana, Eduardo, Laís, Daniel, Cibele, Gabriel, Vitor, Guilherme, Isabella and Arthur who both dedicated themselves and contributed to the accomplishment of this work. You may think you have learned from me, but I am sure that I have learned much more from you. I have a great affection for you and I will always have you in my heart. Thanks to my friends of GrAND, Alexandra, Caio, Rafael Geonmonond, Jiale, Isabel, Luanna for the partnership, help and for the many good times we had together. To my friends from IQ-USP Marco, Cassio, Val, Camila and Gustavo for the friendship and all the help and support they gave me. To the collaborators of this project, Prof. Humberto Fajardo, Prof. José Mansur Assaf, Prof. Luiz Probst, Prof. Leandro Andrade, Prof. Róbson Teixeira, Prof. Adalberto da Silva, who kindly opened the doors of their laboratories to our partnerships and so much contributed to the aggrandizement of this work together with their students and partners Rosana Balzer, Alisson Marques, Janaina Gomes, Camila Kisukui, Valquirio Graia and Lucas de Oliveira. Thanks to Prof. Younan Xia for the magnificent opportunity he gave me to be able to work in his group. This time I was at the Georgia Institute of Technology, was of extreme learning and completely changed my career and perception of science. Thanks to my friends Zach Hood,

Kyle Gilroy, Legna Figueroa, Madeline Vara, Aleksey Ruditskiy, Brian Lee and Steven Fortner for the tremendous support they gave me at this challenging time in my life. You are really special and I will never forget you. I thank the CAPES, CNPq and FAPESP funding agencies for the grant of the doctoral scholarship and for the funding of our research. In particular, to CNPq for granting the scholarship of the program "Sciences without borders", even to the one who at the end of a doctorate of hard work, dedication and productivity have denied me the postdoctoral fellowship and the opportunity to continue my work with decency. I thank my family Ivanilda, Tuno, Lathoya and Suzy for the support and for understanding my absence over the years. I extend to the cousins, uncles and aunts, grandparents and nephews, thanking them for their encouragement. And to my beloved friends of childhood and adolescence Leandro, Geruza, Virginia and Leticia who, to this day, accompany me, support and always receive me with open arms whenever I return. To all my friends on the volleyball team of Química-USP Rodrigo, Murilo (Jaque), Luan (Elisângela), Luiz (Fabiola), Vinícius (Berg), Rafael (Tica), Gustavo, (Thaisa), Jackson (Chuciely), Gustavo (Lia), João (Paula), Val (Wal), Gustavo (Fabiana), Diogo (Joyce), Henrique (Kátia), Sandro (Teny), Guiherme (Tandara), Gabriel (Gaby), Felipe (Sheilla), and Carlos (Carla) for the friendship and companionship we have always had.

Finally, I would like to express deep gratitude to all those who directly and indirectly contributed to my arrival where I arrived! To all of you my most sincere THANK YOU!

***“One of the secrets of success is to refuse
to let temporary setbacks defeat us.”***

- Mary Kay Ash

ABSTRACT

Rodrigues, T.S. **Hollow metal nanostructures as the active phase in supported and unsupported catalysts: optimizing performances by controlled synthesis.** 2017. 234p. PhD Dissertation - Graduate Program in Chemistry. Institute of Chemistry, University of São Paulo, São Paulo.

This dissertation describes the development of a variety of well-defined nanomaterials based on noble metals displaying hollow interiors followed by their application as heterogeneous catalyst towards different chemical transformations. In this work, we employed a simple and robust galvanic replacement reaction approach and its combination with additional metal deposition over preformed templates using hydroquinone as auxiliary reducing agent. This enabled us to precisely control physicochemical features of the produced nanomaterials for catalytic application such as size, composition, shell thickness, surface morphology, number of surface atoms exposed, nature of exposed surface facets, and plasmon band intensity and position. In addition, we could successfully address a well-established challenge in heterogeneous catalysis by noble metals, which is the fabrication of supported materials in which the metal component presents a uniform dispersion over the entire surface of the support without any detectable agglomeration. To this end, the developed approaches for syntheses were scaled up by more than 100 folds, which enabled us to produce enough amount of particles for the uniform incorporation over the commercial silica support. Interestingly, all produced supported nanomaterials displayed satisfactory catalytic activities towards gas phase oxidation reactions and exceptional stabilities on all procedures, demonstrating that our developed approach may inspire the synthesis of noble metal nanostructures displaying attractive features for catalytic applications and uniform dispersion over solid supports to produce solid supported catalysts. As the nanomaterials obtained in this work displayed controlled and well-defined properties, we could establish a precise correlation between their catalytic or photocatalytic performances and the physicochemical properties that define them. Thus, we showed that by relatively simple adjustments in the synthesis protocols, a rational maneuvering over properties such as size, shape, surface morphology, and composition can be successfully achieved. This represents a powerful tool for boosting the catalytic performances of hollow nanomaterials towards a variety of chemical transformations with completely distinctive mechanisms and nature. In fact, only a few groups have demonstrated the synthesis in large scale of nanomaterials with truly well-defined shapes and sizes in which these parameters can be tightly controlled. Thus, we believe that this dissertation contributes towards the manufacture of supported catalysts containing well-defined and controlled nanomaterials for applications in practical catalytic systems.

Keywords: Hollow nanomaterials; noble metals; hybrid nanomaterials; nanocatalysts; heterogeneous catalysis.

TABLE OF CONTENTS

Chapter 1	9
Introduction.....	9
1.1. Nanomaterials and nanotechnology	9
1.2. Nanomaterials in catalysis	13
1.3. Plasmon-enhanced/mediated catalysis.....	18
1.4. Hollow nanomaterials	19
1.5. Scope of this work	32
1.6. References.....	35
Chapter 2.....	41
Probing the Catalytic Activity of Bimetallic versus Trimetallic Nanoshells.....	41
2.1. Introduction.....	41
2.2. Experimental Section	42
2.3. Results and Discussion	45
2.4. Conclusion	56
2.5. References.....	57
Chapter 3.....	60
Rational Design of Plasmonic Catalysts: Matching the Surface Plasmon Resonance with the Lamp Emission Spectra for Improved Performances in AgAu Nanorings.....	60
3.1. Introduction.....	60
3.2. Experimental	61
3.3. Results and discussion	66
3.4. Conclusion	78
3.5. References.....	79
Chapter 4.....	82
AgAu Nanotubes: Investigating the Effect of Surface Morphologies and Optical Properties over Applications in Catalysis and Photocatalysis	82
4.1. Introduction.....	82
4.2. Experimental	83
4.3. Results and discussion	86
4.4. Conclusion	97
4.5. References.....	98
Chapter 5.....	102
AgPt Hollow Nanodendrites: Synthesis and Uniform Dispersion over SiO ₂ Support for Catalytic Applications.....	102
5.1. Introduction.....	102
5.2. Experimental	103
5.3. Results and discussion	107
5.4. Conclusion	119

5.5. References.....	120
Chapter 6.....	123
On the Catalytic Properties of AgPt Nanoshells as a Function of Size: Larger Outer Diameters Lead to Improved Performances	123
6.1. Introduction.....	123
6.2. Experimental.....	125
6.3. Results and discussion	129
6.4. Conclusion	147
6.5. References.....	148
Chapter 7.....	151
Hollow AgPt/SiO ₂ Nanomaterials with Controlled Surface Morphologies: Is the Number of Pt Surface Atoms Imperative to Optimized Catalytic Performances?.....	151
7.1. Introduction.....	151
7.2. Experimental	152
7.3. Results and discussion	156
7.4. Conclusion	171
7.5. References.....	172
Chapter 8.....	176
Cu ₂ O Spheres as an Efficient Source of Catalytic Cu(I) Species for Performing Azide-Alkyne Click Reactions	176
8.1. Introduction.....	176
8.2. Experimental	177
8.3. Results and discussion	180
8.4. Conclusion	191
8.5. References.....	191
Chapter 9.....	194
Kinetic Understanding of Galvanic Replacement Reactions in Cu ₂ O Under Aerobic Conditions: Elucidating the Formation of Bowls, Rattles, and Dendrites.....	194
9.1. Introduction.....	194
9.2. Experimental	195
9.3. Results and discussion	198
9.4. Conclusion	220
9.5. References.....	221
Chapter 10.....	225
Final Remarks and Perspectives	225
CURRICULUM VITAE.....	226

Chapter 1

Introduction

1.1. Nanomaterials and nanotechnology

The concept of nanotechnology was introduced for the first time in 1959 by Richard P. Feynman.¹ Thenceforward the concept demonstrated by Feynman have been widely employed in variety of fields and has made possible many revolutionary developments in physics,² chemistry,³ biology,⁴ medicine,⁵ and engineering,⁶ telecommunications,⁷ etc, by a simple idea of manipulating the matter at an extremely small scale such as molecules and atoms. Thus, a new concept was born in science: “nanotechnology”. With the advance of research, its definition modified from field to field over the last decades.⁸ More specifically, in field of chemistry, the concept of nanotechnology was firstly described considering what was in fact innovative for the time: the obtaining and characterization of materials on a scale inferior to the materials conventionally obtained. Thus, the first definition of nanotechnology comprised only the aspect of size, in which nanomaterials should be an object having a size in the range of approximately 1 - 100 nanometers.⁹

However, many scientific discoveries showed that the manipulation/restructuring of matter creating structures in the nanoscale order of nanometers led to nanomaterials with enhanced or new properties compared to their bulk materials counterparts.⁹ In this context, the IUPAC (International Union of Pure and Applied Chemistry) launched in 2012 a more specific concept, which determines that a nanomaterial should not only be a solid at the nanoscale, but a nanostructured solid that presents significantly superior properties because it is at this scale:

“...materials with dimensions on the nanoscale (approximately 1 nm to 100 nm) have structure, properties, and interactions that can be quite different from macroscopic materials...”

Since the discovery of nanostructured materials, an intense research has been performed for the development of new methods of synthesis to obtain the most diverse materials with the a range of properties (size, shape, composition, and structure). In this context, thanks to the advancement of science and engineering, the number of protocols became huge. However, all of them can be classified as a part of two main approaches defined in 1989 in by Foresight Institute in order to distinguish the molecular manufacturing of conventional manufacturing: “top-down” or “bottom-up” approaches.¹⁰⁻¹² These both concepts consider only the particle size direction in which the process is executed. More specifically, as depicted in Figure 1.1, the “top-down” approach is identified when larger structures are reduced in to smaller sizes (nanoscale) such as nanophotolithography and inkjet printing techniques. On the other hand, in the “bottom-up” approach, the opposite scenario is achieved. Herein, the nanomaterials are produced by chemical or physical methods, in which atoms or molecular components are assembled or self-assembled to originate the target nanodevice.¹⁰⁻¹² Examples of bottom-up approaches include systems that self-assemble, a process that is triggered by a local change in a chemical or physical condition. Related techniques include templating and scaffolding methods, such as biomineralization, which rely on backbone structures to support and guide the nucleation and growth of a nanomaterial.

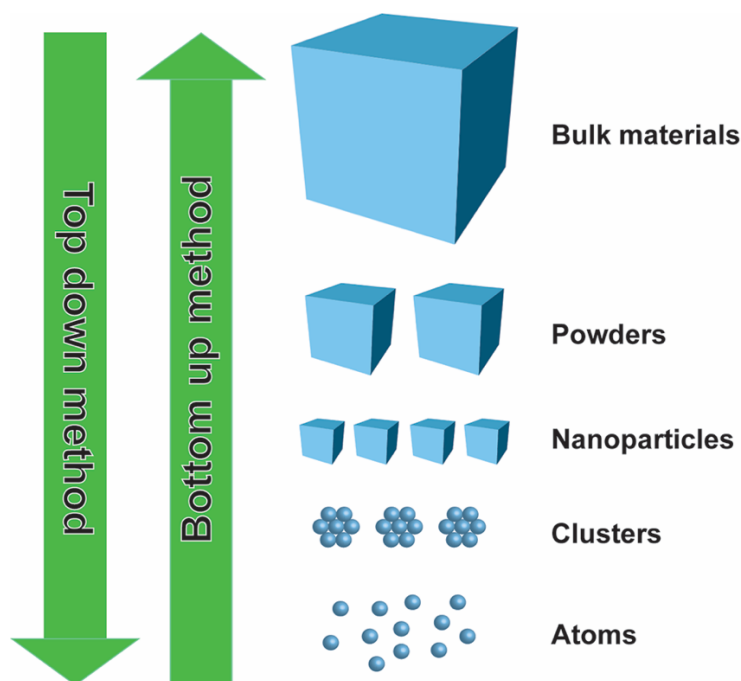


Figure 1.1. Scheme showing the top down and bottom up approaches in nanotechnology¹³

In fact, all methods previously described have their importance in the development of the nanotechnology. However, among them the “bottom-up” approach, the chemical methods (solution-phase methods) stand out due their high productivity in terms of amount of nanoparticles obtained per synthesis (occasionally more than 10^{17} nanoparticles L^{-1})¹⁴ using relatively simple and fast procedures, in which the physicochemical properties that define the nanoparticles (size, shape, composition, crystallinity, and structure) can be controlled by varying the experimental conditions and the reactants. The general approach of the solution-phase method involves the use of solvents, stabilizers, metal precursors, capping and reducing agents.¹⁵ In this context, many reports have evaluated the effect capping agents have in the synthesis of metal nanoparticles based on their different interaction forces with specific crystallographic facets of the nanomaterials.¹⁶⁻¹⁹ In fact, by employing this strategy, numerous exciting results have been reported demonstrating the synthesis of metal nanostructures displaying an exceptional variety of well-defined shapes, as depicted in Figure 1.2.

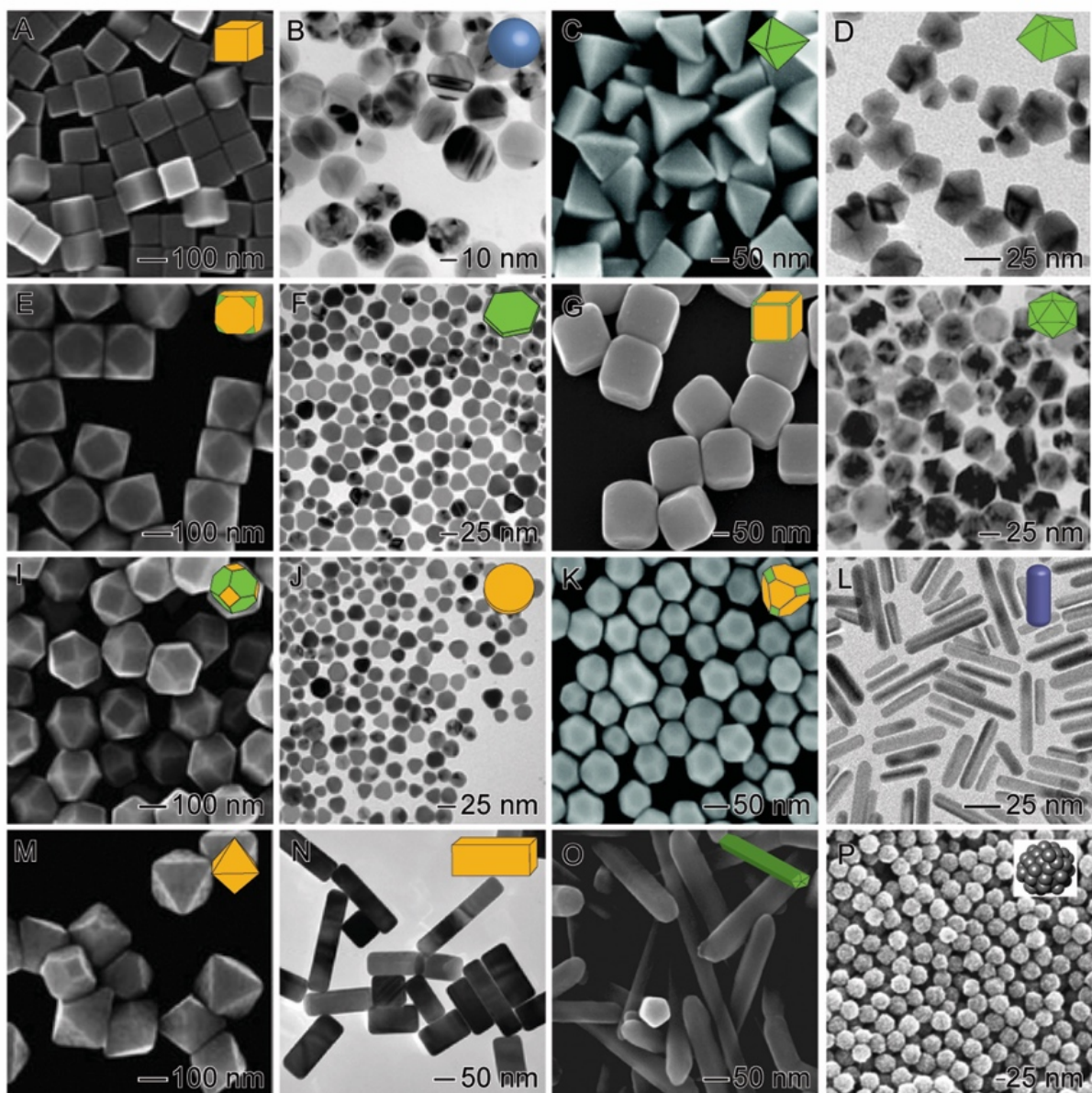


Figure 1.2. Different shapes of metal-based nanostructures synthesized by “bottom-up” approaches (chemical methods).

Thus, thanks to advances in synthesis, significant development have taken place for the engineering of a variety of nanodevices and in fields such as electronics,^{20,21} medicine and healthcare, energy,^{4,5,22,23} biotechnology,⁴ and information technology²⁴. As a consequence, nanoparticles have occupied a prominent place in the modern science and technology being employed in at least one step for the production of many supplies daily consumed. They are also largely employed in the fabrication of a variety of devices such as photography supplies,

catalysts, biological labelers, photonic, electronic, optical, and information storage devices, building materials such as concrete and asphalt, among others.^{6,24–27}

1.2. Nanomaterials in catalysis

The use of catalysts is a reality for about 90% of the current chemical processes, highlighting the great applicability in a variety of fields such as petrochemical, pharmaceutical, agrochemical, environmental remediation, and others.^{27,28} In this context, heterogeneous catalysts occupy a prominent position, considering that these materials, at least in principle, can be easily separated from the reaction mixture, making possible their reuse for several cycles, reducing operational costs and minimizing the production of toxic residue and effluents.²⁷ In this context, heterogeneous catalysts based on nanoparticles stand out due their well-established superior properties compared to conventional industrial catalysts, which are essentially composed of polycrystalline nanoparticles with poorly defined facets and broad distributions in terms of both size and shape. These features consequently lead to deteriorating effects on the catalyst decreasing their stability, durability, and activity and/or selectivity.^{29,30}

In fact, the catalytic behavior presented by a specific material is not only associated with nature of the components in its structure but is also extremely dependent on the physicochemical properties that defined the catalyst.^{31–37} Among these properties, the most fundamental and simple is the size, which emerged as an important property with the discover of nanomaterials and has been intensively demonstrated as a feature that strongly affect the catalytic performance of a catalyst towards a target application.^{32–34,38,39} As depicted in Figure 1.3, the understanding on how the size affects the catalytic behavior of a specific material is intuitive and can be easily explained by geometric parameters. More specifically, for a fixed amount of any solid, the progressive decrease in its size leads to the increase in specific surface

area (surface area per unit of mass) and, consequently, an increase in number of surface atoms (or number of atoms exposed) is also achieved. Thus, the progressive decrease in the size is a powerful tool to maximize the atomic exposition and, thus, enhance the catalytic performance.

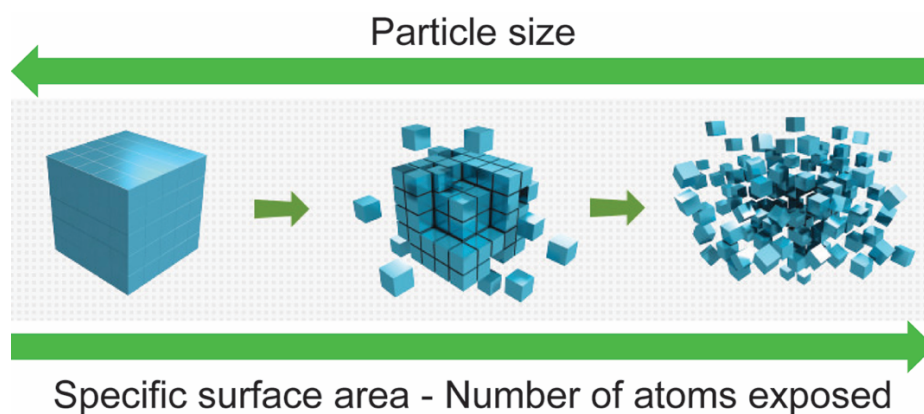


Figure 1.3. Scheme showing the increase in the surface area and number of atoms exposed with the increase in particle size.

As a consequence of the fast growth in the use of nanomaterials as catalysts for a variety of applications, a new and very promising field in nanoscience was created: nanocatalysis. Nanocatalysis has been based on the utilization of a variety of materials that include metals, semiconductors, oxides, and other compounds that play pivotal roles in many important chemical reactions.⁴⁰⁻⁴⁴ The central objective of the research in nanocatalysis is the development of catalysts displaying the highest activity, selectivity, and durability under low energy consumption conditions. Unfortunately, this scenario is merely hypothetical, and most catalysts reported to date do not meet these requirements.

Nanocatalysis fundamentally emerges as a new field in catalysis that combines the best characteristics of homogeneous and heterogeneous catalysis.⁴⁵ In homogeneous catalysis, atoms, ions, or molecules in solution are used as catalysts. Here, the catalytic species are totally dispersed and the maximum of atomic exposition is achieved leading to a good activity and selectivity.⁴⁶ On the other hand, as the catalysts are in solution, their separation and reuse is considerably difficult. In most cases, the catalysts are disposed after the product

purification.⁴⁶ In heterogeneous catalysis, the active material is in a distinct phase relative to the other components. Thus, even presenting lower activity and selectivity, its reusability is a very interesting feature.^{47,48} Consequently, nanocatalysis can be understood as a bridge connecting homogeneous and heterogeneous catalysis (Figure 1.4): ultrasmall nanoparticles with sizes progressively decreased relatively near to atomic dimensions displaying high performances as homogeneous catalysts. However, as solids, can be separated and reused as heterogeneous catalysts.

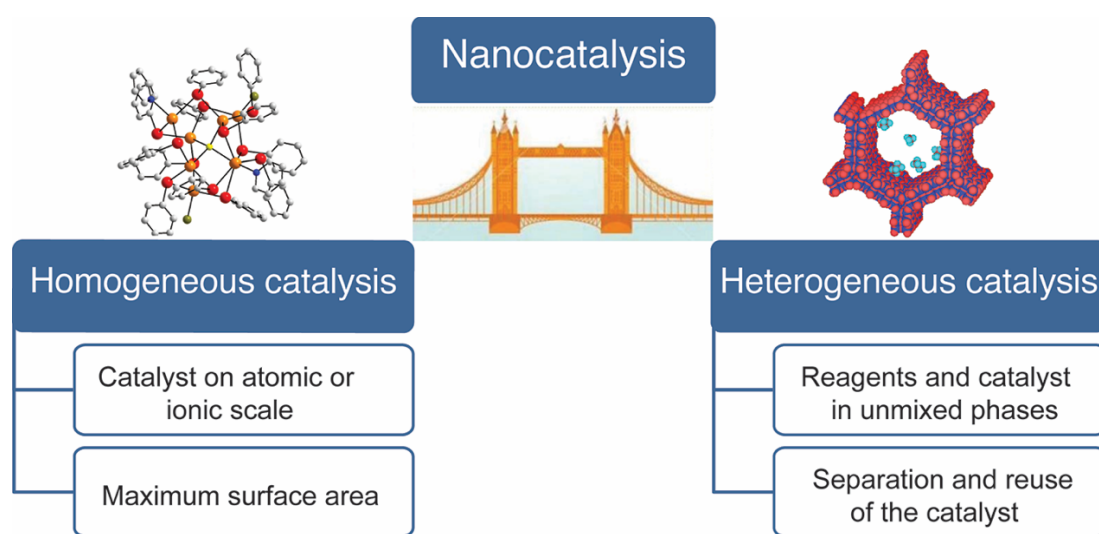


Figure 1.4. Scheme showing the increase in the surface area and number of atoms exposed with the increase in particle size.

Supported nanomaterials

The use of solid materials (such as powders, pellets, pieces, etc) as catalysts is very important for applications in practical catalytic systems. In the context of gas-phase reactions, for example, it is imperative. Supported catalysts contribute to easier separation from the reaction mixture as well as to avoid particle agglomeration, allowing them to be reused for several cycles, reducing operational costs and minimizing the production of toxic waste and effluents. However, the development of efficient methods for the “heterogenization” of catalysts based

on metallic nanoparticles has become a great challenge due to the demand for materials with high catalytic activities and that are stable, recyclable, have high surface areas and are economically attractive.^{49,50} The main limitation is the generation of heterogeneous catalysis based on supported noble metals, in which the metal component presents a uniform dispersion over the entire surface of the support (without agglomeration).⁵¹ For instance, the synthesis of supported catalysts is characterized by poor control over size, shape, composition of the noble metal component.⁵¹⁻⁵³ This scenario is characterized by the rudimentary approaches for the preparation of the most commercial catalysts, which still being produced by "mixing, shaking and baking" of multicomponent. This leads to the formation of nanoscale structures displaying poor control over the structure physicochemical properties. Also, as the synthesis of controlled nanostructures in solution are limited in terms of large-scale production, their deposition over solid supports by post-synthesis impregnation methods, for example, remains difficult. In this context, a heterogeneous catalyst is often a hybrid material composed of active sites that will catalyze the reaction (usually transition metals) on the surface of a solid, which is denoted as support or matrix.²⁷ Usually, they have high surface areas (up to $1400 \text{ m}^2 \cdot \text{g}^{-1}$), which is desired to maximize the number of active sites per unit volume of the material.

Hybrid nanomaterials based on oxides containing metallic nanoparticles with dimensions ranging from 1 to 50 nm on their surface, such as gold (Au) and rhodium (Rh), for example, have played a central role in catalysis.^{50,54} In this context, the preparation of catalysts using the principles of nanoscience opens new perspectives for increasing activity and developing new catalytic systems. Its aim is the control of chemical reactions by changing the size, composition and morphology of the catalysts, which are well-established parameters that defined the properties of a catalyst.^{41,44} Therefore, at least in principle, its properties can be adjusted through the control over these parameters, opening the possibility of the design of nanomaterials presenting optimized or desirable performance for an application of interest.

Because of this, the synthesis of supported nanomaterials has been extensively reported in the last decade.⁵⁵⁻⁶⁰ However, obtaining hybrid materials containing truly controlled metal nanoparticles is still challenging and remains limited. This problem can be illustrated by the synthesis of catalysts containing Au, Rh, or Ni nanoparticles, which, when incorporated into different solids such as TiO₂ (Figure 1.5A),⁶¹ iron oxides (Figure 1.5B),⁶² Mg₄Al₂(OH)₁₂(CO₃)·nH₂O (Figure 1.5C),⁶³ partially reduced graphene oxide (Figure 1.5D),⁶⁴ titanate nanotubes (Figure 1.5E),⁶⁵ CeO₂ (Figure 1.5F),⁶⁶ polystyrene (Figure 1.5G),⁶⁷ carbon nanotubes (Figure 1.5H),⁶⁸ SiO₂ (Figure 1.5I-J),⁶⁹⁻⁷¹ Carbon black (Figure 1.5K),⁷² graphene (Figure 1.5L),⁷³ present poor control over their shape, dispersion and uniformity, which limit the precise correlation between their structures, properties and performances. In addition, most of the synthesis protocols recently reported have large scale limitations, which produce at most hundreds of milligrams of catalysts (at low active phase levels), limiting the application of these systems in Pilot and industrial scales.⁶¹⁻⁶⁸

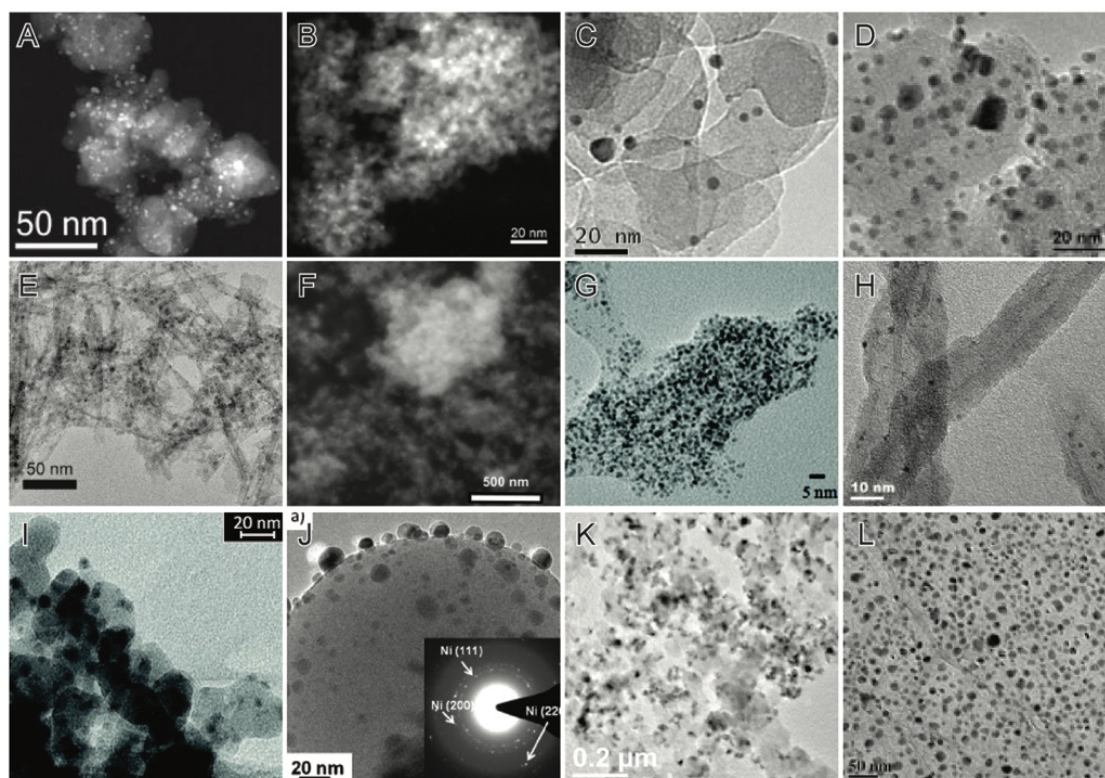


Figure 1.5. Scheme showing the increase in the surface area and number of atoms exposed with the increase in particle size.⁶¹⁻⁷³

1.3. Plasmon-enhanced/mediated catalysis

Ag and Au-based nanostructures have attracted much attention from the scientific community because of their excellent optical properties, which are a result of surface plasmon resonance (SPR) resonance of these metals.^{74,75} This phenomenon refers to the collective oscillation of the conduction electrons in relation to the positive structure of the nuclei that comprise the metal (Figure 1.6). The SPR can be observed through the interaction between the metallic nanostructure and an incident electromagnetic field, in which the oscillation of the electric field of the incident beam is the driving force for the collective oscillation of the electrons. In Ag and Au nanostructures, SPR typically occurs in the spectral region from visible to ultraviolet, which is extremely interesting because it allows the use of visible light as a source of plasmonic excitation.^{74,75}

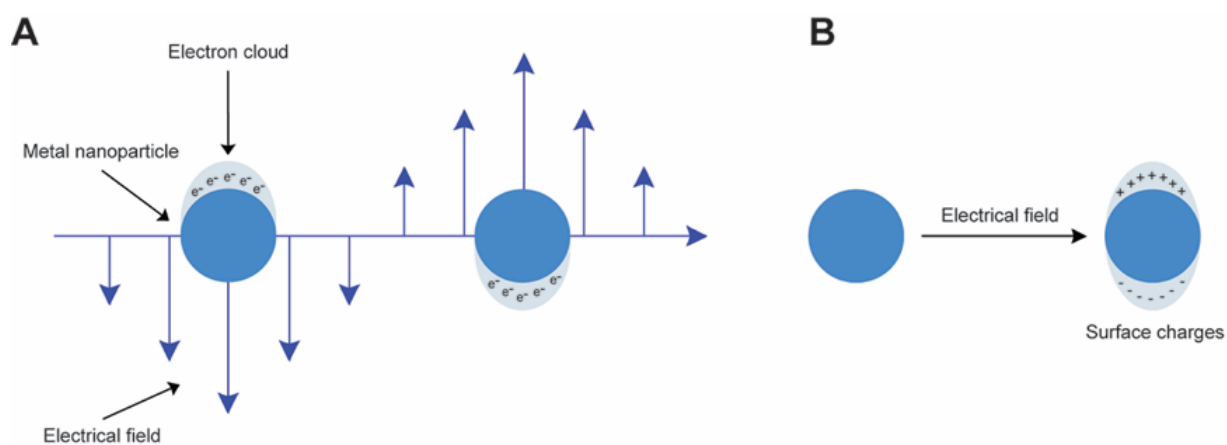


Figure 1.6. (A) Collective oscillation of electrons and (B) separation of charges on the surface of the nanoparticle due to the incidence of an electromagnetic beam.

Interestingly, among several possible applications, the enhancement of catalytic processes by SPR in the surface of Ag and Au nanoparticles has been recently explored. This intensification of catalytic processes due to plasmonic excitation can occur through several pathways, as illustrated in Figure 1.7. More specifically, four different mechanisms can enhance/mediate catalytic processes: i) the antenna effect, in which the plasmonic

nanostructure acts as a truly antenna capturing and transferring electrons from the electron beam to another specie; ii) charge transfer due to the formation of electron-hole pair (transference of electrons or holes), which can enhance both oxidative and reductive process, and iii) local the heating achieved from the constant oscillation of the electron cloud of the plasmonic nanoparticles.⁷⁶

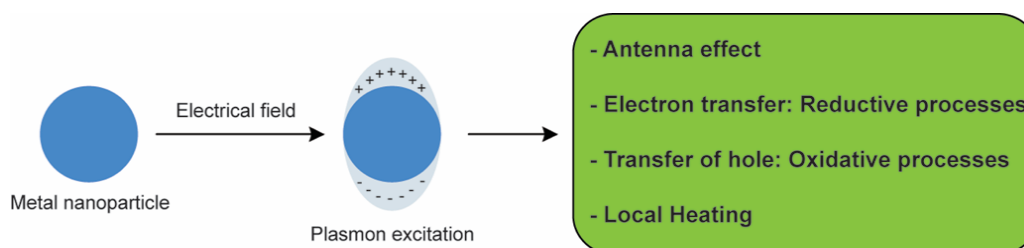


Figure 1.7. Possible routes intensification of reactions via plasmonic excitation of metal nanoparticles.⁷⁶

An important aspect is the fact that SPR is a phenomenon whose magnitude is extremely dependent on nanoparticle properties such as size, morphology and composition, which can be manipulated and allow the maximization of this effect.⁷⁷⁻⁷⁹ In this context, based on the morphology of the proposed nanostructures, the effect of plasmonic excitation of the Ag and Au, for example, can be a powerful tool for the enhancement of the catalytic activities of nanoparticles in which these components are present. Thus, to use of the knowledge generated in the field of plasmon-enhanced catalysis by correlating the performances with properties as size, composition, morphology, and dispersion may serve as a platform for the optimization of variety of processes that are of industrial interest.

1.4. Hollow nanomaterials

Among the huge variety of nanomaterials developed in past decades, nanostructures displaying hollow interiors and porous and thin walls have attracted significant attention because of their special and unique properties such as high chemical and thermal stability, high

specific surface area, high porosity, low overall density, lighter weight, high reactivity (as a consequence of high concentration of defective sites and ultrathin walls) and biocompatibility.⁸⁰⁻⁸⁶ Hollow nanomaterials have been extensively investigated towards many different applications that include catalysis, (conventional heterogeneous catalysis, photocatalysis, electrocatalysis, and plasmon-enhanced catalysis), energy production and storage, medicine (drug delivery, photo and thermal treatments, etc.), surface enhanced raman spectroscopy (SERS), encapsulation, protection of environmentally sensitive biological species, among others.^{5,87,88} Thus, in order to progressively optimize their performances towards these applications, new synthetic approaches have been reported and, consequently, an exceptional number of well-defined hollow nanomaterials have been produced including tubes, shells, cages, frames, dendrites, among other examples, as depicted in Figure 1.8.

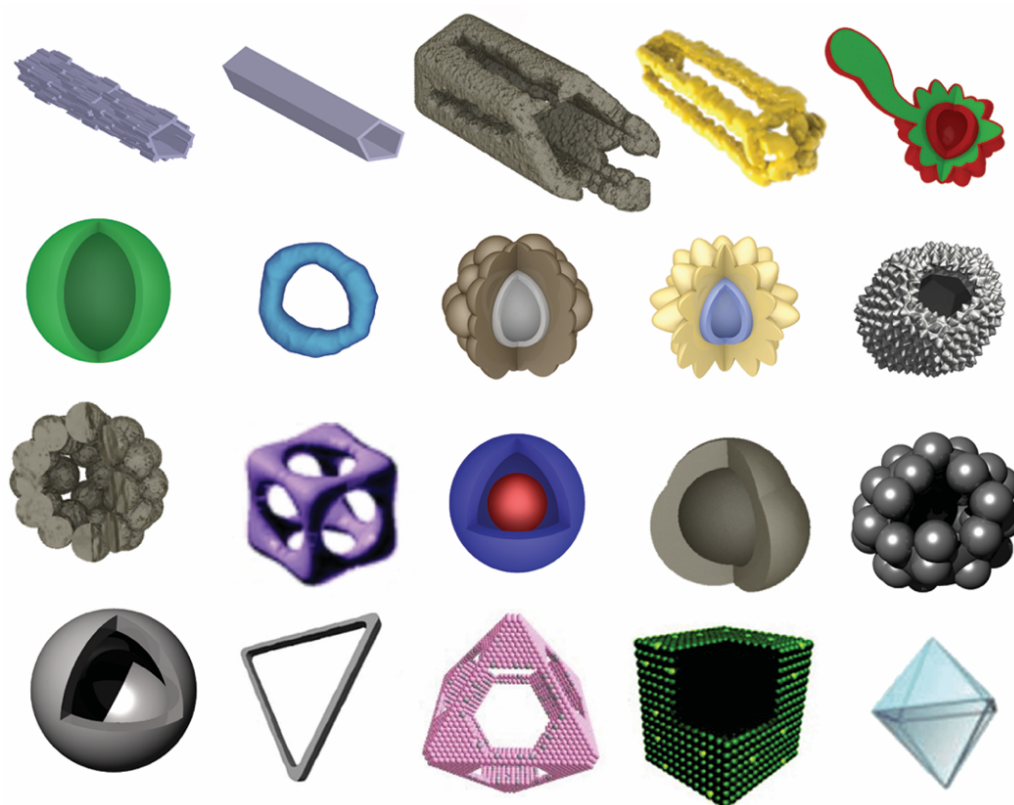


Figure 1.8. Scheme showing examples of well-defined hollow nanomaterials

In the context of catalysis, hollow nanomaterials are considered as a promising candidates due to the presence of high concentration of highly reactive sites such as stacking faults, twin planes, and high index facets.⁸⁷ As this class of nanomaterials present a well-defined hollow center, they are also considered as a type of nanoreactor, in which the cavity plays a pivotal role in the enhancement of the catalytic activity and selectivity.⁸⁹ In fact, the precise understanding on how the hole improve the catalytic behavior remains unclear.⁹⁰ However, as depicted in Figure 1.9, when a hollow nanomaterial is employed as catalyst, the atoms in the interior of the nanoparticles are not “wasted”. Thus, an additional role over catalytic properties is observed. At worst, disregarding the possible higher reactivity of the inner atoms, at least an increase in the number of active sites is obtained. Thus, in addition to the outer atoms, which are already naturally available to catalyze reactions, a significant contribution of the atoms of the interior is achieved.

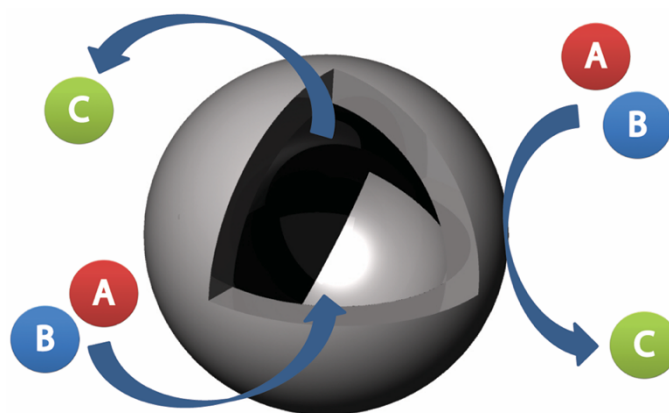


Figure 1.9. Scheme showing examples of well-defined hollow nanomaterials

Concerning the methods for the synthesis of hollow nanomaterials, two main approaches deserve special attention: i) template-mediated approach and ii) template-free approach. Herein, as expected, the main difference is the utilization (or not) of a preformed template (e.g., metal nanoparticles such as Au, Ag, and Pd, SiO₂ beads, polymeric structures) during the synthesis of the hollow material. The employed template can be described as

chemical (sacrificial) or physical depending. This concept is related to the possible consumption (dissolution) of the template during the step of coating of their surfaces. More specifically, chemical templates are consumed in this during the coating step, justifying the sacrificial terminology. However, the physical templates keep unchanged and is only removed in next step. The main reported template-mediated approaches for the synthesis of hollow nanomaterials are the template etching, dissolution, or degradation, nanoscale Kirkendall effect, and galvanic replacement reaction. On the other hand, the only reported template-free approach is the Ostwald ripening. The next four subsections describe the synthesis of hollow nanostructures using the mentioned synthetic approaches.

Template etching, dissolution, or degradation

Template etching or dissolution can be easily described as a two-step process. In the first step, the surface of a preformed template displaying desired properties (usually size, shape, and composition) is covered with a second phase, leading the formation a core-shell structure. In a second step, the selective removal of the template is performed by a post-treatment, which leads to the formation of hollow particles as depicted in Figure 1.10. Interestingly, by using templates based on nanostructures displaying well-defined morphologies that include spheres, triangular plates, cubes, rods, and wires, It is possible the production of hollow structures with various morphologies similar to those of the employed templates.

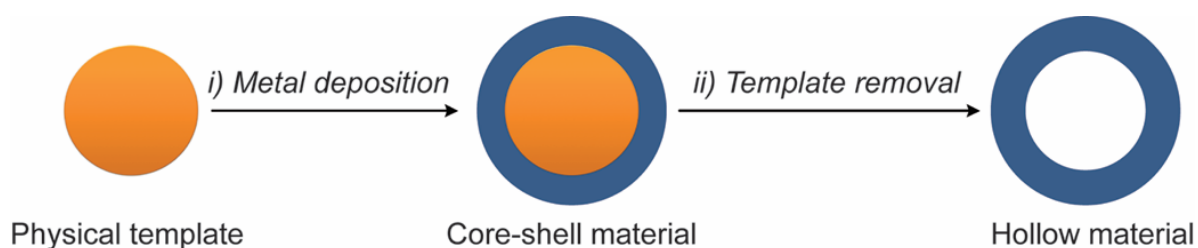


Figure 1.10. Scheme showing the mechanism of formation of hollow nanomaterials by Template etching or dissolution approaches.

Among the several methods developed for coating the surface of preformed templates, chemical deposition, layer-by-layer assembly, and adsorption are the mostly employed techniques. Herein, the chemical deposition stands out due to its relative simplicity, high output (high concentration of nanoparticles per synthesis), and robustness compared to other procedures. Concerning the step for the template removal, chemical and physical methods can be applied. The choice of the best protocol will be made considering the properties of the species involved, which determine the efficacy and selectivity of the process.^{84,91-93}

The chemical methods are based on the selective etching (chemical oxidation/dissolution) by using specific reagents that selectively oxidize and remove the template from the core-shell structure generated in the first step of coating. As an example of this procedure, we can highlight the synthesis of a Pt-enriched icosahedral nanocage displaying ultrathin walls (Figure 1.11).⁹⁴ In this case, in a first step, Pt atoms were uniformly deposited on the surface of preformed Pd icosahedral seeds by chemical reduction of PtCl_6^{2-} precursor in the presence of ethyleneglycol. This leads to the formation of a Pd@Pt core-shell structure. After this step, the selective removal of the Pd core is performed by using a concentrated HNO_3 solution. Herein, the selective Pd dissolution is achieved by the stability of Pt in a HNO_3 solution. Thus, only Pd is dissolved and the outer layer of Pt remains unaffected, making possible the formation of the icosahedral Pt-enriched nanocage. Interestingly, as only a few layers of Pt were deposited over the Pd template, an ultrathin wall of Pt was obtained. However, for the synthesis of hollow nanomaterials displaying thicker walls more layers of Pt could be deposited in the first step.

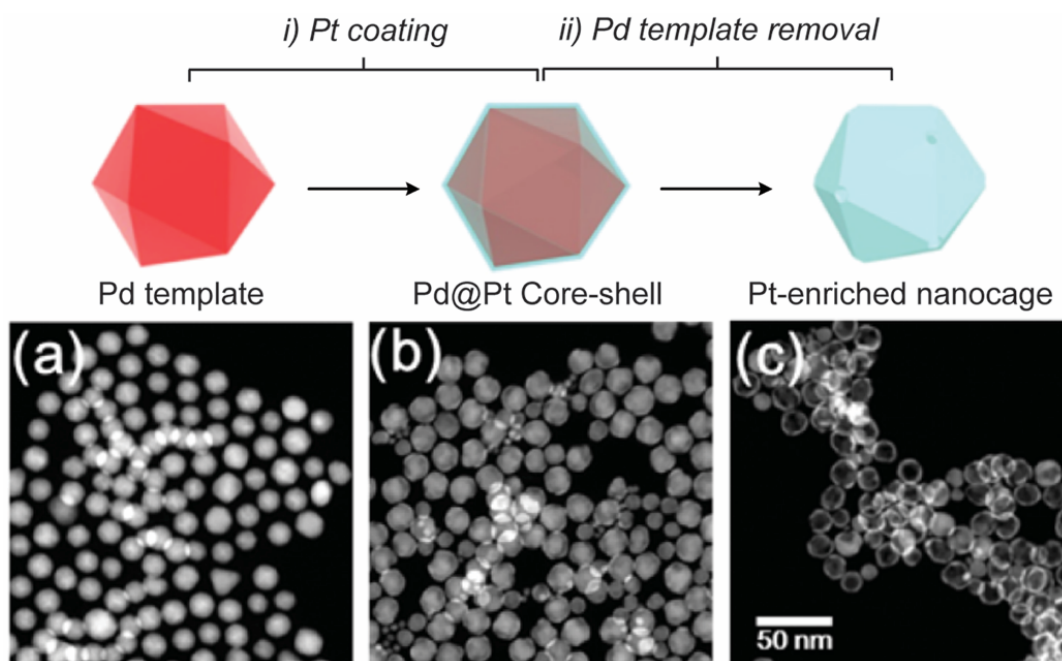


Figure 1.11. Pt-enriched icosahedral nanocages displaying ultrathin walls obtained by selective removal of the Pd core from Pd@Pt icosahedral structure by using a concentrated HNO₃ solution.⁹⁴

On the other hand, the physical methods (template dissolution or degradation) are basically performed under the same steps described in the template etching approach. However, the removal of the template is performed by dissolution using specific solvents (usually organic solvents) or by thermal treatments (calcination or pyrolysis).⁹² In this context, for the use of these procedures organic templates such as polymers are demanded due their solubility in organic solvents and relatively low temperature of degradation. An interesting illustrative example of this strategy is the synthesis of metal oxide hollow (SnO₂, Al₂O₃, Ga₂O₃, CoO, NiO, Mn₃O₄, Cr₂O₃, La₂O₃, Y₂O₃, Lu₂O₃, CeO₂, TiO₂, and ZrO₂) spheres by using carbonaceous polysaccharide microspheres as templates (Figure 1.12).⁹² In this reported approach, the first step concerns in the adsorption of metal ions in solution onto the surface of the template, which presents a high concentration of -OH functional groups at the surface. Thus, the metal ions are strongly attached to the surface of the carbonaceous saccharide microspheres making possible a subsequent step of template removal without loss of shape of

the metallic outer layer. Finally, due its relatively low thermal stability compared to the metallic outer, the carbonaceous template can be easily, selectively, and efficiently removed by a step of calcination, which leads the formation of hollow spheres.

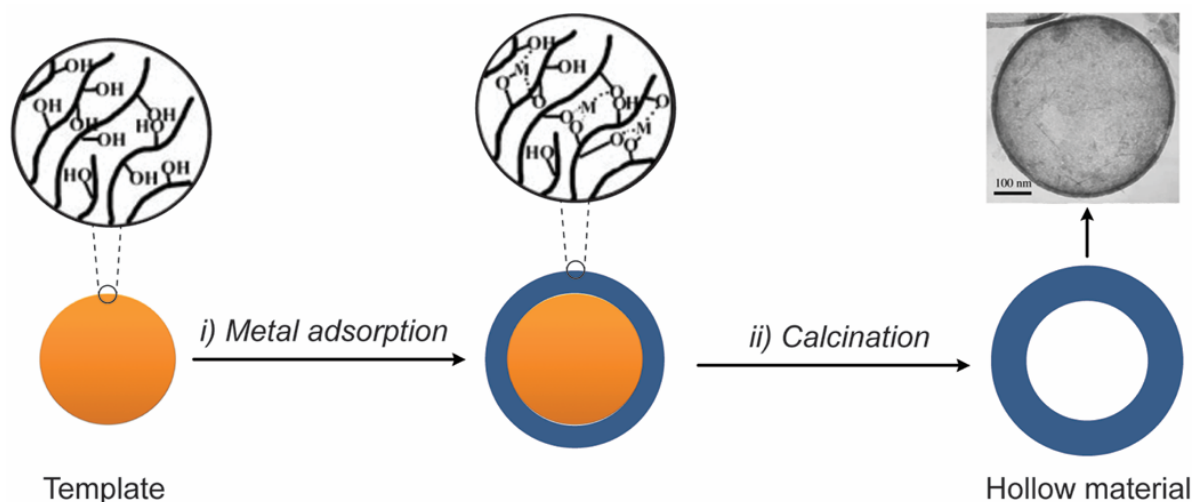


Figure 1.12. Schematic representation of the formation of metal oxide hollow spheres by using carbonaceous microspheres as templates.⁹²

Nanoscale Kirkendall effect

The Kirkendall effect is a general procedure for the production of hollow nanostructures, which concerns in the concise explanation on why holes can be formed in multicomponent structures. More specifically, this effect associated the formation holes as consequence of diffusive migrations among different atomic species in metals and alloys under heating conditions due to the differences in diffusion rates between the involved components. Mechanistically, as depicted in Figure 1.13, the Kirkendall effect starts when vacancies are concentrated in a region of fast diffusion region of the nanostructures. Thus, when the vacancy concentration exceeds the saturation limit, the formation of holes is observed as consequence of the nucleation of the vacancies leading to the formation of diverse variety of hollow micro and nanostructures. Herein, the formation of filaments that connect the core and the shell is

commonly associated to the preferential nucleation of holes near the core–shell interface.^{91,95–}

98

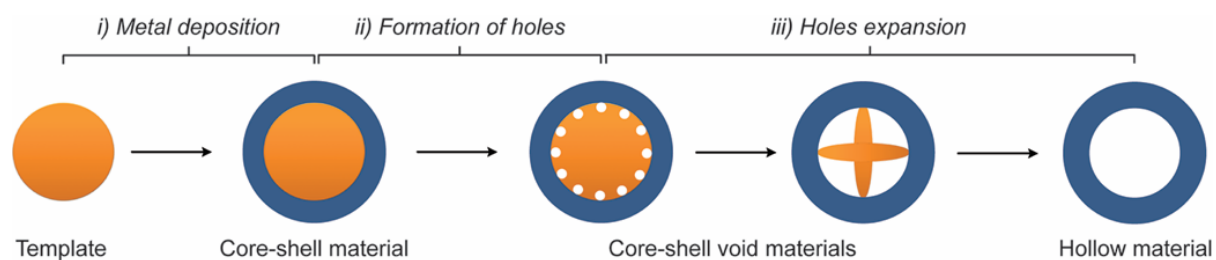


Figure 1.13. Scheme showing the mechanism of formation of hollow nanomaterials by Template etching or dissolution approaches.

The first demonstration of the nanoscale Kirkendall effect was the synthesis of hollow CoS by the reaction between Co nanoparticles elemental sulfur (S) under heating at 180 °C.⁹⁵ Herein, in agreement with the original proposition by Kirkendall, during the reaction process, an outward migration Co is observed due to its superior diffusion rate compared to S. Thus, the supersaturation of vacancies is achieved leading to their aggregation and formation a hole in the center of the nanomaterial. Interestingly, the same behavior is observed for the synthesis employing Se instead of S. However, the slower reaction rate between Co and Se made possible the isolation of particles at the different stages of the hollowing process. As depicted in Figure 1.14, the shape evolution matches exactly the Kirkendall mechanism applied for the synthesis of hollow nanomaterials.

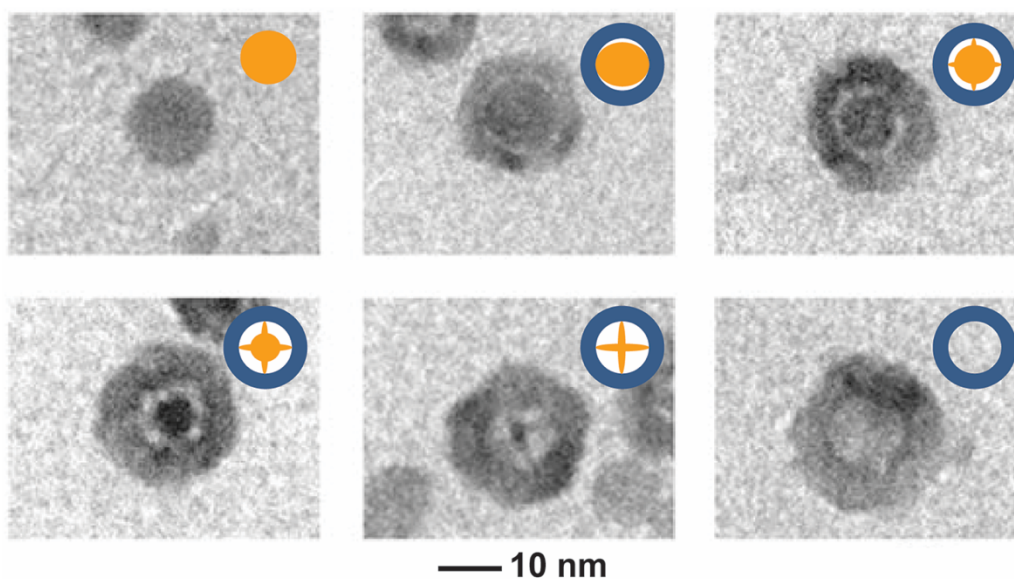


Figure 1.14. Scheme showing the mechanism of formation of hollow nanomaterials by Template etching or dissolution approaches.⁹⁵

Ostwald ripening

Ostwald ripening is considered a well-established mechanism in the synthesis of a variety of nanomaterials and, interestingly, is also used to explain the formation of nanoparticles displaying hollow interiors. The driving force for the occurrence of Ostwald ripening is the difference in the chemical potential among particles with different sizes, which grow into bigger nanoparticles, which present higher stability due to the minimization in total surface area of the system. More specifically, the target process involves the dissolution of smaller particles, which have higher solubility than the large ones, followed by the redeposition over the surface of large crystals which consequently grow. In the context of the synthesis of hollow nanomaterials, Ostwald ripening is the only example of a self-templating method (performed under the absence of a preformed template during the synthesis).^{84,96,99}

In order to illustrate the mechanism involved in the formation of hollow nanomaterials by Ostwald ripening, we selected the formation of hollow Cu_2O nanospheres by aggregation and reductive transformation of colloidal CuO nanoparticles.¹⁰⁰ This present work

demonstrated clearly the Ostwald ripening mechanism by providing the evolution of the crystal morphology as function of reaction time, as depicted in Figure 1.15. In the first step, small nanoparticles are generated in the reaction mixture and attach each other into spherical aggregates with diameters in the range of 100–200 nm. With the reaction progress, the formation of a hole at the center of the obtained agglomerate showing a type of core evacuation. Interesting, the hollowing process is achieved gradually in the center of Cu₂O nanospheres leading the formation of thinner shells. As the formation of larger nanoparticles is thermodynamically favored and smaller nanoparticles show superior solubility compared to larger ones, the observation of Ostwald ripening mechanism is intuitive for this target system. However, why hollow interiors are observed in the obtained Cu₂O nanospheres? This explanation can be easily provided by a precise analysis in the TEM images of the obtained agglomerates. Herein, it is observed that the smaller nanoparticles are located at the center of the agglomerates. Thus, as a consequence of their higher surface energy, solubility, and tendency of relocation, the Ostwald ripening mechanism is observed.

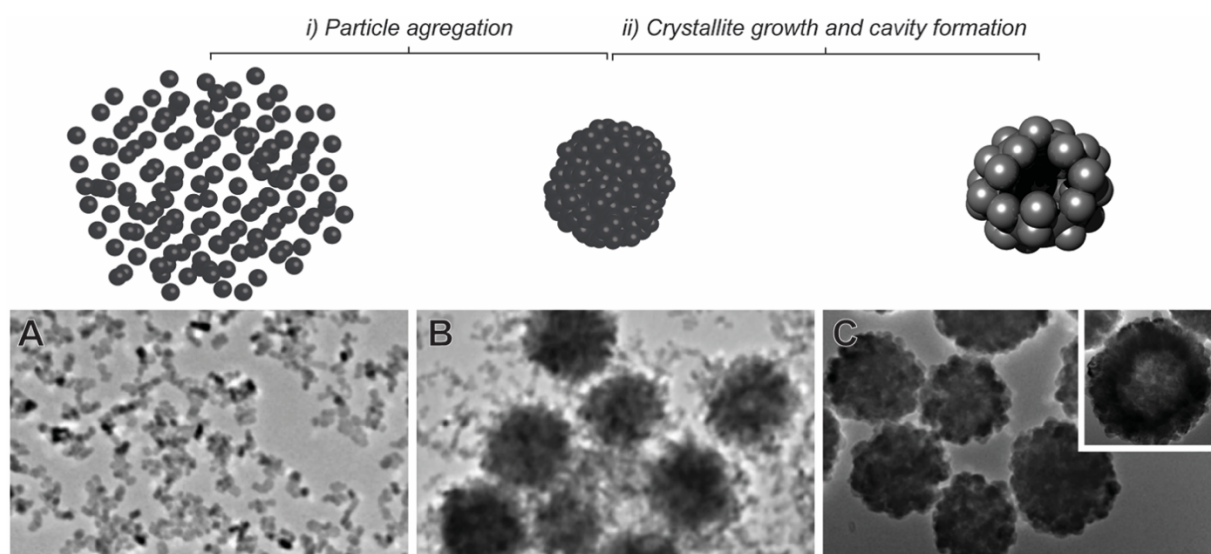


Figure 1.15. Scheme showing the mechanism of formation of hollow nanomaterials by Template etching or dissolution approaches.¹⁰⁰

Galvanic replacement reaction

Galvanic replacement reaction is largely employed template-mediated approach for the fabrication of a wide variety of hollow nanocrystals and is considered a very simple approach compared to the other procedures to the same end especially considering that the additional step of template removal is not required. Galvanic replacement reaction can be easily described a typical electrochemical process between one performed metal template (also denoted as sacrificial template) and metal ions with higher reduction potential. Thus, electrons are transferred from the template, which is partially oxidized and dissolved together with the reduction and deposition of metal ions to metal atoms. Interesting, the final structure of the obtained nanomaterials is characterized by a hollow nanostructure that presents a similar shape of the initial template as depicted in Figure 1.16.^{81,82,84,91,101}

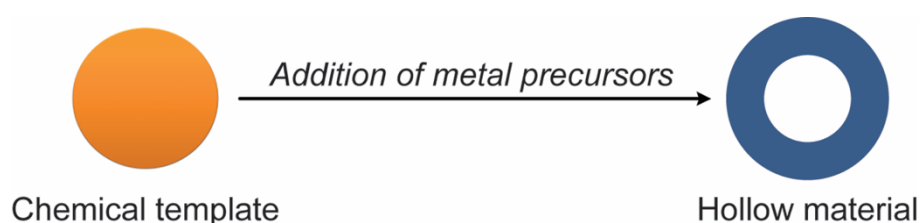


Figure 1.16. Scheme showing the mechanism of formation of hollow nanomaterials by Template etching or dissolution approaches.

The best example that illustrates the galvanic replacement reaction approach for the synthesis of hollow nanomaterials is the synthesis of bimetallic AgAu nanoparticles (shells, cages, frames, and tubes). This system is basically described by the progressive addition of AuCl_4^- precursor into a suspension containing preformed of Ag nanoparticles (spheres, cubes, wires, etc). Herein, the galvanic replacement reaction is started by the corrosion of Ag atoms at more reactive sites such as defects, stacking faults, or steps. During this process, Ag atoms are oxidized to Ag^+ and dissolved into solution and simultaneously AuCl_4^- is reduced and

deposited on the surface of the Ag template leading to the formation of a thin and incomplete layer of Au on the Ag template, which prevent the direct oxidation of Ag. However, due to an alloying process, additional Ag is oxidized and a small surface hole is typically formed, which serves as site for continuous dissolution of Ag from the core and AuCl_4^- deposition. In this context, with the increase in the amount of AuCl_4^- precursor added to the suspension, an increase in the hollowing degree is achieved and a variety of hollow structures can be obtained. Thus, by the careful tuning in the molar ratio $\text{AuCl}_4^-:\text{Ag}$ it is possible to create hollow nanomaterials displaying different hollowing degrees and, consequently, different structures.^{82,91,102} Figure 1.17 shows an example of this strategy employing Ag nanospheres as sacrificial templates in the reaction with Au^{3+} precursor.

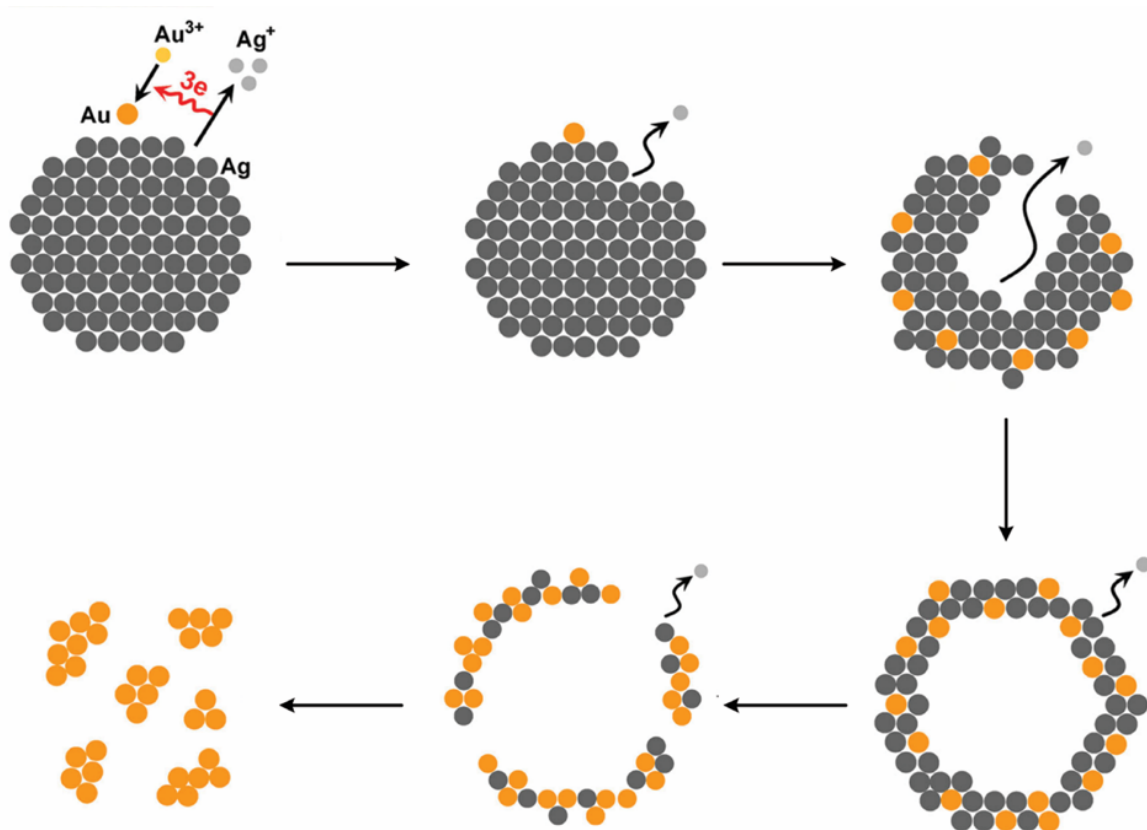


Figure 1.17. Scheme showing the mechanism of formation of hollow nanomaterials by Template etching or dissolution approaches.⁸²

Another promising strategy involving the galvanic replacement reaction is the combination with a co-reduction process involving the employing of an auxiliary reducing agent such as ascorbic acid, hydrazine, and hydroquinone, for example.^{103,104} In this procedure, the galvanic replacement process enables the formation of hollow interiors and, as expected, the final structure of the generated nanoparticles also resembles the sacrificial template. However, additional metal deposition onto the surface of the hollow nanoparticles is achieved by reduction of metal ions promoted by the auxiliary reducing agent. Thus, another strategy for shape control is achieved by coupling both galvanic replacement and coreduction processes.¹⁰¹ More specifically, the control over surface morphology can be enabled by adjusting reaction parameter such as molar ratio metal:metal precursor, temperature, and nature and amount of the auxiliary reducing agent.^{14,37,38,101,105,106}

An example of this strategy is the control of the size and surface morphology of AgAu nanodendrites (Figure 1.18).¹⁴ Herein, the precise adjust in the number of Ag nanoparticles used as templates in the process provided a fast and effective approach for the manipulation over the size and morphology of nanoparticles produced via a combined galvanic replacement and reduction reaction. More specifically, when the number of Ag nanoparticles employed is increased, larger nanodendrites are obtained as consequence of the increase in the number of sites available for Au heterogeneous nucleation and growth. More specifically, for a fixed concentration of AuCl_4^- (aq), when the number of Ag nanospheres is increased, a decrease in the amount of Au available for the growth of Au branches at the surface of each seed is achieved. Thus, a decrease in the overall diameter and in the size of the individual branches is observed in the resulting nanodendrites.

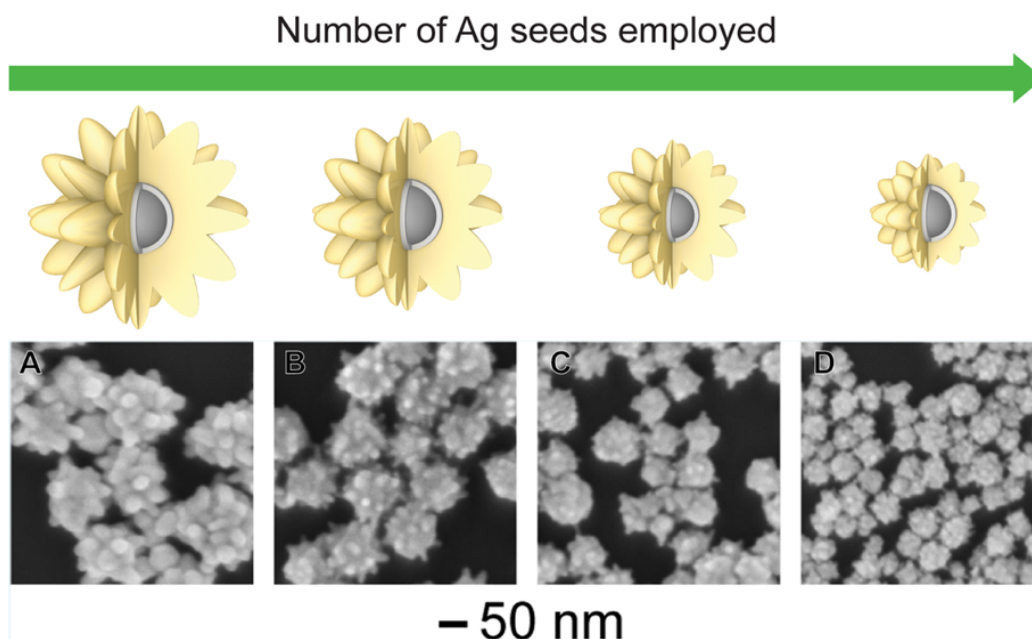


Figure 1.18. SEM images of AgAu nanodendrites displaying controlled surface morphologies obtained by varying the volume of Ag NP seed suspension employed during the synthesis: (A) 1 μL , (B) 3 μL , (C) 5 μL , and (D) 10 μL .

1.5. Scope of this work

This project proposes the use of methodologies based on the galvanic replacement reaction and its combination with additional metal deposition in the presence of hydroquinone as an auxiliary reducing agent as a platform for obtaining a variety of metallic nanostructures with hollow interiors displaying controlled and well-defined morphologies, sizes, and compositions for applications in catalysis and plasmonic photocatalysis. In addition, to enable the application of nanomaterials in gas-phase transformations, the synthetic developed approaches need to be scale-up in order to produce sufficient amount of nanoparticles, which must be incorporated on a solid support for the production of a powdered catalyst.

In the first part of this work (Chapters 2, 3, and 4), we present the use of the galvanic replacement reaction between preformed Ag nanoparticles (spheres and wires) as strategy for the synthesis of nanoshells and nanotubes for application in catalysis and plasmonic photocatalysis. More specifically, in Chapter 2, trimetallic nanoshells having AgAuPd,

AgAuPt, and AgPdPt compositions were obtained by a sequential galvanic reaction between Ag nanospheres and the corresponding metal precursors, i.e., AuCl_4^- (aq), PdCl_4^{2-} (aq), and/or PtCl_6^{2-} (aq). The obtained nanoshells were employed as model systems to investigate the effect of the addition of the third metal over the catalytic activities towards the 4-nitrophenol reduction, which demonstrated a significant enhancement in the catalytic activities relative to the sum of their bimetallic counterparts. In the Chapter 3, by the galvanic reaction between Ag nanospheres and AuCl_4^- (aq), well-defined AgAu nanorings displaying SPR extinction that matched the emission spectra of a commercial halogen-tungsten lamp were obtained. Thus, they were employed as catalysts for SPR-mediated oxidation of methylene blue, under ambient conditions, and using the halogen-tungsten lamp as the only energy input. The nanorings showed superior performances compared to Ag, Au, and AgAu nanospheres. In the chapter 4, AgAu nanotubes displaying controlled and well-defined surface morphologies and optical properties were obtained by the galvanic reaction between Ag nanowires and AuCl_4^- (aq) at 25 or 100 °C. Herein, the reaction temperature was the key element for the control over the nanotubes properties. AgAu nanotubes were then employed as catalysts towards the methylene blue oxidation by “classical” heterogeneous catalysts and plasmonic photocatalysis, in which the understanding on how their performances were dependent on their surface morphologies (branched or smooth surfaces) and optical properties (position and intensity of SPR extinction bands) was investigated.

In the second part of this dissertation (Chapters 5, 6, and 7), a combination between galvanic reaction between Ag nanoparticles (spheres and wires) and additional metal deposition in the presence of hydroquinone was the strategy for the precise control over the nanoparticles properties. Chapter 5, describes the synthesis of AgPt hollow nanodendrites, which could be scaled up by 100 folds and uniformly supported onto a commercial silica. The AgPt nanodendrites displayed good catalytic activities for both the 4-nitrophenol reduction

(non supported catalyst) and the BTX oxidation reactions (supported catalyst). In the Chapter 6, the same strategy was employed. However, Ag nanoparticles with different sizes were as templates leading to differences in the outer diameter, shell thickness, and the number of Pt surface atoms of the produced nanoshells. The produced AgPt nanoshells were supported onto SiO₂, and evaluated towards the gas-phase oxidation of benzene, toluene and o-xylene, in which their catalytic performances could be correlated with their controlled properties. In the Chapter 7, both galvanic replacement and its combination with additional metal deposition with hydroquinone were employed for the synthesis of AgPt nanoshells and nanotubes displaying controlled surface morphologies. Thus, a systematic investigation on how the number of Pt surface atoms and nature of exposed surface facets affected the catalytic performances of AgPt nanomaterials towards the CO oxidation (gas-phase) was performed. Herein, AgPt/SiO₂ catalysts were produced after scale-up the synthesis of nanostructures and their uniform incorporation over a commercial SiO₂.

Finally, in the last part of this work (Chapters 8 and 9), we present the synthesis in high yields of Cu₂O spheres displaying well-defined shapes and monodisperse sizes and their utilization as catalyst for a “click reaction” and as templates for the synthesis of complexes bimetallic nano hybrids. More specifically, in Chapter 8, Cu₂O spheres were employed as the source of highly catalytic active Cu(I) species towards click reactions between several of alkynes and azides to produce a variety of 1,2,3-triazoles under ligand-free and ambient conditions (in an open reactor) showing superior performance as compared to a conventional homogenous protocol and enabling the synthesis of seven not previously reported products. On the other hand, in Chapter 9, Cu₂O spheres were employed as sacrificial templates for reducing PdCl₄²⁻_(aq), AuCl₄⁻_(aq), and Ru³⁺_(aq), metal precursors. Herein, by simply changing the nature of the precursor the final morphologies were strongly affected as consequence of the difference

of their kinetic of reduction. The mechanisms concerning of the formation of all nanohybrids were provided as well as their catalytic performances toward the 4-nitrophenol reduction.

1.6. References

- (1) From an Idea to a Vision: There's Plenty of Room at the Bottom. *Am. J. Phys.* **2006**, *74* (9), 825–830.
- (2) Buot, F. A. Mesoscopic Physics and Nanoelectronics: Nanoscience and Nanotechnology. *Phys. Rep.* **1993**, *234* (2), 73–174.
- (3) Whitesides, G. M. Nanoscience, Nanotechnology, and Chemistry. *Small* **2005**, *1* (2), 172–179.
- (4) Salata, O. V. Applications of Nanoparticles in Biology and Medicine. *J. Nanobiotechnology* **2004**, *2* (1), 3.
- (5) Aguilar, Z. P.; Aguilar, Y.; Xu, H.; Jones, B.; Dixon, J.; Xu, H.; Wang, Y. A. Nanomaterials in Medicine. *ECS Trans.* **2010**, *33* (8), 69–74.
- (6) Fang, C.; Yu, R.; Liu, S.; Li, Y. Nanomaterials Applied in Asphalt Modification: A Review. *J. Mater. Sci. Technol.* **2013**, *29* (7), 589–594.
- (7) Colloidal Nanocrystals for Telecommunications. Complete Coverage of the Low-Loss Fiber Windows by Mercury Telluride Quantum Dot . *Pure and Applied Chemistry* . 2000, p 295.
- (8) Ramsden, J. J. Chapter 1 - What Is Nanotechnology? BT - Applied Nanotechnology (Second Edition). In *Micro and Nano Technologies*; William Andrew Publishing: Oxford, 2014; pp 3–12.
- (9) Ramsden, J. J. Chapter 2 - The Nanoscale BT - Nanotechnology. In *Micro and Nano Technologies*; William Andrew Publishing: Oxford, 2016; pp 19–40.
- (10) Sabatier, P. A. Top-Down and Bottom-Up Approaches to Implementation Research: A Critical Analysis and Suggested Synthesis. *J. Public Policy* **1986**, *6* (1), 21–48.
- (11) Mijatovic, D.; Eijkel, J. C. T.; van den Berg, A. Technologies for Nanofluidic Systems: Top-down vs. Bottom-up-a Review. *Lab Chip* **2005**, *5* (5), 492–500.
- (12) Sarter, M.; Givens, B.; Bruno, J. P. The Cognitive Neuroscience of Sustained Attention: Where Top-down Meets Bottom-Up. *Brain Res. Rev.* **2001**, *35* (2), 146–160.
- (13) Silva, G. A. Neuroscience Nanotechnology: Progress, Opportunities and Challenges. *Nat Rev Neurosci* **2006**, *7* (1), 65–74.
- (14) da Silva, A. G. M.; Rodrigues, T. S.; Slater, T. J. A.; Lewis, E. A.; Alves, R. S.; Fajardo, H. V.; Balzer, R.; da Silva, A. H. M.; de Freitas, I. C.; Oliveira, D. C.; et al. Controlling Size, Morphology, and Surface Composition of AgAu Nanodendrites in 15 S for Improved Environmental Catalysis under Low Metal Loadings. *ACS Appl. Mater. Interfaces* **2015**, *7* (46), 25624–25632.
- (15) Yu, C.-H.; Tam, K.; Tsang, E. S. C. Chapter 5 Chemical Methods for Preparation of Nanoparticles in Solution. In *Metallic Nanoparticles*; Physics, J. A. B. B. T.-H. of M., Ed.; Elsevier, 2008; Vol. Volume 5, pp 113–141.
- (16) Wiley, B.; Sun, Y.; Mayers, B.; Xia, Y. Shape-Controlled Synthesis of Metal Nanostructures: The Case of Silver. *Chem. – A Eur. J.* **2005**, *11* (2), 454–463.
- (17) Zeng, J.; Xia, X.; Rycenga, M.; Henneghan, P.; Li, Q.; Xia, Y. Successive Deposition of Silver on Silver Nanoplates: Lateral versus Vertical Growth. *Angew. Chemie Int. Ed.* **2011**, *50* (1), 244–249.
- (18) Xia, X.; Zeng, J.; Oetjen, L. K.; Li, Q.; Xia, Y. Quantitative Analysis of the Role Played by Poly(vinylpyrrolidone) in Seed-Mediated Growth of Ag Nanocrystals. *J. Am. Chem.*

- Soc.* **2012**, *134* (3), 1793–1801.
- (19) Zeng, J.; Zheng, Y.; Rycenga, M.; Tao, J.; Li, Z.-Y.; Zhang, Q.; Zhu, Y.; Xia, Y. Controlling the Shapes of Silver Nanocrystals with Different Capping Agents. *J. Am. Chem. Soc.* **2010**, *132* (25), 8552–8553.
 - (20) Shen, W.; Zhang, X.; Huang, Q.; Xu, Q.; Song, W. Preparation of Solid Silver Nanoparticles for Inkjet Printed Flexible Electronics with High Conductivity. *Nanoscale* **2014**, *6* (3), 1622–1628.
 - (21) Minari, T.; Kanehara, Y.; Liu, C.; Sakamoto, K.; Yasuda, T.; Yaguchi, A.; Tsukada, S.; Kashizaki, K.; Kanehara, M. Printed Electronics: Room-Temperature Printing of Organic Thin-Film Transistors with π -Junction Gold Nanoparticles (Adv. Funct. Mater. 31/2014). *Adv. Funct. Mater.* **2014**, *24* (31), 4869.
 - (22) Lane, L. A.; Qian, X.; Nie, S. SERS Nanoparticles in Medicine: From Label-Free Detection to Spectroscopic Tagging. *Chem. Rev.* **2015**, *115* (19), 10489–10529.
 - (23) Lohse, S. E.; Murphy, C. J. Applications of Colloidal Inorganic Nanoparticles: From Medicine to Energy. *J. Am. Chem. Soc.* **2012**, *134* (38), 15607–15620.
 - (24) *Nanoelectronics and Information Technology: Advanced Electronic Materials and Novel Devices*; Waser, R., Ed.; John Wiley & Sons, Inc.: New York, NY, USA, 2003.
 - (25) Denicourt-Nowicki, A.; Roucoux, A. Metallic Nanoparticles in Neat Water for Catalytic Applications. In *Nanomaterials in Catalysis*; Wiley-VCH Verlag GmbH & Co. KGaA, 2013; pp 55–95.
 - (26) Yu, W.; Porosoff, M. D.; Chen, J. G. Review of Pt-Based Bimetallic Catalysis: From Model Surfaces to Supported Catalysts. *Chem. Rev.* **2012**, *112* (11), 5780–5817.
 - (27) Mizuno, N.; Misono, M. Heterogeneous Catalysis. *Chem. Rev.* **1998**, *98* (1), 199–218.
 - (28) Copéret, C.; Chabanas, M.; Petroff Saint-Arroman, R.; Basset, J.-M. Homogeneous and Heterogeneous Catalysis: Bridging the Gap through Surface Organometallic Chemistry. *Angew. Chemie Int. Ed.* **2003**, *42* (2), 156–181.
 - (29) Stark, W. J.; Stoessel, P. R.; Wohlleben, W.; Hafner, A. Industrial Applications of Nanoparticles. *Chem. Soc. Rev.* **2015**, *44* (16), 5793–5805.
 - (30) Otera, J.; Nishikido, J. Industrial Uses. In *Esterification*; Wiley-VCH Verlag GmbH & Co. KGaA, 2009; pp 293–322.
 - (31) Chanda, K.; Rej, S.; Huang, M. H. Facet-Dependent Catalytic Activity of Cu₂O Nanocrystals in the One-Pot Synthesis of 1,2,3-Triazoles by Multicomponent Click Reactions. *Chem. – A Eur. J.* **2013**, *19* (47), 16036–16043.
 - (32) Shibata, T.; Bunker, B. A.; Zhang, Z.; Meisel, D.; Vardeman, C. F.; Gezelter, J. D. Size-Dependent Spontaneous Alloying of Au–Ag Nanoparticles. *J. Am. Chem. Soc.* **2002**, *124* (40), 11989–11996.
 - (33) Silva, A. G. M. da; Rodrigues, T. S.; Macedo, A.; Silva, R. T. P. da; Camargo, P. H. C. An Undergraduate Level Experiment on the Synthesis of Au Nanoparticles and Their Size-Dependent Optical and Catalytic Properties. *Química Nova*. scielo 2014, pp 1716–1720.
 - (34) Watanabe, Y.; Wu, X.; Hirata, H.; Isomura, N. Size-Dependent Catalytic Activity and Geometries of Size-Selected Pt Clusters on TiO₂(110) Surfaces. *Catal. Sci. Technol.* **2011**, *1* (8), 1490–1495.
 - (35) Yin, A.-X.; Min, X.-Q.; Zhang, Y.-W.; Yan, C.-H. Shape-Selective Synthesis and Facet-Dependent Enhanced Electrocatalytic Activity and Durability of Monodisperse Sub-10 Nm Pt–Pd Tetrahedrons and Cubes. *J. Am. Chem. Soc.* **2011**, *133* (11), 3816–3819.
 - (36) Rodrigues, T. S.; Silva, A. G. M.; Macedo, A.; Farini, B. W.; Alves, R. da S.; Camargo, P. H. C. Probing the Catalytic Activity of Bimetallic versus Trimetallic Nanoshells. *J.*

- Mater. Sci.* **2015**, *50* (16), 5620–5629.
- (37) Rodrigues, T. S.; da Silva, A. H. M.; da Silva, A. G. M.; Ceara, D. G.; Gomes, J. F.; Assaf, J. M.; Camargo, P. H. C. Hollow AgPt/SiO₂ Nanomaterials with Controlled Surface Morphologies: Is the Number of Pt Surface Atoms Imperative to Optimize Catalytic Performances? *Catal. Sci. Technol.* **2016**, *6* (7), 2162–2170.
- (38) da Silva, A. G. M.; Rodrigues, T. S.; Taguchi, L. S. K.; Fajardo, H. V.; Balzer, R.; Probst, L. F. D.; Camargo, P. H. C. Pd-Based Nanoflowers Catalysts: Controlling Size, Composition, and Structures for the 4-Nitrophenol Reduction and BTX Oxidation Reactions. *J. Mater. Sci.* **2016**, *51* (1), 603–614.
- (39) de Oliveira, C. C. S.; Ando, R. A.; Camargo, P. H. C. Size-Controlled Synthesis of Silver Micro/nanowires as Enabled by HCL Oxidative Etching. *Phys. Chem. Chem. Phys.* **2013**, *15* (6), 1887–1893.
- (40) Narayanan, R.; El-Sayed, M. A. Effect of Nanocatalysis in Colloidal Solution on the Tetrahedral and Cubic Nanoparticle SHAPE: Electron-Transfer Reaction Catalyzed by Platinum Nanoparticles. *J. Phys. Chem. B* **2004**, *108* (18), 5726–5733.
- (41) Mahmoud, M. A.; O’Neil, D.; El-Sayed, M. A. Hollow and Solid Metallic Nanoparticles in Sensing and in Nanocatalysis. *Chem. Mater.* **2014**, *26* (1), 44–58.
- (42) Mahmoud, M. A.; Narayanan, R.; El-Sayed, M. A. Enhancing Colloidal Metallic Nanocatalysis: Sharp Edges and Corners for Solid Nanoparticles and Cage Effect for Hollow Ones. *Acc. Chem. Res.* **2013**, *46* (8), 1795–1805.
- (43) Zhu, Y.; Chakrabarti, A.; Hosmane, N. S. Applications of Nanocatalysis in Boron Chemistry BT - Boron: The Fifth Element; Hnyk, D., McKee, M., Eds.; Springer International Publishing: Cham, 2015; pp 199–217.
- (44) Fihri, A.; Bouhrara, M.; Nekoueishahraki, B.; Basset, J.-M.; Polshettiwar, V. Nanocatalysts for Suzuki Cross-Coupling Reactions. *Chem. Soc. Rev.* **2011**, *40* (10), 5181–5203.
- (45) Mohamed, R. M.; McKinney, D. L.; Sigmund, W. M. Enhanced Nanocatalysts. *Mater. Sci. Eng. R Reports* **2012**, *73* (1), 1–13.
- (46) Cole-Hamilton, D. J. Homogeneous Catalysis--New Approaches to Catalyst Separation, Recovery, and Recycling. *Science*. **2003**, *299* (5613), 1702 LP-1706.
- (47) Corma, A. Heterogeneous Catalysis: Understanding for Designing, and Designing for Applications. *Angew. Chemie Int. Ed.* **2016**, n/a-n/a.
- (48) Bond, G. C. *Heterogeneous Catalysis*; Oxford University Press, New York, NY: United States, 1987.
- (49) Norskov, J. K.; Bligaard, T.; Hvolbaek, B.; Abild-Pedersen, F.; Chorkendorff, I.; Christensen, C. H. The Nature of the Active Site in Heterogeneous Metal Catalysis. *Chem. Soc. Rev.* **2008**, *37* (10), 2163–2171.
- (50) Zaera, F. Nanostructured Materials for Applications in Heterogeneous Catalysis. *Chem. Soc. Rev.* **2013**, *42* (7), 2746–2762.
- (51) Astruc, D.; Lu, F.; Aranzaes, J. R. Nanoparticles as Recyclable Catalysts: The Frontier between Homogeneous and Heterogeneous Catalysis. *Angew. Chemie Int. Ed.* **2005**, *44* (48), 7852–7872.
- (52) Bell, A. T. The Impact of Nanoscience on Heterogeneous Catalysis. *Sci.* **2003**, *299* (5613), 1688–1691.
- (53) White, R. J.; Luque, R.; Budarin, V. L.; Clark, J. H.; Macquarrie, D. J. Supported Metal Nanoparticles on Porous Materials. Methods and Applications. *Chem. Soc. Rev.* **2009**, *38* (2), 481–494.
- (54) Polshettiwar, V.; Varma, R. S. Green Chemistry by Nano-Catalysis. *Green Chem.* **2010**, *12* (5), 743–754.
- (55) da Silva, A. G. M.; Fajardo, H. V.; Balzer, R.; Probst, L. F. D.; Lovón, A. S. P.; Lovón-

- Quintana, J. J.; Valença, G. P.; Schreine, W. H.; Robles-Dutenhefner, P. A. Versatile and Efficient Catalysts for Energy and Environmental Processes: Mesoporous Silica Containing Au, Pd and Au-Pd. *J. Power Sources* **2015**, *285*, 460–468.
- (56) Zhang, R.; Guo, L.; Chen, C.; Chen, J.; Chen, A.; Zhao, X.; Liu, X.; Xiu, Y.; Hou, Z. The Role of Mn Doping in CeO₂ for Catalytic Synthesis of Aliphatic Carbamate from CO₂. *Catal. Sci. Technol.* **2015**.
- (57) Yin, H.; Tang, H.; Wang, D.; Gao, Y.; Tang, Z. Facile Synthesis of Surfactant-Free Au Cluster/Graphene Hybrids for High-Performance Oxygen Reduction Reaction. *ACS Nano* **2012**, *6* (9), 8288–8297.
- (58) Wen, Z.; Wu, W.; Liu, Z.; Zhang, H.; Li, J.; Chen, J. Ultrahigh-Efficiency Photocatalysts Based on Mesoporous Pt-WO₃ Nanohybrids. *Phys. Chem. Chem. Phys.* **2013**, *15* (18), 6773–6778.
- (59) Liu, T.; Yang, F.; Li, Y.; Ren, L.; Zhang, L.; Xu, K.; Wang, X.; Xu, C.; Gao, J. Plasma Synthesis of Carbon Nanotube-Gold Nanohybrids: Efficient Catalysts for Green Oxidation of Silanes in Water. *J. Mater. Chem. A* **2014**, *2* (1), 245–250.
- (60) Qiu, L.; Peng, Y.; Liu, B.; Lin, B.; Peng, Y.; Malik, M. J.; Yan, F. Polypyrrole Nanotube-Supported Gold Nanoparticles: An Efficient Electrocatalyst for Oxygen Reduction and Catalytic Reduction of 4-Nitrophenol. *Appl. Catal. A Gen.* **2012**, *413–414* (0), 230–237.
- (61) Freakley, S. J.; He, Q.; Kiely, C. J.; Hutchings, G. J. Gold Catalysis: A Reflection on Where We Are Now. *Catal. Letters* **2015**, *145* (1), 71–79.
- (62) Guo, Y.; Gu, D.; Jin, Z.; Du, P.-P.; Si, R.; Tao, J.; Xu, W.-Q.; Huang, Y.-Y.; Senanayake, S.; Song, Q.-S.; et al. Uniform 2 Nm Gold Nanoparticles Supported on Iron Oxides as Active Catalysts for CO Oxidation Reaction: Structure-Activity Relationship. *Nanoscale* **2015**, *7* (11), 4920–4928.
- (63) Yatabe, T.; Jin, X.; Yamaguchi, K.; Mizuno, N. Gold Nanoparticles Supported on a Layered Double Hydroxide as Efficient Catalysts for the One-Pot Synthesis of Flavones. *Angew. Chemie Int. Ed.* **2015**, *54* (45), 13302–13306.
- (64) Wang, H.; Thia, L.; Li, N.; Ge, X.; Liu, Z.; Wang, X. Selective Electro-Oxidation of Glycerol over Au Supported on Extended poly(4-Vinylpyridine) Functionalized Graphene. *Appl. Catal. B Environ.* **2015**, *166–167*, 25–31.
- (65) László, B.; Baán, K.; Varga, E.; Oszkó, A.; Erdöhelyi, A.; Kónya, Z.; Kiss, J. Photo-Induced Reactions in the CO₂-Methane System on Titanate Nanotubes Modified with Au and Rh Nanoparticles. *Appl. Catal. B Environ.* **2016**, *199*, 473–484.
- (66) Varga, E.; Pusztai, P.; Ovari, L.; Oszko, A.; Erdohelyi, A.; Papp, C.; Steinruck, H.-P.; Konya, Z.; Kiss, J. Probing the Interaction of Rh, Co and Bimetallic Rh-Co Nanoparticles with the CeO₂ Support: Catalytic Materials for Alternative Energy Generation. *Phys. Chem. Chem. Phys.* **2015**, *17* (40), 27154–27166.
- (67) Guha, N. R.; Sharma, S.; Bhattacharjee, D.; Thakur, V.; Bharti, R.; Reddy, C. B.; Das, P. Oxidative “reverse-Esterification” of Ethanol with Benzyl/alkyl Alcohols or Aldehydes Catalyzed by Supported Rhodium Nanoparticles. *Green Chem.* **2016**, *18* (5), 1206–1211.
- (68) Yao, Q.; Lu, Z.-H.; Jia, Y.; Chen, X.; Liu, X. In Situ Facile Synthesis of Rh Nanoparticles Supported on Carbon Nanotubes as Highly Active Catalysts for H₂ Generation from NH₃BH₃ Hydrolysis. *Int. J. Hydrogen Energy* **2015**, *40* (5), 2207–2215.
- (69) Baudouin, D.; Rodemerck, U.; Krumeich, F.; Mallmann, A. de; Szeto, K. C.; Ménard, H.; Veyre, L.; Candy, J.-P.; Webb, P. B.; Thieuleux, C.; et al. Particle Size Effect in the Low Temperature Reforming of Methane by Carbon Dioxide on Silica-Supported Ni Nanoparticles. *J. Catal.* **2013**, *297*, 27–34.

- (70) Chenna, S.; Crozier, P. A. In Situ Environmental Transmission Electron Microscopy to Determine Transformation Pathways in Supported Ni Nanoparticles. *Micron* **2012**, *43* (11), 1188–1194.
- (71) Xie, T.; Shi, L.; Zhang, J.; Zhang, D. Immobilizing Ni Nanoparticles to Mesoporous Silica with Size and Location Control via a Polyol-Assisted Route for Coking- and Sintering-Resistant Dry Reforming of Methane. *Chem. Commun.* **2014**, *50* (55), 7250–7253.
- (72) Xia, J.; He, G.; Zhang, L.; Sun, X.; Wang, X. Hydrogenation of Nitrophenols Catalyzed by Carbon Black-Supported Nickel Nanoparticles under Mild Conditions. *Appl. Catal. B Environ.* **2016**, *180*, 408–415.
- (73) Bajpai, R.; Roy, S.; kulshrestha, N.; Rafiee, J.; Koratkar, N.; Misra, D. S. Graphene Supported Nickel Nanoparticle as a Viable Replacement for Platinum in Dye Sensitized Solar Cells. *Nanoscale* **2012**, *4* (3), 926–930.
- (74) Krug, J. T.; Wang, G. D.; Emory, S. R.; Nie, S. Efficient Raman Enhancement and Intermittent Light Emission Observed in Single Gold Nanocrystals. *J. Am. Chem. Soc.* **1999**, *121* (39), 9208–9214.
- (75) Bell, S. E. J.; McCourt, M. R. SERS Enhancement by Aggregated Au Colloids: Effect of Particle Size. *Phys. Chem. Chem. Phys.* **2009**, *11* (34), 7455–7462.
- (76) Scaiano Juan C; Netto-Ferreira José C; Alarcon Emilio; Billone Paul; Alejo Carlos J Bueno; Crites Charles-Oneil L; Decan Matthew; Fasciani Chiara; González-Béjar María; Hallett-Tapley Geniece; et al. Tuning Plasmon Transitions and Their Applications in Organic Photochemistry . *Pure and Applied Chemistry* . 2011, p 913.
- (77) Thompson, D. T. Using Gold Nanoparticles for Catalysis. *Nano Today* **2007**, *2* (4), 40–43.
- (78) Sinha, A. K.; Seelan, S.; Tsubota, S.; Haruta, M. Catalysis by Gold Nanoparticles: Epoxidation of Propene. *Top. Catal.* **2004**, *29* (3), 95–102.
- (79) Campbell, C. T. The Active Site in Nanoparticle Gold Catalysis. *Science*. **2004**, *306* (5694), 234 LP-235.
- (80) Singh, A. K.; Xu, Q. Synergistic Catalysis over Bimetallic Alloy Nanoparticles. *ChemCatChem* **2013**, *5* (3), 652–676.
- (81) Sun, Y.; Mayers, B.; Xia, Y. Metal Nanostructures with Hollow Interiors. *Adv. Mater.* **2003**, *15* (7–8), 641–646.
- (82) Xia, X.; Wang, Y.; Ruditskiy, A.; Xia, Y. 25th Anniversary Article: Galvanic Replacement: A Simple and Versatile Route to Hollow Nanostructures with Tunable and Well-Controlled Properties. *Adv. Mater.* **2013**, *25* (44), 6313–6333.
- (83) Jiang, H.-L.; Xu, Q. Recent Progress in Synergistic Catalysis over Heterometallic Nanoparticles. *J. Mater. Chem.* **2011**, *21* (36), 13705–13725.
- (84) An, K.; Hyeon, T. Synthesis and Biomedical Applications of Hollow Nanostructures. *Nano Today* **2009**, *4* (4), 359–373.
- (85) Lou, X. W. (David); Archer, L. A.; Yang, Z. Hollow Micro-/Nanostructures: Synthesis and Applications. *Adv. Mater.* **2008**, *20* (21), 3987–4019.
- (86) da Silva, A. G. M.; de Souza, M. L.; Rodrigues, T. S.; Alves, R. S.; Temperini, M. L. A.; Camargo, P. H. C. Rapid Synthesis of Hollow Ag–Au Nanodendrites in 15 Seconds by Combining Galvanic Replacement and Precursor Reduction Reactions. *Chem. – A Eur. J.* **2014**, *20* (46), 15040–15046.
- (87) Wang, X.; Figueroa-Cosme, L.; Yang, X.; Luo, M.; Liu, J.; Xie, Z.; Xia, Y. Pt-Based Icosahedral Nanocages: Using a Combination of {111} Facets, Twin Defects, and Ultrathin Walls to Greatly Enhance Their Activity toward Oxygen Reduction. *Nano Lett.* **2016**, *16* (2), 1467–1471.
- (88) Lai, W.; Zhou, J.; Jia, Z.; Petti, L.; Mormile, P. Ag@Au Hexagonal Nanorings:

- Synthesis, Mechanistic Analysis and Structure-Dependent Optical Characteristics. *J. Mater. Chem. C* **2015**, *3* (37), 9726–9733.
- (89) Yen, C. W.; Mahmoud, M. A.; El-Sayed, M. A. Photocatalysis in Gold Nanocage Nanoreactors. *J. Phys. Chem. A* **2009**, *113* (16), 4340–4345.
- (90) Mahmoud, M. A.; Saira, F.; El-Sayed, M. A. Experimental Evidence For The Nanocage Effect In Catalysis With Hollow Nanoparticles. *Nano Lett.* **2010**, *10* (9), 3764–3769.
- (91) Zhang, Q.; Wang, W.; Goebel, J.; Yin, Y. Self-Templated Synthesis of Hollow Nanostructures. *Nano Today* **2009**, *4* (6), 494–507.
- (92) Sun, X.; Liu, J.; Li, Y. Use of Carbonaceous Polysaccharide Microspheres as Templates for Fabricating Metal Oxide Hollow Spheres. *Chem. – A Eur. J.* **2006**, *12* (7), 2039–2047.
- (93) Yang, Z.; Niu, Z.; Lu, Y.; Hu, Z.; Han, C. C. Templated Synthesis of Inorganic Hollow Spheres with a Tunable Cavity Size onto Core–Shell Gel Particles. *Angew. Chemie* **2003**, *115* (17), 1987–1989.
- (94) He, D. S.; He, D.; Wang, J.; Lin, Y.; Yin, P.; Hong, X.; Wu, Y.; Li, Y. Ultrathin Icosahedral Pt-Enriched Nanocage with Excellent Oxygen Reduction Reaction Activity. *J. Am. Chem. Soc.* **2016**, *138* (5), 1494–1497.
- (95) Yin, Y.; Rioux, R. M.; Erdonmez, C. K.; Hughes, S.; Somorjai, G. A.; Alivisatos, A. P. Formation of Hollow Nanocrystals Through the Nanoscale Kirkendall Effect. *Science*. **2004**, *304* (5671), 711 LP-714.
- (96) Zeng, H. C. Synthetic Architecture of Interior Space for Inorganic Nanostructures. *J. Mater. Chem.* **2006**, *16* (7), 649–662.
- (97) Fan, H. J.; Gösele, U.; Zacharias, M. Formation of Nanotubes and Hollow Nanoparticles Based on Kirkendall and Diffusion Processes: A Review. *Small* **2007**, *3* (10), 1660–1671.
- (98) Zhou, S.; Varughese, B.; Eichhorn, B.; Jackson, G.; McIlwrath, K. Pt–Cu Core–Shell and Alloy Nanoparticles for Heterogeneous NO_x Reduction: Anomalous Stability and Reactivity of a Core–Shell Nanostructure. *Angew. Chemie* **2005**, *117* (29), 4615–4619.
- (99) Yang, H. G.; Zeng, H. C. Preparation of Hollow Anatase TiO₂ Nanospheres via Ostwald Ripening. *J. Phys. Chem. B* **2004**, *108* (11), 3492–3495.
- (100) Chang, Y.; Teo, J. J.; Zeng, H. C. Formation of Colloidal CuO Nanocrystallites and Their Spherical Aggregation and Reductive Transformation to Hollow Cu₂O Nanospheres. *Langmuir* **2005**, *21* (3), 1074–1079.
- (101) Gilroy, K. D.; Ruditskiy, A.; Peng, H.-C.; Qin, D.; Xia, Y. Bimetallic Nanocrystals: Syntheses, Properties, and Applications. *Chem. Rev.* **2016**, *116* (18), 10414–10472.
- (102) Lu, X.; Tuan, H.-Y.; Chen, J.; Li, Z.-Y.; Korgel, B. A.; Xia, Y. Mechanistic Studies on the Galvanic Replacement Reaction between Multiply Twinned Particles of Ag and HAuCl₄ in an Organic Medium. *J. Am. Chem. Soc.* **2007**, *129* (6), 1733–1742.
- (103) Yang, Y.; Zhang, Q.; Fu, Z.-W.; Qin, D. Transformation of Ag Nanocubes into Ag–Au Hollow Nanostructures with Enriched Ag Contents to Improve SERS Activity and Chemical Stability. *ACS Appl. Mater. Interfaces* **2014**, *6* (5), 3750–3757.
- (104) Zhang, H.; Jin, M.; Liu, H.; Wang, J.; Kim, M. J.; Yang, D.; Xie, Z.; Liu, J.; Xia, Y. Facile Synthesis of Pd–Pt Alloy Nanocages and Their Enhanced Performance for Preferential Oxidation of CO in Excess Hydrogen. *ACS Nano* **2011**, *5* (10), 8212–8222.
- (105) Xu, J.; Wilson, A. R.; Rathmell, A. R.; Howe, J.; Chi, M.; Wiley, B. J. Synthesis and Catalytic Properties of Au–Pd Nanoflowers. *ACS Nano* **2011**, *5* (8), 6119–6127.
- (106) Rodrigues, T. S.; da Silva, A. G. M.; Gonçalves, M. C.; Fajardo, H. V.; Balzer, R.; Probst, L. F. D.; Camargo, P. H. C. AgPt Hollow Nanodendrites: Synthesis and Uniform Dispersion over SiO₂ Support for Catalytic Applications. *ChemNanoMat* **2015**.

Chapter 2

Probing the Catalytic Activity of Bimetallic versus Trimetallic Nanoshells

2.1. Introduction

Bimetallic and hollow metallic nanostructures, such as nanoshells, are very attractive for catalytic and electrocatalytic applications.¹⁻⁷ While bimetallic compositions allow for the combination and/or synergism of catalytic properties between the metal components, their hollow interiors provide higher surface-to-volume ratios relative to their solid analogues^{4,8-13}. In this context, several investigations on the catalytic activities of bimetallic and hollow nanostructures containing gold (Au), palladium (Pd), and platinum (Pt) have been demonstrated.¹⁴⁻¹⁹

The addition of a third metal to produce trimetallic compositions represents an emerging approach to optimize catalytic activities on noble-metal nanostructures.^{11,20-22} Trimetallic nanoparticles have shown improved catalytic performances relative to their mono- and bimetallic counterparts for a variety of reactions that include cyclohexene and glucose oxidation, the electrooxidation of formic acid, and C-C coupling.²³⁻²⁶ It has been proposed that trimetallic systems may present distinct properties relative to their mono- and bimetallic counterparts, which enables, at least in principle, the design of nanomaterials with optimized performances.^{11,21,22,27,28} Despite these very attractive features, studies on the synthesis of trimetallic noble-metal nanomaterials are still limited, and the role of the third metal over the performances, relative to their bimetallic systems, remains unclear. This is probably due to the lack of experimental procedures to the synthesis of trimetallic nanostructures with well-defined

shapes and controllable compositions, which hinders the systematic correlation between shape, composition, and performance.^{11,22,27,29–31}

In this paper, we describe a facile and rapid strategy to the synthesis of trimetallic nanoshells having AgAuPd, AgAuPt, and AgPdPt compositions by a sequential galvanic replacement reaction approach between Ag nanospheres as sacrificial templates and the corresponding metal precursors, i.e., AuCl_4^- (aq), PdCl_4^{2-} (aq), and/or PtCl_6^{2-} (aq).³² In each of these systems, the composition could be systematically tuned by varying the molar ratios between Ag and each metal precursor. As the galvanic reaction employing Ag nanospheres as templates leads to nanoshells displaying similar sizes/morphology,¹ it enables us to separate and investigate the effect of composition in the trimetallic materials relative to their bimetallic counterparts over their catalytic performances towards the reduction of 4-nitrophenol as a model reaction.³³ Our data demonstrates a significant enhancement on the catalytic activities upon the formation of the trimetallic nanoshells, and the magnitude of this enhancement relative to the bimetallic nanoshells of similar compositions was dependent on the nature of the metals.

2.2. Experimental Section

Materials and Instrumentation

Analytical grade silver nitrate (AgNO_3 , 99%, Sigma-Aldrich), polyvinylpyrrolidone (PVP, Sigma-Aldrich, M.W. 55,000 g/mol), ethylene glycol (EG, 99.8%, Sigma-Aldrich), chloroplatinic acid hexahydrate ($\text{H}_2\text{PtCl}_6 \cdot 6\text{H}_2\text{O}$, $\geq 37.50\%$ Pt basis, Sigma-Aldrich), tetrachloroauric acid ($\text{HAuCl}_4 \cdot 3\text{H}_2\text{O}$, $\geq 99.9\%$, Sigma-Aldrich), potassium tetrachloropalladate (K_2PdCl_4 , $\geq 99.99\%$, Sigma-Aldrich), 4-nitrophenol ($\text{C}_6\text{H}_5\text{NO}_2$, $\geq 99\%$, Sigma-Aldrich), and sodium borohydride (NaBH_4 , 98%, Sigma-Aldrich) were used as received.

Transmission electron microscopy (TEM) images were obtained with a JEOL 1010 microscope operating at 80 kV. Samples for TEM were prepared by drop-casting an aqueous suspension of the nanostructures over a carbon-coated copper grid, followed by drying under ambient conditions. UV-VIS spectra were obtained from aqueous suspensions containing the nanostructures with a Shimadzu UV-1700 spectrophotometer. The Ag, Au, Pd and Pt atomic percentages were measured by inductively coupled plasma optical emission spectrometry (ICP-OES) using a Spectro Arcos equipment at the IQ-USP analytical center facilities.

Synthesis of Ag nanospheres

Ag nanospheres were prepared by the polyol process.²⁹ In a typical procedure, 5 g of polyvinylpyrrolidone (PVP) was dissolved in 37.5 mL of ethylene glycol (EG). Then, AgNO₃ (200 mg, 1.2 mmol) was added and mixed until the complete dissolution. The resulting solution was heated to 125 °C for 2.5 hours, leading to the appearance of a greenish-yellow color, allowed to cool down to room temperature, and diluted to 125 mL of water.

Synthesis of bi- and trimetallic nanoshells

The syntheses of bi- and trimetallic nanoshells were based on the sequential galvanic replacement reaction between Ag nanospheres and Pd, Au, and Pt precursors (PdCl₄²⁻_(aq), AuCl₄⁻_(aq), and PtCl₆²⁻_(aq)). In order to obtain the bimetallic nanoshells having AgM controlled compositions (M = Au, Pd, or Pt), a mixture containing 5 mL of PVP aqueous solution (0.1 wt %) and 1 mL of as-prepared suspension containing the Ag nanospheres was stirred at 100 °C for 10 min in a 25 mL round-bottom flask. Then, 2 mL of aqueous solutions of the respective metal precursor (0.2, 0.4, 0.6, and 0.8 mM) was added dropwise and the reaction allowed to proceed at 100 °C for another 10 min. Similarly, the synthesis of AgAuPd, AgAuPt, and AgPdPt nanoshells were obtained by sequentially adding AuCl₄⁻_(aq) and PdCl₄²⁻_(aq), AuCl₄⁻_(aq)

and $\text{PtCl}_6^{2-}(\text{aq})$, and $\text{PtCl}_6^{2-}(\text{aq})$ and $\text{PdCl}_4^{2-}(\text{aq})$, respectively, in the galvanic replacement reaction. In all cases, the volume of each precursor solution corresponded to 2 mL and their concentrations were 0.2, 0.4, 0.6, and 0.8 mM in order to control their compositions. After the galvanic replacement reaction, all the suspensions were allowed to cool down to room temperature and washed twice with a supersaturated NaCl solution and three times with water by successive rounds of centrifugation at 15000 rpm and removal of the supernatant. After washing, the nanoshells were suspended in 8 mL of PVP aqueous solution (0.1 wt %). This suspension was then employed in the catalytic tests for the 4-nitrophenol reduction reaction.

Catalytic reduction of 4-nitrophenol

Typically, 0.3 mL of a 1.4×10^{-4} M 4-nitrophenol aqueous solution, 2 mL of 4.2×10^{-2} M sodium borohydride aqueous solution, and 200 μL of the suspension containing the synthesized nanoshells (diluted in the ratio 1:40 of nanoshell:water) was added into a quartz cuvette. The catalytic transformation was monitored by UV–VIS spectroscopy, in which the intensity in the absorbance at 400 nm (assigned to 4-nitrophenolate ions) was monitored as a function of time (this signal decreased as the consumption of 4-nitrophenolate ions and formation of 4-aminophenol take place). In this case, the UV-VIS spectra were collected at 13 s time intervals in the 350 to 500 nm range. A calibration curve for absorbance as a function of the 4-nitrophenolate concentration was employed in order to calculate the 4-nitrophenol conversion %. The catalytic activities were expressed in terms of substrate conversion versus time.

2.3. Results and Discussion

Our studies started with the synthesis of Ag nanospheres by a polyol approach.³⁴ The Ag nanospheres were 34 ± 3 nm in diameter, displayed spherical shape and relatively monodisperse sizes (Figure 2.1).

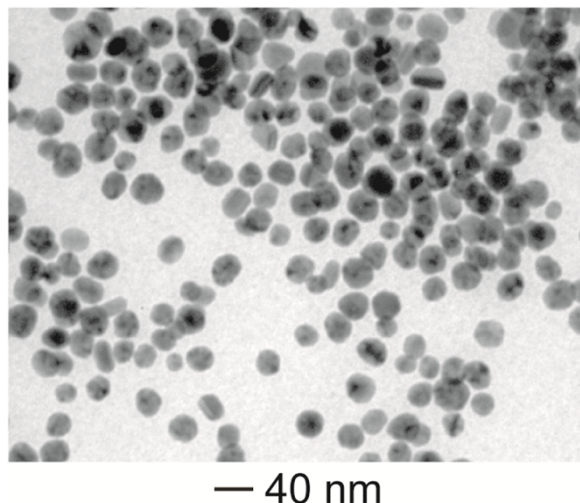


Figure 2.1. TEM image for Ag NPs employed as templates for the synthesis of bimetallic and trimetallic nanoshells with controlled compositions following the addition of AuCl_4^- (aq), PdCl_4^{2-} (aq), and PtCl_6^{2-} (aq) to aqueous suspensions containing Ag NPs and PVP.

It is well-established that Ag can be employed as templates for the synthesis of nanomaterials having bimetallic compositions, hollow interiors, and ultrathin walls by a galvanic replacement reaction approach between Ag, employed as sacrificial templates, and a more noble metal precursor, such as AuCl_4^- (aq), PtCl_6^{2-} (aq), and PdCl_4^{2-} (aq).^{1,9} In this process, while the shape of the produced nanostructures can be controlled by employing Ag nanomaterials displaying distinct shapes as templates, the composition and structure can be tailored by adjusting the molar ratio between Ag and the metal precursor during the galvanic reaction.^{1,32} In fact, this route has been employed to the synthesis of bimetallic nanoshells, nanotubes, and nanocages, for example.⁹ Here, we were interested in employing this approach to obtain bi- and trimetallic nanoshells having controlled compositions and similar

morphologies so that we could probe the effect of the addition of a third metal over the catalytic activities as compared to their bimetallic counterparts.

In order to achieve this goal, the produced Ag nanospheres were employed as chemical templates for the synthesis of AgAuPd, AgAuPt, and AgPdPt trimetallic nanoshells by the sequential addition of the corresponding metal precursors (AuCl_4^- (aq) and PdCl_4^{2-} (aq); AuCl_4^- (aq) and PtCl_6^{2-} (aq); and PtCl_6^{2-} (aq) and PdCl_4^{2-} (aq), respectively) during the galvanic replacement reaction as depicted in Figure 2.2.

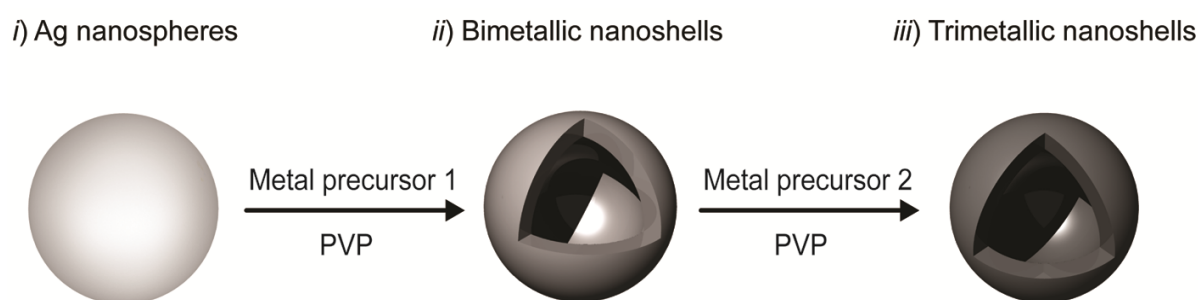


Figure 2.2. Scheme for the synthesis of bimetallic and trimetallic nanoshells by sequential galvanic replacement reactions between Ag nanospheres (chemical templates) and Pd, Au, and/or Pt precursors (PdCl_4^{2-} (aq), AuCl_4^- (aq), and PtCl_6^{2-} (aq), respectively) using PVP as the stabilizer, water as solvent, 100 °C as the reaction temperature, and 10 min as the reaction time.

By this route, trimetallic nanoshells having a variety of well-controlled compositions as determined by ICP-OES were synthesized as shown in Table 2.1-2.3.

Table 2.1. Atomic percentages of Ag, Au, and Pd in the trimetallic AgAuPd nanoshells obtained by ICP-OES. The number in parenthesis denotes the concentration (in mM) for the corresponding metal precursor solutions (2 mL) added in the galvanic replacement reaction.

	Ag (mol %)	Au (mol%)	Pd (mol%)	Sample
Au(0.2)Pd(0.2)	83	12	5	Ag ₈₃ Au ₁₂ Pd ₅
Au(0.2)Pd(0.4)	72	10	16	Ag ₇₂ Au ₁₀ Pd ₁₆
Au(0.2)Pd(0.6)	75	9	16	Ag ₇₅ Au ₉ Pd ₁₆
Au(0.2)Pd(0.8)	72	9	19	Ag ₇₂ Au ₉ Pd ₁₉
Au(0.4)Pd(0.2)	82	14	4	Ag ₈₂ Au ₁₄ Pd ₄
Au(0.4)Pd(0.4)	76	12	12	Ag ₇₆ Au ₁₂ Pd ₁₂
Au(0.4)Pd(0.4)	72	12	16	Ag ₇₂ Au ₁₂ Pd ₁₆
Au(0.4)Pd(0.8)	69	12	19	Ag ₆₉ Au ₁₂ Pd ₁₉
Au(0.6)Pd(0.2)	65	29	6	Ag ₆₅ Au ₂₉ Pd ₆
Au(0.6)Pd(0.4)	60	26	14	Ag ₆₀ Au ₂₆ Pd ₁₄
Au(0.6)Pd(0.6)	58	23	19	Ag ₅₈ Au ₂₃ Pd ₁₉
Au(0.6)Pd(0.8)	58	23	19	Ag ₅₈ Au ₂₃ Pd ₁₉
Au(0.8)Pd(0.2)	61	32	7	Ag ₆₁ Au ₃₂ Pd ₇
Au(0.8)Pd(0.4)	57	30	13	Ag ₅₇ Au ₃₀ Pd ₁₃
Au(0.8)Pd(0.6)	57	29	14	Ag ₅₇ Au ₂₉ Pd ₁₄
Au(0.8)Pd(0.8)	56	28	16	Ag ₅₆ Au ₂₈ Pd ₁₆

Table 2.2. Atomic percentages of Ag, Au, and Pt in the trimetallic AgAuPt nanoshells obtained by ICP-OES. The number in parenthesis denotes the concentration (in mM) for the corresponding metal precursor solutions (2 mL) added in the galvanic replacement reaction.

	Ag (mol %)	Au (mol%)	Pt (mol%)	Sample
Au(0.2)Pt(0.2)	81	9	10	Ag ₈₁ Au ₉ Pt ₁₀
Au(0.2)Pt(0.4)	78	9	13	Ag ₇₈ Au ₉ Pt ₁₃
Au(0.2)Pt(0.6)	75	9	16	Ag ₇₅ Au ₉ Pt ₁₆
Au(0.2)Pt(0.8)	75	9	16	Ag ₇₂ Au ₉ Pt ₁₆
Au(0.4)Pt(0.2)	84	10	6	Ag ₈₄ Au ₁₀ Pt ₆
Au(0.4)Pt(0.4)	78	13	9	Ag ₇₈ Au ₁₃ Pt ₉
Au(0.4)Pt(0.6)	76	13	11	Ag ₇₆ Au ₁₃ Pt ₁₁
Au(0.4)Pt(0.8)	76	9	15	Ag ₇₆ Au ₉ Pt ₁₅
Au(0.6)Pt(0.2)	79	17	4	Ag ₇₉ Au ₁₇ Pt ₄
Au(0.6)Pt(0.4)	79	15	6	Ag ₇₉ Au ₁₅ Pt ₆
Au(0.6)Pt(0.6)	78	11	11	Ag ₇₈ Au ₁₁ Pt ₁₁
Au(0.6)Pt(0.8)	75	12	13	Ag ₇₅ Au ₁₂ Pt ₁₃
Au(0.8)Pt(0.2)	66	32	2	Ag ₆₆ Au ₃₂ Pt ₂
Au(0.8)Pt(0.4)	65	24	11	Ag ₆₅ Au ₂₄ Pt ₁₁
Au(0.8)Pt(0.6)	64	24	12	Ag ₆₄ Au ₂₄ Pt ₁₂
Au(0.8)Pt(0.8)	63	23	14	Ag ₆₃ Au ₂₃ Pt ₁₄

Table 2.3. Atomic percentages of Ag, Pd, and Pt in the trimetallic AgPdPt nanoshells obtained by ICP-OES. The number in parenthesis denotes the concentration (in mM) for the corresponding metal precursor solutions (2 mL) added in the galvanic replacement reaction.

	Ag (mol %)	Pd (mol%)	Pt (mol%)	Sample
Pd(0.2)Pt(0.2)	86	8	6	Ag ₈₆ Pd ₈ Pt ₆
Pd(0.2)Pt(0.4)	80	8	12	Ag ₈₀ Pd ₉ Pt ₁₃
Pd(0.2)Pt(0.6)	75	7	18	Ag ₇₅ Pd ₇ Pt ₁₈
Pd(0.2)Pt(0.8)	68	7	25	Ag ₆₈ Pd ₇ Pt ₂₅
Pd(0.4)Pt(0.2)	83	13	4	Ag ₈₃ Pd ₁₃ Pt ₄
Pd(0.4)Pt(0.4)	75	13	12	Ag ₇₅ Pd ₁₃ Pt ₁₂
Pd(0.4)Pt(0.6)	71	13	16	Ag ₇₁ Pd ₁₃ Pt ₁₆
Pd(0.4)Pt(0.8)	66	12	22	Ag ₆₆ Pd ₁₂ Pt ₂₂
Pd(0.6)Pt(0.2)	80	19	1	Ag ₈₀ Pd ₁₉ Pt ₁
Pd(0.6)Pt(0.4)	77	19	4	Ag ₇₇ Pd ₁₉ Pt ₄
Pd(0.6)Pt(0.6)	77	13	10	Ag ₇₇ Pd ₁₃ Pt ₁₀
Pd(0.6)Pt(0.8)	76	12	12	Ag ₇₆ Pd ₁₂ Pt ₁₂
Pd(0.8)Pt(0.2)	74	25	1	Ag ₇₄ Pd ₂₅ Pt ₁
Pd(0.8)Pt(0.4)	71	25	4	Ag ₇₁ Pd ₂₅ Pt ₄
Pd(0.8)Pt(0.6)	71	23	6	Ag ₇₁ Pd ₂₃ Pt ₆
Pd(0.8)Pt(0.8)	71	16	13	Ag ₇₁ Pd ₁₆ Pt ₁₃

For comparison, bimetallic nanoshells having similar compositions were also obtained by this route (Table 2.4). It is important to emphasize that the composition was controlled by varying the concentration of the 2 mL metal precursor solutions employed during the galvanic replacement reaction. Specifically, this was performed by employing 0.2, 0.4, 0.6, and 0.8 mM as the concentrations for each precursor solution.

Table 2.4. Atomic percentages of Ag, Au, Pd and Pt in the bimetallic nanoshells obtained by ICP-OES. The number in parenthesis denotes the concentration (in mM) for the corresponding metal precursor solutions (2 mL) added in the galvanic replacement reaction.

	Ag (mol %)	Au (mol%)	Sample
Au(0.2)	91	9	Ag ₉₁ Au ₉
Au(0.4)	88	12	Ag ₈₈ Au ₁₂
Au(0.6)	86	14	Ag ₈₆ Au ₁₄
Au(0.8)	72	28	Ag ₇₂ Au ₂₈
	Ag (mol %)	Pd (mol%)	Sample
Pd(0.2)	96	4	Ag ₉₆ Pd ₄
Pd(0.4)	90	10	Ag ₉₀ Pd ₁₀
Pd(0.6)	84	16	Ag ₈₄ Pd ₁₆
Pd(0.8)	81	19	Ag ₈₁ Pd ₁₉
	Ag (mol %)	Pt (mol%)	Sample
Pt(0.2)	87	13	Ag ₈₇ Pt ₁₃
Pt(0.4)	81	19	Ag ₈₁ Pt ₁₉
Pt(0.6)	75	25	Ag ₇₅ Pt ₂₅
Pt(0.8)	73	27	Ag ₇₃ Pt ₂₇

In order to study the catalytic activity of the trimetallic nanoshells relative to their bimetallic counterparts, we focused on one trimetallic composition for each metal combination. More specifically, we focused on the Ag₅₆Au₂₈Pd₁₆, Ag₇₈Au₉Pt₁₃, and Ag₇₁Pd₁₆Pt₁₃ compositions for nanoshells containing Ag, Au, and Pd; Ag, Au, and Pt; and Ag, Pd, and Pt, respectively. Consequently, we also studied on their bimetallic counterparts: Ag₇₂Au₂₈ and Ag₈₄Pd₁₆; Ag₉₁Au₉ and Ag₈₇Pt₁₃; and Ag₈₄Pd₁₆ and Ag₈₇Pt₁₃, respectively.

Figure 2.3A-C display TEM images for $\text{Ag}_{56}\text{Au}_{28}\text{Pd}_{16}$, $\text{Ag}_{78}\text{Au}_9\text{Pt}_{13}$, and $\text{Ag}_{71}\text{Pd}_{16}\text{Pt}_{13}$ trimetallic nanoshells, respectively. The nanoshells presented spherical shape and were relatively uniform in sizes (38 ± 2 , 39 ± 3 , and 39 ± 3 nm for $\text{Ag}_{56}\text{Au}_{28}\text{Pd}_{16}$, $\text{Ag}_{78}\text{Au}_9\text{Pt}_{13}$, and $\text{Ag}_{71}\text{Pd}_{16}\text{Pt}_{13}$, respectively). The mass-thickness contrast in the TEM images clearly indicates the formation of hollow interiors and thin walls (< 10 nm in shell thickness) for all trimetallic nanoshells. Another interesting feature is that the surface of the $\text{Ag}_{56}\text{Au}_{28}\text{Pd}_{16}$ nanoshells (Figure 2.3A) appears to be slightly smoother relative to $\text{Ag}_{78}\text{Au}_9\text{Pt}_{13}$ and $\text{Ag}_{71}\text{Pd}_{16}\text{Pt}_{13}$ (Figure 2.3B and 2.3C). EDX analysis revealed no significant particle-to-particle variations in composition.

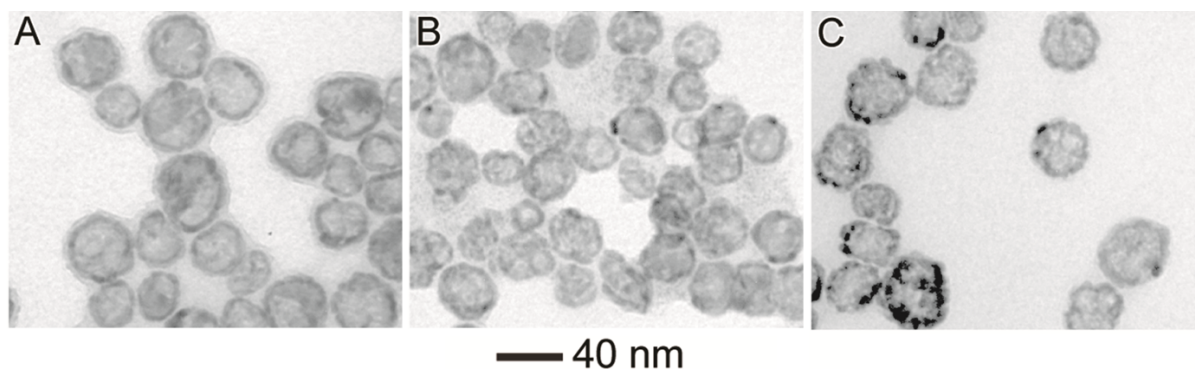


Figure 2.3. TEM images for $\text{Ag}_{56}\text{Au}_{28}\text{Pd}_{16}$ (A), $\text{Ag}_{78}\text{Au}_9\text{Pt}_{13}$ (B), and $\text{Ag}_{71}\text{Pd}_{16}\text{Pt}_{13}$ (C) trimetallic nanoshells obtained by the galvanic replacement reaction between Ag and AuCl_4^- (aq) and PdCl_4^{2-} (aq); AuCl_4^- (aq) and PtCl_6^{2-} (aq); and PtCl_6^{2-} (aq) and PdCl_4^{2-} (aq), respectively.

Figure 2.4A-F shows TEM images for the bimetallic nanoshells counterparts: $\text{Ag}_{72}\text{Au}_{28}$ (Figure 2.4A), $\text{Ag}_{84}\text{Pd}_{16}$ (Figure 2.4B), $\text{Ag}_{91}\text{Au}_9$ (Figure 2.4C), $\text{Ag}_{87}\text{Pt}_{13}$ (Figure 2.4D), $\text{Ag}_{84}\text{Pd}_{16}$ (Figure 2.4E), and $\text{Ag}_{87}\text{Pt}_{13}$ (Figure 2.4F).

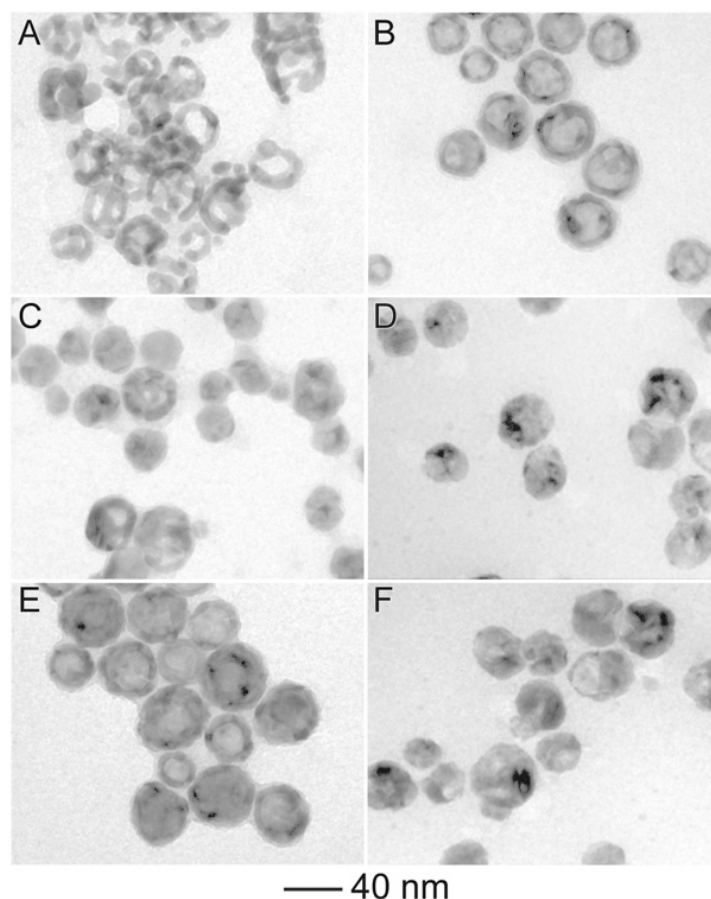


Figure 2.4. TEM images for the bimetallic nanoshells having similar compositions relative to the trimetallic systems Figure 2.3: $\text{Ag}_{72}\text{Au}_{28}$ (A), $\text{Ag}_{84}\text{Pd}_{16}$ (B), $\text{Ag}_{91}\text{Au}_9$ (C), $\text{Ag}_{87}\text{Pt}_{13}$ (D), $\text{Ag}_{84}\text{Pd}_{16}$ (E), and $\text{Ag}_{87}\text{Pt}_{13}$ (F).

Figure 2.5A-C shows the UV-VIS extinction spectra recorded from aqueous suspensions containing the Ag nanospheres and the bi- and trimetallic nanoshells having Ag, Au, and Pd (Figure 2.5A), Ag, Au and Pt (Figure 2.5B), and Ag, Pt, and Pd (Figure 2.5C) compositions. The Ag nanospheres displayed a peak centered at ~ 410 nm assigned to the dipolar mode of the localized surface plasmon resonance (LSPR) excitation.^{35,36} This peak red-shifted in all bimetallic compositions as a result of Ag dissolution from the templates (leading to hollow interiors) and deposition of Au, Pd, or Pt at their surface. Conversely, this peak disappeared in all trimetallic nanoshells, which is probably related to further oxidation and dissolution of Ag from the templates by the sequential galvanic reactions. Therefore, the absence of plasmonic peaks for all trimetallic compositions occurs as Ag is dissolved during the galvanic reaction for

the synthesis of trimetallic nanoshells (leading to hollow interiors), which is also accompanied by the deposition of Pd and Pt at the surface (Pd and Pt do not display LSPR excitation in the visible range).

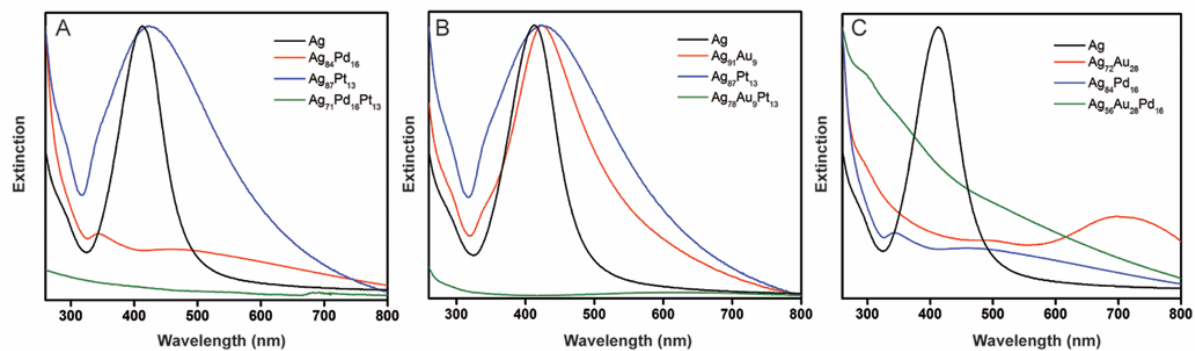


Figure 2.5. UV–VIS extinction spectra recorded from aqueous suspensions containing the Ag NPs employed as templates for the synthesis of bi- and trimetallic nanoshells having Ag, Au, and Pd (A), Ag, Au and Pt (B), and Ag, Pt, and Pd (C) compositions.

After the characterization of their composition, morphological features, and optical properties, we turned our attention to the investigation of the catalytic activities of Ag₅₆Au₂₈Pd₁₆, Ag₇₈Au₉Pt₁₃, and Ag₇₁Pd₁₆Pt₁₃ nanoshells as compared to their respective bimetallic counterparts, i.e., Ag₇₂Au₂₈ and Ag₈₄Pd₁₆; Ag₉₁Au₉ and Ag₈₇Pt₁₃; and Ag₈₄Pd₁₆ and Ag₈₇Pt₁₃, respectively. We employed the 4-nitrophenol reduction in the presence of excess NaBH₄ as a model reaction (Figure 2.6A), which can be catalyzed by noble-metal nanoparticles via particle-mediated electron transfer from borohydride to 4-nitrophenolate ions.^{37,38} This reaction is relevant as the product from the 4-nitrophenol reduction, 4-aminophenol, represents an important intermediate in the synthesis of analgesic and antipyretic drugs³². It is important to emphasize that all the catalytic investigations described in this paper were performed employing the same concentration metal nanoshells, and 4-aminophenol is the only product from the 4-nitrophenol reduction.

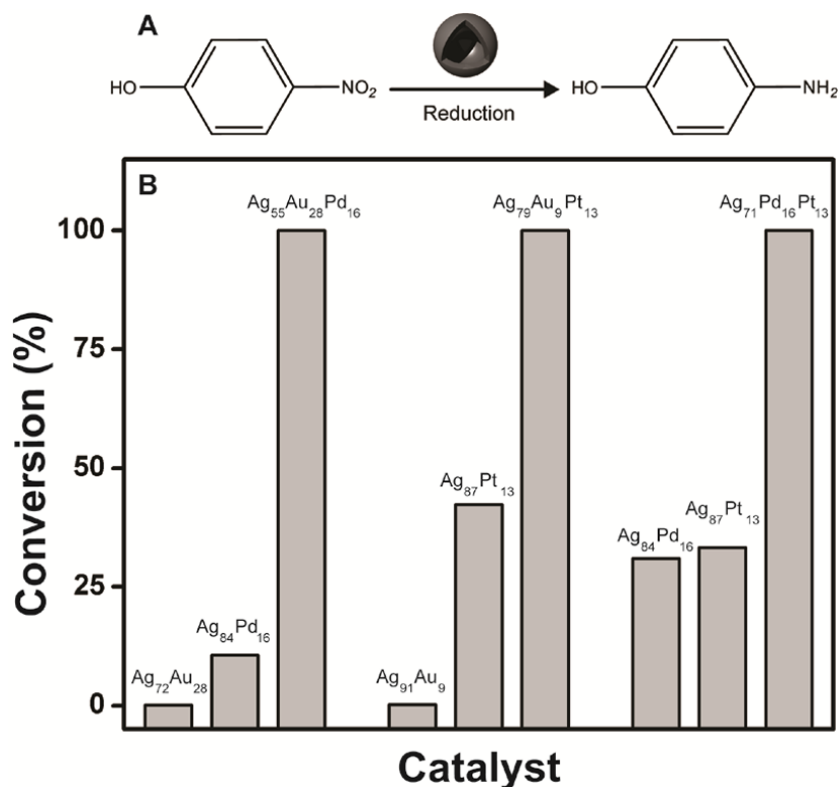


Figure 2.6. (A) Scheme for the 4-nitrophenol reduction catalyzed by metallic nanoshells. (B) Bar graphs illustrating the 4-nitrophenol conversion % as a function of the composition in bi- and trimetallic nanoshells having Ag, Au, and Pd (left), Ag, Au and Pt (middle), and Ag, Pt, and Pd (right) compositions. All catalytic investigations were performed employing the same concentration of metal nanoshells. The 4-nitrophenol conversion was calculated at 130, 208, and 195 s for Ag, Au, and Pd (left); Ag, Au and Pt (middle); and Ag, Pt, and Pd (right) compositions, respectively.

Figure 2.6B displays the 4-nitrophenol conversion percentages as a function of the composition in bi- and trimetallic nanoshells having Ag, Au, and Pd (left), Ag, Au and Pt (middle), and Ag, Pt, and Pd (right) compositions. Interestingly, all trimetallic compositions displayed higher conversion percentages and thus catalytic activities relative to the sum of their bimetallic counterparts, demonstrating the synergism of properties between the three metallic constituents relative to the bimetallic nanoshells. As the trimetallic and bimetallic nanoshells displayed similar shapes and sizes (and thus surface areas), it is plausible that these detected differences in catalytic activities may be assigned to the variation in their composition. Moreover, it can be noted that the relative increase in conversion percentages was also dependent on the composition of the trimetallic nanoshells, and decreased in the following

order: $\text{Ag}_{56}\text{Au}_{28}\text{Pd}_{16} > \text{Ag}_{78}\text{Au}_9\text{Pt}_{13} > \text{Ag}_{71}\text{Pd}_{16}\text{Pt}_{13}$. It is important to note that the 4-nitrophenol reduction catalyzed by noble-metal nanoparticles is strongly dependent on the nature of the metal employed as catalyst. Therefore, it is plausible that the reason for the detected variations in activity for the trimetallic nanoshells ($\text{Ag}_{56}\text{Au}_{28}\text{Pd}_{16} > \text{Ag}_{78}\text{Au}_9\text{Pt}_{13} > \text{Ag}_{71}\text{Pd}_{16}\text{Pt}_{13}$) may be related to the differences in the nature of the metal present in each nanoshell as well as the distinct synergism of properties among the three metals in the nanoshell structure as a function of composition.

In order to gain further insights on the observed differences in catalytic activities, Figure 2.7 depicts the conversion percentage profiles as a function of time for bi- and trimetallic nanoshells having Ag, Au, and Pd (A), Ag, Au and Pt (B), and Ag, Pt, and Pd (C) compositions. Although all bi- and trimetallic nanoshells can achieve 100 % conversion, the trimetallic nanoshells achieve 100 % conversion much faster than their bimetallic counterparts. The highest conversion percentages at shorter reaction times were achieved by the $\text{Ag}_{56}\text{Au}_{28}\text{Pd}_{16}$ nanoshells. In this systems, its conversion percentage achieve 100 after 130 s, while for $\text{Ag}_{72}\text{Au}_{28}$ and $\text{Ag}_{84}\text{Pd}_{16}$ these values corresponded to of 0.2 and 10.6, respectively, suggesting an increase of 826 % in catalytic activity upon the addition of a third metal in the nanoshell structure. Similarly, 100 % conversion could be achieved after 208 and 195 s for $\text{Ag}_{79}\text{Au}_9\text{Pt}_{13}$ and $\text{Ag}_{71}\text{Pd}_{16}\text{Pt}_{13}$ nanoshells, respectively. At these time intervals, this corresponded to an increased of 135 and 56 % relative to the sum of their bimetallic counterparts, i.e., calculated using the conversion % obtained for the trimetallic nanoshells relative to the sum of the conversion % for both bimetallic counterparts as depicted in Figure 2.6. These results clearly show the strong correlation between catalytic activity and composition in metallic nanoshells, and that the incorporation of a third metal represent a promising approach to boost the catalytic activity in this class of nanostructures.

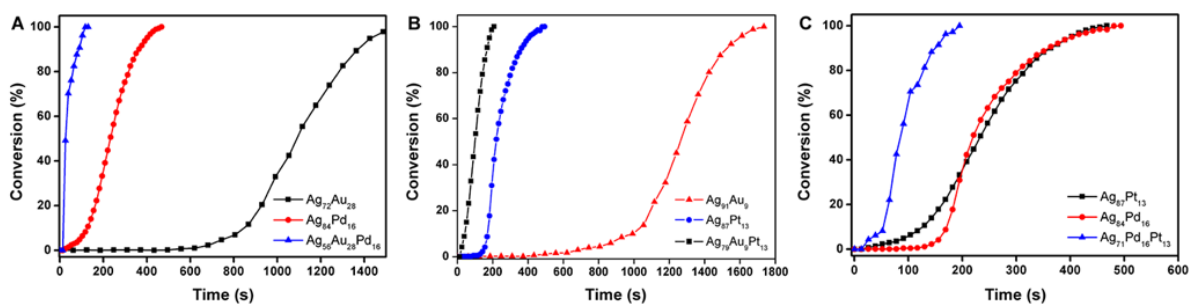


Figure 2.7. 4-nitrophenol conversion % profiles as a function of time for bi- and trimetallic nanoshells having Ag, Au, and Pd (A), Ag, Au and Pt (B), and Ag, Pt, and Pd (C) compositions.

Interestingly, our stability tests showed that all the trimetallic nanoshells could be reused with no loss of activity even after 5 catalytic cycles (100 % conversion after each cycle), indicating that all trimetallic catalysts were stable under our employed conditions, as depicted in Figure 2.8.

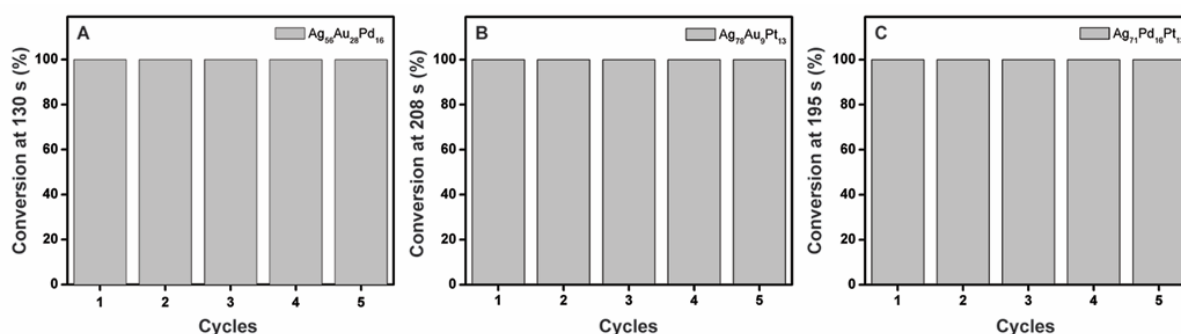


Figure 2.8. Catalytic activity expressed in terms of 4-nitrophenol conversion as a function of number of catalytic cycles for (A) $\text{Ag}_{56}\text{Au}_{28}\text{Pd}_{16}$, (B) $\text{Ag}_{78}\text{Au}_9\text{Pt}_{13}$, (C) $\text{Ag}_{71}\text{Pd}_{16}\text{Pt}_{13}$ nanoshells.

2.4. Conclusion

In summary, we described a facile strategy for the synthesis of trimetallic nanoshells based on AgAuPd, AgAuPt, and AgPdPt which was based on the sequential galvanic replacement reaction between Ag and the corresponding metal precursors ($(\text{AuCl}_4^-)_{\text{(aq)}}$, $(\text{PtCl}_6^{2-})_{\text{(aq)}}$, and $(\text{PdCl}_4^{2-})_{\text{(aq)}}$). This approach enabled us to systematically control the composition in each of these systems. Then, nanoshells having $\text{Ag}_{56}\text{Au}_{28}\text{Pd}_{16}$, $\text{Ag}_{78}\text{Au}_9\text{Pt}_{13}$, and $\text{Ag}_{71}\text{Pd}_{16}\text{Pt}_{13}$ compositions

were employed as model systems to investigate the effect of the addition of the third metal in their composition over the catalytic activities relative to their bimetallic counterparts. Here, the 4-nitrophenol reduction in the presence of sodium borohydride was employed as the probe reaction. Interestingly, our data indicated that all trimetallic compositions displayed significantly higher conversion percentages and thus catalytic activities relative to the sum of their bimetallic counterparts, demonstrating the synergism of properties between the three metals relative to their bimetallic analogues. The relative increase in conversion percentages was also dependent on the composition and decreased in the following order: $\text{Ag}_{56}\text{Au}_{28}\text{Pd}_{16} > \text{Ag}_{78}\text{Au}_9\text{Pt}_{13} > \text{Ag}_{71}\text{Pd}_{16}\text{Pt}_{13}$. The results presented herein clearly show the strong correlation between catalytic activity and composition in multimetallic nanoshells, and that the incorporation of a third metal may represent a promising approach to boost catalytic activities.

2.5. References

- (1) Slater, T. J. A.; Macedo, A.; Schroeder, S. L. M.; Burke, M. G.; O'Brien, P.; Camargo, P. H. C.; Haigh, S. J. Correlating Catalytic Activity of Ag–Au Nanoparticles with 3D Compositional Variations. *Nano Lett.* **2014**, *14* (4), 1921–1926.
- (2) Yu, X.; Wang, D.; Peng, Q.; Li, Y. High Performance Electrocatalyst: Pt-Cu Hollow Nanocrystals. *Chem. Commun.* **2011**, *47* (28), 8094–8096.
- (3) Hong, J. W.; Kang, S. W.; Choi, B.-S.; Kim, D.; Lee, S. B.; Han, S. W. Controlled Synthesis of Pd–Pt Alloy Hollow Nanostructures with Enhanced Catalytic Activities for Oxygen Reduction. *ACS Nano* **2012**, *6* (3), 2410–2419.
- (4) Lou, X. W. (David); Archer, L. A.; Yang, Z. Hollow Micro-/Nanostructures: Synthesis and Applications. *Adv. Mater.* **2008**, *20* (21), 3987–4019.
- (5) Zheng, J.-N.; Lv, J.-J.; Li, S.-S.; Xue, M.-W.; Wang, A.-J.; Feng, J.-J. One-Pot Synthesis of Reduced Graphene Oxide Supported Hollow Ag@Pt Core-Shell Nanospheres with Enhanced Electrocatalytic Activity for Ethylene Glycol Oxidation. *J. Mater. Chem. A* **2014**, *2* (10), 3445–3451.
- (6) Mahmoud, M. A.; Garlyyev, B.; El-Sayed, M. A. Controlling the Catalytic Efficiency on the Surface of Hollow Gold Nanoparticles by Introducing an Inner Thin Layer of Platinum or Palladium. *J. Phys. Chem. Lett.* **2014**, *5* (23), 4088–4094.
- (7) Xue, J.; Xiang, H.; Wang, K.; Zhang, X.; Wang, S.; Wang, X.; Cao, H. The Preparation of Carbon-Encapsulated Fe/Co Nanoparticles and Their Novel Applications as Bifunctional Catalysts to Promote the Redox Reaction for P-Nitrophenol. *J. Mater. Sci.* **2012**, *47* (4), 1737–1744.
- (8) Singh, A. K.; Xu, Q. Synergistic Catalysis over Bimetallic Alloy Nanoparticles. *ChemCatChem* **2013**, *5* (3), 652–676.
- (9) Sun, Y.; Mayers, B.; Xia, Y. Metal Nanostructures with Hollow Interiors. *Adv. Mater.*

- 2003**, *15* (7–8), 641–646.
- (10) Xia, X.; Wang, Y.; Ruditskiy, A.; Xia, Y. 25th Anniversary Article: Galvanic Replacement: A Simple and Versatile Route to Hollow Nanostructures with Tunable and Well-Controlled Properties. *Adv. Mater.* **2013**, *25* (44), 6313–6333.
 - (11) Jiang, H.-L.; Xu, Q. Recent Progress in Synergistic Catalysis over Heterometallic Nanoparticles. *J. Mater. Chem.* **2011**, *21* (36), 13705–13725.
 - (12) An, K.; Hyeon, T. Synthesis and Biomedical Applications of Hollow Nanostructures. *Nano Today* **2009**, *4* (4), 359–373.
 - (13) da Silva, A. G. M.; de Souza, M. L.; Rodrigues, T. S.; Alves, R. S.; Temperini, M. L. A.; Camargo, P. H. C. Rapid Synthesis of Hollow Ag–Au Nanodendrites in 15 Seconds by Combining Galvanic Replacement and Precursor Reduction Reactions. *Chem. – A Eur. J.* **2014**, *20* (46), 15040–15046.
 - (14) Mahmoud, M. A.; Narayanan, R.; El-Sayed, M. A. Enhancing Colloidal Metallic Nanocatalysis: Sharp Edges and Corners for Solid Nanoparticles and Cage Effect for Hollow Ones. *Acc. Chem. Res.* **2013**, *46* (8), 1795–1805.
 - (15) Chen, H. M.; Liu, R.-S.; Lo, M.-Y.; Chang, S.-C.; Tsai, L.-D.; Peng, Y.-M.; Lee, J.-F. Hollow Platinum Spheres with Nano-Channels: Synthesis and Enhanced Catalysis for Oxygen Reduction. *J. Phys. Chem. C* **2008**, *112* (20), 7522–7526.
 - (16) Wang, W.; Pang, Y.; Yan, J.; Wang, G.; Suo, H.; Zhao, C.; Xing, S. Facile Synthesis of Hollow Urchin-like Gold Nanoparticles and Their Catalytic Activity. *Gold Bull.* **2012**, *45* (2), 91–98.
 - (17) Yu, W.; Porosoff, M. D.; Chen, J. G. Review of Pt-Based Bimetallic Catalysis: From Model Surfaces to Supported Catalysts. *Chem. Rev.* **2012**, *112* (11), 5780–5817.
 - (18) Chai, J.; Li, F.; Hu, Y.; Zhang, Q.; Han, D.; Niu, L. Hollow Flower-like AuPd Alloy Nanoparticles: One Step Synthesis, Self-Assembly on Ionic Liquid-Functionalized Graphene, and Electrooxidation of Formic Acid. *J. Mater. Chem.* **2011**, *21* (44), 17922–17929.
 - (19) Wu, H.; Wang, P.; He, H.; Jin, Y. Controlled Synthesis of Porous Ag/Au Bimetallic Hollow Nanoshells with Tunable Plasmonic and Catalytic Properties. *Nano Res.* **2012**, *5* (2), 135–144.
 - (20) Khanal, S.; Bhattarai, N.; McMaster, D.; Bahena, D.; Velazquez-Salazar, J. J.; Jose-Yacaman, M. Highly Monodisperse Multiple Twinned AuCu-Pt Trimetallic Nanoparticles with High Index Surfaces. *Phys. Chem. Chem. Phys.* **2014**, *16* (30), 16278–16283.
 - (21) Ostrom, C. K.; Chen, A. Synthesis and Electrochemical Study of Pd-Based Trimetallic Nanoparticles for Enhanced Hydrogen Storage. *J. Phys. Chem. C* **2013**, *117* (40), 20456–20464.
 - (22) Qiao, P.; Xu, S.; Zhang, D.; Li, R.; Zou, S.; Liu, J.; Yi, W.; Li, J.; Fan, J. Sub-10 Nm Au-Pt-Pd Alloy Trimetallic Nanoparticles with a High Oxidation-Resistant Property as Efficient and Durable VOC Oxidation Catalysts. *Chem. Commun.* **2014**, *50* (79), 11713–11716.
 - (23) Zhang, H.; Toshima, N. Glucose Oxidation Using Au-Containing Bimetallic and Trimetallic Nanoparticles. *Catal. Sci. Technol.* **2013**, *3* (2), 268–278.
 - (24) Ghiaci, M.; Aghabarari, B.; Botelho do Rego, A. M.; Ferraria, A. M.; Habibollahi, S. Efficient Allylic Oxidation of Cyclohexene Catalyzed by Trimetallic Hybrid Nano-Mixed Oxide (Ru/Co/Ce). *Appl. Catal. A Gen.* **2011**, *393* (1–2), 225–230.
 - (25) Jiang, K.; Cai, W.-B. Carbon Supported Pd-Pt-Cu Nanocatalysts for Formic Acid Electrooxidation: Synthetic Screening and Componential Functions. *Appl. Catal. B Environ.* **2014**, *147* (0), 185–192.
 - (26) Venkatesan, P.; Santhanalakshmi, J. Designed Synthesis of Au/Ag/Pd Trimetallic

- Nanoparticle-Based Catalysts for Sonogashira Coupling Reactions. *Langmuir* **2010**, *26* (14), 12225–12229.
- (27) Wu, H.; Pantaleo, G.; La Parola, V.; Venezia, A. M.; Collard, X.; Aprile, C.; Liotta, L. F. Bi- and Trimetallic Ni Catalysts over Al₂O₃ and Al₂O₃-MO_x Oxides for Methane Dry Reforming: Au and Pt Additive Effects. *Appl. Catal. B Environ.* **2014**, *156–157* (0), 350–361.
- (28) Wu, Y.; Wang, D.; Zhou, G.; Yu, R.; Chen, C.; Li, Y. Sophisticated Construction of Au Islands on Pt–Ni: An Ideal Trimetallic Nanoframe Catalyst. *J. Am. Chem. Soc.* **2014**, *136* (33), 11594–11597.
- (29) Wang, H.-L.; Yan, J.-M.; Wang, Z.-L.; Jiang, Q. One-Step Synthesis of Cu@FeNi Core-shell Nanoparticles: Highly Active Catalyst for Hydrolytic Dehydrogenation of Ammonia Borane. *Int. J. Hydrogen Energy* **2012**, *37* (13), 10229–10235.
- (30) Kang, S. W.; Lee, Y. W.; Park, Y.; Choi, B.-S.; Hong, J. W.; Park, K.-H.; Han, S. W. One-Pot Synthesis of Trimetallic Au@PdPt Core-Shell Nanoparticles with High Catalytic Performance. *ACS Nano* **2013**, *7* (9), 7945–7955.
- (31) Hungria, A. B.; Raja, R.; Adams, R. D.; Captain, B.; Thomas, J. M.; Midgley, P. A.; Golovko, V.; Johnson, B. F. G. Single-Step Conversion of Dimethyl Terephthalate into Cyclohexanedimethanol with Ru₅PtSn, a Trimetallic Nanoparticle Catalyst. *Angew. Chemie Int. Ed.* **2006**, *45* (29), 4782–4785.
- (32) Petri, M. V.; Ando, R. A.; Camargo, P. H. C. Tailoring the Structure, Composition, Optical Properties and Catalytic Activity of Ag–Au Nanoparticles by the Galvanic Replacement Reaction. *Chem. Phys. Lett.* **2012**, *531*, 188–192.
- (33) Endo, T.; Kuno, T.; Yoshimura, T.; Esumi, K. Preparation and Catalytic Activity of AuPd, AuPt, and PtPd Binary Metal Dendrimer Nanocomposites. *Journal of Nanoscience and Nanotechnology*. pp 1875–1882.
- (34) Silvert, P.-Y.; Herrera-Urbina, R.; Duvauchelle, N.; Vijayakrishnan, V.; Elhsissen, K. T. Preparation of Colloidal Silver Dispersions by the Polyol Process. Part 1-Synthesis and Characterization. *J. Mater. Chem.* **1996**, *6* (4), 573–577.
- (35) Cobley, C. M.; Skrabalak, S. E.; Campbell, D. J.; Xia, Y. Shape-Controlled Synthesis of Silver Nanoparticles for Plasmonic and Sensing Applications. *Plasmonics* **2009**, *4* (2), 171–179.
- (36) Zhang, C.; Li, C.; Chen, Y.; Zhang, Y. Synthesis and Catalysis of Ag Nanoparticles Trapped into Temperature-Sensitive and Conductive Polymers. *J. Mater. Sci.* **2014**, *49* (20), 6872–6882.
- (37) Silva, A. G. M. da; Rodrigues, T. S.; Macedo, A.; Silva, R. T. P. da; Camargo, P. H. C. An Undergraduate Level Experiment on the Synthesis of Au Nanoparticles and Their Size-Dependent Optical and Catalytic Properties. *Química Nova*. scielo 2014, pp 1716–1720.
- (38) Wang, X.; Fu, J.; Wang, M.; Wang, Y.; Chen, Z.; Zhang, J.; Chen, J.; Xu, Q. Facile Synthesis of Au Nanoparticles Supported on Polyphosphazene Functionalized Carbon Nanotubes for Catalytic Reduction of 4-Nitrophenol. *J. Mater. Sci.* **2014**, *49* (14), 5056–5065.

Chapter 3

Rational Design of Plasmonic Catalysts: Matching the Surface Plasmon Resonance with the Lamp Emission Spectra for Improved Performances in AgAu Nanorings

3.1. Introduction

Silver (Ag) and gold (Au) nanostructures display remarkable optical properties in the visible range as a result of their localized surface plasmon resonance excitation (SPR).³⁹⁻⁴⁴ Specially, Ag and Au nanorings have attracted interest in the field of plasmonic as their SPR can be tuned as a function of their sizes (along longitudinal and transverse directions), wall thickness, hollow interiors, and composition (in the case of AgAu nanorings).⁴⁵⁻⁴⁷ However, many strategies for the synthesis of Ag and Au nanorings still rely on lithography techniques, which require special facilities and complex procedures.⁴⁸⁻⁵⁰ Albeit chemical approaches have also been developed, they often rely on the use of 2D nanocrystals (nanoplates) as seeds and/or require the utilization of metals such as palladium (Pd) and platinum (Pt), making it not attractive for large-scale production.^{47,51-53} Therefore, despite the progress, facile procedures for the synthesis of Ag and Au nanorings remain challenging.

It has been demonstrated that the SPR excitation in Ag and Au nanomaterials can be put to work to mediate and/or enhance a variety of catalytic transformations, such as oxidations,⁵⁴⁻⁵⁶ reductions,⁵⁶⁻⁵⁸ and coupling reactions.^{55,56,58,59} Regarding practical applications in the field of plasmonic catalysis, the utilization of commercially available and inexpensive lamps as the SPR excitation source would be highly desirable. Consequently, the design of Ag and Au

nanoparticles having SPR extinction that closely matches the emission spectra of commercial lamps represent an intuitive strategy to maximize performance towards SPR-mediated transformations.^{60,61} However, most studies employing white light as the excitation sources (instead of lasers or LEDs) still focus on the utilization of conventional nanoparticles as catalysts, such as Ag and Au nanospheres, whose SPR extinction do not necessarily match the lamp emission. Thus, in principle, a large amount of light power may be wasted in these systems.^{56,58,60–62}

We report the rational design of AgAu nanorings displaying SPR extinction that closely matches the emission spectra of a commercial and inexpensive halogen-tungsten lamp by a facile strategy using Ag nanospheres as starting materials. The AgAu nanorings were employed as catalysts for the SPR-mediated oxidation of methylene blue in the liquid phase (water as the solvent), under ambient conditions, and using a halogen-tungsten lamp as the only energy input. We found that the catalytic activity for the AgAu nanorings was significantly higher as compared to its Ag and Au nanospheres counterparts. We also performed a series of control experiments to unravel the role of hot electrons and holes over the SPR-mediated oxidation of methylene blue.

3.2. Experimental

Materials and Instrumentation

Analytical grade silver nitrate (AgNO_3 , 99%, Sigma-Aldrich), polyvinylpyrrolidone (PVP, Sigma-Aldrich, M.W. 10,000 g/mol), polyvinylpyrrolidone (PVP, Sigma-Aldrich, M.W. 55,000 g/mol), ethylene glycol (EG, 99.8%, Sigma-Aldrich), sodium citrate dihydrate ($\text{C}_6\text{H}_5\text{Na}_3\text{O}_2 \cdot 2\text{H}_2\text{O}$, $\geq 99.9\%$, Sigma-Aldrich), tetrachloroauric acid ($\text{HAuCl}_4 \cdot 3\text{H}_2\text{O}$, $\geq 99.9\%$, Sigma-Aldrich), 4-nitrophenol ($\text{C}_6\text{H}_5\text{NO}_2$, $\geq 99\%$, Sigma-Aldrich), MB hydrate

(C₁₆H₁₈ClN₃S.xH₂O, ≥95%, Sigma-Aldrich), and sodium borohydride (NaBH₄, 98%, Sigma-Aldrich) were used as received.

The scanning electron microscopy (SEM) images were obtained using a JEOL field emission gun electron microscope JSM6330F operated at 5 kV. The samples were prepared by drop-casting an aqueous suspension containing the nanostructures over a silicon wafer, followed by drying under ambient conditions. High-resolution transmission electron microscopy (HRTEM) images were obtained with a JEOL JEM2100 microscope operated at 200 kV. Energy dispersive X-ray (EDX) spectrum was obtained in this instrument with an EDX detector configuration which has a total solid angle of ~0.13 sr. Samples for HRTEM were prepared by drop-casting an aqueous suspension of the nanostructures over a carbon-coated copper grid, followed by drying under ambient conditions. UV-VIS spectra were obtained from aqueous suspensions containing the nanostructures with a Shimadzu UV-1700 spectrophotometer. The Ag and Au atomic percentages were measured by inductively coupled plasma optical emission spectrometry (ICP-OES) using a Spectro Arcos equipment at the IQ-USP analytical center facilities. The X-ray diffraction (XRD) data were obtained using a Rigaku - Miniflex equipment, CuK α radiation. The diffraction pattern was measured in the range of 10 – 90 ° 2 θ with a 1 ° min⁻¹ angular speed scan.

Synthesis of Ag nanospheres

Ag nanospheres were prepared by the polyol process. In a typical procedure, 5 g of polyvinylpyrrolidone (M.W. 10,000 g/mol) were dissolved in 37.5 mL of ethylene glycol (EG). Then, AgNO₃ (200 mg, 1.2 mmol) was added and mixed until complete dissolution. The resulting solution was heated to 125 °C for 2.5 hours, leading to the appearance of a greenish-yellow color, allowed to cool down to room temperature, and diluted to 125 mL of water. For the catalytic tests, 1 mL of Ag nanospheres suspension was washed three times with water by

successive rounds of centrifugation at 15,000 rpm and removal of the supernatant. After washing, the Ag nanoparticles were suspended in 1 mL of deionized water. In this case, the concentration of Ag in the nanoparticles suspensions corresponded to 2.2 mM (measured by ICP-OES).

Synthesis of Au nanospheres

The synthesis of Au nanospheres was performed by a seeded growth approach. In the first step, Au seeds were synthesized by adding 150 mL of a 2.2 mM sodium citrate aqueous solution to a 250 mL round-bottom flask under magnetic stirring. This system was heated to 100 °C for 15 minutes. Then, 1 mL of a 25 mM AuCl_4^- (aq) solution was added, and the reaction mixture was kept at 100°C under vigorous stirring for 30 minutes. The obtained Au nanoparticles were employed as seeds for the synthesis of Au NPs having larger sizes by two successive steps of Au deposition. For the first deposition step, 1 mL of a 60 mM sodium citrate solution was added to the same 250 mL round-bottom flask containing the Au NPs seeds under magnetic stirring at 100°C for 5 minutes. Afterwards, 1 mL of a 25 mM AuCl_4^- (aq) solution was added to the reaction mixture containing the Au NPs seeds and the reaction mixture was carried out for another 30 min. Similarly, a second deposition step could be performed by adding another 1 mL of a 60 mM sodium citrate solution and 1 mL of a 25 mM AuCl_4^- (aq) solution to the reaction mixture obtained after the first deposition step, in which the Au NPs produced after the first deposition step served as seeds for further growth. After the reaction, the resulting suspension was allowed to cool down to room temperature. For the catalytic tests, 5 mL of Au nanospheres suspension was washed three times with water by successive rounds of centrifugation at 15,000 rpm and removal of the supernatant. After washing, the Au nanoparticles were suspended in 1 mL of deionized water. Here, the concentration of Au in the nanoparticles suspensions corresponded to 2.2 mM (measured by ICP-OES).

Synthesis of AgAu nanorings

The synthesis of AgAu nanorings was based on the galvanic replacement reaction between Ag nanospheres and AuCl_4^- (aq). In a typical procedure, a mixture containing 5 mL of PVP aqueous solution (0.1 wt %, M.W. 55,000 g/mol) and 1 mL of the as-prepared suspension containing the Ag nanospheres (2.2 mM in terms of Ag) was stirred at 100 °C for 10 min in a 25 mL round-bottom flask. Then, 2 mL of AuCl_4^- (aq) (1.5 mM) was added dropwise and the reaction allowed to proceed at 100 °C for another 1 h. After that, the suspension was allowed to cool down to room temperature and 10 mL were washed twice with a supersaturated NaCl solution and three times with water by successive rounds of centrifugation at 15,000 rpm and removal of the supernatant. After washing, the product was suspended in 1 mL of deionized water and then employed in the catalytic tests. After this step, the concentration of metal (Ag + Au) in the nanoparticles suspensions corresponded to 2.2 mM (measured by ICP-OES).

Synthesis of AgAu alloyed nanospheres

In a typical procedure, 0.7 mL of an aqueous 2.0 mM AgNO_3 solution, 95 mL of deionized water, and 1.0 mL of an aqueous 35 mM sodium citrate solution were transferred to a round bottom flask. This flask was placed on an oil bath pre-heated at 105 °C. After boiling for 1 min, 3.6 mL of a 2.4 mM AuCl_4^- (aq) solution was added and the reaction mixture was further boiled for 40 min. After the reaction, the resulting suspension was allowed to cool down to room temperature. For the catalytic tests, 4.5 mL of AgAu alloyed nanospheres suspension was washed three times with water by successive rounds of centrifugation at 15,000 rpm and removal of the supernatant. After washing, the AgAu alloyed nanospheres were suspended in 1 mL of deionized water. After this step, the concentration of metal (Ag + Au) in the nanoparticles suspensions corresponded to 0.1 mM (measured by ICP-OES).

SPR-mediated oxidation of methylene blue

Typically, 10 mL of a 10 mg/L MB aqueous solution and 1 mL of the suspension containing the washed catalysts was added in a 25 mL round-bottom flask. The resulting mixture was stirred for 30 min in the dark to achieve the adsorption and desorption equilibrium. Subsequently, the suspensions were irradiated with a 300 W halogen tungsten lamp (OSRAM) mounted at a 5 cm distance from the glass reactor. In all photocatalytic experiments, the temperature of the reaction mixture was carefully controlled and corresponded to 40 °C. During the experiments, 1 mL aliquots were taken and centrifuged at 15,000 rpm for 10 min to isolate the supernatant. Then, the UV–VIS spectra of the supernatant were measured as a function of time in the 500 to 750 nm range to probe the MB photodegradation. A calibration curve for absorbance as a function of the MB concentration was employed in order to monitor the transformation.

Catalytic reduction of 4-nitrophenol

Typically, 2 mL of 4.2×10^{-2} M sodium borohydride aqueous solution and the suspension containing the catalysts was added into a quartz cuvette. After 5 min, 1 mL of a 1.4×10^{-4} M 4-nitrophenol aqueous solution was added to the same cuvette. The catalytic transformation was monitored by UV–VIS spectroscopy, in which the intensity in the absorbance at 400 nm (assigned to 4-nitrophenolate ions) was monitored as a function of time (this signal decreased as the consumption of 4-nitrophenolate ions and formation of 4-aminophenol took place). In this case, the UV-VIS spectra were collected at 13 s time intervals in the 350 to 500 nm range. A calibration curve for absorbance as a function of the 4-nitrophenolate concentration was employed in order to monitor the transformation. All reactions were performed under the same amount of catalyst (2.2×10^{-6} mmol of metal, which corresponds to 1, 5, and 10 μ L of Ag nanospheres, Au nanospheres, and AgAu nanorings, respectively).

3.3. Results and discussion

We started our studies with the synthesis of AgAu nanorings having SPR positions that could match, as much as possible, the emission spectra of a commercial halogen-tungsten lamp which is shown in Figure 3.1 (yellow trace). Although the halogen-tungsten lamp emission covers the entire visible range, the emission becomes increasingly larger as a function of the wavelength, i.e., it steadily increases from 400 to 800 nm. It can be observed that the SPR extinction of conventional Ag and Au nanospheres does not match the lamp emission spectra. (Figure 3.1, green and red traces respectively). In this case, Ag and Au nanospheres display SPR bands centered at 405 and ~ 522 nm, respectively.

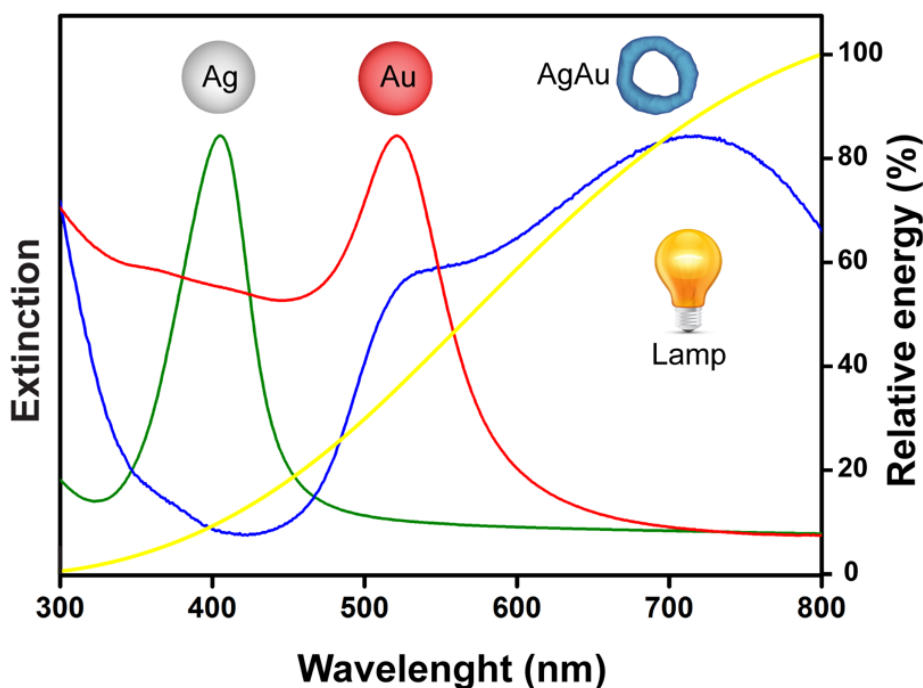


Figure 3.1. UV–VIS extinction spectra recorded from aqueous suspensions containing Ag nanospheres (green trace), Au nanospheres (red trace), and AgAu nanorings (blue trace). The yellow trace shows the emission spectrum for the commercial tungsten-halogen lamp employed as the excitation source in our SPR-mediated catalytic experiments.

It has been established that the galvanic replacement reaction between Ag nanospheres and AuCl_4^- (aq) represents an effective strategy for tuning the SPR position in the entire visible

range.^{10,32,63} In this case, the control over the Ag to AuCl_4^- (aq) molar ratios enables one to control the composition, structure (solid vs hollow interiors), optical properties, and catalytic activity of the obtained AgAu nanomaterials.^{1,10,32,63} Rather than using 2D nanocrystals as seeds, AgAu nanorings having a SPR spectrum that closely resembles the emission spectra of the halogen-tungsten lamp could be obtained from the aforementioned galvanic replacement reaction using “conventional” Ag nanospheres as seeds as shown in Figure 3.1 (blue trace). Specifically, the SPR spectra for the AgAu nanorings displayed two SPR bands: one shoulder located at 536 nm and a broad signal centered at 725 nm. The detected red-shift and broadening of the SPR in the nanorings relative to the Ag and Au nanospheres are in agreement with the Au deposition as well as the formation of the hollow interiors in during the galvanic reaction (Figure 3.2A).^{64–66}

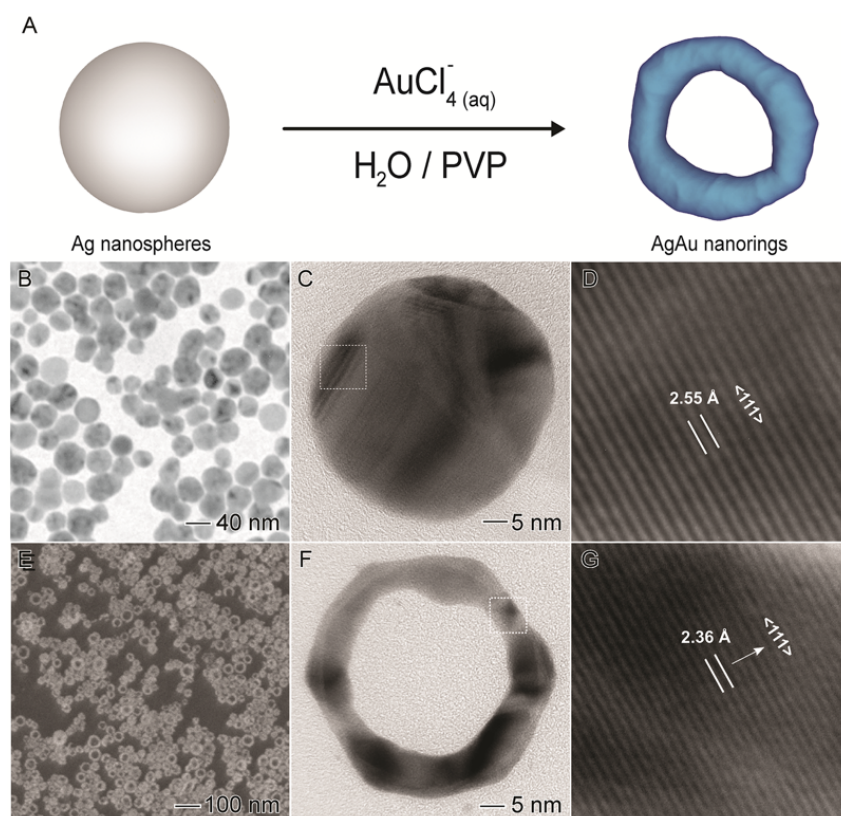


Figure 3.2. (A) Synthesis of AgAu nanorings by galvanic replacement reaction between Ag nanospheres and AuCl_4^- (aq). TEM (B) and HRTEM (C and D) images for Ag nanospheres. SEM (E) and HRTEM (F and G) images for AgAu nanorings. The image in (D) and (G) correspond to phase contrast images of the areas highlighted by the white squares in (C) and (F).

Figure 3.2B-D shows TEM and HRTEM images of the Ag nanospheres employed as templates (whose spectra is shown in Figure 3.1). They were relatively uniform, polycrystalline, and 38 ± 3 nm in diameter. The 0.255 nm $\langle 111 \rangle$ lattice spacing characteristic of *fcc* Ag could be identified in the HRTEM image. The SEM and HRTEM images of AgAu nanorings (Figure 3.2E-G) confirmed that they were also uniform. Moreover, they displayed well-defined shapes comprised of hollow interiors and ultrathin walls. The AgAu nanorings were 38 ± 4 nm in outer diameter and 8 ± 1 nm in wall-thickness. HRTEM images confirmed the presence of 0.255 nm $\langle 111 \rangle$ lattice spacing that can be assigned to the presence of *fcc* Ag and Au. ICP-OES results showed that the nanorings contained 81 at. % in terms of Au, which is also in agreement with EDX spectra obtained from an individual nanoring (Figure 3.3, 80 at. % in terms of Au).

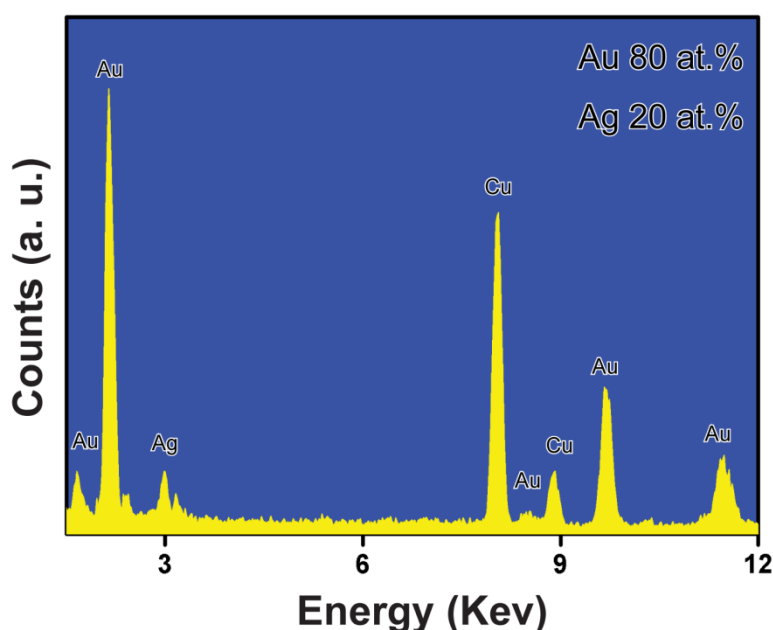


Figure 3.3. EDX spectrum obtained from an individual AgAu nanoring.

Figure 3.4A and 3.4B show the histograms of size distribution for Ag nanoparticles and AgAu nanorings.

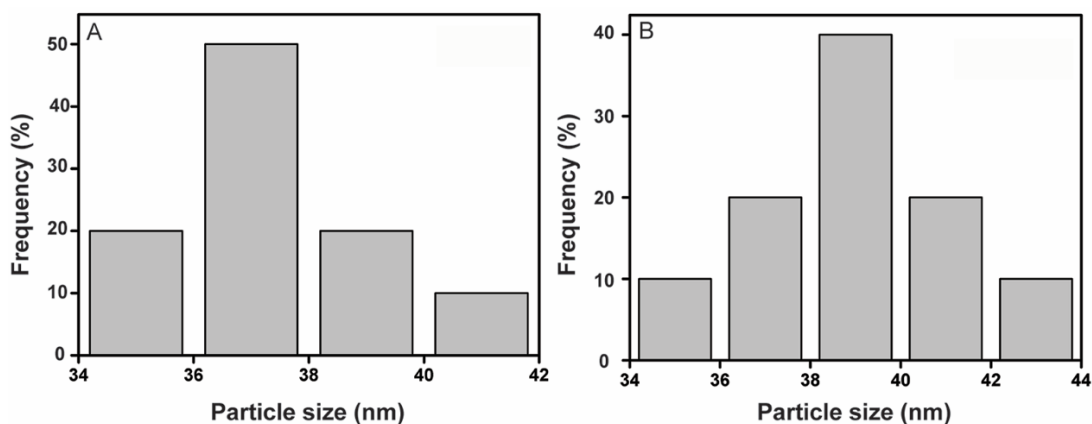


Figure 3.4. Histograms showing the particle size distribution for the obtained Ag nanospheres (A) and AgAu nanorings (B).

The XRD patterns (Figure 3.5) also confirmed the formation of Ag and AgAu nanostructures without the presence of any significant crystalline impurities.

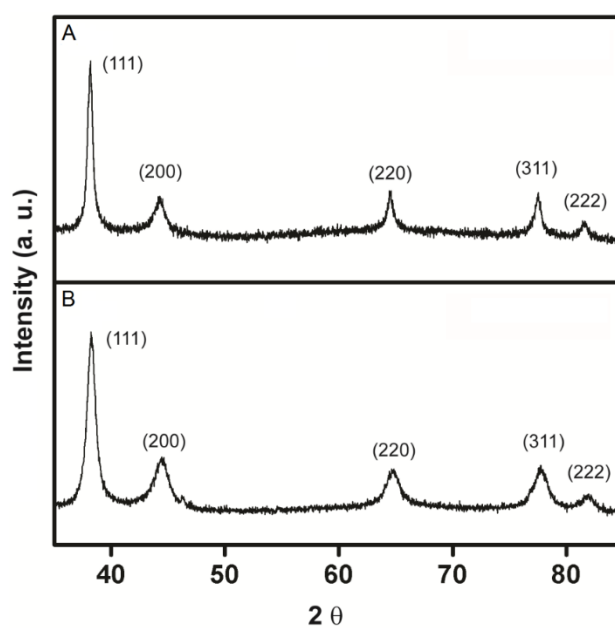


Figure 3.5. X-ray diffraction patterns recorded from the obtained Ag nanospheres (A) and AgAu nanorings (B).

The obtained AuAu nanorings presents two very attractive features for SPR-mediated catalytic applications: *i*) their SPR extinction that matches the emission spectra of the halogen-tungsten lamp; and *ii*) the ultrathin walls/hollow interiors that enable one to get higher surface

to volume ratios, and thus surface areas, relative to their solid counterparts. In the next step, we employed the SPR-mediated oxidation of methylene blue (Figure 3.6A) as a model transformation to benchmark the performance of the AgAu nanorings against its Ag and Au nanospheres counterparts. This reaction was carried out under ambient conditions, in the liquid phase (water as the solvent), and employing a commercial halogen-tungsten lamp (300 W) as the only energy input.

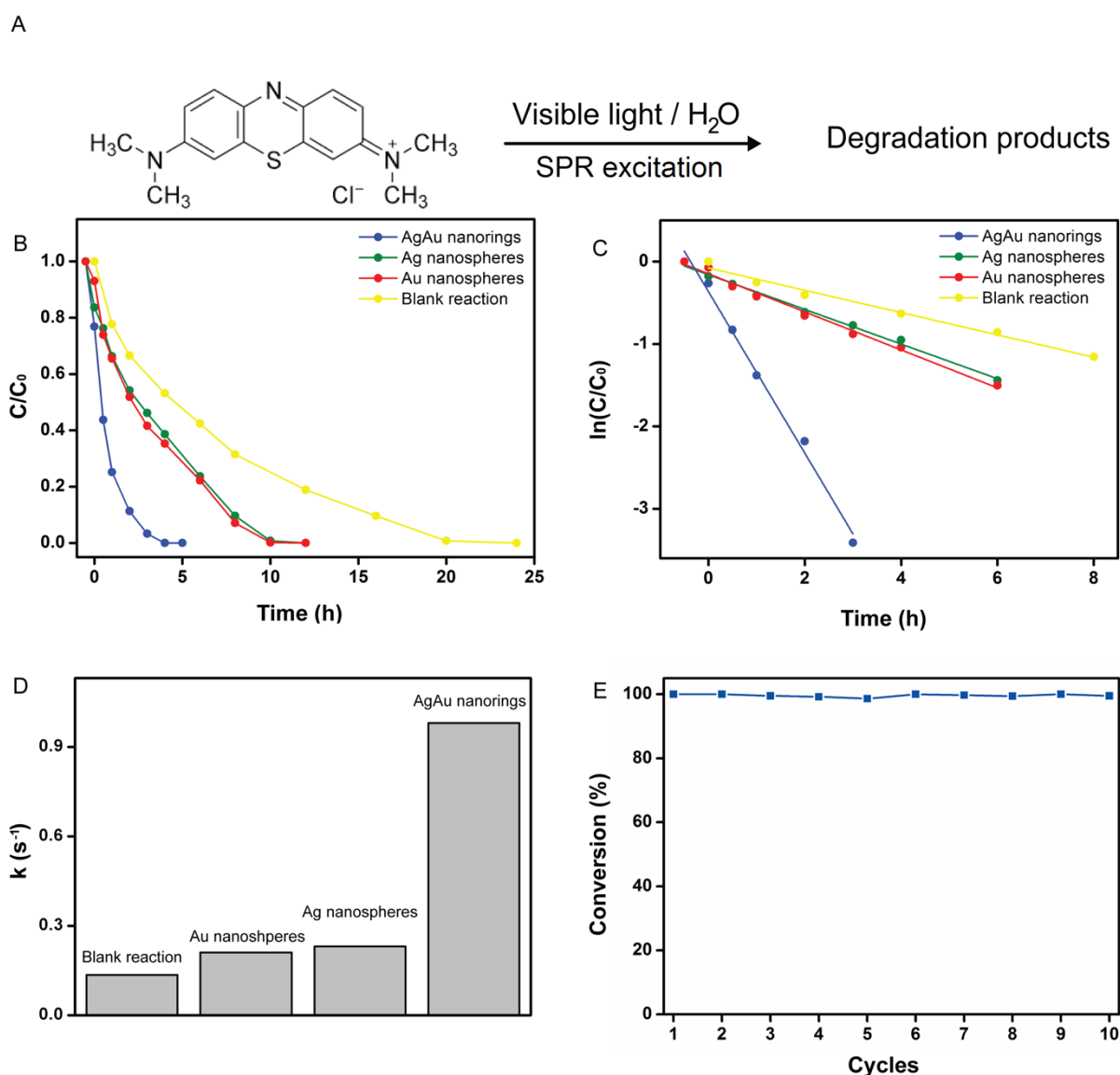


Figure 3.6. (A) SPR-mediated oxidation of methylene blue. C/C_0 (B) and $\ln(C/C_0)$ (C) profiles as a function of time employing Ag nanospheres (red trace), Au nanospheres (blue trace), and AgAu nanorings (blue trace) as catalysts. A blank reaction without any catalyst was also performed (green trace). (D) Pseudo-first order rate constants (k) calculated from (C). (E) Stability tests employing AgAu nanorings as catalysts.

Figure 3.6B and 3.6C show the variations in C/C_0 and $\ln(C/C_0)$ for the methylene blue oxidation as a function of time employing AuAg nanorings, Ag nanospheres, and Au nanospheres as catalysts (blue, green, and red traces, respectively) under visible light illumination. In all photocatalytic experiments, the temperature of the reaction mixture was carefully controlled and corresponded to 40 °C. It can be observed that the utilization of AgAu nanorings as catalyst led to an increase in the reaction rate relative to the nanospheres as illustrated by the C/C_0 profiles as a function of time (Figure 3.6B). The C/C_0 ratios after 5h corresponded to 0 (total oxidation), 0.22, 0.24, and 0.53 for AgAu nanorings, Au nanospheres, Ag nanospheres, and for a blank reaction, respectively. This behavior is also supported by the $\ln(C/C_0)$ profiles as a function of time (Figure 3.6C) and the calculated pseudo-first-order rate constants (k) (Figure 3.6D). For instance, k corresponded to 0.98, 0.23, 0.21, and 0.14 h⁻¹ for AgAu nanorings, Au nanospheres, Ag nanospheres, and blank reaction, respectively. All catalytic experiments were performed under the same metal loading, in which the metal concentration in all catalyst suspensions was adjusted to 2.2 mM (as measured by ICP-OES) by centrifugation of the suspensions followed by the addition of a water to re-suspend the nanostructures. Our results showed that AgAu nanorings displayed improved performances relative to Ag and Au nanospheres of similar sizes. The activity for the AgAu nanorings was 4.3 and 4.7-fold higher relative to the Au and Ag nanospheres, respectively. The AgAu nanorings could be recovered from the suspension after at the end of the oxidation reaction by centrifugation and re-used for at least ten reaction cycles without any loss of activity, indicating their good stability towards this SPR-mediated transformation (Figure 3.6E). For comparison, we also synthesized Au nanoparticles 39 ± 2 nm in diameter by a seeded growth approach as shown in Figure 3.7.³⁷ Their extinction spectra is shown in Figure 3.1 (red trace).

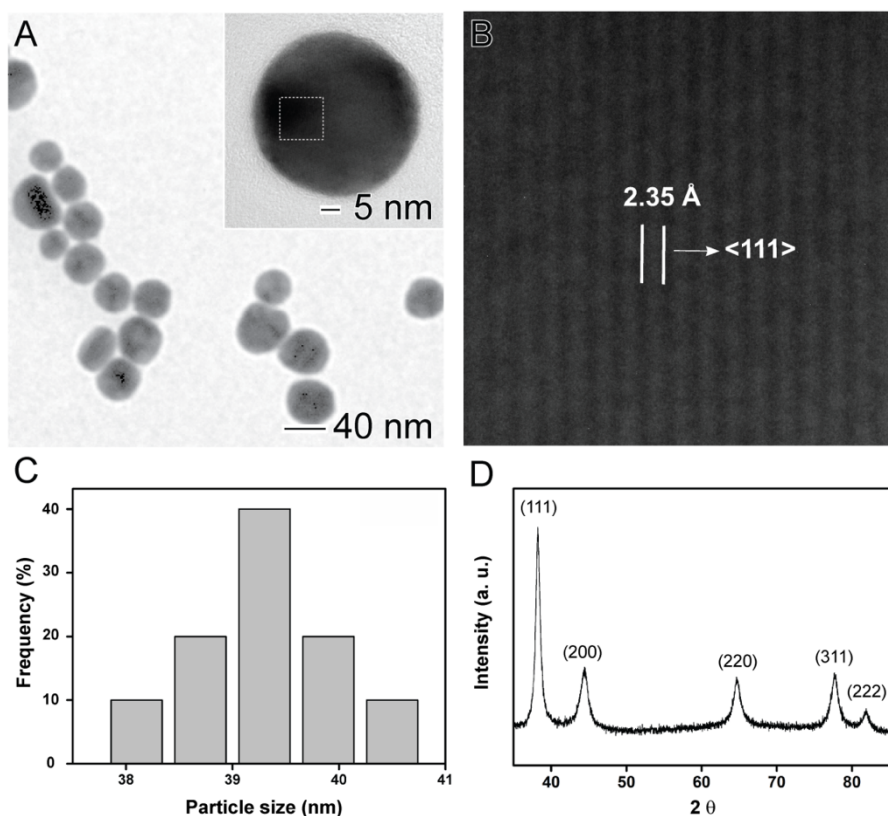


Figure 3.7. TEM and HRTEM (A and B) images for Au nanospheres employed in our photocatalytic and catalytic experiments. The image in (B) corresponds to a zoom-in image of the area highlighted by the white square in inset of (A). (C) Histogram showing the particle size distribution and (D) X-ray diffraction pattern from the Au nanospheres.

In order to exclude the effect of the nanorings bimetallic composition over the catalytic performances, we also prepared AgAu alloy nanoparticles having with similar compositions relative to the nanorings as shown in Figure 3.8 (81 mol % in terms of Au).

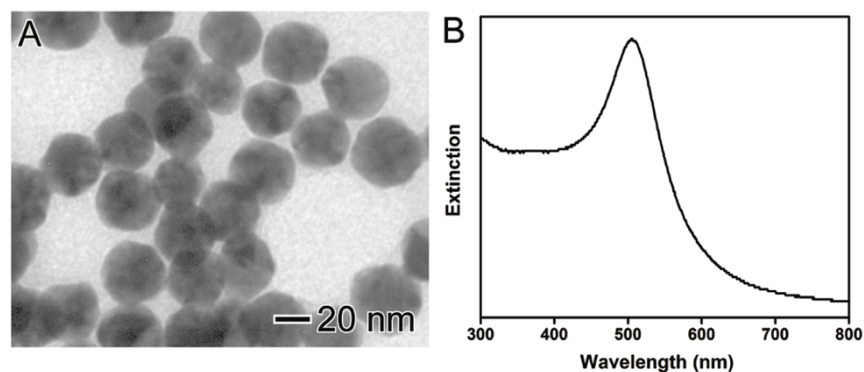


Figure 3.8. (A) TEM image and (B) UV-Vis extinction spectra for AgAu alloyed nanospheres employed in our photocatalytic and catalytic experiments.

No significant differences in the SPR-mediated methylene blue conversion was observed for the bimetallic AgAu alloys as compared to the monometallic Ag and Au nanospheres (Figure 3.9).

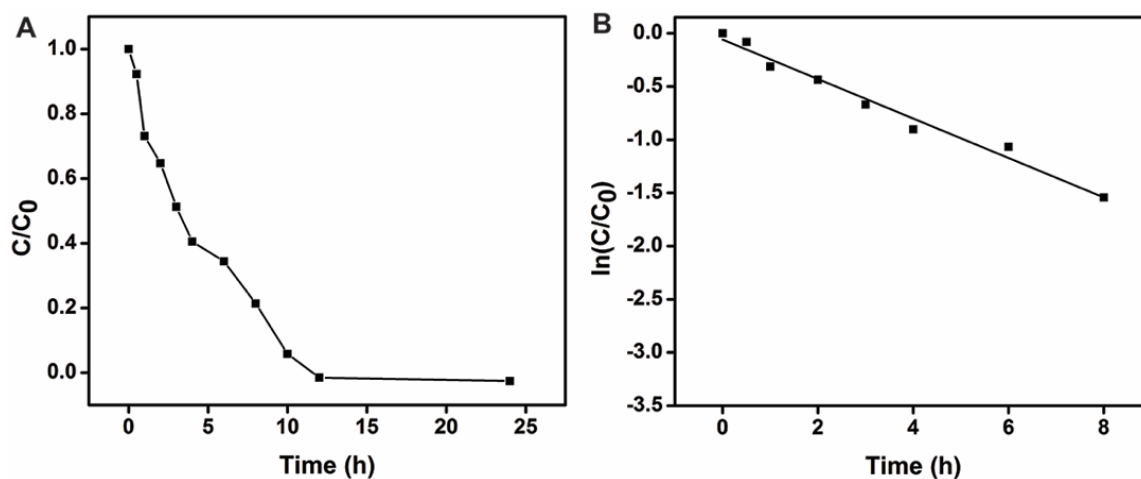


Figure 3.9. SPR-mediated oxidation of methylene blue. C/C_0 (A) and $\ln(C/C_0)$ (B) profiles as a function of time employing AgAu alloyed nanospheres as catalysts.

It is plausible that the higher activity of the nanorings relative to the nanospheres can be explained both by its increased surface-to-volume ratios and better matching between its SPR extinction and the lamp emission spectra. It is important to note that, considering the surface area of the nanostructures and the metal loading employed in the catalytic experiments, the calculated surface areas corresponded 1,630, 1,570, and 5,100 $\text{m}^2 \cdot \text{mol}^{-1}$ for Ag nanospheres, Au nanospheres, and AgAu nanorings, respectively. This indicates that the available surface area for the nanorings was 3.1 and 3.2-fold higher relative to Ag and Au NPs, respectively. Encouragingly, no degradation products were identified in the GC-MS chromatogram from the reaction mixture after the reaction, indicating that the methylene blue was completely mineralized by the SPR-mediated oxidation process (Figure 3.10).

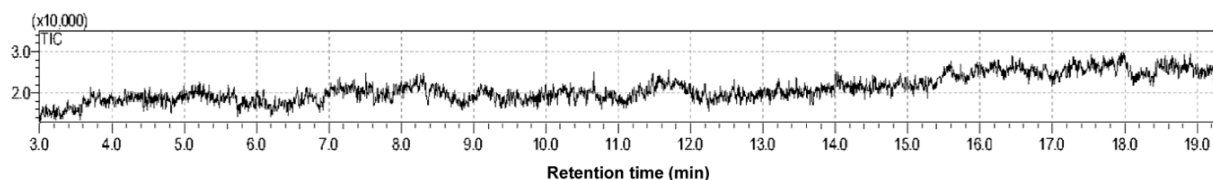


Figure 3.10. GC-MS chromatogram from the reaction mixture obtained after the SPR-mediated oxidation of methylene blue catalyzed by AgAu nanorings.

Figure 3.11A-D show the UV-VIS spectra collected as function of time during the methylene blue oxidation in presence of AgAu nanorings (Figure 3.11A), Ag nanospheres (Figure 3.11B), Au nanospheres (Figure 3.11C), and in the absence of any catalyst (Figure 3.11D).

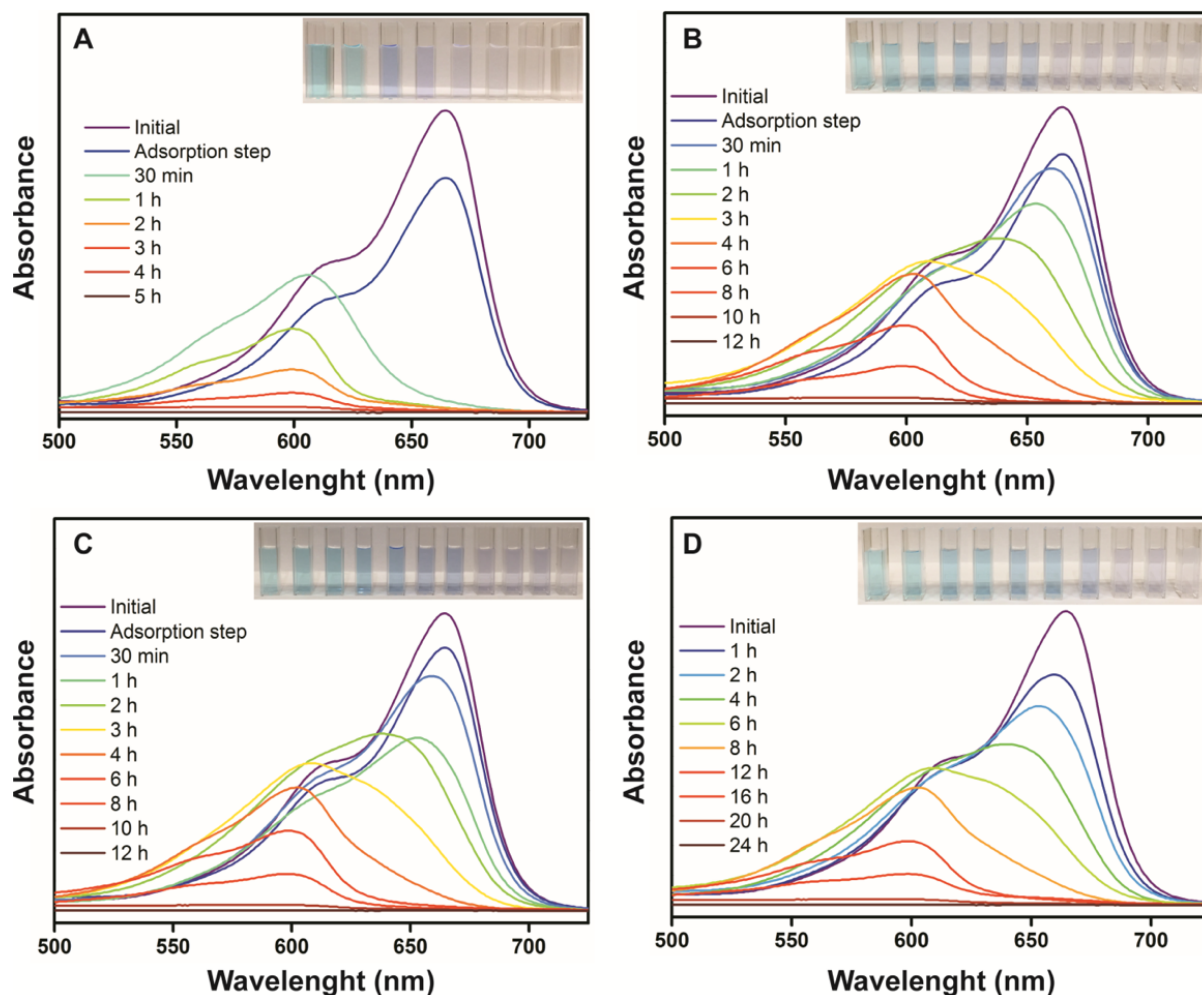


Figure 3.11. UV-VIS spectra collected as function of time during the methylene blue oxidation experiments in presence of AgAu nanorings (A), Ag nanospheres (B), Au nanospheres (C), and in the absence of any catalyst (D).

Figure 3.12 shows the proposed mechanism for the SPR-mediated oxidation of methylene blue. The SPR excitation leads to the formation of hot electrons (electrons that transiently occupy levels above the Fermi level in the metal) and holes. In this case, hot electrons can be charge-transferred to adsorbed O₂ molecules to generate $\cdot\text{O}_2$ (activated oxygen). Meanwhile, holes can also react with water to form the hydroxyl radical ($\cdot\text{OH}$).^{39,67-74} Therefore, it is plausible that both the activated oxygen and hydroxyl radical species can participate in the methylene blue oxidation. In order to confirm this hypothesis, we performed a series of control experiments. When the reaction was performed in the absence of external illumination, no oxidation of methylene blue was detected. When acetonitrile was employed as the solvent and the reaction was carried out in N₂, no degradation was detected even after 30 min of reaction. This is in agreement with the fact that neither $\cdot\text{O}_2$ oxygen or $\cdot\text{OH}$ species could be generated in the absence of O₂ and water. When the reaction was carried out in air (and acetonitrile as the solvent), 25 % conversion after 30 min was detected (as opposed to 56 % for the reaction under O₂ atmosphere and employing water as the solvent). This decrease in the conversion occurred because only $\cdot\text{O}_2$ species can be generated when no water is present. When water was employed as the solvent and N₂ as the reaction atmosphere, only 34 % conversion after was detected. Here, no $\cdot\text{O}_2$ species were generated, and only $\cdot\text{OH}$ can participate in the methylene blue oxidation. Therefore, these results demonstrate that hot electron and holes have similar contributions towards the SPR-mediated catalytic oxidation of methylene blue.

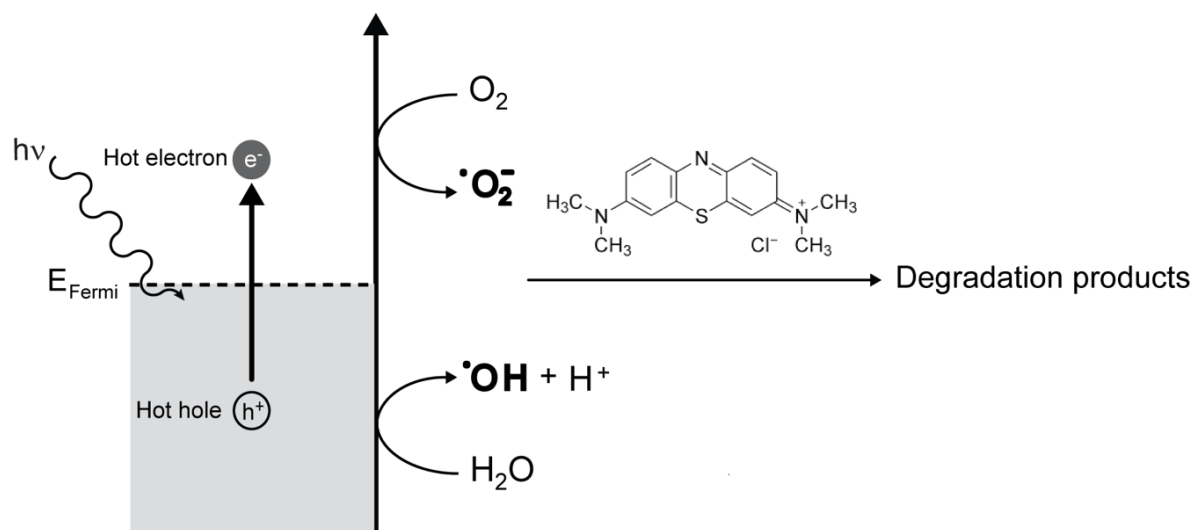


Figure 3.12. Proposed mechanism for the SPR-mediated oxidation of methylene blue employing AgAu nanorings as catalysts, in which the generation of both activated oxygen and hydroxyl radicals following the SPR excitation contributed to the oxidation of methylene blue.

In order to estimate the contribution from external thermal effects, we compared the conversion (%) with and without the visible-light excitation (Figure 3.13). In the absence of visible-light excitation and using 40 °C as the reaction temperature, a low conversion of methylene blue was detected (Figure 3.13A). Specifically, only 5 % of conversion was observed after 24 h as compared to 100 % after only 3 h under visible-light excitation. We also performed a control experiment at 80 °C (without visible-light excitation, Figure 3.13B), and no improvement in the conversion (%) were observed as compared to the reaction performed at 40 °C, indicating that thermal effects should play a minor role over the detected activities as compared to the charge-transfer mechanism involving hot electrons and holes.

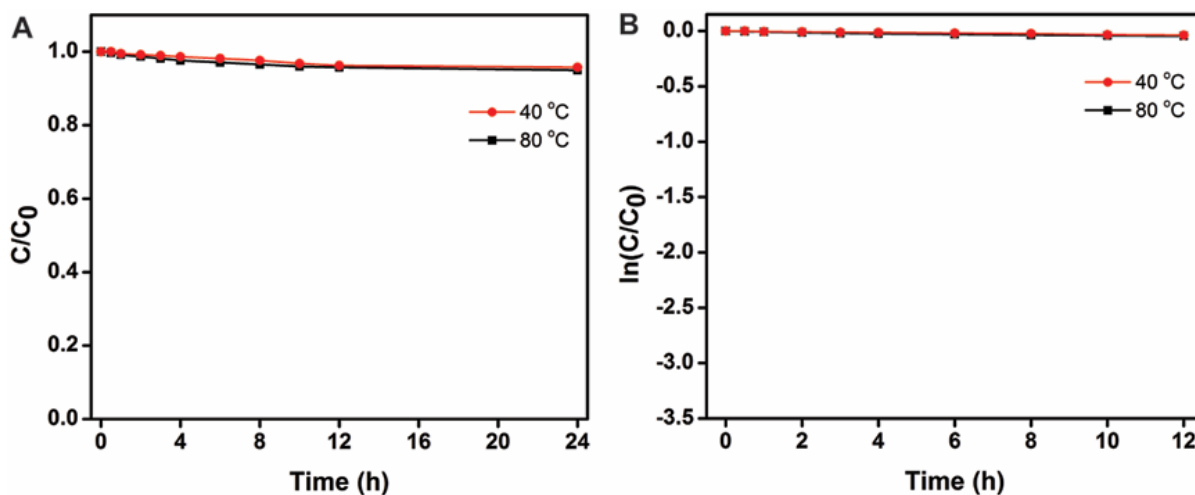


Figure 3.13. C/C_0 (A) and $\ln(C/C_0)$ (B) profiles as a function of time for the methylene blue oxidation experiments in the dark employing AgAu nanorings as catalysts at 40 (red trace) and 80 °C (black trace).

In order to further illustrate the versatility of the AgAu nanorings as catalyst, we also studied their activity as heterogeneous catalysts towards the 4-nitrophenol reduction relative to the Au and Ag nanospheres as shown in Figure 3.14. The AgAu nanorings displayed significantly improved performances relative to the nanospheres, which can be assigned to their higher surface to volume ratios as enabled by their hollow interiors and ultrathin walls. They also could be re-used for at least ten reaction cycles without any loss of activity.

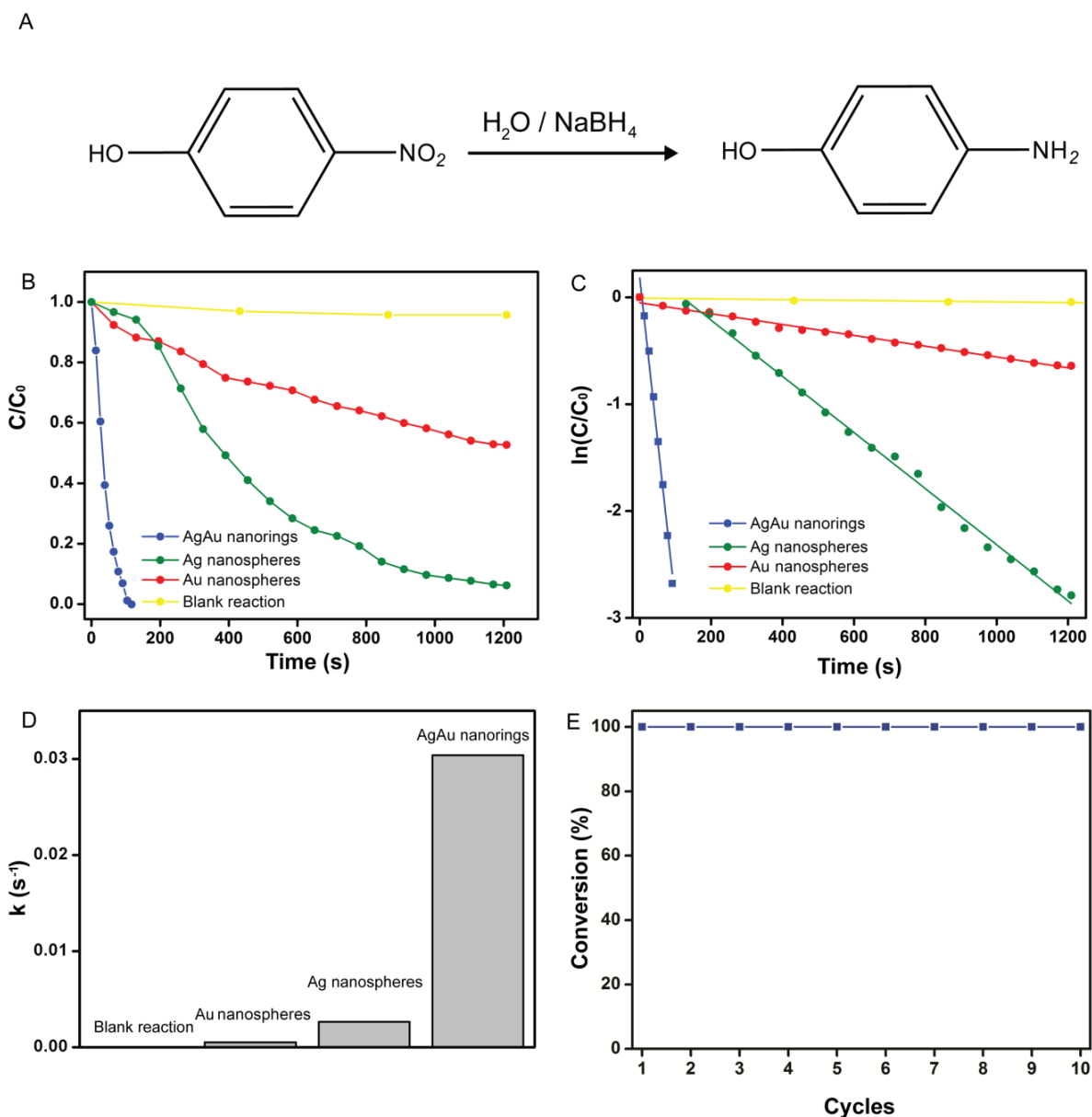


Figure 3.14. (A) Scheme for the 4-nitrophenol reduction by NaBH_4 in the presence catalyzed by the AgAu nanorings. C/C_0 (B) and $\ln(C/C_0)$ (C) profiles as a function of time employing of AgAu nanorings (blue trace), Ag nanospheres (green trace), and Au nanospheres (red trace) as catalysts. A blank reaction without any catalyst was also performed (yellow trace). (D) Bar graph showing the pseudo-first order rate constants calculated from (C). Stability tests (E) employing AgAu nanorings as catalysts.

3.4. Conclusion

In summary, we have demonstrated that the utilization of a plasmonic nanomaterial, the AgAu nanorings, displaying SPR extinction that closely matches the emission spectra of a commercial halogen-tungsten lamp as catalyst led to superior performances towards the SPR-

mediated oxidation of methylene blue relative to conventional nanoparticles (Ag and Au nanospheres). Rather than relying on the utilization of 2D nanocrystals as templates, Pd or Pt, complicated procedures, and expensive facilities, the AgAu nanorings could be obtained by the facile galvanic replacement reaction between Ag nanospheres and AuCl_4^- (aq), making it very attractive for large-scale production. The SPR-mediated catalytic activity of the AuAg nanorings was 4.3 and 4.7-fold higher than Au and Ag nanospheres, respectively. Moreover, by performing a series of control experiments, we found that both the generation of hot electrons and holes contributed to the SPR-mediated oxidation of methylene blue. While hot electrons led to the generation of activated oxygen species, holes led to the formation of hydroxyl radicals. Both these species can subsequently participate in the methylene blue oxidation process with similar contributions. We believe that our results demonstrate that the rational design of metallic nanoparticles plays an important role for enabling practical applications in the field of plasmonic catalysis, in which facile procedures can be employed for the synthesis of the catalysts (attractive for large-scale production) and commercial lamps may be used as the only energy input.

3.5. References

- (1) Baffou, G.; Quidant, R. Nanoplasmonics for Chemistry. *Chem. Soc. Rev.* **2014**, *43* (11), 3898–3907.
- (2) Lincic, S.; Christopher, P.; Xin, H.; Marimuthu, A. Catalytic and Photocatalytic Transformations on Metal Nanoparticles with Targeted Geometric and Plasmonic Properties. *Acc. Chem. Res.* **2013**, *46* (8), 1890–1899.
- (3) Lincic, S.; Aslam, U.; Boerigter, C.; Morabito, M. Photochemical Transformations on Plasmonic Metal Nanoparticles. *Nat Mater* **2015**, *14* (6), 567–576.
- (4) Christopher, P.; Xin, H.; Lincic, S. Visible-Light-Enhanced Catalytic Oxidation Reactions on Plasmonic Silver Nanostructures. *Nat Chem* **2011**, *3* (6), 467–472.
- (5) Kale, M. J.; Avanesian, T.; Christopher, P. Direct Photocatalysis by Plasmonic Nanostructures. *ACS Catal.* **2014**, *4* (1), 116–128.
- (6) Wang, C.; Astruc, D. Nanogold Plasmonic Photocatalysis for Organic Synthesis and Clean Energy Conversion. *Chem. Soc. Rev.* **2014**, *43* (20), 7188–7216.
- (7) Lai, W.; Zhou, J.; Jia, Z.; Petti, L.; Mormile, P. Ag@Au Hexagonal Nanorings: Synthesis, Mechanistic Analysis and Structure-Dependent Optical Characteristics. *J. Mater. Chem. C* **2015**, *3* (37), 9726–9733.

- (8) Hu, Y.; Chou, T.; Wang, H.; Du, H. Monodisperse Colloidal Gold Nanorings: Synthesis and Utility for Surface-Enhanced Raman Scattering. *J. Phys. Chem. C* **2014**, *118* (29), 16011–16018.
- (9) Métraux, G. S.; Cao, Y. C.; Jin, R.; Mirkin, C. A. Triangular Nanoframes Made of Gold and Silver. *Nano Lett.* **2003**, *3* (4), 519–522.
- (10) Liusman, C.; Li, S.; Chen, X.; Wei, W.; Zhang, H.; Schatz, G. C.; Boey, F.; Mirkin, C. A. Free-Standing Bimetallic Nanorings and Nanoring Arrays Made by On-Wire Lithography. *ACS Nano* **2010**, *4* (12), 7676–7682.
- (11) Near, R.; Tabor, C.; Duan, J.; Pachter, R.; El-Sayed, M. Pronounced Effects of Anisotropy on Plasmonic Properties of Nanorings Fabricated by Electron Beam Lithography. *Nano Lett.* **2012**, *12* (4), 2158–2164.
- (12) Halpern, A. R.; Corn, R. M. Lithographically Patterned Electrodeposition of Gold, Silver, and Nickel Nanoring Arrays with Widely Tunable Near-Infrared Plasmonic Resonances. *ACS Nano* **2013**, *7* (2), 1755–1762.
- (13) Wang, W.; Yan, Y.; Zhou, N.; Zhang, H.; Li, D.; Yang, D. Seed-Mediated Growth of Au Nanorings with Size Control on Pd Ultrathin Nanosheets and Their Tunable Surface Plasmonic Properties. *Nanoscale* **2016**, *8* (6), 3704–3710.
- (14) Jang, H.-J.; Ham, S.; Acapulco, J. A. I.; Song, Y.; Hong, S.; Shuford, K. L.; Park, S. Fabrication of 2D Au Nanorings with Pt Framework. *J. Am. Chem. Soc.* **2014**, *136* (50), 17674–17680.
- (15) Sun, Y.; Xia, Y. Triangular Nanoplates of Silver: Synthesis, Characterization, and Use as Sacrificial Templates For Generating Triangular Nanorings of Gold. *Adv. Mater.* **2003**, *15* (9), 695–699.
- (16) Yang, H.; He, L.-Q.; Hu, Y.-W.; Lu, X.; Li, G.-R.; Liu, B.; Ren, B.; Tong, Y.; Fang, P.-P. Quantitative Detection of Photothermal and Photoelectrocatalytic Effects Induced by SPR from Au@Pt Nanoparticles. *Angew. Chemie* **2015**, *127* (39), 11624–11628.
- (17) Wang, J.; Ando, R. A.; Camargo, P. H. C. Controlling the Selectivity of the Surface Plasmon Resonance Mediated Oxidation of P-Aminothiophenol on Au Nanoparticles by Charge Transfer from UV-Excited TiO₂. *Angew. Chemie Int. Ed.* **2015**, *54* (23), 6909–6912.
- (18) Lang, X.; Chen, X.; Zhao, J. Heterogeneous Visible Light Photocatalysis for Selective Organic Transformations. *Chem. Soc. Rev.* **2014**, *43* (1), 473–486.
- (19) Hou, W.; Hung, W. H.; Pavaskar, P.; Goepfert, A.; Aykol, M.; Cronin, S. B. Photocatalytic Conversion of CO₂ to Hydrocarbon Fuels via Plasmon-Enhanced Absorption and Metallic Interband Transitions. *ACS Catal.* **2011**, *1* (8), 929–936.
- (20) Sun, M.; Xu, H. A Novel Application of Plasmonics: Plasmon-Driven Surface-Catalyzed Reactions. *Small* **2012**, *8* (18), 2777–2786.
- (21) Wang, F.; Li, C.; Chen, H.; Jiang, R.; Sun, L.-D.; Li, Q.; Wang, J.; Yu, J. C.; Yan, C.-H. Plasmonic Harvesting of Light Energy for Suzuki Coupling Reactions. *J. Am. Chem. Soc.* **2013**, *135* (15), 5588–5601.
- (22) Wang, J. L.; Ando, R. A.; Camargo, P. H. C. Investigating the Plasmon-Mediated Catalytic Activity of AgAu Nanoparticles as a Function of Composition: Are Two Metals Better than One? *ACS Catal.* **2014**, *4* (11), 3815–3819.
- (23) Verbruggen, S. W.; Keulemans, M.; Filippousi, M.; Flahaut, D.; Van Tendeloo, G.; Lacombe, S.; Martens, J. A.; Lenaerts, S. Plasmonic Gold–silver Alloy on TiO₂ Photocatalysts with Tunable Visible Light Activity. *Appl. Catal. B Environ.* **2014**, *156–157*, 116–121.
- (24) Naik, G. V.; Shalaev, V. M.; Boltasseva, A. Alternative Plasmonic Materials: Beyond Gold and Silver. *Adv. Mater.* **2013**, *25* (24), 3264–3294.
- (25) Xia, X.; Wang, Y.; Ruditskiy, A.; Xia, Y. 25th Anniversary Article: Galvanic

- Replacement: A Simple and Versatile Route to Hollow Nanostructures with Tunable and Well-Controlled Properties. *Adv. Mater.* **2013**, *25* (44), 6313–6333.
- (26) Xia, Y.; Li, W.; Cobley, C. M.; Chen, J.; Xia, X.; Zhang, Q.; Yang, M.; Cho, E. C.; Brown, P. K. Gold Nanocages: From Synthesis to Theranostic Applications. *Acc. Chem. Res.* **2011**, *44* (10), 914–924.
- (27) Petri, M. V.; Ando, R. A.; Camargo, P. H. C. Tailoring the Structure, Composition, Optical Properties and Catalytic Activity of Ag–Au Nanoparticles by the Galvanic Replacement Reaction. *Chem. Phys. Lett.* **2012**, *531*, 188–192.
- (28) Slater, T. J. A.; Macedo, A.; Schroeder, S. L. M.; Burke, M. G.; O’Brien, P.; Camargo, P. H. C.; Haigh, S. J. Correlating Catalytic Activity of Ag–Au Nanoparticles with 3D Compositional Variations. *Nano Lett.* **2014**, *14* (4), 1921–1926.
- (29) Rycenga, M.; Hou, K. K.; Cobley, C. M.; Schwartz, A. G.; Camargo, P. H. C.; Xia, Y. Probing the Surface-Enhanced Raman Scattering Properties of Au-Ag Nanocages at Two Different Excitation Wavelengths. *Phys. Chem. Chem. Phys.* **2009**, *11* (28), 5903–5908.
- (30) Au, L.; Chen, Y.; Zhou, F.; Camargo, P. H. C.; Lim, B.; Li, Z.-Y.; Ginger, D. S.; Xia, Y. Synthesis and Optical Properties of Cubic Gold Nanoframes. *Nano Res.* **2008**, *1* (6), 441–449.
- (31) Rodrigues, T. S.; Silva, A. G. M.; Macedo, A.; Farini, B. W.; Alves, R. da S.; Camargo, P. H. C. Probing the Catalytic Activity of Bimetallic versus Trimetallic Nanoshells. *J. Mater. Sci.* **2015**, *50* (16), 5620–5629.
- (32) Silva, A. G. M. da; Rodrigues, T. S.; Macedo, A.; Silva, R. T. P. da; Camargo, P. H. C. An Undergraduate Level Experiment on the Synthesis of Au Nanoparticles and Their Size-Dependent Optical and Catalytic Properties. *Química Nova* **2014**, *37*, 1716–1720.
- (33) Huang, Y.-F.; Zhang, M.; Zhao, L.-B.; Feng, J.-M.; Wu, D.-Y.; Ren, B.; Tian, Z.-Q. Activation of Oxygen on Gold and Silver Nanoparticles Assisted by Surface Plasmon Resonances. *Angew. Chemie Int. Ed.* **2014**, *53* (9), 2353–2357.
- (34) Zhao, L.-B.; Liu, X.-X.; Zhang, M.; Liu, Z.-F.; Wu, D.-Y.; Tian, Z.-Q. Surface Plasmon Catalytic Aerobic Oxidation of Aromatic Amines in Metal/Molecule/Metal Junctions. *J. Phys. Chem. C* **2016**, *120* (2), 944–955.
- (35) Zheng, Z.; Huang, B.; Qin, X.; Zhang, X.; Dai, Y.; Whangbo, M.-H. Facile in Situ Synthesis of Visible-Light Plasmonic Photocatalysts M@TiO₂ (M = Au, Pt, Ag) and Evaluation of Their Photocatalytic Oxidation of Benzene to Phenol. *J. Mater. Chem.* **2011**, *21* (25), 9079–9087.
- (36) Xiao, M.; Jiang, R.; Wang, F.; Fang, C.; Wang, J.; Yu, J. C. Plasmon-Enhanced Chemical Reactions. *J. Mater. Chem. A* **2013**, *1* (19), 5790–5805.
- (37) Zhao, L.-B.; Zhang, M.; Huang, Y.-F.; Williams, C. T.; Wu, D.-Y.; Ren, B.; Tian, Z.-Q. Theoretical Study of Plasmon-Enhanced Surface Catalytic Coupling Reactions of Aromatic Amines and Nitro Compounds. *J. Phys. Chem. Lett.* **2014**, *5* (7), 1259–1266.
- (38) Boerigter, C.; Campana, R.; Morabito, M.; Lincic, S. Evidence and Implications of Direct Charge Excitation as the Dominant Mechanism in Plasmon-Mediated Photocatalysis. *Nat Commun* **2016**, *7*.
- (39) Moskovits, M. The Case for Plasmon-Derived Hot Carrier Devices. *Nat Nano* **2015**, *10* (1), 6–8.
- (40) Brongersma, M. L.; Halas, N. J.; Nordlander, P. Plasmon-Induced Hot Carrier Science and Technology. *Nat Nano* **2015**, *10* (1), 25–34.

Chapter 4

AgAu Nanotubes: Investigating the Effect of Surface Morphologies and Optical Properties over Applications in Catalysis and Photocatalysis

4.1. Introduction

Metal nanostructures have played a central role in several branches of science and technology including electronics,^{75,76} photonics,⁷⁷⁻⁷⁹ medicine,^{80,81} energy production,^{82,83} environmental remediation,^{84,85} and catalysis.^{40,86-88} Among various metallic nanomaterials, those based on gold (Au) and silver (Ag) have attracted special attention due to their fascinating optical properties in the visible range as a result of their localized surface plasmon resonance (LSPR) excitation.^{67,89} In addition to properties in sensing (enhanced spectroscopies), the LSPR excitation can also be put to work towards the promotion and/or enhancement of chemical processes, the so-called plasmonic catalysis that has emerged as a new frontier in the field of photocatalysis.^{41,90,91}

Nanoparticles based on noble metals have also been widely employed in the field of heterogeneous catalysis and electrocatalysis due to their good stability and catalytic activities towards a wealth of transformations including oxidations,^{42,88,92,93} reductions,^{83,94} coupling reactions,^{59,95-97} among others.^{82,98-100} In these applications, it has been established that the precise control over their morphological and optical properties is a promising strategy to enhance/optimize their performances.^{98,101-106} Even though a large number of protocols have been described for the synthesis of plasmonic nanoparticles, new protocols that further enable the understanding and correlation of how catalytic responses are dependent on their morphological and optical features are needed to offer further insights into the rational design

of catalysts with improved performances. Moreover, difficulties regarding their controlled synthesis in relatively larger scales still make their application in real catalytic and photocatalytic systems very challenging.^{104,107}

We report herein the synthesis, in relatively large scales, of well-defined AgAu nanotubes displaying controlled and well-defined surface morphologies and optical properties. The AgAu nanotubes were obtained by the galvanic replacement reaction between Ag nanowires and AuCl_4^- ions at 25 or 100 °C. In this case, the reaction temperature control enabled us to maneuver the surface morphology and optical properties of the nanotubes in the visible range. The AgAu nanotubes were then employed as model catalysts towards the methylene blue oxidative degradation due to its importance in the field of environmental remediation. More specifically, regarding this transformation, the catalytic performance was investigated towards the “classical” heterogeneous catalysts and plasmonic photocatalysis. We focused on the understanding on how the catalytic and plasmonic photocatalytic activities of the AgAu nanotubes were dependent on their surface morphologies (branched or smooth surfaces) and optical properties (position and intensity of SPR extinction bands).

4.2. Experimental

Materials and Instrumentation

Analytical grade chemicals silver nitrate (AgNO_3 , 99%, Sigma-Aldrich), polyvinylpyrrolidone (PVP, Sigma-Aldrich, M.W. 55,000 g mol^{-1}), polyvinylpyrrolidone (PVP, Sigma-Aldrich, M.W. 10,000 g mol^{-1}), ethylene glycol (EG, 99.8%, Sigma-Aldrich), tetrachloroauric acid ($\text{HAuCl}_4 \cdot 3\text{H}_2\text{O}$, $\geq 99.9\%$, Sigma-Aldrich), hydrochloric acid (HCl, 37%, Sigma-Aldrich), Hydrogen peroxide (30 wt.% in H_2O , Sigma-Aldrich), *ter*-Butyl hydroperoxide (70 wt.% in H_2O , Sigma-Aldrich) and methylene blue hydrate

($C_{16}H_{18}ClN_3S \cdot xH_2O$, $\geq 95\%$, Sigma-Aldrich) were used as received.

The scanning electron microscopy (SEM) images were obtained using a JEOL field emission gun electron microscope JSM6330F operated at 5 kV. The samples were prepared by drop-casting an aqueous suspension containing the nanostructures over a silicon wafer, followed by drying under ambient conditions. High-resolution transmission electron microscopy (HRTEM) images were obtained with a JEOL JEM2100 microscope operated at 200 kV. Energy dispersive X-ray (EDX) spectra were obtained in this instrument with an EDX detector configuration which has a total solid angle of ~ 0.13 srad. Samples for HRTEM were prepared by drop-casting an aqueous suspension of the nanostructures over a carbon-coated copper grid, followed by drying under ambient conditions. UV-VIS spectra were obtained from aqueous suspensions containing the nanostructures with a Shimadzu UV-1700 spectrophotometer. The Ag and Au atomic percentages were measured by inductively coupled plasma optical emission spectrometry (ICP-OES) using a Spectro Arcos equipment. The X-ray diffraction (XRD) data were obtained using a Rigaku - Miniflex equipment, $CuK\alpha$ radiation. The diffraction pattern was measured in the range of 10 – 90 degree with a $1 \text{ degree min}^{-1}$ angular speed scan.

Synthesis of Ag nanowires

In a typical procedure, 250 mL of EG was pre-heated for 1 hour at 140 °C with vigorous stirring, followed by the addition of 10 mL of 3 mmol L^{-1} HCl (in EG). After 10 min, 150 mL of 94 mmol L^{-1} $AgNO_3$ and 150 mL of 147 mmol L^{-1} PVP (both in EG) were simultaneously added dropwise to this mixture (at a speed of 45 mL h^{-1}) and left overnight, yielding a beige suspension. The reaction flask was then allowed to cool down to room temperature.

Synthesis of AgAu nanotubes with controlled surface morphologies

In a typical procedure, a mixture containing 250 mL of PVP aqueous solution (0.1 wt %) and 50 mL of as prepared suspension containing the Ag wires was stirred at 25 or 100 °C for 10 min in a 1 L round-bottom flask. Then, 100 mL of a 0.6 mmol L⁻¹ AuCl₄⁻_(aq) solution was added dropwise and the reaction allowed to proceed at 25 °C or 100 °C for 1 h. After the syntheses, the reaction mixture volumes were reduced to 25 mL and washed twice with a 35 g mL⁻¹ NaCl_(aq) solution and three times with water by successive rounds of centrifugation at 7000 rpm and removal of the supernatant. After washing, the AgAu nanomaterials were suspended in 400 mL of PVP aqueous solution (0.1 wt %) and storage at room temperature. For the catalytic applications, 10 mL of the AgAu nanotubes suspended in PVP aqueous solution (0.1 wt %) were washed twice with water by successive rounds of centrifugation at 7000 rpm and removal of the supernatant and concentrated to 1 mL with water. After this step, the concentration of metal (Ag + Au) in the nanoparticles suspensions corresponded to 5.5 mmol L⁻¹ (as measured by ICP-OES).

Photocatalytic oxidation of methylene blue

Typically, 10 mL of a 10 mg L⁻¹ MB aqueous solution and 1 mL of the suspension containing the washed catalysts were added in a 25 mL round-bottom flask. The resulting mixture was stirred for 1 h in the dark to achieve the adsorption and desorption equilibrium. Subsequently, the suspension was irradiated with a 300 W halogen tungsten lamp (OSRAM) mounted at a 2 cm distance from the glass reactor. During the experiments, 1 mL aliquots were taken and centrifuged at 15,000 rpm for 10 min to isolate the supernatant. Then, the UV–VIS spectra of the supernatant were measured as a function of time in the 500 to 750 nm range to probe the MB photodegradation. A calibration curve for absorbance as a function of the MB concentration was employed in order to monitor the transformation. The experiments

employing hydrogen peroxide and *ter*-Butyl hydroperoxide were performed by adding stoichiometric amount of oxidants necessary to the complete oxidation of methylene blue after 1 h of stirring in the dark, which correspond to 1.7 and 2.2 μL of hydrogen peroxide and *ter*-Butyl hydroperoxide, respectively.

4.3. Results and discussion

Our studies started with the synthesis of Ag nanowires displaying well-defined shapes, smooth surfaces, and monodisperse sizes by a polyol approach¹⁰⁸ as shown in Figure 4.1.

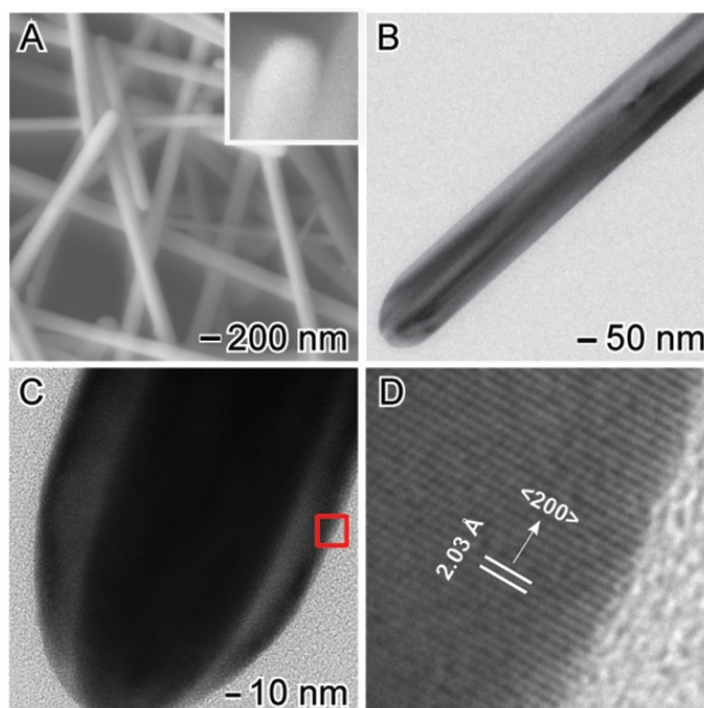


Figure 4.1. SEM (A) and HRTEM (B-D) images for Ag nanowires employed as starting materials for the synthesis of AgAu nanotubes. The image in (D) corresponds to phase contrast images of the areas highlighted by the red square in (C).

The obtained Ag nanowires were 155 ± 15 nm in width and > 1 μm in length. Figure 4.1B-D depict high-resolution transmission electron microscopy (HRTEM) images for the Ag nanowires, indicating that they present sharp tips (Figure 4.1B-C) and are enclosed by $\{200\}$ sides facets with lattice spacings of 2.03 \AA of characteristic of *fcc* Ag (Figure 4.1D) in

agreement with previous reports.^{108–110} The histograms of size distribution (Figure 4.2A-B) indicate that the nanowires displayed a narrow size distribution, demonstrating the robustness of this approach for the synthesis of Ag nanowires in a large scale, which corresponds to an increase of 100-folds compared to the conventional polyol protocol.¹⁰⁸

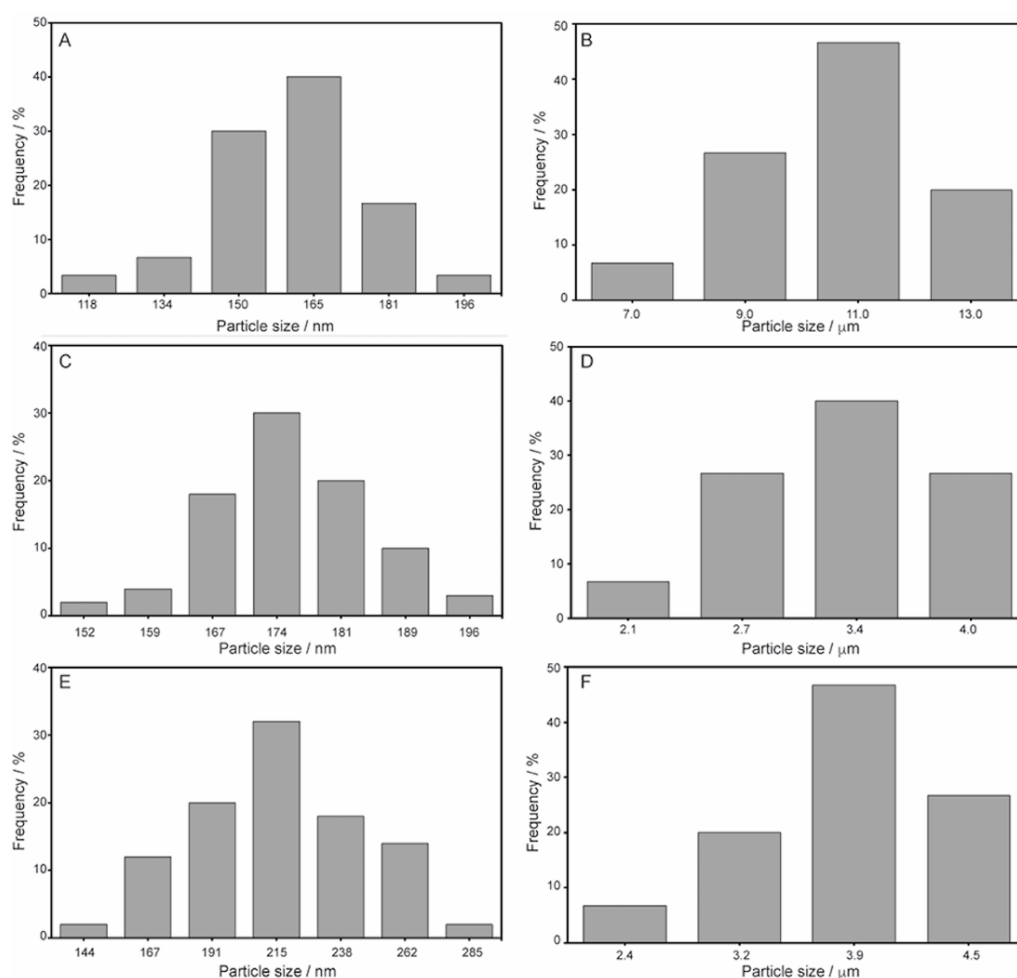


Figure 4.2. Histograms showing the distribution of width (left column) and length (right column) for the obtained Ag nanowires (A-B), AgAu 25 nanotubes (C-D), and AgAu 100 nanotubes (E-F).

As illustrated in Figures 4.3, the strategy for the synthesis of AgAu nanotubes displaying controlled surface morphologies was based on the galvanic replacement reaction between Ag nanowires and AuCl_4^- (aq) in the presence of PVP at different temperatures: 25 and 100 °C. Therefore, the nanotubes obtained in the synthesis carried out at 25 and 100 °C were denoted AgAu 25 and 100, respectively.

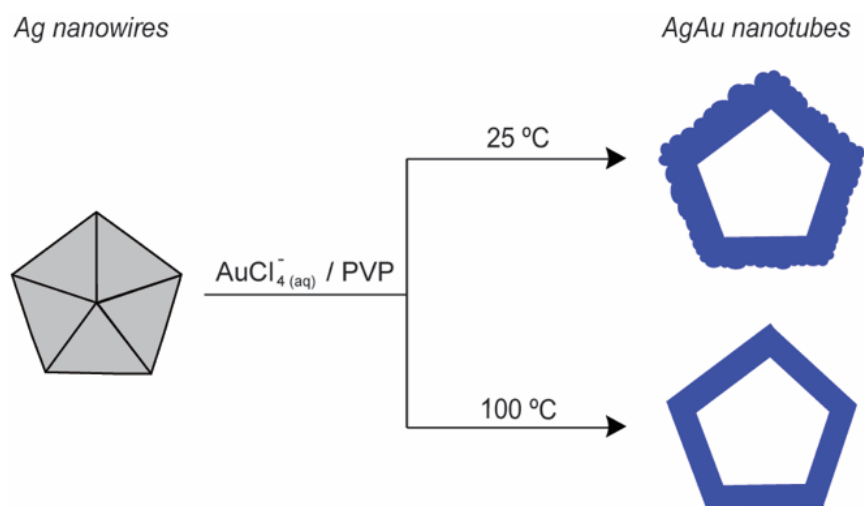


Figure 4.3. SEM (A) and HRTEM (B-D) images for Ag nanowires employed as starting materials for the synthesis of AgAu nanotubes. The image in (D) corresponds to phase contrast images of the areas highlighted by the red square in (C).

At $25\text{ }^\circ\text{C}$, AgAu nanotubes displaying branched surfaces. This occurs due to the precipitation of AgCl crystals ($K_{\text{ps}} \sim 1.8 \times 10^{-10}$) onto the surface of Ag during the galvanic replacement, which may act as templates for further Au deposition by an island-mode growth, which is associated with a lower rate of reconstruction processes such as Ostwald ripening and atomic diffusion.^{9,10,104,111} On the other hand, at $100\text{ }^\circ\text{C}$, no precipitation of AgCl crystals is observed, which drives the Au deposition favored by surface reconstruction/diffusion processes leading to the formation of hollow structures with smooth surfaces that replicate the surface morphology of the Ag nanowires used as templates.^{9,111,112} Thus, by employing this approach, it is possible to obtain AgAu nanotubes displaying distinct surface morphologies and thus systematically investigate this effect towards their optical, catalytic, and photocatalytic properties.

Figure 4.4A-D show SEM (Figure 4.4A) and HRTEM (Figure 4.4B-D) images for AgAu 25 nanotubes, while Figure 4.4E-H show SEM (Figure 4.4E) and HRTEM (Figure 4.4F-H) images for AgAu 100 nanotubes.

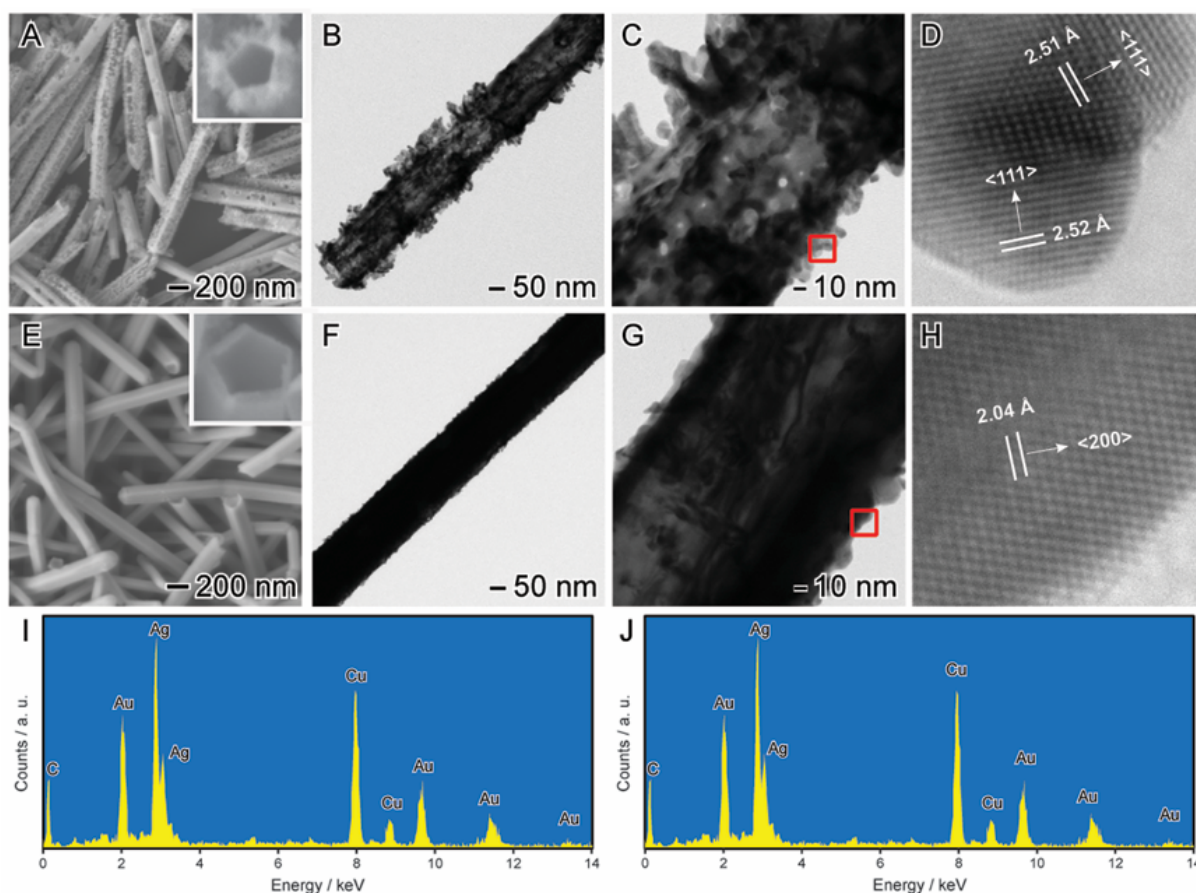


Figure 4.4. SEM (A and E) and HRTEM (B-D and F-H) images for AgAu 25 (A-D) and AgAu 100 (E-H) nanotubes. The images in (D) and (H) correspond to phase contrast images of the areas highlighted by the red squares in (C) and (G), respectively. (I) and (J) show EDX spectra obtained from individual AgAu 25 (I) and AgAu 100 (J) nanotubes.

It can be observed that both nanotubes displayed well-defined shapes and relatively monodisperse sizes (also depicted by their size distribution histograms in the Figure 4.2C-F). The elongated structures (from the Ag nanowires templates) was kept in both cases. However, it is very clear that the nanotubes displayed significant differences in their surface morphologies as a function of the temperature in which the galvanic reaction was performed. More specifically, at 25 °C AgAu nanotubes displayed branched surfaces, while nanotubes with smooth walls were obtained at 100 °C. Also, both AgAu nanotubes presented hollow interiors, which can be clearly visualized from the HRTEM images (Figure 4.4B-C and 4.4F-G) due to differences in mass-thickness contrast at the center of each nanotube. The AgAu 25 and AgAu 100 nanotubes were 178 ± 15 and 203 ± 31 nm in width, respectively, and their shell thickness

corresponded to 44 and 40 nm, respectively. Interestingly, the HRTEM images for AgAu 25 and AgAu 100 (Figure 4.4D and 4.4H, respectively) showed that AgAu 25 presented a polycrystalline surface comprised of crystalline islands that are randomly oriented as a consequence of the island-mode Au deposition at 25 °C. However, AgAu 100 displayed a surface enclosed by {200} side facets similarly to the original Ag nanowires as a result of the Au epitaxial deposition over the surface of the Ag nanowires.^{9,111} EDX spectra obtained from individual AgAu 25 (Figure 4.4I) and AgAu 100 (Figure 4.4J) nanotubes revealed that their composition corresponded to 30.0 and 26.6 at. % in terms of Au, respectively, in agreement with ICP-OES results (Table 4.1), which showed 26.7 and 27.2 at. % in terms of Au for AgAu 25 and AgAu 100, respectively.

The XRD patterns (Figure 4.5) confirmed the formation of AgAu nanostructures in both cases without the presence of any crystalline impurities.

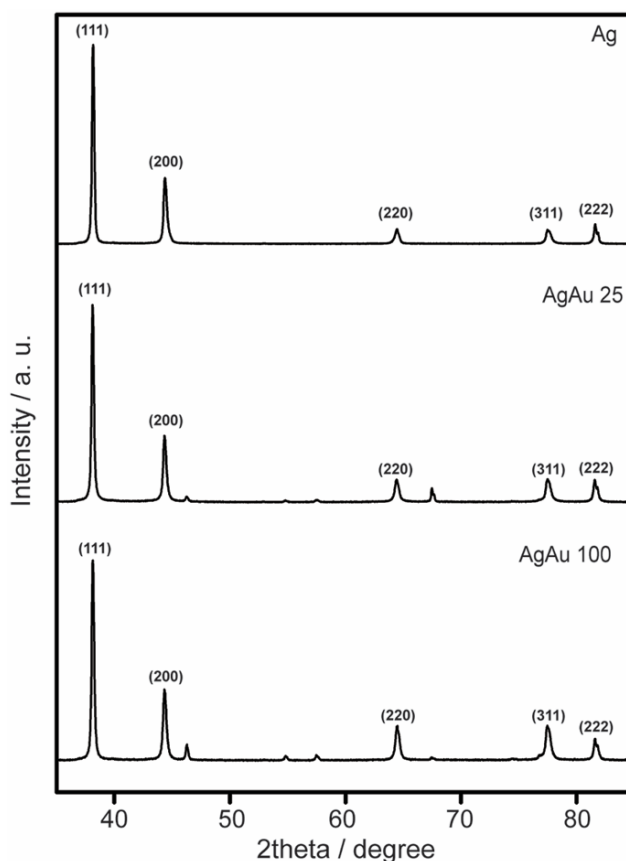


Figure 4.5. X-ray diffraction patterns recorded from the obtained Ag nanowires, AgAu 25, and AgAu 100 nanotubes.

However, as both *fcc* Ag and Au present a mismatch of only 0.17 % in their lattice constants,¹¹³ the XRD diffraction peaks for these two species could not be resolved under our experimental conditions. Thus, the similar compositions, sizes, and wall thicknesses of the AgAu nanotubes enabled us to isolate the effect of the variation in the surface morphologies over their optical and catalytic properties. The optical properties of the AgAu nanotubes was investigated by UV-VIS spectroscopy (Figure 4.6).

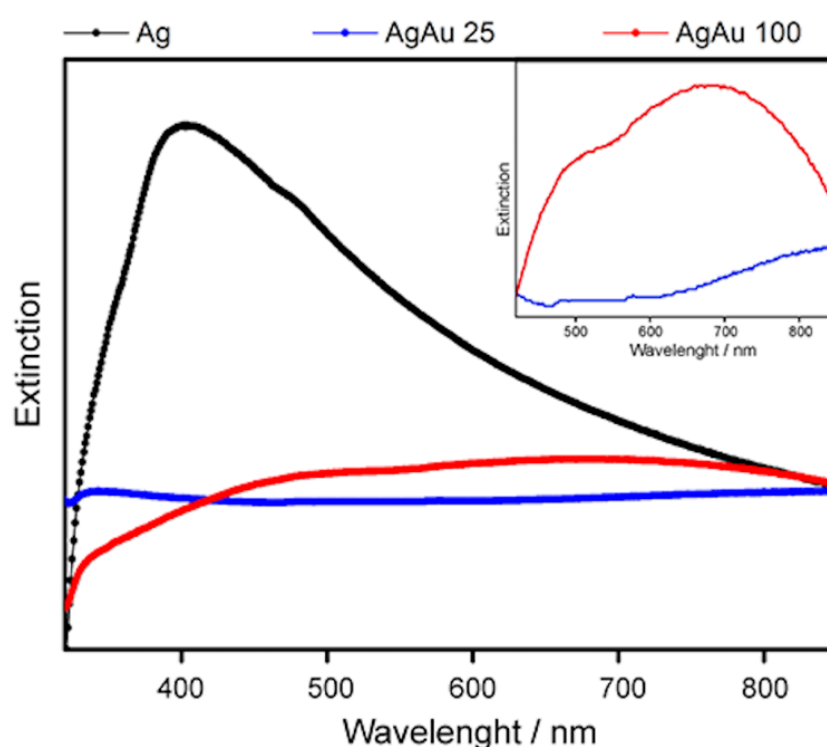


Figure 4.6. UV–VIS extinction spectra recorded from aqueous suspensions containing Ag nanowires (black trace), AgAu 25 (red trace), and AgAu 100 (blue trace) nanotubes. The inset depicts a zoom in the 430-850 nm range for AgAu and AgAu 100 nanotubes.

Our results revealed the disappearance of the band associated to LSPR excitation in the Ag nanowires (black trace) at 405 nm in the nanotubes as a consequence of Ag dissolution from the template by the galvanic reaction with AuCl_4^- (aq) ions together with the Au deposition.^{9,52,112,114,115} In addition, the SPR spectra for both AgAu nanotubes displayed significant red-shifts of their SPR bands relative to the Ag nanowires, which is in agreement

with the Au deposition as well as the formation of the hollow interiors during the galvanic reaction.^{9,111} As depicted by the inset in the Figure 4.6, the AgAu 100 nanotubes displayed two SPR bands (one shoulder located at 510 nm and a broad signal centered at 690 nm) with significantly higher intensities as compared the only broad band centered at 850 nm presented by the AgAu 25.

It is important to note that the UV-VIS spectrum for AgAu 100 nanotubes closely matches the emission spectra of a commercial halogen-tungsten lamp (Figure 4.7). Therefore, they represent potential candidates for improved efficiencies as plasmonic photocatalysis employing commercial halogen-tungsten lamp as the energy input.^{61,114}

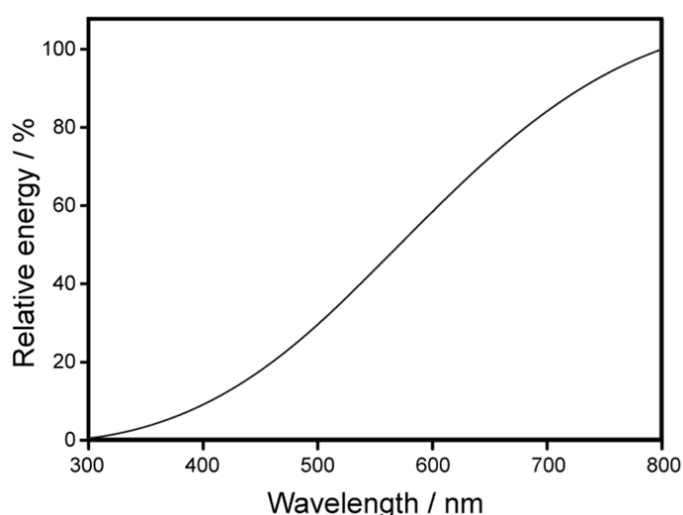


Figure 4.7. Emission spectrum for the commercial tungsten-halogen lamp employed as the excitation source in our photocatalytic experiments.

Conversely, due to the presence of small islands/branches at the surface as well as hollow interiors, the AgAu 25 nanotubes represent a promising catalyst for application in conventional catalytic process (without light) as the branches/islands at the surface is expect to lead to increased surface areas relative to the smooth nanotubes.^{10,116} Therefore, after the synthesis of AgAu nanotubes displaying controlled surface morphologies and optical properties, we turned our attention for the investigation of their catalytic and photocatalytic

properties towards an oxidative process. To this end, we employed methylene blue oxidative degradation as a model reaction due to its relevance in the field of environmental remediation.^{117–119}

Figure 4.8A and 4.8B show the kinetics profiles for methylene blue adsorption in the dark using different initial concentrations of this substrate in the presence of AgAu 25 and AgAu 100, respectively.

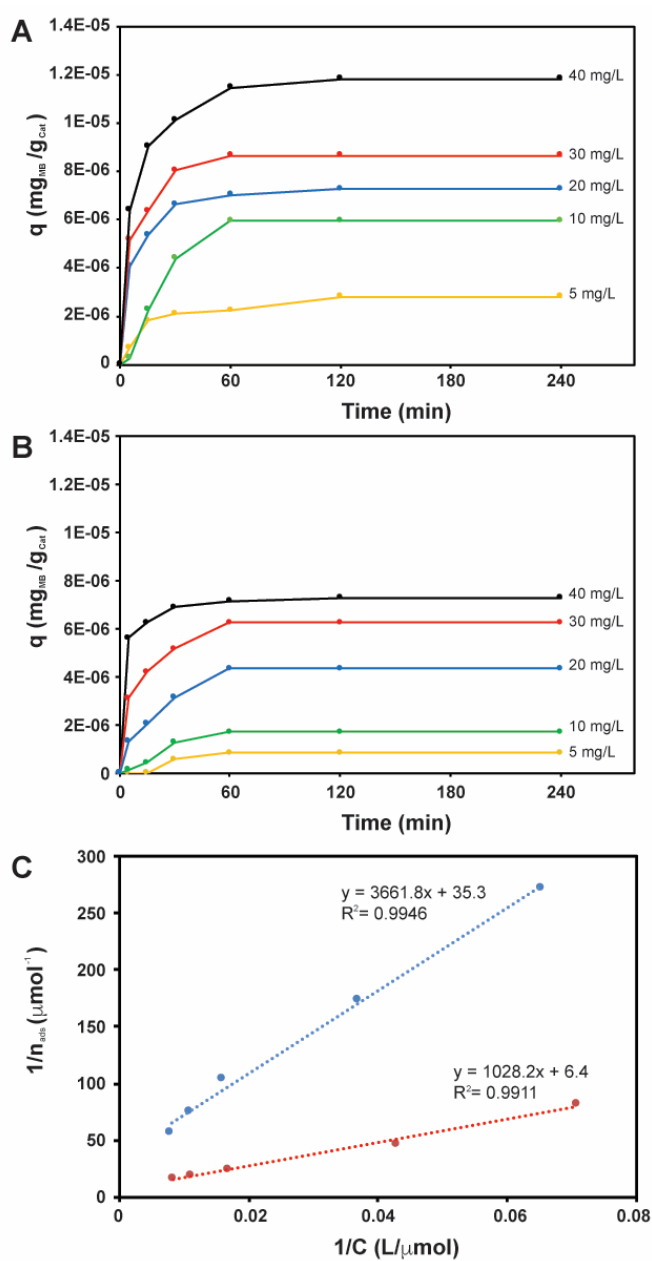


Figure 4.8. Kinetics of adsorption profiles of methylene blue in the dark in the presence of AgAu 25 (A) and AgAu 100 (B) nanotubes. (C) Langmuirian linear transform of the curves in (A) and (B): AgAu 25 (blue trace) and AgAu 100 (red trace) nanotubes.

Interestingly, for both AgAu nanotubes and for all employed initial concentrations of methylene blue, the equilibrium of adsorption/desorption was reached within 1 h.^{120–122} However, in the presence of AgAu 25 (Figure 4.8A), the amount of methylene blue adsorbed per mass unit of catalyst (q) were significant higher for all concentrations as compared to AgAu 100 (Figure 4.8B). This behavior can be associated to the morphological features presented by AgAu 25 such as the presence of islands/branches at the surface that lead to increased surface areas relative to the smooth nanotubes.^{10,116} Figure 4.8C shows a linear transformation of the curves depicted in 4.8A and 4.8B, which was determined by plotting the inverse of the number of mols of methylene blue adsorbed onto AgAu nanotubes ($1/n_{\text{ads}}$) as a function of final concentration of methylene blue in solution (C). Thus, according to the Langmuir model (Equation 1), we can determine the constant of adsorption of methylene blue (k) for each AgAu nanotube under our employed conditions.

$$1/n_{\text{ads}} = 1/n_0 + (1/n_0 k) \cdot 1/C \quad (1)$$

Herein, the calculated adsorption constants for methylene blue (k) corresponded to 9.75×10^{-3} and $4.32 \times 10^{-3} \text{ Lmol}^{-1}$ for AgAu 25 and AgAu 100, respectively, which is also in agreement with previous reports.¹²⁰

Figure 4.9 shows the methylene blue degradation employing different oxidizing agents under visible light illumination (left column) and without visible-light illumination (right column) using AgAu 25 (blue trace) and AgAu 100 (red trace) as catalysts and a commercial halogen-tungsten lamp as the light source (left column).

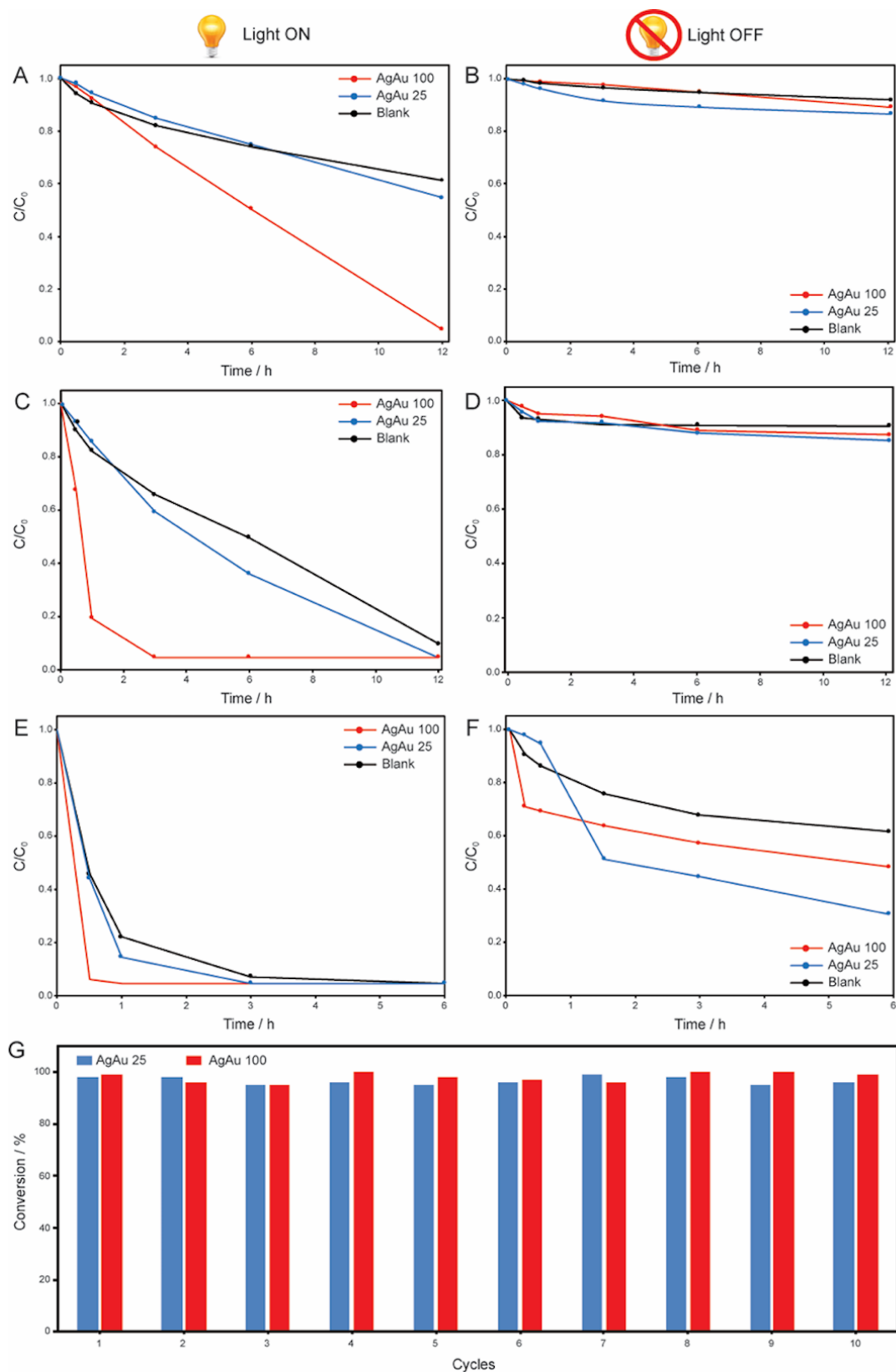


Figure 4.9. C/C_0 profiles as a function of time for the oxidation of methylene blue by atmospheric air (A-B), hydrogen peroxide (C-D), and tert-butylhydroperoxide (E-F) employing AgAu 25 (blue trace) and AgAu 100 (red trace) nanotubes as catalysts. Blank reactions without any catalyst are shown as the black traces. (G) Catalytic stability tests employing AgAu 25 and 100 nanotubes as catalysts (blue and red bars, respectively).

For comparison, reactions without any catalyst (black trace) were also performed for all oxidizing systems. In all experiments, no organic degradation products were identified by GC-MS analyses, which indicate the complete mineralization of methylene blue during the oxidation processes.^{114,123,124} In fact, as expected, a progressive increase in the methylene blue conversion was observed when stronger oxidizing agents were employed. More specifically, the conversion of methylene blue using both AgAu nanotubes as function of the oxidizing agent increased in the following order: atmospheric air (Figure 4.9A-B) < hydrogen peroxide (Figure 4.9C-D) < *ter*-butyl hydroperoxide (Figure 4.9E-F). However, when the reactions were performed with and without illumination an interesting tendency was observed: without illumination (right column), the AgAu 25 nanotubes showed a superior catalytic activity compared to AgAu 100 in agreement with their larger surface area corroborated by the adsorption experiments. However, under visible light illumination (left column), AgAu 100 presented superior performances. This behavior can be associated with two very important features for photocatalytic processes presented by AgAu 100: *i*) broader and more intense SPR bands in the visible range, and *ii*) close matching between UV-VIS extinction spectrum for the photocatalyst and the emission spectra of the light source employed in the experiments. Thus, under the same experimental conditions, AgAu 100 tends to absorb more efficiently the light energy and enhance the photo-oxidative process in greater magnitude compared to AgAu 25.^{114,125} This results indicate that the control over the morphological and optical properties play a very important role in the optimization of catalytic and photocatalytic processes. Figure 4.9G shows the catalytic stability for the AgAu 25 (blue bars) and AgAu 100 (red bars) nanotubes towards methylene blue oxidation using *ter*-butyl hydroperoxide under visible light illumination (the most severe condition employed) expressed as a function of methylene blue conversion and the number of catalytic cycles. Interestingly, no significant loss of catalytic activity was detected even after 10 catalytic cycles for both materials. This result is in

agreement with the SEM images for both materials after the catalytic experiments (Figure 4.10), which showed both AgAu nanotubes remained unchanged (without any aggregation or morphology loss), thus representing promising candidates for application as catalysts towards oxidation reactions without the need of a support to stabilize the catalyst.

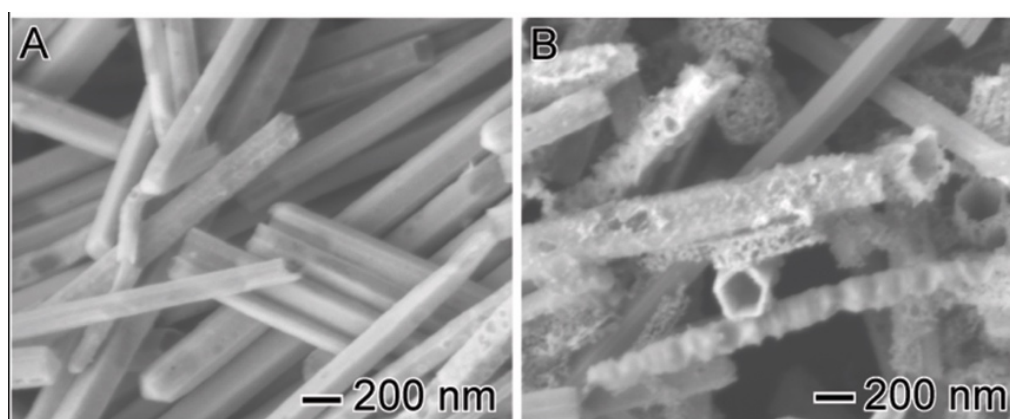


Figure 4.10. SEM images for (A) AgAu 100 and (B) AgAu 25 nanotubes after catalytic tests using tert-butyl hydroperoxide as oxidizing agent under visible light illumination.

4.4. Conclusion

In this paper, we systematically investigated the dependence of the catalytic and plasmonic photocatalytic performances of AgAu nanotubes as a function of their surface morphologies and optical properties towards the oxidative degradation of methylene blue. We started by developing the synthesis of AgAu nanotubes having smooth or branched surfaces by controlling the temperature during the galvanic replacement reaction between Ag nanowires and AuCl_4^- (aq). This difference in surface morphologies also led to distinct optical properties (SPR extinction) in the visible range. Interestingly, the catalytic and photocatalytic performances of the AgAu nanotubes towards the methylene blue oxidative degradation showed a strong dependence on their morphological and optical properties. More specifically, AgAu 25 showed a superior catalytic performance without visible-light illumination due to its higher surface area as a consequence of its branched walls. However, AgAu 100 showed

superior activity in the experiments performed under visible light illumination due to its broader and more intense SPR bands which close matched the emission spectrum of the light source employed in the photocatalytic reactions. These results show that surface morphologies and optical properties play an important and distinct role over the optimization of the catalytic or plasmonic photocatalytic properties.

4.5. References

- (1) Shen, W.; Zhang, X.; Huang, Q.; Xu, Q.; Song, W. Preparation of Solid Silver Nanoparticles for Inkjet Printed Flexible Electronics with High Conductivity. *Nanoscale* **2014**, *6* (3), 1622–1628.
- (2) Minari, T.; Kanehara, Y.; Liu, C.; Sakamoto, K.; Yasuda, T.; Yaguchi, A.; Tsukada, S.; Kashizaki, K.; Kanehara, M. Printed Electronics: Room-Temperature Printing of Organic Thin-Film Transistors with π -Junction Gold Nanoparticles (Adv. Funct. Mater. 31/2014). *Adv. Funct. Mater.* **2014**, *24* (31), 4869.
- (3) Clavero, C. Plasmon-Induced Hot-Electron Generation at Nanoparticle/metal-Oxide Interfaces for Photovoltaic and Photocatalytic Devices. *Nat Phot.* **2014**, *8* (2), 95–103.
- (4) Zhang, Z.; Zhang, L.; Hedhili, M. N.; Zhang, H.; Wang, P. Plasmonic Gold Nanocrystals Coupled with Photonic Crystal Seamlessly on TiO₂ Nanotube Photoelectrodes for Efficient Visible Light Photoelectrochemical Water Splitting. *Nano Lett.* **2013**, *13* (1), 14–20.
- (5) Singh, A.; Kim, W.; Kim, Y.; Jeong, K.; Kang, C. S.; Kim, Y.; Koh, J.; Mahajan, S. D.; Prasad, P. N.; Kim, S. Multifunctional Photonics Nanoparticles for Crossing the Blood–Brain Barrier and Effecting Optically Trackable Brain Theranostics. *Adv. Funct. Mater.* **2016**, n/a-n/a.
- (6) Lane, L. A.; Qian, X.; Nie, S. SERS Nanoparticles in Medicine: From Label-Free Detection to Spectroscopic Tagging. *Chem. Rev.* **2015**, *115* (19), 10489–10529.
- (7) Lohse, S. E.; Murphy, C. J. Applications of Colloidal Inorganic Nanoparticles: From Medicine to Energy. *J. Am. Chem. Soc.* **2012**, *134* (38), 15607–15620.
- (8) Zeng, Z.; Tan, C.; Huang, X.; Bao, S.; Zhang, H. Growth of Noble Metal Nanoparticles on Single-Layer TiS₂ and TaS₂ Nanosheets for Hydrogen Evolution Reaction. *Energy Environ. Sci.* **2014**, *7* (2), 797–803.
- (9) Zhao, X.; Long, R.; Liu, D.; Luo, B.; Xiong, Y. Pd-Ag Alloy Nanocages: Integration of Ag Plasmonic Properties with Pd Active Sites for Light-Driven Catalytic Hydrogenation. *J. Mater. Chem. A* **2015**, *3* (18), 9390–9394.
- (10) Wu, L.; Li, F.; Xu, Y.; Zhang, J. W.; Zhang, D.; Li, G.; Li, H. Plasmon-Induced Photoelectrocatalytic Activity of Au Nanoparticles Enhanced TiO₂ Nanotube Arrays Electrodes for Environmental Remediation. *Appl. Catal. B Environ.* **2015**, *164*, 217–224.
- (11) Khin, M. M.; Nair, A. S.; Babu, V. J.; Murugan, R.; Ramakrishna, S. A Review on Nanomaterials for Environmental Remediation. *Energy Environ. Sci.* **2012**, *5* (8), 8075–8109.
- (12) Linic, S.; Christopher, P.; Xin, H.; Marimuthu, A. Catalytic and Photocatalytic Transformations on Metal Nanoparticles with Targeted Geometric and Plasmonic

- Properties. *Acc. Chem. Res.* **2013**, *46* (8), 1890–1899.
- (13) Alves, A. K.; Berutti, F. A.; Sánchez, F. A. L. Nanomaterials and Catalysis BT - Nanostructured Materials for Engineering Applications; Bergmann, C. P., de Andrade, M. J., Eds.; Springer Berlin Heidelberg: Berlin, Heidelberg, 2011; pp 93–117.
 - (14) Polshettiwar, V.; Varma, R. S. Green Chemistry by Nano-Catalysis. *Green Chem.* **2010**, *12* (5), 743–754.
 - (15) Freakley, S. J.; He, Q.; Kiely, C. J.; Hutchings, G. J. Gold Catalysis: A Reflection on Where We Are Now. *Catal. Letters* **2015**, *145* (1), 71–79.
 - (16) Sun, Y.; Xia, Y. Gold and Silver Nanoparticles: A Class of Chromophores with Colors Tunable in the Range from 400 to 750 Nm. *Analyst* **2003**, *128* (6), 686–691.
 - (17) Huang, Y.-F.; Zhang, M.; Zhao, L.-B.; Feng, J.-M.; Wu, D.-Y.; Ren, B.; Tian, Z.-Q. Activation of Oxygen on Gold and Silver Nanoparticles Assisted by Surface Plasmon Resonances. *Angew. Chemie Int. Ed.* **2014**, *53* (9), 2353–2357.
 - (18) Wang, P.; Huang, B.; Dai, Y.; Whangbo, M.-H. Plasmonic Photocatalysts: Harvesting Visible Light with Noble Metal Nanoparticles. *Phys. Chem. Chem. Phys.* **2012**, *14* (28), 9813–9825.
 - (19) Hou, W.; Cronin, S. B. A Review of Surface Plasmon Resonance-Enhanced Photocatalysis. *Adv. Funct. Mater.* **2013**, *23* (13), 1612–1619.
 - (20) Linic, S.; Aslam, U.; Boerigter, C.; Morabito, M. Photochemical Transformations on Plasmonic Metal Nanoparticles. *Nat Mater* **2015**, *14* (6), 567–576.
 - (21) Christopher, P.; Xin, H.; Linic, S. Visible-Light-Enhanced Catalytic Oxidation Reactions on Plasmonic Silver Nanostructures. *Nat Chem* **2011**, *3* (6), 467–472.
 - (22) da Silva, A. M.; Rodrigues, T.; Taguchi, L. K.; Fajardo, H.; Balzer, R.; Probst, L. D.; Camargo, P. C. Pd-Based Nanoflowers Catalysts: Controlling Size, Composition, and Structures for the 4-Nitrophenol Reduction and BTX Oxidation Reactions. *J. Mater. Sci.* **2015**, 1–12.
 - (23) Smolentseva, E.; Costa, V. V.; Cotta, R. F.; Simakova, O.; Beloshapkin, S.; Gusevskaya, E. V.; Simakov, A. Aerobic Oxidative Esterification of Benzyl Alcohol and Acetaldehyde over Gold Supported on Nanostructured Ceria–Alumina Mixed Oxides. *ChemCatChem* **2015**, *7* (6), 1011–1017.
 - (24) Fang, J.; Li, J.; Zhang, B.; Yuan, X.; Asakura, H.; Tanaka, T.; Teramura, K.; Xie, J.; Yan, N. The Support Effect on the Size and Catalytic Activity of Thiolated Au₂₅ Nanoclusters as Precatalysts. *Nanoscale* **2015**, *7* (14), 6325–6333.
 - (25) da Silva, A. G. M.; Rodrigues, T. S.; Correia, V. G.; Alves, T. V.; Alves, R. S.; Ando, R. A.; Ornellas, F. R.; Wang, J.; Andrade, L. H.; Camargo, P. H. C. Plasmonic Nanorattles as Next-Generation Catalysts for Surface Plasmon Resonance-Mediated Oxidations Promoted by Activated Oxygen. *Angew. Chemie Int. Ed.* **2016**, *55* (25), 7111–7115.
 - (26) Wang, F.; Li, C.; Chen, H.; Jiang, R.; Sun, L.-D.; Li, Q.; Wang, J.; Yu, J. C.; Yan, C.-H. Plasmonic Harvesting of Light Energy for Suzuki Coupling Reactions. *J. Am. Chem. Soc.* **2013**, *135* (15), 5588–5601.
 - (27) Fihri, A.; Bouhrara, M.; Nekoueishahraki, B.; Basset, J.-M.; Polshettiwar, V. Nanocatalysts for Suzuki Cross-Coupling Reactions. *Chem. Soc. Rev.* **2011**, *40* (10), 5181–5203.
 - (28) Guha, N. R.; Sharma, S.; Bhattacharjee, D.; Thakur, V.; Bharti, R.; Reddy, C. B.; Das, P. Oxidative “reverse-Esterification” of Ethanol with Benzyl/alkyl Alcohols or Aldehydes Catalyzed by Supported Rhodium Nanoparticles. *Green Chem.* **2016**, *18* (5), 1206–1211.
 - (29) Wang, X.; Figueroa-Cosme, L.; Yang, X.; Luo, M.; Liu, J.; Xie, Z.; Xia, Y. Pt-Based Icosahedral Nanocages: Using a Combination of {111} Facets, Twin Defects, and

- Ultrathin Walls to Greatly Enhance Their Activity toward Oxygen Reduction. *Nano Lett.* **2016**, *16* (2), 1467–1471.
- (30) Hu, P.; Song, Y.; Chen, L.; Chen, S. Electrocatalytic Activity of Alkyne-Functionalized AgAu Alloy Nanoparticles for Oxygen Reduction in Alkaline Media. *Nanoscale* **2015**, *7* (21), 9627–9636.
- (31) Liu, Q.; Xu, Y.-R.; Wang, A.-J.; Feng, J.-J. A Single-Step Route for Large-Scale Synthesis of Core-shell Palladium@platinum Dendritic Nanocrystals/reduced Graphene Oxide with Enhanced Electrocatalytic Properties. *J. Power Sources* **2016**, *302*, 394–401.
- (32) da Silva, A. G. M.; Rodrigues, T. S.; Wang, J.; Yamada, L. K.; Alves, T. V.; Ornellas, F. R.; Ando, R. A.; Camargo, P. H. C. The Fault in Their Shapes: Investigating the Surface-Plasmon-Resonance-Mediated Catalytic Activities of Silver Quasi-Spheres, Cubes, Triangular Prisms, and Wires. *Langmuir* **2015**, *31* (37), 10272–10278.
- (33) da Silva, A. G. M.; Rodrigues, T. S.; Taguchi, L. S. K.; Fajardo, H. V.; Balzer, R.; Probst, L. F. D.; Camargo, P. H. C. Pd-Based Nanoflowers Catalysts: Controlling Size, Composition, and Structures for the 4-Nitrophenol Reduction and BTX Oxidation Reactions. *J. Mater. Sci.* **2016**, *51* (1), 603–614.
- (34) Xu, R.; Wang, D.; Zhang, J.; Li, Y. Shape-Dependent Catalytic Activity of Silver Nanoparticles for the Oxidation of Styrene. *Chem. – An Asian J.* **2006**, *1* (6), 888–893.
- (35) Rodrigues, T. S.; da Silva, A. H. M.; da Silva, A. G. M.; Ceara, D. G.; Gomes, J. F.; Assaf, J. M.; Camargo, P. H. C. Hollow AgPt/SiO₂ Nanomaterials with Controlled Surface Morphologies: Is the Number of Pt Surface Atoms Imperative to Optimize Catalytic Performances? *Catal. Sci. Technol.* **2016**, *6* (7), 2162–2170.
- (36) Chanda, K.; Rej, S.; Huang, M. H. Facet-Dependent Catalytic Activity of Cu₂O Nanocrystals in the One-Pot Synthesis of 1,2,3-Triazoles by Multicomponent Click Reactions. *Chem. – A Eur. J.* **2013**, *19* (47), 16036–16043.
- (37) Tsai, Y.-H.; Chanda, K.; Chu, Y.-T.; Chiu, C.-Y.; Huang, M. H. Direct Formation of Small Cu₂O Nanocubes, Octahedra, and Octapods for Efficient Synthesis of Triazoles. *Nanoscale* **2014**, *6* (15), 8704–8709.
- (38) Stark, W. J.; Stoessel, P. R.; Wohlleben, W.; Hafner, A. Industrial Applications of Nanoparticles. *Chem. Soc. Rev.* **2015**, *44* (16), 5793–5805.
- (39) Chen, J.; Wiley, B. J.; Xia, Y. One-Dimensional Nanostructures of Metals: Large-Scale Synthesis and Some Potential Applications. *Langmuir* **2007**, *23* (8), 4120–4129.
- (40) Sun, Y.; Gates, B.; Mayers, B.; Xia, Y. Crystalline Silver Nanowires by Soft Solution Processing. *Nano Lett.* **2002**, *2* (2), 165–168.
- (41) Wiley, B.; Sun, Y.; Mayers, B.; Xia, Y. Shape-Controlled Synthesis of Metal Nanostructures: The Case of Silver. *Chem. – A Eur. J.* **2005**, *11* (2), 454–463.
- (42) Sun, Y.; Mayers, B. T.; Xia, Y. Template-Engaged Replacement Reaction: A One-Step Approach to the Large-Scale Synthesis of Metal Nanostructures with Hollow Interiors. *Nano Lett.* **2002**, *2* (5), 481–485.
- (43) Sun, Y.; Mayers, B.; Xia, Y. Metal Nanostructures with Hollow Interiors. *Adv. Mater.* **2003**, *15* (7–8), 641–646.
- (44) Xia, X.; Wang, Y.; Ruditskiy, A.; Xia, Y. 25th Anniversary Article: Galvanic Replacement: A Simple and Versatile Route to Hollow Nanostructures with Tunable and Well-Controlled Properties. *Adv. Mater.* **2013**, *25* (44), 6313–6333.
- (45) Sun, Y.; Mayers, B.; Herricks, T.; Xia, Y. Polyol Synthesis of Uniform Silver Nanowires: A Plausible Growth Mechanism and the Supporting Evidence. *Nano Lett.* **2003**, *3* (7), 955–960.
- (46) Foiles, S. M.; Baskes, M. I.; Daw, M. S. Embedded-Atom-Method Functions for the Fcc Metals Cu, Ag, Au, Ni, Pd, Pt, and Their Alloys. *Phys. Rev. B* **1986**, *33* (12), 7983–

- 7991.
- (47) Rodrigues, T. S.; da Silva, A. G. M.; de Moura, A. B. L.; Freitas, I. G.; Camargo, P. H. C. Rational Design of Plasmonic Catalysts: Matching the Surface Plasmon Resonance with Lamp Emission Spectra for Improved Performance in AgAu Nanorings. *RSC Adv.* **2016**, *6* (67), 62286–62290.
 - (48) Skrabalak, S. E.; Chen, J.; Sun, Y.; Lu, X.; Au, L.; Cobley, C. M.; Xia, Y. Gold Nanocages: Synthesis, Properties, and Applications. *Acc. Chem. Res.* **2008**, *41* (12), 1587–1595.
 - (49) Jang, H.-J.; Ham, S.; Acapulco, J. A. I.; Song, Y.; Hong, S.; Shuford, K. L.; Park, S. Fabrication of 2D Au Nanorings with Pt Framework. *J. Am. Chem. Soc.* **2014**, *136* (50), 17674–17680.
 - (50) Verbruggen, S. W.; Keulemans, M.; Filippousi, M.; Flahaut, D.; Van Tendeloo, G.; Lacombe, S.; Martens, J. A.; Lenaerts, S. Plasmonic Gold–silver Alloy on TiO₂ Photocatalysts with Tunable Visible Light Activity. *Appl. Catal. B Environ.* **2014**, *156–157*, 116–121.
 - (51) Rodrigues, T. S.; da Silva, A. G. M.; Gonçalves, M. C.; Fajardo, H. V.; Balzer, R.; Probst, L. F. D.; Camargo, P. H. C. AgPt Hollow Nanodendrites: Synthesis and Uniform Dispersion over SiO₂ Support for Catalytic Applications. *ChemNanoMat* **2015**, *1* (1), 46–51.
 - (52) Paul, B.; Bhuyan, B.; Dhar Purkayastha, D.; Dey, M.; Dhar, S. S. Green Synthesis of Gold Nanoparticles Using Pogestemon Bengalensis (B) O. Ktz. Leaf Extract and Studies of Their Photocatalytic Activity in Degradation of Methylene Blue. *Mater. Lett.* **2015**, *148*, 37–40.
 - (53) Zhou, G.; Fang, F.; Chen, Z.; He, Y.; Sun, H.; Shi, H. Facile Synthesis of Paper Mill Sludge-Derived Heterogeneous Catalyst for the Fenton-like Degradation of Methylene Blue. *Catal. Commun.* **2015**, *62*, 71–74.
 - (54) Naraginti, S.; Stephen, F. B.; Radhakrishnan, A.; Sivakumar, A. Zirconium and Silver Co-Doped TiO₂ Nanoparticles as Visible Light Catalyst for Reduction of 4-Nitrophenol, Degradation of Methyl Orange and Methylene Blue. *Spectrochim. Acta Part A Mol. Biomol. Spectrosc.* **2015**, *135*, 814–819.
 - (55) Houas, A.; Lachheb, H.; Ksibi, M.; Elaloui, E.; Guillard, C.; Herrmann, J.-M. Photocatalytic Degradation Pathway of Methylene Blue in Water. *Appl. Catal. B Environ.* **2001**, *31* (2), 145–157.
 - (56) Shahabuddin, S.; Muhamad Sarih, N.; Mohamad, S.; Joon Ching, J. SrTiO₃ Nanocube-Doped Polyaniline Nanocomposites with Enhanced Photocatalytic Degradation of Methylene Blue under Visible Light. *Polymers* . 2016.
 - (57) Matos, J.; Fierro, V.; Montaña, R.; Rivero, E.; de Yuso, A. M.; Zhao, W.; Celzard, A. High Surface Area Microporous Carbons as Photoreactors for the Catalytic Photodegradation of Methylene Blue under UV–vis Irradiation. *Appl. Catal. A Gen.* **2016**, *517*, 1–11.
 - (58) Sahoo, C.; Gupta, A. K. Photocatalytic Degradation of Methyl Blue by Silver Ion-Doped Titania: Identification of Degradation Products by GC-MS and IC Analysis. *J. Environ. Sci. Heal. Part A* **2015**, *50* (13), 1333–1341.
 - (59) Lin, J.; Weng, X.; Jin, X.; Megharaj, M.; Naidu, R.; Chen, Z. Reactivity of Iron-Based Nanoparticles by Green Synthesis under Various Atmospheres and Their Removal Mechanism of Methylene Blue. *RSC Adv.* **2015**, *5* (87), 70874–70882.
 - (60) Hollow Metal Nanostructures for Enhanced Plasmonics: Synthesis, Local Plasmonic Properties and Applications . *Nanophotonics* . 2016.

Chapter 5

AgPt Hollow Nanodendrites: Synthesis and Uniform Dispersion over SiO₂ Support for Catalytic Applications

5.1. Introduction

Platinum (Pt) nanostructures have been extensively employed as catalysts for a variety of transformations such as hydrogenation,^{17,126} oxidation,^{127–129} coupling reactions,^{96,130} and electrochemical oxidation/reduction.^{131–134} As Pt is expensive and low in reserve, approaches that enable one to maximize its catalytic performance (and thus reduce the required Pt loading in the catalyst) are highly desirable.^{135,136} Although maneuvering size, shape, and composition may improve catalytic performances,^{1,137–141} the synthesis of Pt nanocrystals in which these parameters can be tightly controlled remains limited in terms of large-scale production and robustness. In fact, only a few groups have demonstrated the synthesis of Pt nanomaterials with truly well-defined shapes and sizes.^{137,141,142}

Another challenge in heterogeneous catalysis by noble metals comprises the generation of supported materials in which the metal component presents a uniform dispersion over the entire surface of the support (without agglomeration).¹⁴³ For instance, the synthesis of supported catalysts is characterized by poor control over size, shape, composition of the noble metal component.^{143–145} Also, as the synthesis of controlled nanostructures in solution are limited in terms of large-scale production, their deposition over solid supports by post-synthesis impregnation methods, for example, remains difficult.

In order to address the synthesis of Pt based nanostructures with the potential for improved catalytic performances, we described herein an approach based on the galvanic

replacement reaction between Ag and PtCl_6^{2-} as well as the PtCl_6^{2-} reduction to Pt by hydroquinone for the rapid synthesis of AgPt nanodendrites displaying hollow interiors.^{10,13} While hollow nanomaterials may enable higher surface-to-volume ratios relative to their solid counterparts,^{2,14,146} most methods to their synthesis rely on templates that require an additional removal steps, use of expensive/toxic reagents (in addition to the Pt precursor), and offer limited control over size, structure, shell-thickness, among others.^{4,9,15,147,148} Here, hollow AgPt nanodendrites could be obtained in only 15 s following the addition of PtCl_6^{2-} to a suspension containing Ag nanospheres employing water as the solvent, PVP as a stabilizer, hydroquinone as a reducing agent, and 100 °C as the reaction temperature. The composition and size (shell thickness) could be precisely controlled as a function of the growth time, and the catalytic activities towards the 4-nitrophenol reduction were investigated as a function of these parameters. With the purpose of tackling the synthesis of supported Pt based catalysts, we demonstrate that the synthesis of AgPt nanodendrites could be scale up by 100 folds, and the nanodendrites supported onto commercial silica displaying uniform dispersion and no significant agglomeration. This material was employed as a solid catalyst towards gas phase benzene, toluene, and o-xylene oxidation reactions to demonstrate its application.

5.2. Experimental

Materials and Instrumentation

Analytical grade chemicals silver nitrate (AgNO_3 , 99%, Sigma-Aldrich), polyvinylpyrrolidone (PVP, Sigma-Aldrich, M.W. 55,000 g/mol), ethylene glycol (EG, 99.8%, Sigma-Aldrich), chloroplatinic acid hexahydrate ($\text{H}_2\text{PtCl}_6 \cdot 6\text{H}_2\text{O}$, $\geq 37.50\%$ Pt basis, Sigma-Aldrich), hydroquinone ($\text{C}_6\text{H}_6\text{O}_2$, 99%, Vetec), L-ascorbic acid ($\text{C}_6\text{H}_8\text{O}_6$, 99%, Sigma-Aldrich), sodium borohydride (NaBH_4 , 98%, Sigma-Aldrich), sodium citrate dihydrate ($\text{C}_6\text{H}_5\text{Na}_3\text{O}_7 \cdot 2\text{H}_2\text{O}$, 99%, Sigma-Aldrich), 4-nitrophenol ($\text{C}_6\text{H}_5\text{NO}_3$, 99.8%, Merck), silica

(pore size 22 Å, 800 m²/g, CAS number 112926-00-8, Sigma-Aldrich), benzene (C₆H₆, >99%, Vetec), toluene (C₇H₈, >99%, Vetec), o-xylene (C₈H₁₀, >99%, Vetec) were used as received.

Transmission electron microscopy (TEM) images were obtained with a JEOL 1010 microscope operating at 80 kV or a JEOL JEM2100 microscope operated at 200 kV. Samples for TEM were prepared by drop-casting an aqueous suspension of the nanostructures over a carbon-coated copper grid, followed by drying under ambient conditions. UV-VIS spectra were obtained from aqueous solutions or aqueous suspensions containing the nanostructures with a Shimadzu UV-1700 spectrophotometer. The Ag and Pt atomic percentages were measured by inductively coupled plasma optical emission spectrometry (ICP-OES) using a Spectro Arcos equipment at the IQ-USP analytical center facilities.

Synthesis of Ag seeds

Ag seeds were prepared by the polyol process.³⁴ In a typical procedure, 5 g of polyvinylpyrrolidone (PVP) was dissolved in 37.5 mL of ethylene glycol (EG). Then, AgNO₃ (200 mg, 1.2 mmol) was added and mixed until the complete dissolution. The resulting solution was heated to 125 °C for 2.5 hours, leading to the appearance of a greenish-yellow color, allowed to cool down to room temperature, and diluted to 125 mL of water.

Synthesis of AgPt hollow nanodendrites

In a typical synthesis, a mixture containing 9.4 mL of PVP aqueous solution (0.3 wt %) and 60 µL of the as-prepared Ag nanospheres suspension was stirred at 100 °C for 10 min in a 25 mL round-bottom flask. Then, 0.1 mL of hydroquinone aqueous solution (30 mM) was added. After 30 s, 47.8 µL of PtCl₆²⁻_(aq) (12 mM) was added. In order to control and monitor the growth of the nanodendrites as a function of time, parallel reactions were performed in the same conditions and quenched by cooling the reaction flask in ice water at different intervals:

15 s, 1 min, 5 min, 10 min, 30 min and 1 hour. After cooling down to room temperature, each suspension containing the hollow nanodendrites was washed twice with a supersaturated $\text{NaCl}_{(\text{aq})}$ and three times with water by successive rounds of centrifugation at 12000 rpm and removal of the supernatant. After washing, the hollow nanodendrites were suspended in 10 mL of PVP aqueous solution (0.3 wt %). This suspension was then employed in the catalytic tests for the 4-nitrophenol reduction reaction.

Catalytic activity towards the 4-nitrophenol reduction

In a typical procedure, 1 mL of a 1.4×10^{-4} M 4-nitrophenol aqueous solution, 2 mL of 4.2×10^{-2} M sodium borohydride aqueous solution, and 100 μL of the suspension containing the respective AgPt nanodendrites was added into a quartz cuvette. The catalytic transformation was studied by UV–VIS spectroscopy, in which the variations in the absorbance at 400 nm (assigned to 4-nitrophenolate ions) at 400 nm was monitored (this signal decreased as the consumption of 4-nitrophenolate ions and formation of 4-aminophenol take place). In this case, the UV-VIS spectra were collected at 13 s time intervals in the 350 to 500 nm range. A calibration curve for absorbance as a function of the 4-nitrophenolate concentration was employed in order to calculate the % conversions. The catalytic activities were expressed in terms of substrate conversion and TOF (turnover frequency), which was estimated by the slope of the TON curves (turnover numbers) up to ~50 % conversion versus time.

Synthesis of 1 wt. % AgPt supported onto SiO_2 (AgPt/ SiO_2)

In order to prepare AgPt hollow nanodendrites supported on SiO_2 , the AgPt synthesis was firstly scaled up by 100 folds. In this case, the synthesis was performed in a 2000 mL round-bottom flask under magnetic stirring at 100 °C and the growth time corresponded to 30 min.

The incorporation of AgPt nanodendrites onto the silica support (1 % wt, Pt basis) was performed using a wet impregnation approach.¹⁴⁹ Typically, the AgPt nanodendrites obtained after 30 min growth by the scaled up procedure were washed and concentrated to 50 mL. This suspension was added to a beaker containing 1 g of commercial silica. The resulting mixture was stirred at 80 °C, yielding the formation of a paste. Then, 50 mL of water was added and this suspension was stirred in same conditions until dryness. The resulting mixture was heated at 120 °C for 2 h under air in order to produce the AgPt/SiO₂ catalyst.

Catalytic activity towards benzene, toluene and o-xylene oxidation (BTX oxidation)

The catalytic oxidation of volatile organic compounds (benzene, toluene, and *o*-xylene) was performed in a fixed bed tubular quartz reactor under atmospheric pressure. The following conditions were chosen: 0.030 g of AgPt/SiO₂ catalyst, inlet benzene (1.2 g.m⁻³), toluene (0.7 g.m⁻³), *o*-xylene (0.5 g.m⁻³) in air, gas flow rate 20 cm³.min⁻¹, residence time 0.3s, gas hourly space velocity 12000 h⁻¹, and temperature in the 25-300 °C range. The reaction data was collected after at least 2 h on-stream at room temperature and the products were determined by GC-MS. The reactant and product mixtures were analyzed using two on-line gas chromatographs equipped with FID and TCD detector and an HP-5 column. The performances of the catalysts in an oxidation reaction were studied in the complete oxidation of benzene, toluene, *o*-xylene by atmospheric air. The catalytic activity was expressed in terms of the % conversion of benzene, toluene and *o*-xylene, respectively. The conversion of the BTX compounds was calculated using the equation 3:

$$CBTXs (\%) = [(BTXs)_{in} - (BTXs)_{out}] \cdot 100 / (BTXs)_{in} \quad (1)$$

where CBTXs (%) = percentage of BTX conversion; $[\text{BTXs}]_{\text{in}}$ = input quantity and $[\text{BTXs}]_{\text{out}}$ = output quantity.

5.3. Results and discussion

Our studies started with the synthesis of Ag nanospheres 32 ± 3 nm in diameter by a polyol approach as shown in Figure 5.1A.³⁴ It can be observed that the Ag nanospheres displayed spherical shape and relatively monodisperse sizes.

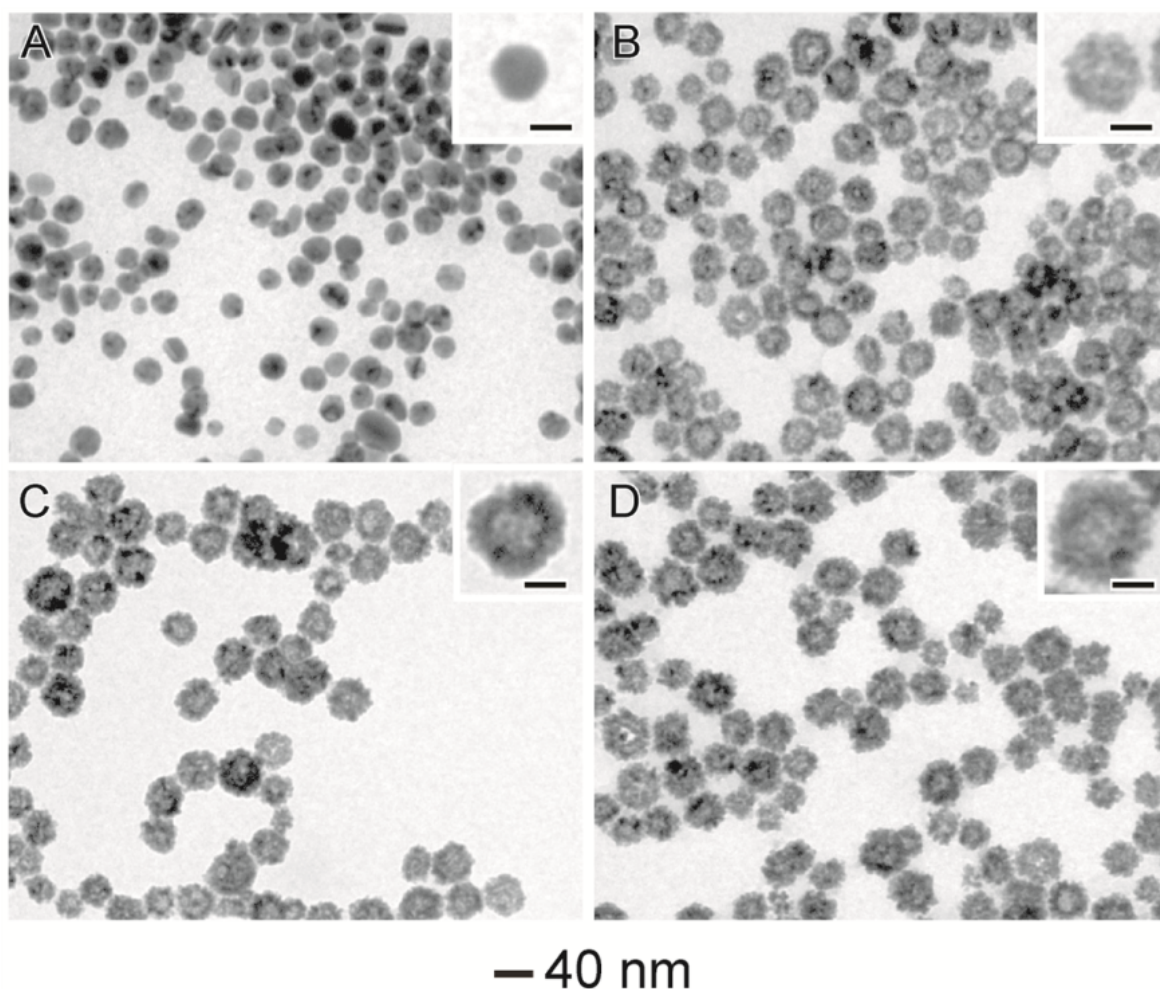


Figure 5.1. TEM images for Ag NPs (A) employed as templates for the synthesis of AgPt hollow nanodendrites with different sizes as a function of the Pt growth time: 15 s (B), 5 min (C), and 30 min (D) following the addition of $\text{PtCl}_6^{2-}(\text{aq})$ to a suspension containing Ag NPs, PVP, and hydroquinone. The scale bar in the insets corresponds to 20 nm.

They were employed as chemical templates for the synthesis of AgPt hollow nanodendrites by a combination of galvanic replacement reaction between Ag nanospheres and $\text{PtCl}_6^{2-}(\text{aq})$ as well as $\text{PtCl}_6^{2-}(\text{aq})$ reduction to Pt in the presence of hydroquinone (Figure 5.2).

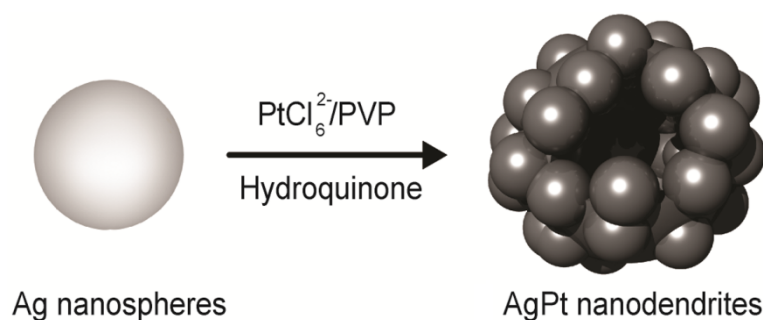


Figure 5.2. Approach for the synthesis of Ag-Pt nanodendrites by the combination of the galvanic replacement reaction between Ag nanospheres and $\text{PtCl}_6^{2-}(\text{aq})$ and the reduction of $\text{PtCl}_6^{2-}(\text{aq})$ by hydroquinone using PVP as the stabilizer, water as the solvent, and 100 °C as the reaction temperature.

Figure 5.1B-D display TEM images of the AgPt nanodendrites obtained at different growth times following the addition of the $\text{PtCl}_6^{2-}(\text{aq})$ precursor to a suspension containing Ag nanospheres and hydroquinone. In this case, the $\text{PtCl}_6^{2-}(\text{aq})$ reduction to Pt could be quenched in order to control the growth time by cooling at 0°C in an ice bath. Specifically, the growth times corresponded to 15 s, 5 min, and 30 min in Figure 5.1B-D, respectively. The formation of the hollow interiors can be clearly observed for all AgPt nanostructures, as illustrated by the brighter mass-thickness contrast at the center of each nanostructure. Also, it can be observed that the surface of the AgPt hollow materials was comprised of Pt islands, even at growth times as low as 15 s. The size/shell thickness as well as the Pt content in the hollow nanodendrites increased as a function of the growth time. The size (outer diameter) of the AgPt nanodendrites corresponded to 36 ± 2 ; 42 ± 2 ; and 48 ± 3 nm for 15 s, 5 min, and 30 min growth, respectively, while the shell thicknesses were ~ 4 , 10, and 16 nm, respectively. The Pt at. % in the AgPt nanodendrites were determined by ICP-OES analyses and corresponded to 30, 48 and 51 for the materials obtained after 15 s, 5 min, and 30 min, growth, respectively. This is in agreement

with the TEM results and the increased deposition of Pt as a function of time. It is important to note that the Ag:Pt molar ratio employed in the synthesis of AgPt nanodendrites corresponded to 1:20. Thus, it is plausible that higher Pt percentages or Pt hollow nanodendrites may be difficult to achieve by adding more PtCl_6^{2-} during the synthesis, as the Ag oxidation/dissolution becomes less favored as more Pt is deposited over the surface of the templates during the galvanic reaction.^[24]

In order to gain further insights into the morphological features of the AgPt nanodendrites, the AgPt materials obtained after 30 min was analyzed by HRTEM, and the results are shown in Figure 5.3. Figure 5.3A shows that the formation of the hollow interiors and the dendritic morphology comprised of several Pt islands ~ 6 nm in diameter uniformly deposited over the surface of the Ag templates. Phase-contrast HRTEM images indicate that, while the AgPt nanodendrites are polycrystalline, the individual Pt islands were single-crystalline, and ~ 0.22 nm lattice spacings assigned to the Pt $\{111\}$ could be clearly observed (Figure 5.3B).

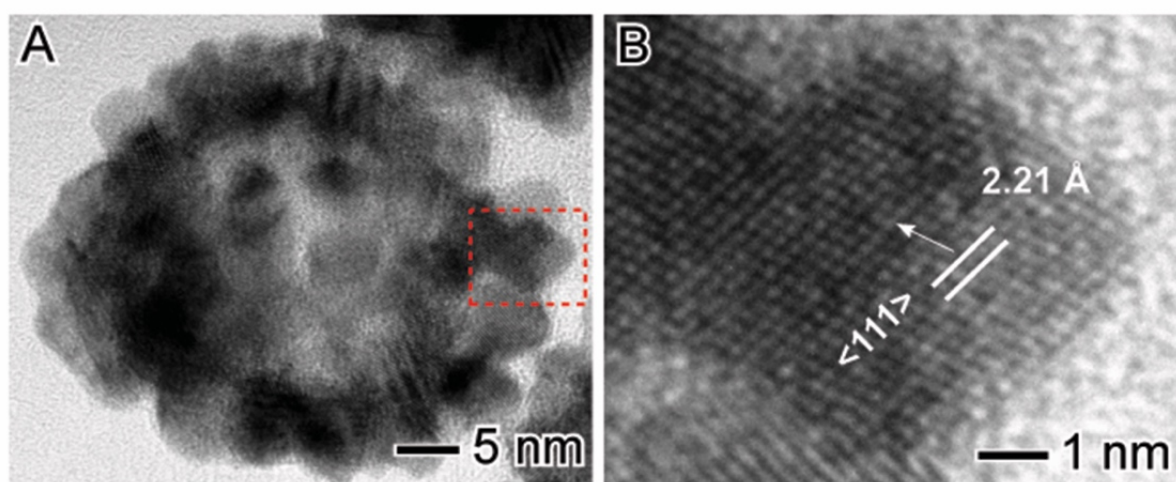


Figure 5.3. HRTEM images for the AgPt hollow nanodendrites obtained after 30 min growth following the addition of PtCl_6^{2-} (aq) to a suspension containing Ag NPs, PVP, and hydroquinone. While (A) depicts an individual nanodendrite, (B) shows a zoom-in image of the area highlighted in red in (A).

The formation of AgPt materials as a function of the growth time was also monitored by UV-VIS spectroscopy as shown in Figure 5.4. The Ag nanospheres employed as templates displayed a clear extinction peak centered at ~ 410 nm assigned to the dipolar mode of the surface plasmon resonance excitation. This peak completely disappeared after 15 s growth, in agreement with the Pt deposition together with the Ag dissolution from the templates as a result of the galvanic reaction. The appearance of a band at ~ 245 nm¹⁵⁰ associated with the deposition of Pt was also observed. This signal became more intense after 30 min growth as a result of the increased Pt deposition as a function of growth time in the presence of hydroquinone, which displays a band around ~ 290 nm.¹⁵¹ After 30 min growth, no significant changes were observed in the UV-VIS extinction spectra, in agreement with the absence of significant morphological (Figure 5.1B-D) and compositional variations (Table 5.1) after 30 min growth.

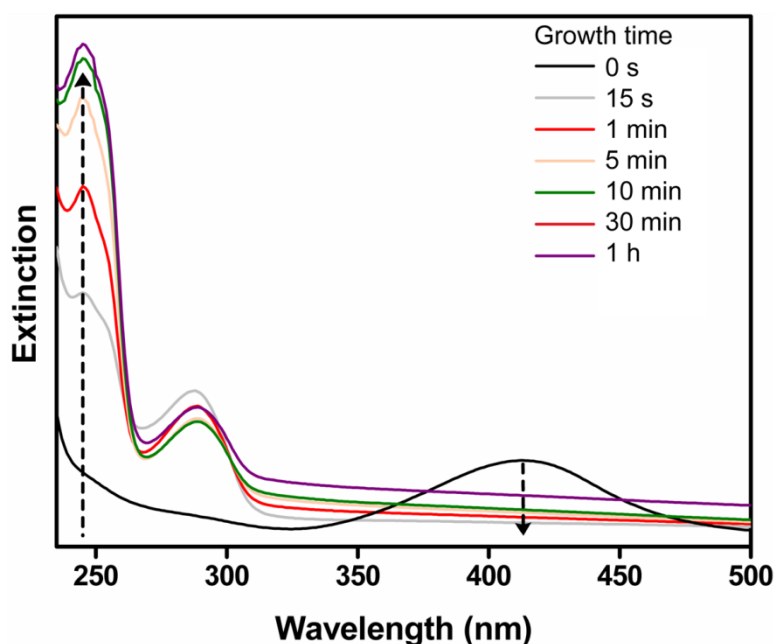


Figure 5.4. UV-VIS extinction spectra as a function of the Pt growth time during the synthesis of AgPt hollow nanodendrites employing Ag nanospheres as seeds. The spectra for the Ag and AgPt materials were recorded after 0 s (Ag), 15 s, 1 min, 5 min, 10 min, 30 min, and 1 h growth.

Table 5.1. Ag and Pt atomic percentages in the AgPt nanodendrites obtained by ICP-OES as a function of growth time.

Growth time	Ag (at. %)	Pt (at. %)	Sample
15s	70	30	Ag ₇₀ Pt ₃₀
1 min	54	46	Ag ₅₄ Pt ₄₆
5 min	52	48	Ag ₅₂ Pt ₄₈
10 min	52	48	Ag ₅₂ Pt ₄₈
30 min	49	51	Ag ₄₉ Pt ₅₁
1 h	49	51	Ag ₄₉ Pt ₅₁

In order to unravel the role played by hydroquinone over the formation of the hollow nanodendrites, we performed a series of control experiments in which hydroquinone was replaced by ascorbic acid, sodium citrate, and sodium borohydride under similar conditions as described in Figure 5.1 (30 min growth). The utilization of ascorbic acid led to the formation of a Pt chain-like morphology (Figure 5.5A), while sodium borohydride led to the formation of relatively big and irregular dendrites (Figure 5.5B). In presence of sodium citrate, the formation of AgPt nanoshells together with the deposition of isolated Pt or Ag nanoparticles were detected (Figure 5.5C). These results demonstrate that the utilization of hydroquinone was crucial to the formation of uniform and hollow nanodendrites.

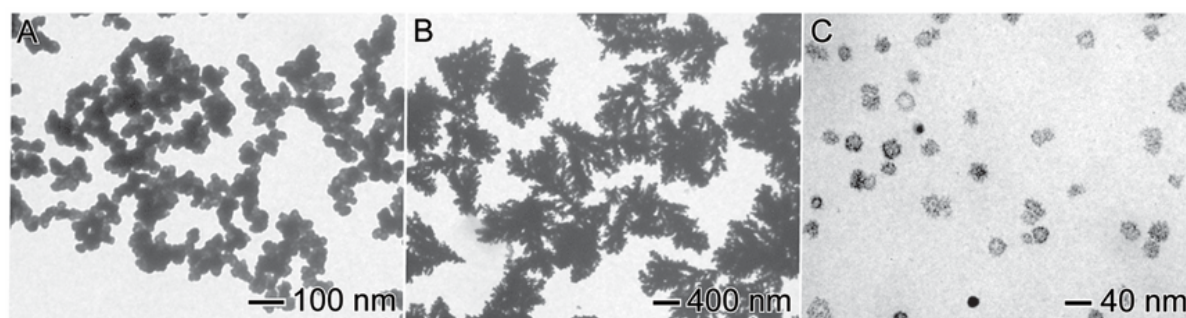


Figure 5.5. TEM images of AgPt nanostructures obtained after 30 min growth by replacing hydroquinone with ascorbic acid (A) sodium borohydride (B), and sodium citrate (C) as the reducing agents under the same experimental conditions as described in Figure 5.1.

The formation of AgPt hollow nanodendrites can be explained by a combination of two processes: while the galvanic replacement process enables one to obtain hollow interiors as Ag oxides to Ag^+ , the $\text{PtCl}_6^{2-}(\text{aq})$ reduction to Pt in the presence of hydroquinone enables one to control the morphology of the deposited Pt at the surface of the Ag nanospheres templates, i.e., the deposition of Pt islands over the Ag surface as opposed to the formation of a smooth shell as observed in the conventional galvanic replacement approach (Figure 5.6).¹⁰

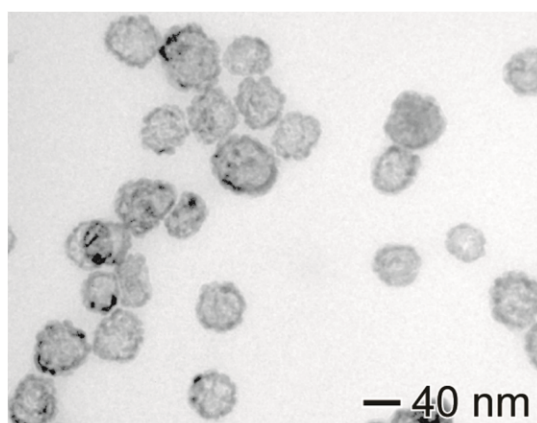


Figure 5.6. TEM images of AgPt nanoshells obtained after 10 min by the galvanic replacement reaction between Ag nanospheres and $\text{PtCl}_6^{2-}(\text{aq})$ in the presence of PVP as the stabilizer, water as the solvent, and 100 °C as the reaction temperature.

Due to their morphology comprised of hollow interiors and Pt islands ~ 6 nm in diameter over the surface, the AgPt nanodendrites are attractive for catalytic applications. Our catalytic studies started with the 4-nitrophenol reduction (Figure 5.7A). Specifically, we were interested in probing the catalytic activity as a function of the AgPt morphological and compositional changes. Therefore, we chose the AgPt nanodendrites obtained after 15 s, 5 min, and 30 min as catalysts, which were denoted according to their atomic compositions determined by ICP-OES as $\text{Ag}_{70}\text{Pt}_{30}$, $\text{Ag}_{52}\text{Pt}_{48}$ and $\text{Ag}_{49}\text{Pt}_{51}$, respectively (Table 5.1). It is important to note that the same concentration of particles was employed in all our catalysis studies.

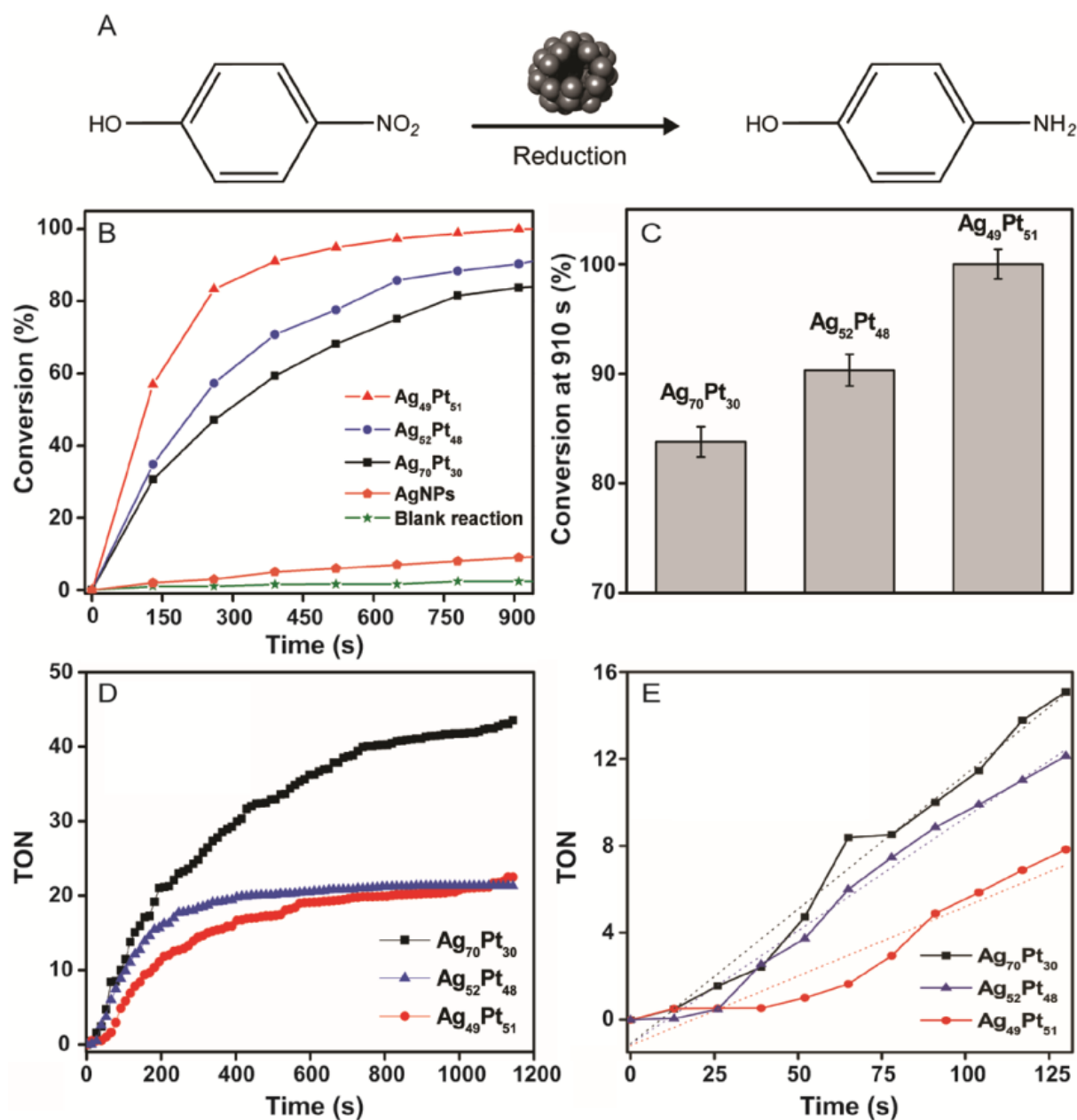


Figure 5.7. (A) Scheme for the 4-nitrophenol reduction by NaBH_4 in the presence of AgPt hollow nanodendrites as catalysts. (B) Product conversion percentages as a function of time for Ag, $\text{Ag}_{70}\text{Pt}_{30}$, $\text{Ag}_{52}\text{Pt}_{48}$, and $\text{Ag}_{49}\text{Pt}_{51}$ compositions (a blank reaction is also shown). (C) Conversion percentages at 910 s for $\text{Ag}_{70}\text{Pt}_{30}$, $\text{Ag}_{52}\text{Pt}_{48}$, and $\text{Ag}_{49}\text{Pt}_{51}$ compositions. (D) Catalytic activities expressed in terms of TON (turnover number) and (E) TON at the beginning of the reactions (up to $\sim 50\%$ of conversion) as a function of time for $\text{Ag}_{70}\text{Pt}_{30}$, $\text{Ag}_{52}\text{Pt}_{48}$, and $\text{Ag}_{49}\text{Pt}_{51}$ compositions.

Figure 5.7B shows the conversion % profiles as a function of time for the $\text{Ag}_{70}\text{Pt}_{30}$, $\text{Ag}_{52}\text{Pt}_{48}$, and $\text{Ag}_{49}\text{Pt}_{51}$ nanodendrites (black, blue, and red traces, respectively) as well as for Ag nanoparticles (orange trace). A blank reaction without any catalyst was also included for

comparison (green trace). In the absence of any catalyst, only 3 % conversion was observed after 910 s under our employed conditions. When Ag nanoparticles were used as the catalysts, this value corresponded to 12 %, showing that Ag NPs have poor activity towards this transformation under our employed conditions. All AgPt nanodendrites displayed much higher conversion % at all time intervals relative to Ag nanoparticles. The conversion % values increased as a function of the growth time during the synthesis, i.e., increased according to the order: $\text{Ag}_{70}\text{Pt}_{30} < \text{Ag}_{52}\text{Pt}_{48} < \text{Ag}_{49}\text{Pt}_{51}$. The conversion % for $\text{Ag}_{70}\text{Pt}_{30}$, $\text{Ag}_{52}\text{Pt}_{48}$, and $\text{Ag}_{49}\text{Pt}_{51}$ at 910 s corresponded to 84, 90, and 100 %, respectively (Figure 5.7C). This increase in catalytic activity is in agreement with the increase in the Pt content in the nanodendrites as a function of the growth time during the synthesis. When the catalytic activity is taken into account relative to the concentration of Pt, as expressed by TON values in Figure 5.7D, both $\text{Ag}_{52}\text{Pt}_{48}$ and $\text{Ag}_{49}\text{Pt}_{51}$ catalysts exhibited similar TON profiles probably due to their structural and compositional similarities. Their TON values increased to 14 and 18, respectively, up to ~ 300 s, and no further increase was observed at longer time intervals. Interestingly, $\text{Ag}_{70}\text{Pt}_{30}$ catalysts displayed the highest TON values, which progressively increased as a function of time during the reaction. The initial TOF values, calculated from the slope of the TON curves versus time up to ~ 50 % of conversion (Figure 5.7E) are in agreement with this result, decreasing in the order: $\text{Ag}_{70}\text{Pt}_{30} > \text{Ag}_{52}\text{Pt}_{48} > \text{Ag}_{49}\text{Pt}_{51}$. This behavior in catalytic activity in terms of TON was the opposite to what was observed from the % conversion profile. More specifically, although the catalysts containing higher Pt contents displayed higher conversion % under the same concentration of particles, when the concentration of Pt is taken into account, catalysts with lower Pt contents displayed increased activity. It is important to recall that our TEM results (Figure 5.1) indicated that an increase in the Pt content in the nanodendrites is accompanied by an increase in the size of the nanodendrites. Thus, it is plausible that there is a decrease on the Pt specific surface area as the growth time and the Pt content in the

nanodendrites increased, which in turn leads to an increase in catalytic activity in terms of Pt. In addition to the TON, TOF values were also calculated according to Equation 2 considering the concentration of 4-nitrophenol converted up to a time “t” as depicted in Figure 5.8A.

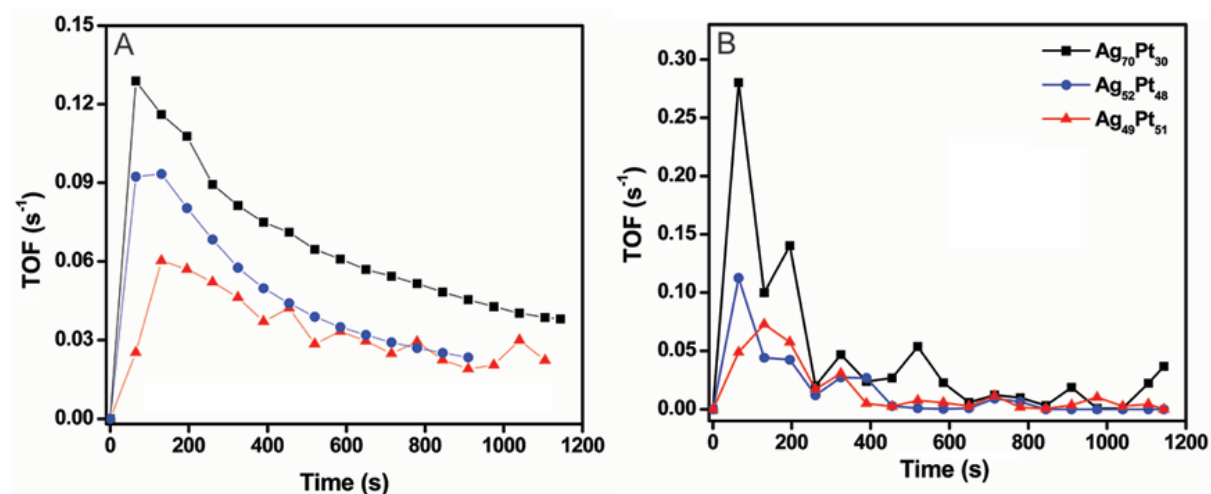


Figure 5.8. Catalytic activity expressed in terms of (A) TOF as a function of time and (B) TOF calculated at fixed 13 s intervals as a function of time for Ag₇₀Pt₃₀, Ag₅₂Pt₄₈, and Ag₄₉Pt₅₁ compositions.

The maximum TOF values were observed at 130 s, and the maximum values corresponded to 0.1289; 0.0973 and 0.06027 s⁻¹ for Ag₇₀Pt₃₀; Ag₅₂Pt₄₈ and Ag₄₉Pt₅₁, respectively. However, higher values of TOF were observed when we employed the concentration of 4-nitrophenol converted at 13 s time intervals as depicted in Figure 5.8B. These values corresponded to 0.2803; 0.1124 and 0.0728 s⁻¹ for Ag₇₀Pt₃₀; Ag₅₂Pt₄₈ and Ag₄₉Pt₅₁, respectively. Regarding their catalytic stability, the Ag₇₀Pt₃₀; Ag₅₂Pt₄₈ and Ag₄₉Pt₅₁ nanodendrites could be reused with no significant loss of catalytic activity after 5 catalytic cycles (Figure 5.9).

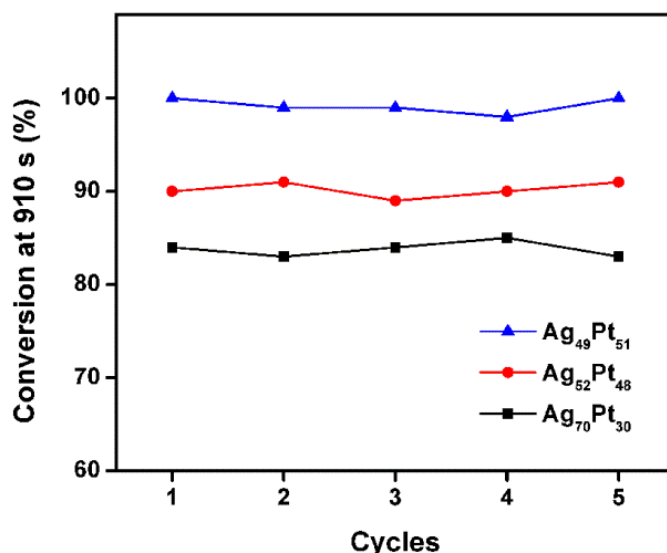


Figure 5.9. Catalytic activity expressed in terms of substrate conversion as a function of number of catalytic cycles for Ag₇₀Pt₃₀, Ag₅₂Pt₄₈, and Ag₄₉Pt₅₁ nanodendrites. It can be observed that no significant loss of catalytic activity was detected after 5 catalytic cycles.

After the synthesis of AgPt hollow nanodendrites with well-defined features and the investigation of their catalytic activities as a function of size and composition, we turned our attention to the possibility of employing the AgPt nanodendrites supported on commercial SiO₂ as solid catalysts for gas-phase transformations. While the use of solid materials as catalysts is imperative in the context gas-phase reactions, they also may allow for easier separation from the reaction mixture as well as avoid particle agglomeration relative to unsupported nanoparticles in the liquid-phase transformations.¹⁴³ Despite these attractive features, poor control over size, composition and dispersion of the metal component over the support is often observed in the synthesis of solid catalysts.^{143–145} Also, the relatively small scale in which controlled metal nanostructures can be currently synthesized limit their deposition over solid materials by post synthesis strategies. Interestingly, we found that the described experimental approach to the synthesis of hollow AgPt nanodendrites could be scaled up by 100 folds (relative to what is described in the experimental section) without any significant changes on the morphology (Figure 5.10) and optical (Figure 5.11) properties.

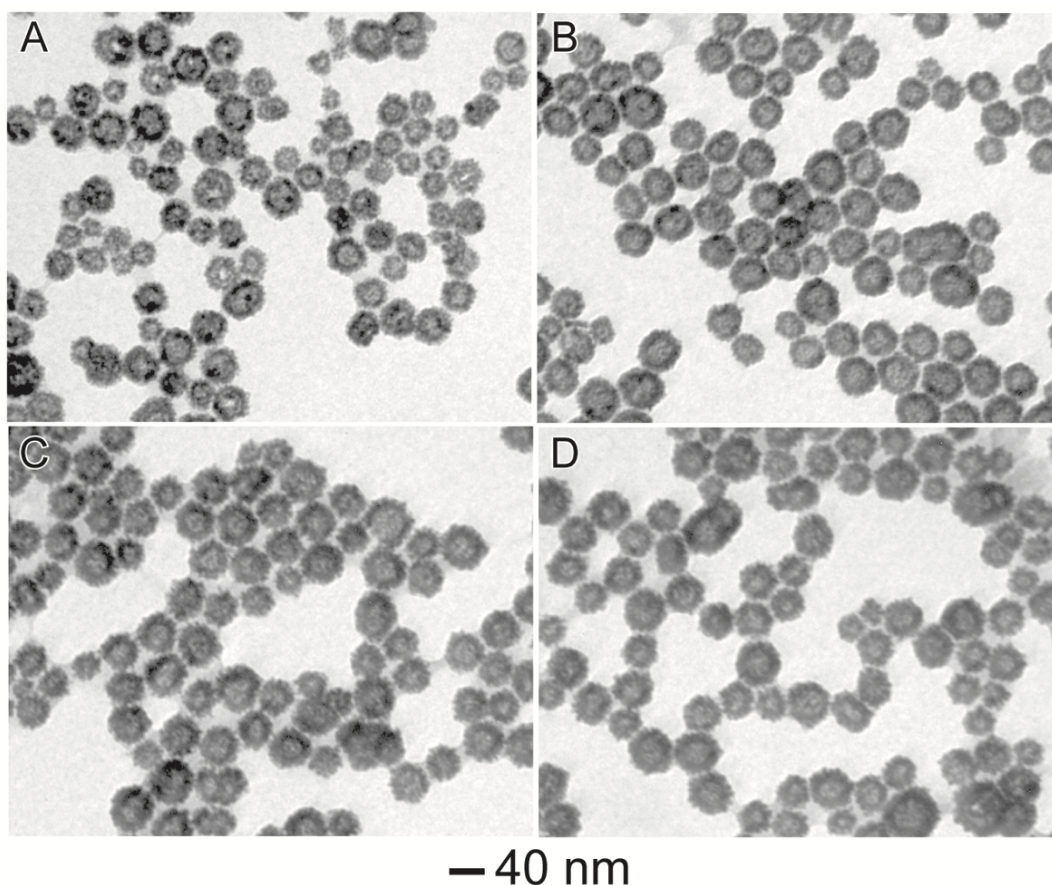


Figure 5.10. TEM images for AgPt hollow nanodendrites obtained by scaling up the synthesis procedure described in Figure 1 by 100 folds as a function of growth time: (A) 15 s, (B) 5 min, (C) 30 min, and (D) 1 h.

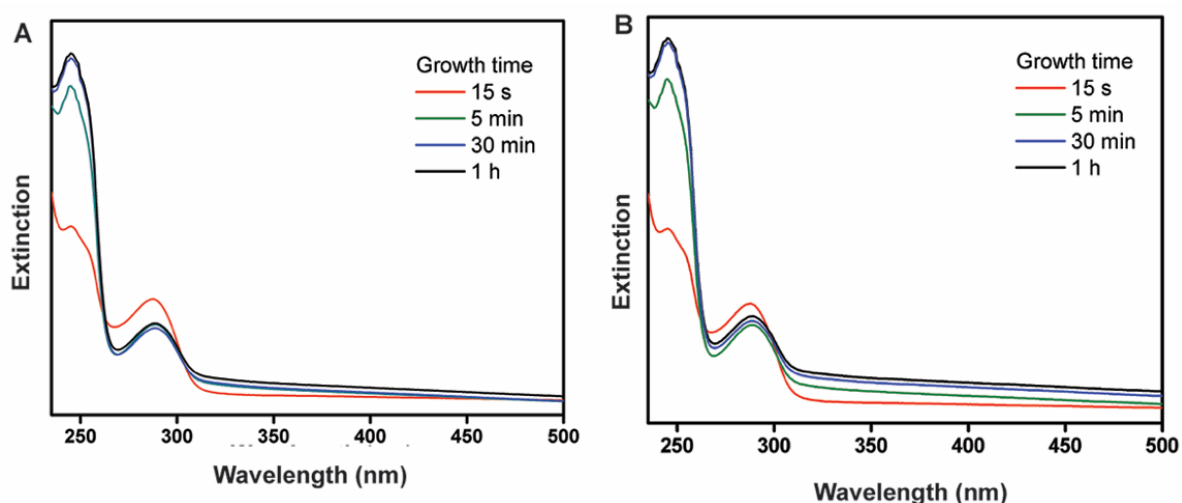


Figure 5.11. UV-VIS extinction spectra as a function of the Pt growth time during the synthesis of AgPt hollow nanodendrites employing Ag nanospheres as seeds: (A) AgPt materials obtained by scaling up the synthesis by 100 folds; and (B) AgPt materials obtained by the standard procedure.

We could then deposit the $\text{Ag}_{49}\text{Pt}_{51}$ nanostructure over commercial silica by wet impregnation methods to produce solid $\text{Ag}_{49}\text{Pt}_{51}/\text{SiO}_2$ catalysts, as shown in Figure 5.12. Here, The Pt loading corresponded to 1 wt. %. It can be observed that the dispersion of $\text{Ag}_{49}\text{Pt}_{51}$ was uniform over the entire SiO_2 surface, and no significant agglomeration was detected.

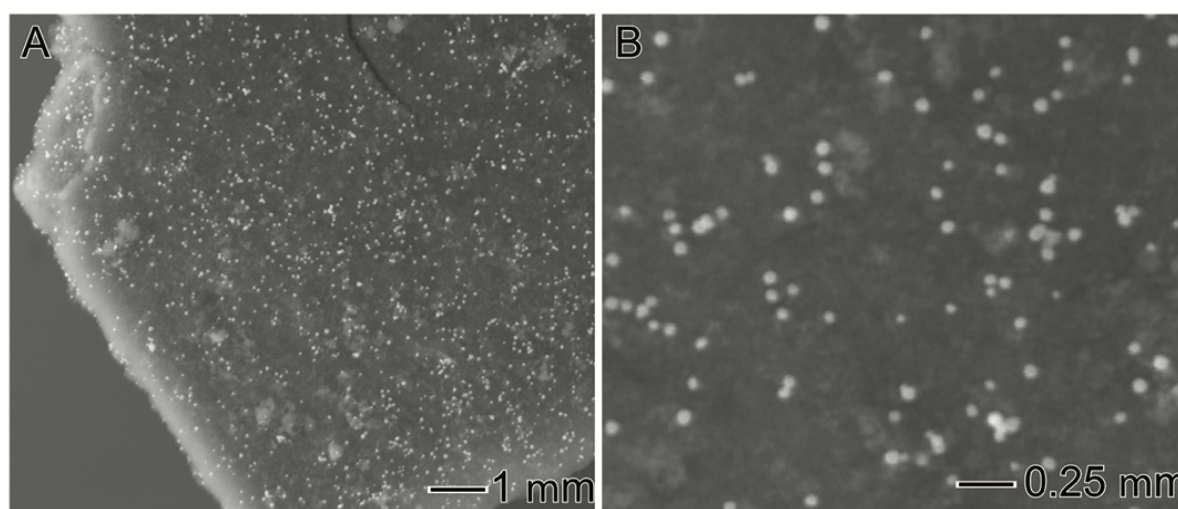


Figure 5.12. SEM images of $\text{Ag}_{49}\text{Pt}_{51}/\text{SiO}_2$ catalyst obtained by wet impregnation of $\text{Ag}_{49}\text{Pt}_{51}$ nanodendrites onto commercial SiO_2 . The Pt loading corresponded to 1 wt %.

The $\text{Ag}_{49}\text{Pt}_{51}/\text{SiO}_2$ material was investigated as a solid catalyst towards the gas-phase benzene, toluene, and *o*-xylene (BTX) oxidation reactions. Figure 5.13 shows the obtained BTX conversion percentages (%) as a function of temperature. The oxidation of benzene, toluene and *o*-xylene are depicted as the black (squares), red (circles), and blue (triangles) curves, respectively. In all experiments, only H_2O and CO_2 were detected as products as a result of the complete BTX oxidation. The BTX % conversion increased with reaction temperature. Also, the following order of BTX conversion was observed: benzene > toluene > *o*-xylene. At 300 °C, the conversion corresponded to 100, 89, and 60 % for benzene; toluene; and *o*-xylene, respectively. The structure of the aromatic compounds is one important feature that influences the catalytic activity.³⁹ The presence of methyl groups in the aromatic ring can makes the substrate less susceptible for the oxidation. These results are in agreement with previous

reports on BTX oxidation¹⁵² and also indicated that the AgPt nanodendrites works as catalysts displaying good activities for both reduction and oxidation reactions.

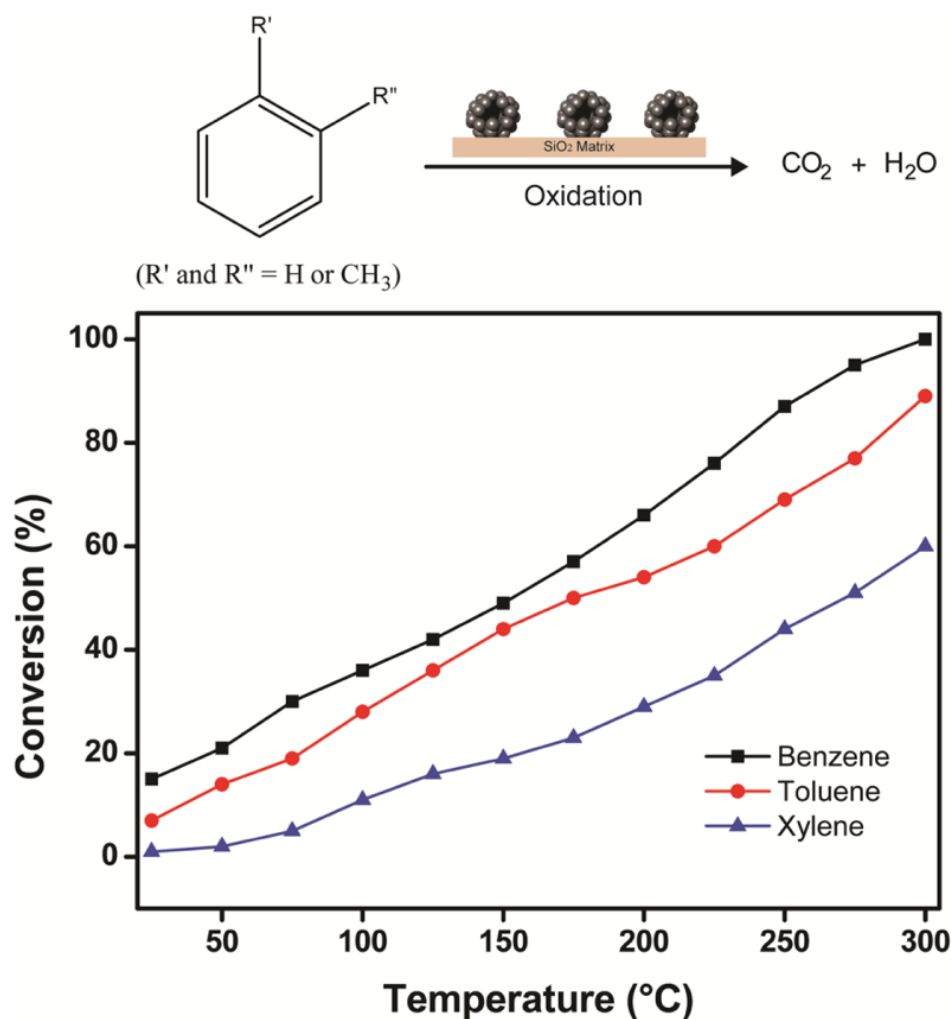


Figure 5.13. Conversion percentages of benzene, toluene, and *o*-xylene oxidation (black, red, and blue traces, respectively) as a function of temperature catalyzed by Ag₄₉Pt₅₁/SiO₂.

5.4. Conclusion

We addressed herein two challenges in heterogeneous catalysis by Pt: *i*) the development of facile and robust methods to the synthesis of Pt-based nanomaterials with the potential for improved catalytic performance, and *ii*) the generation of supported materials in which the metal component presents a uniform dispersion over the entire surface of the support (without agglomeration). To achieve these goals, we first described a facile approach to the

synthesis of AgPt hollow nanodendrites employing Ag nanospheres as seeds by combining a galvanic replacement reaction between Ag nanospheres and $\text{PtCl}_6^{2-}(\text{aq})$ and $\text{PtCl}_6^{2-}(\text{aq})$ reduction to Pt in the presence of hydroquinone. AgPt hollow nanodendrites comprised of several Pt islands ~ 6 nm in diameter could be obtained in only 15 s following the addition of $\text{PtCl}_6^{2-}(\text{aq})$ to a suspension containing Ag nanospheres, and their size/shell thickness as well as composition (Pt molar fraction) could be manipulated as a function of the growth time. To demonstrate the robustness of our approach, the synthesis of AgPt nanodendrites could be scaled up by 100 folds, which enabled us to support the AgPt nanostructures onto commercial silica with uniform dispersion and no agglomeration for catalytic applications. Interestingly, the hollow nanodendrites worked as catalysts displaying good catalytic activities for both the 4-nitrophenol reduction (liquid phase catalysis) and the BTX oxidation (gas phase catalysis) reactions. We believe the results presented herein may inspire the synthesis of noble metal nanostructures displaying attractive features for catalytic applications, such as hollow interiors, ultrathin walls, controlled compositions and size, and uniform dispersion over solid supports to produce solid supported catalysts.

5.5. References

- (1) Yu, W.; Porosoff, M. D.; Chen, J. G. Review of Pt-Based Bimetallic Catalysis: From Model Surfaces to Supported Catalysts. *Chem. Rev.* **2012**, *112* (11), 5780–5817.
- (2) Bratlie, K. M.; Lee, H.; Komvopoulos, K.; Yang, P.; Somorjai, G. A. Platinum Nanoparticle Shape Effects on Benzene Hydrogenation Selectivity. *Nano Lett.* **2007**, *7* (10), 3097–3101.
- (3) Li, Y.; Gao, W.; Ci, L.; Wang, C.; Ajayan, P. M. Catalytic Performance of Pt Nanoparticles on Reduced Graphene Oxide for Methanol Electro-Oxidation. *Carbon N. Y.* **2010**, *48* (4), 1124–1130.
- (4) Matam, S. K.; Kondratenko, E. V.; Aguirre, M. H.; Hug, P.; Rentsch, D.; Winkler, A.; Weidenkaff, A.; Ferri, D. The Impact of Aging Environment on the Evolution of Al_2O_3 Supported Pt Nanoparticles and Their NO Oxidation Activity. *Appl. Catal. B Environ.* **2013**, *129* (0), 214–224.
- (5) Wang, H.; Sapi, A.; Thompson, C. M.; Liu, F.; Zherebetsky, D.; Krier, J. M.; Carl, L. M.; Cai, X.; Wang, L.-W.; Somorjai, G. A. Dramatically Different Kinetics and Mechanism at Solid/Liquid and Solid/Gas Interfaces for Catalytic Isopropanol Oxidation over Size-Controlled Platinum Nanoparticles. *J. Am. Chem. Soc.* **2014**, *136*

- (29), 10515–10520.
- (6) Fihri, A.; Bouhrara, M.; Nekoueishahraki, B.; Basset, J.-M.; Polshettiwar, V. Nanocatalysts for Suzuki Cross-Coupling Reactions. *Chem. Soc. Rev.* **2011**, *40* (10), 5181–5203.
 - (7) Zhong, J.-J.; Meng, Q.-Y.; Wang, G.-X.; Liu, Q.; Chen, B.; Feng, K.; Tung, C.-H.; Wu, L.-Z. A Highly Efficient and Selective Aerobic Cross-Dehydrogenative-Coupling Reaction Photocatalyzed by a Platinum(II) Terpyridyl Complex. *Chem. – A Eur. J.* **2013**, *19* (20), 6443–6450.
 - (8) Lim, B.; Jiang, M.; Yu, T.; Camargo, P. C.; Xia, Y. Nucleation and Growth Mechanisms for Pd-Pt Bimetallic Nanodendrites and Their Electrocatalytic Properties. *Nano Res.* **2010**, *3* (2), 69–80.
 - (9) Shao, M.; Peles, A.; Shoemaker, K. Electrocatalysis on Platinum Nanoparticles: Particle Size Effect on Oxygen Reduction Reaction Activity. *Nano Lett.* **2011**, *11* (9), 3714–3719.
 - (10) Xiong, B.; Zhou, Y.; Zhao, Y.; Wang, J.; Chen, X.; O’Hayre, R.; Shao, Z. The Use of Nitrogen-Doped Graphene Supporting Pt Nanoparticles as a Catalyst for Methanol Electrocatalytic Oxidation. *Carbon N. Y.* **2013**, *52* (0), 181–192.
 - (11) Zhou, X.; Gan, Y.; Du, J.; Tian, D.; Zhang, R.; Yang, C.; Dai, Z. A Review of Hollow Pt-Based Nanocatalysts Applied in Proton Exchange Membrane Fuel Cells. *J. Power Sources* **2013**, *232* (0), 310–322.
 - (12) Martin, S.; Garcia-Ybarra, P. L.; Castillo, J. L. High Platinum Utilization in Ultra-Low Pt Loaded PEM Fuel Cell Cathodes Prepared by Electrospraying. *Int. J. Hydrogen Energy* **2010**, *35* (19), 10446–10451.
 - (13) Hatanaka, M.; Takahashi, N.; Tanabe, T.; Nagai, Y.; Dohmae, K.; Aoki, Y.; Yoshida, T.; Shinjoh, H. Ideal Pt Loading for a Pt/CeO₂-Based Catalyst Stabilized by a Pt–O–Ce Bond. *Appl. Catal. B Environ.* **2010**, *99* (1–2), 336–342.
 - (14) Mostafa, S.; Behafarid, F.; Croy, J. R.; Ono, L. K.; Li, L.; Yang, J. C.; Frenkel, A. I.; Cuenya, B. R. Shape-Dependent Catalytic Properties of Pt Nanoparticles. *J. Am. Chem. Soc.* **2010**, *132* (44), 15714–15719.
 - (15) Yin, A.-X.; Min, X.-Q.; Zhang, Y.-W.; Yan, C.-H. Shape-Selective Synthesis and Facet-Dependent Enhanced Electrocatalytic Activity and Durability of Monodisperse Sub-10 Nm Pt–Pd Tetrahedrons and Cubes. *J. Am. Chem. Soc.* **2011**, *133* (11), 3816–3819.
 - (16) Watanabe, Y.; Wu, X.; Hirata, H.; Isomura, N. Size-Dependent Catalytic Activity and Geometries of Size-Selected Pt Clusters on TiO₂(110) Surfaces. *Catal. Sci. Technol.* **2011**, *1* (8), 1490–1495.
 - (17) Slater, T. J. A.; Macedo, A.; Schroeder, S. L. M.; Burke, M. G.; O’Brien, P.; Camargo, P. H. C.; Haigh, S. J. Correlating Catalytic Activity of Ag–Au Nanoparticles with 3D Compositional Variations. *Nano Lett.* **2014**, *14* (4), 1921–1926.
 - (18) Crespo-Quesada, M.; Yarulin, A.; Jin, M.; Xia, Y.; Kiwi-Minsker, L. Structure Sensitivity of Alkynol Hydrogenation on Shape- and Size-Controlled Palladium Nanocrystals: Which Sites Are Most Active and Selective? *J. Am. Chem. Soc.* **2011**, *133* (32), 12787–12794.
 - (19) Kang, Y.; Pyo, J. B.; Ye, X.; Diaz, R. E.; Gordon, T. R.; Stach, E. A.; Murray, C. B. Shape-Controlled Synthesis of Pt Nanocrystals: The Role of Metal Carbonyls. *ACS Nano* **2012**, *7* (1), 645–653.
 - (20) Maksimuk, S.; Teng, X.; Yang, H. Roles of Twin Defects in the Formation of Platinum Multipod Nanocrystals. *J. Phys. Chem. C* **2007**, *111* (39), 14312–14319.
 - (21) Astruc, D.; Lu, F.; Aranzaes, J. R. Nanoparticles as Recyclable Catalysts: The Frontier between Homogeneous and Heterogeneous Catalysis. *Angew. Chemie Int. Ed.* **2005**, *44*

- (48), 7852–7872.
- (22) Bell, A. T. The Impact of Nanoscience on Heterogeneous Catalysis. *Sci.* **2003**, *299* (5613), 1688–1691.
- (23) White, R. J.; Luque, R.; Budarin, V. L.; Clark, J. H.; Macquarrie, D. J. Supported Metal Nanoparticles on Porous Materials. Methods and Applications. *Chem. Soc. Rev.* **2009**, *38* (2), 481–494.
- (24) Xia, X.; Wang, Y.; Ruditskiy, A.; Xia, Y. 25th Anniversary Article: Galvanic Replacement: A Simple and Versatile Route to Hollow Nanostructures with Tunable and Well-Controlled Properties. *Adv. Mater.* **2013**, *25* (44), 6313–6333.
- (25) da Silva, A. G. M.; de Souza, M. L.; Rodrigues, T. S.; Alves, R. S.; Temperini, M. L. A.; Camargo, P. H. C. Rapid Synthesis of Hollow Ag–Au Nanodendrites in 15 Seconds by Combining Galvanic Replacement and Precursor Reduction Reactions. *Chem. – A Eur. J.* **2014**, *20* (46), 15040–15046.
- (26) Xiao, Y.-P.; Wan, S.; Zhang, X.; Hu, J.-S.; Wei, Z.-D.; Wan, L.-J. Hanging Pt Hollow Nanocrystal Assemblies on Graphene Resulting in an Enhanced Electrocatalyst. *Chem. Commun.* **2012**, *48* (83), 10331–10333.
- (27) Yu, X.; Wang, D.; Peng, Q.; Li, Y. High Performance Electrocatalyst: Pt-Cu Hollow Nanocrystals. *Chem. Commun.* **2011**, *47* (28), 8094–8096.
- (28) Mahmoud, M. A.; Narayanan, R.; El-Sayed, M. A. Enhancing Colloidal Metallic Nanocatalysis: Sharp Edges and Corners for Solid Nanoparticles and Cage Effect for Hollow Ones. *Acc. Chem. Res.* **2013**, *46* (8), 1795–1805.
- (29) Chen, H. M.; Liu, R.-S.; Lo, M.-Y.; Chang, S.-C.; Tsai, L.-D.; Peng, Y.-M.; Lee, J.-F. Hollow Platinum Spheres with Nano-Channels: Synthesis and Enhanced Catalysis for Oxygen Reduction. *J. Phys. Chem. C* **2008**, *112* (20), 7522–7526.
- (30) Lou, X. W. (David); Archer, L. A.; Yang, Z. Hollow Micro-/Nanostructures: Synthesis and Applications. *Adv. Mater.* **2008**, *20* (21), 3987–4019.
- (31) Sun, Y.; Mayers, B.; Xia, Y. Metal Nanostructures with Hollow Interiors. *Adv. Mater.* **2003**, *15* (7–8), 641–646.
- (32) Mohanty, A.; Garg, N.; Jin, R. A Universal Approach to the Synthesis of Noble Metal Nanodendrites and Their Catalytic Properties. *Angew. Chemie Int. Ed.* **2010**, *49* (29), 4962–4966.
- (33) Wang, W.; Wang, D.; Liu, X.; Peng, Q.; Li, Y. Pt-Ni Nanodendrites with High Hydrogenation Activity. *Chem. Commun.* **2013**, *49* (28), 2903–2905.
- (34) Silvert, P.-Y.; Herrera-Urbina, R.; Duvauchelle, N.; Vijayakrishnan, V.; Elhsissen, K. T. Preparation of Colloidal Silver Dispersions by the Polyol Process. Part 1-Synthesis and Characterization. *J. Mater. Chem.* **1996**, *6* (4), 573–577.
- (35) Jiang, S. P. A Review of Wet impregnation—An Alternative Method for the Fabrication of High Performance and Nano-Structured Electrodes of Solid Oxide Fuel Cells. *Mater. Sci. Eng. A* **2006**, *418* (1–2), 199–210.
- (36) Lee, H.; Habas, S. E.; Kwek, S.; Butcher, D.; Somorjai, G. A.; Yang, P. Morphological Control of Catalytically Active Platinum Nanocrystals. *Angew. Chemie* **2006**, *118* (46), 7988–7992.
- (37) Sirajuddin; Bhangar, M. I.; Niaz, A.; Shah, A.; Rauf, A. Ultra-Trace Level Determination of Hydroquinone in Waste Photographic Solutions by UV–vis Spectrophotometry. *Talanta* **2007**, *72* (2), 546–553.
- (38) Liotta, L. F. Catalytic Oxidation of Volatile Organic Compounds on Supported Noble Metals. *Appl. Catal. B Environ.* **2010**, *100* (3–4), 403–412.

Chapter 6

On the Catalytic Properties of AgPt Nanoshells as a Function of Size: Larger Outer Diameters Lead to Improved Performances

6.1. Introduction

Platinum (Pt) based nanostructures have been extensively employed for catalysis and electrocatalysis applications.^{153–157} As Pt represents an expensive metal which is also low in reserve, the quest for improved catalytic properties has been a very relevant topic.^{116,135,136} Improving catalytic performances in Pt-based catalysts not only has the potential to enable the utilization of lower Pt loadings, thus reducing costs, but may also contribute to more sustainable industrial processes and clean energy generation.^{135,136} Consequently, several synthetic strategies have been proposed to improve the catalytic performance of Pt-based materials. These include the control over the shape and size, the combination with other metals (bimetallic and trimetallic compositions), and the generation of Pt-based materials with hollow interiors.^{66,116,158–161}

In order to enable practical applications in catalysis, procedures for the synthesis Pt-based materials must be robust, scalable, and allow for the preparation of supported catalysts in which the active phase (Pt) is well-dispersed over the surface of a solid material (without agglomeration). Unfortunately, several reported procedures remain limited towards these requirements.^{100,162} Moreover, a precise correlation and understanding of how catalytic properties depend on the various physical and chemical parameters that define a nanocatalyst is imperative to optimize performances.¹⁶³ This, in turn, require the controlled synthesis of

well-defined nanocatalysts, which remains a bottleneck in the field of heterogeneous catalysis.¹⁶⁴

We report herein on the effect of the size of silver nanoparticles (Ag NPs) employed as starting materials over the morphological features and catalytic performances of AgPt nanoshells produced by a galvanic replacement between Ag and PtCl_6^{2-} coupled with co-reduction by hydroquinone. Specifically, we focused on Ag NPs of four different sizes as starting materials, and found that the outer diameter and shell thickness of the AgPt nanoshells increased with the size of the starting Ag NPs. However, the surface of the nanoshells were comprised of small nanoparticle islands, whose size decreased with the increase in the outer diameter and shell thickness. The obtained AgPt nanoshells were supported into SiO_2 , and the catalytic performances of the AgPt/ SiO_2 nanocatalysts towards the gas-phase oxidation of benzene, toluene and o-xylene (BTX oxidation) was investigated as a function of outer diameter and surface morphology. As our synthetic procedures led to uniform and well-defined nanoshells, it enabled the correlation among activity, size, and surface morphology. Our results demonstrated that the presence of smaller nanoparticle islands at the surface (despite the larger outer diameters and thicker walls) led to a higher Pt surface area and thus catalytic performances. It is important to note that gas-phase transformations are highly relevant in the context of both science and industry, having direct applications in environmental remediation, for example.¹⁶⁵ Even though these compounds are proven to be dangerous to our health and atmosphere, a variety of processes and activities still contribute to their release to the environment.

6.2. Experimental

Materials and Instrumentation

Analytical grade silver nitrate (AgNO_3 , 99%, Sigma-Aldrich), polyvinylpyrrolidone (PVP, Sigma-Aldrich, M.W. 10,000 g/mol), polyvinylpyrrolidone (PVP, Sigma-Aldrich, M.W. 55,000 g/mol), chloroplatinic acid hexahydrate ($\text{H}_2\text{PtCl}_6 \cdot 6\text{H}_2\text{O}$, $\geq 37.50\%$ Pt basis, Sigma-Aldrich), hydroquinone ($\text{C}_6\text{H}_6\text{O}_2$, 99%, Vetec), silica ($\sim 175 \text{ m}^2/\text{g}$, Degussa), benzene (C_6H_6 , $>99\%$, Vetec), toluene (C_7H_8 , $>99\%$, Vetec), and o-xylene (C_8H_{10} , $>99\%$, Vetec) were used as received.

Transmission electron microscopy (TEM) and high-resolution transmission electron microscopy (HRTEM) images were obtained with a JEOL 1010 microscope operating at 80 kV or a JEOL JEM2100 microscope operated at 200 kV. Samples for TEM/HRTEM were prepared by drop-casting an aqueous suspension of the nanostructures over a carbon-coated copper grid, followed by drying under ambient conditions. The scanning electron microscopy (SEM) images were obtained using a JEOL field emission gun electron microscope JSM6330F operated at 5 kV. The samples were prepared by drop-casting an aqueous suspension containing the nanostructures over a silicon wafer, followed by drying under ambient conditions. UV-VIS spectra were obtained from aqueous suspensions containing the nanostructures with a Shimadzu UV-1700 spectrophotometer. The Ag and Pt atomic percentages were measured by inductively coupled plasma optical emission spectrometry (ICP-OES) using a Spectro Arcos equipment. The X-ray diffraction (XRD) data were obtained using a Rigaku - Miniflex equipment, $\text{CuK}\alpha$ radiation. The diffraction pattern was measured in the range of $10 - 90^\circ 2\theta$ with a 1° min^{-1} angular speed scan. The determination of the number of Pt active sites was carried out in a Micrometrics Chemisorb 2705. Typically, 0.1 g of catalysts was dried with N_2 flow at 125°C for 1 h. Then, the system was heated at 500°C for 1 h under

O₂ flow to remove remaining organic compounds. Afterwards, the samples were cooled down to room temperature and then reduced at 550 °C under H₂ flow for 80 min and cooled down to room temperature under N₂ flow. Finally, H₂ pulses were provided to the samples until the H₂ consumption ceased. The amount of H₂ adsorbed on the catalyst was estimated considering the following reaction: $\text{H}_2 + 2\text{Pt} \rightarrow 2\text{PtH}$, in which 1 H atom is quimisorbed onto 1 Pt atom. The value of 0.08 nm²/atom Pt surface area and the 21.45 g.cm⁻³ Pt density was considered. Temperature-programmed reduction with hydrogen (H₂-TPR) experiments were performed in a Micrometrics Chemisorb 2705 equipment, using 50 mg of catalyst, a temperature ramp from 25 to 1100 °C at 10 °C·min⁻¹, and a flow rate of 30 mL·min⁻¹ of 5% H₂/N₂. Surface areas of the oxides were measured by N₂ adsorption/desorption cycles, according to the BET method, using a Micrometrics ASAP 2020 surface area analyzer and Porosity Analyzer.

Synthesis of Ag seeds

Ag seeds were prepared by the polyol process.³⁴ In a typical experiment, 5 g of polyvinylpyrrolidone (PVP) was dissolved in 37.5 mL of ethylene glycol. Then, AgNO₃ (200 mg, 1.2 mmol) was added and mixed until the complete dissolution. The resulting solution was heated to 125 °C for 2.5 hours, leading to the appearance of a greenish-yellow color, allowed to cool down to room temperature, and diluted to 125 mL of water.

Size controlled synthesis of Ag nanoparticles

The synthesis of Ag nanoparticles with controlled sizes was based on seed-mediated approach, in which pre-formed Ag nanoparticles were employed as physical templates for further Ag deposition. Specifically, the size of the produced Ag nanoparticles was controlled by varying the volume of a AgNO₃ aqueous solution employed during seeded growth. In a typical synthesis, a mixture containing 9.4 mL of a PVP aqueous solution (0.1% wt), 10 μL of

as-prepared Ag seeds suspensions, and 150 μL of hydroquinone aqueous solution (30 mM) was stirred at 50 $^{\circ}\text{C}$ for 10 min. Then, 43 μL of a $\text{AgNO}_{3(\text{aq})}$ was added to the reaction mixture, which was allowed to proceed at 50 $^{\circ}$ C for another 1h. Similar procedures, in which the volume of the added $\text{AgNO}_{3(\text{aq})}$ corresponded to 85, 170, and 340 μL were also performed to produce Ag nanoparticles of different sizes. After cooling down to room temperature all Ag suspensions were diluted to 10 mL with water. The Ag nanoparticles obtained by employing 43, 85, 170, and 340 μL of $\text{AgNO}_{3(\text{aq})}$ were denoted Ag 50 nm, Ag 59 nm, Ag 96 nm, and Ag 114 nm, in which these values corresponded to the obtained diameters.

Synthesis of size-controlled AgPt nanoshells

In a typical synthesis, a mixture containing 8 mL of a PVP aqueous solution (0.3 wt %), 2 mL of the each of the produced Ag NPs suspension, and hydroquinone (30 mM) were stirred at 100 $^{\circ}\text{C}$ for 10 min in a 15 mL round-bottom flask. Then, $\text{PtCl}_6^{2-}(\text{aq})$ (12 mM) was added to the reaction mixture, which was kept under 100 $^{\circ}\text{C}$ and magnetic stirring for 1 hour. When Ag 50 nm, Ag 59 nm, Ag 96 nm, and Ag 114 nm were employed as starting material, the volumes of 30 mM hydroquinone and 12 mM $\text{PtCl}_6^{2-}(\text{aq})$ corresponded to 20 and 11.2; 41.5 and 20.5; 83.0 and 39.3; and 166 and 76.8 μL , respectively. In all cases, the Ag:hydroquinone:Pt molar ratios were kept constant. The AgPt materials obtained from Ag 50 nm, Ag 59 nm, Ag 96 nm, and Ag 114 nm nanoparticles were denoted AgPt 95 nm, AgPt 105 nm, AgPt 133 nm, and AgPt 163 nm, respectively. Similarly, these values corresponded to the diameters in the obtained AgPt nanoshells. After their synthesis, all AgPt nanomaterials were washed twice with a supersaturated $\text{NaCl}_{(\text{aq})}$ solution and three times with water by successive rounds of centrifugation at 7000 rpm and removal of the supernatant. After washing, the AgPt nanomaterials were suspended in 10 mL of PVP aqueous solution (0.3 wt %).

Synthesis of 0.25 wt. % AgPt supported with SiO₂ (AgPt/SiO₂)

The incorporation of AgPt nanoshells with controlled sizes onto the silica support (0.25 % wt, Pt basis) was performed using a wet impregnation approach.¹⁴⁹ Typically, a suspension containing the AgPt nanoshells were added to a beaker containing commercial silica (SiO₂, A-175 aerosil, Degussa/Germany, specific surface area 175 m²/g). The resulting mixture was stirred at room temperature for 24 h. Then, the resulting solid was washed twice with water and twice with ethanol by successive rounds of centrifugation at 7,000 rpm and removal of the supernatant. After washing, the catalysts were dried at 120 °C for 2 h under air to produce the AgPt/SiO₂ catalysts. In order to obtain the needed amount of Pt required for the syntheses of AgPt/SiO₂ catalysts displaying 0.25 % wt in Pt basis, the syntheses of AgPt 95 nm, AgPt 105 nm, AgPt 133 nm, and AgPt 163 nm nanoshells as described above was scaled-up by 210, 81, 35 and 18 folds, respectively.

Catalytic oxidation of volatile organic compounds (VOC)

The catalytic oxidation of volatile organic compounds was performed using the AgPt/SiO₂ as catalysts. The catalytic experiments were performed in a fixed bed tubular quartz reactor under atmospheric pressure using benzene, toluene and o-xylene (BTX) as model molecules. The following conditions were chosen: 0.030 g catalyst, inlet benzene (1.2 g.m⁻³), toluene (0.7 g.m⁻³), o-xylene (0.5 g.m⁻³) in air and temperature range 25-300 °C. The reaction data were collected after at least 2 h on-stream at room temperature. The reaction products were determined by GC-MS. The reactant and product mixtures were analyzed using two on-line gas chromatographs equipped with FID and TCD detectors and an HP-5 column. The performances of the catalysts were studied towards the complete oxidation of benzene, toluene, and o-xylene by atmospheric air. The catalytic activity was expressed in terms of the

conversion (%) of benzene, toluene and o-xylene, respectively. The conversion of the BTX compounds was calculated using the equation 1:

$$\text{CBTXs (\%)} = ([\text{BTXs}]_{\text{in}} - [\text{BTXs}]_{\text{out}}) \cdot 100 / [\text{BTXs}]_{\text{in}} \quad (1)$$

where CBTXs (%) = percentage of BTX conversion; $[\text{BTXs}]_{\text{in}}$ = input quantity and $[\text{BTXs}]_{\text{out}}$ = output quantity.

6.3. Results and discussion

Our studies started with the synthesis of Ag NPs displaying controlled sizes by a seed-mediated approach, in which relatively monodisperse Ag NPs displaying 33 ± 3 nm in diameter (Figure 6.1) obtained by a polyol approach^{34,110} were employed as physical templates for additional Ag deposition (Figure 6.2).

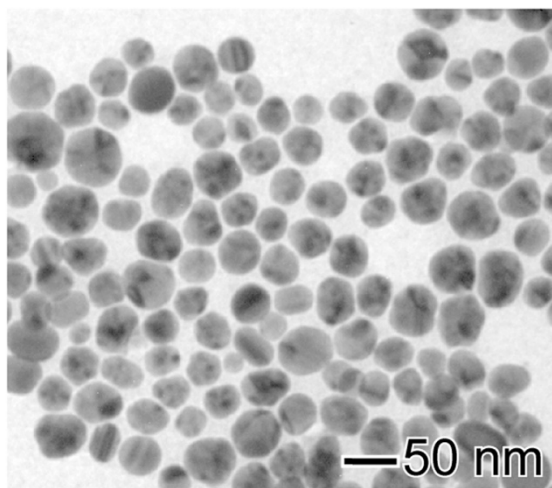


Figure 6.1. TEM image for Ag NPs employed as templates for the synthesis of Ag nanoparticles with different sizes as a function of the volume of $\text{Ag}^+_{(\text{aq})}$ added to the reaction.

In this case, by varying the amount of Ag^+ precursor employed during seeded growth, Ag NPs having different outer diameters were obtained. These Ag NPs were then employed as

starting materials for the synthesis of AgPt nanoshells by a galvanic replacement reaction between Ag and $\text{PtCl}_6^{2-}(\text{aq})$ and $\text{PtCl}_6^{2-}(\text{aq})$ in the presence of hydroquinone as a co-reducing agent. Specifically, we were interested in controlling size and surface morphology of the AgPt nanoshells by employing Ag NPs of different sizes as the starting materials, followed by the investigation on how the catalytic activities were dependent upon these parameters. For instance, would AgPt nanoshells having smaller outer diameters lead to better catalytic performances as intuitively expected (that particles having larger outer diameters tend to present poorer catalytic activities due to their lower surface to volume ratios as compared to smaller particles)?

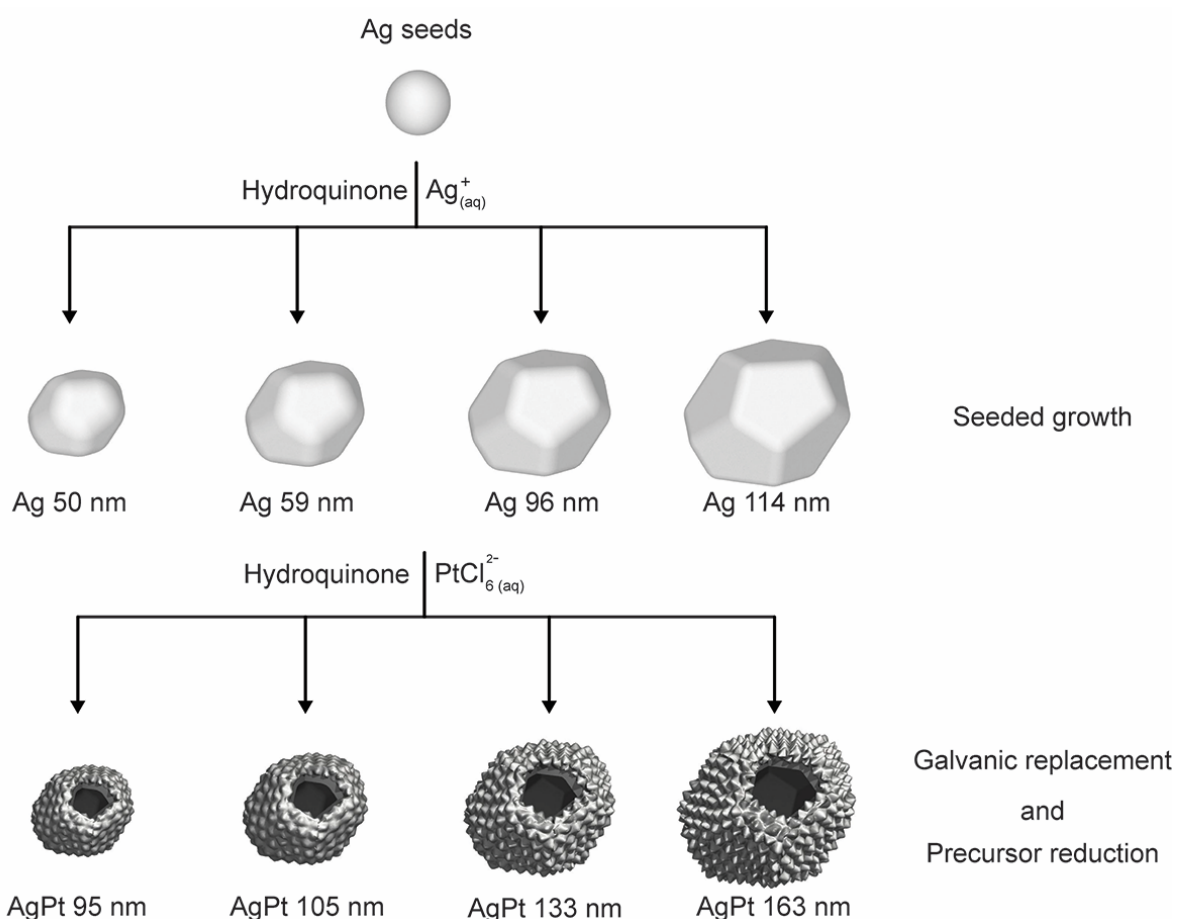


Figure 6.2. Schematic showing the syntheses of Ag nanoparticles with controlled sizes by Ag deposition over preformed Ag NPs, and AgPt nanoshells by galvanic replacement reaction between $\text{PtCl}_6^{2-}(\text{aq})$ and the respective Ag nanoparticle. Both approaches were performed using PVP as the stabilizer and water as solvent.

Figure 6.3A-D display SEM images for Ag NPs having controlled sizes obtained by seeded growth varying the volume of $\text{Ag}^+_{(\text{aq})}$ added to a suspension containing Ag NPs seeds (Figure 6.1), PVP, and hydroquinone. A progressive increase in the size of the Ag nanoparticles as a function of the volume of a 12 mM $\text{Ag}^+_{(\text{aq})}$ employed during seeded growth could be clearly detected. Specifically, the size of the Ag NPs corresponded to 50 ± 6 (Figure 6.3A), 59 ± 4 (Figure 6.3B), 96 ± 9 (Figure 6.3C), and 114 ± 17 nm (Figure 6.3D) when the volume of a 12 mM $\text{Ag}^+_{(\text{aq})}$ employed during seeded growth was 43, 85, 170, and 340 μL , respectively. The corresponding histograms of size distribution are shown in Figure 6.4A-D. As compared to the initial Ag seeds (33 nm, Figure 6.1), the average size of the obtained Ag NPs increased by 17 nm (52 %), 26 nm (79 %), 63 nm (191 %), and 81 nm (246 %), for Ag 50, 59, 96, and 114 nm, respectively. Also, a gradual appearance of faceted surfaces could be observed with the increase in size resulting in polyhedral Ag nanoparticles. The exposure of surface facets is often observed for *fcc* metals at sizes > 20 nm due to the minimization of their surface free energy.¹⁶⁶⁻

168

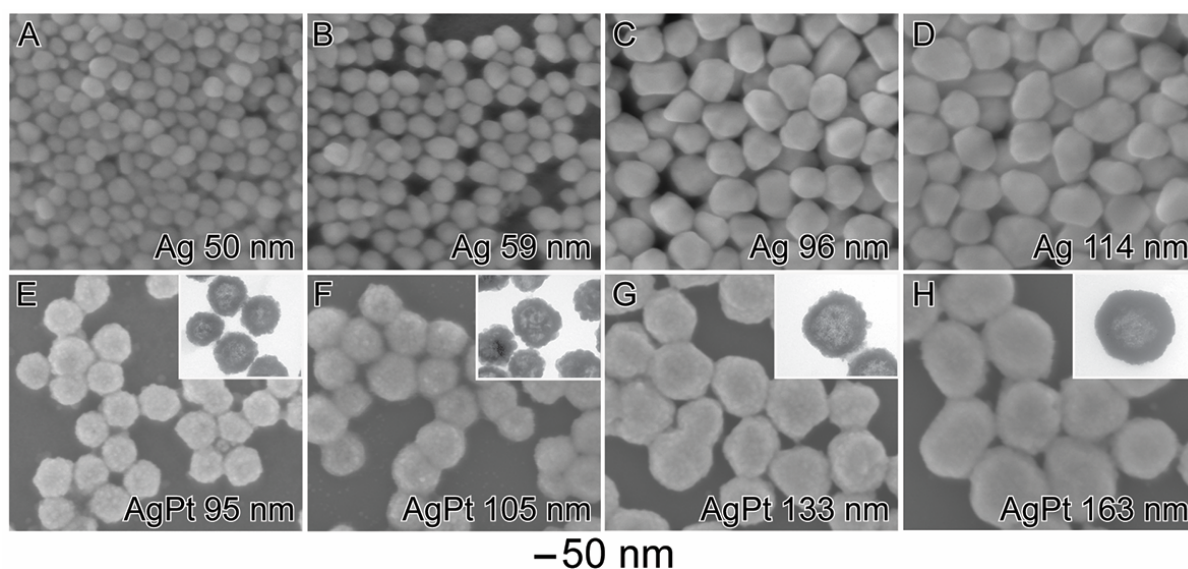


Figure 6.3. (A-D) SEM images for Ag NPs with controlled sizes obtained by varying the volume of $\text{Ag}^+_{(\text{aq})}$ added to a suspension containing preformed Ag NPs, PVP, and hydroquinone: (A) 43 μL , (B) 86 μL , (C) 172 μL , and (D) 344 μL . (E-H) SEM images for AgPt nanoshells with controlled sizes obtained by the addition of $\text{PtCl}_6^{2-}_{(\text{aq})}$ to a suspension containing the respective Ag nanoparticle, PVP, and hydroquinone. The insets in the figure correspond to TEM images.

After the synthesis of Ag nanoparticles having controlled sizes in the 50-114 nm range, we turned our attention to their utilization as starting materials to AgPt nanoshells by a combination of galvanic replacement reaction with $\text{PtCl}_6^{2-}(\text{aq})$ in the presence of hydroquinone. Figure 6.3E-H depict SEM and TEM (insets) images of the AgPt nanoshells employing the Ag nanoparticles depicted in Figure 6.3A-D, respectively, as templates. In all AgPt materials, the formation of rough surfaces comprised by small nanoparticle islands could be observed. In addition, the formation of hollow interiors could be clearly identified due to the brighter mass-thickness contrast at the center of each nanostructure (TEM insets). The size (outer diameter) of the AgPt nanoshells depicted in Figure 6.3E-H corresponded to 95 ± 7 , 105 ± 7 , 133 ± 8 , and 163 ± 11 nm, respectively (histograms of size distribution are shown in Figure 6.4E-H, respectively).

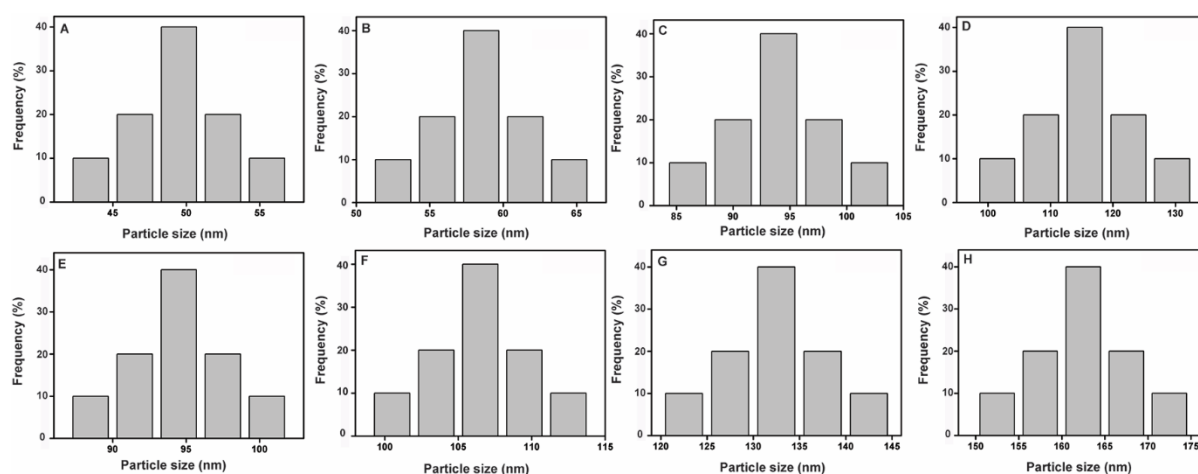


Figure 6.4. Histograms showing the size distribution for the obtained Ag nanoparticles (first row) A, B, C, and D for Ag 50 nm, Ag 59 nm, Ag 96 nm, and Ag 114 nm, respectively; and AgPt nanoshells (second row) E, F, G, and H for AgPt 95 nm, AgPt 105 nm, AgPt 133 nm, and AgPt 163 nm, respectively.

Therefore, these AgPt nanoshells were denoted AgPt 95, AgPt 105, AgPt 133, and AgPt 163 nm, respectively. In addition to the outer diameters, the shell thicknesses corresponded to ~19, 21, 24, and 44 nm for the AgPt 95, AgPt 105, AgPt 133, and AgPt 163 nm, respectively. These results indicate that, in all cases, a significant growth was observed in the AgPt

nanoshells relative to their Ag NPs employed as starting materials as depicted in Figure 6.5. More specifically, a growth of 45 nm (90 %), 46 nm (78 %), 37 nm (39 %), and 49 nm (43 %) was detected for AgPt 95, AgPt 105, AgPt 133, and AgPt 163 nm, respectively, relative to their corresponding initial Ag nanoparticles.

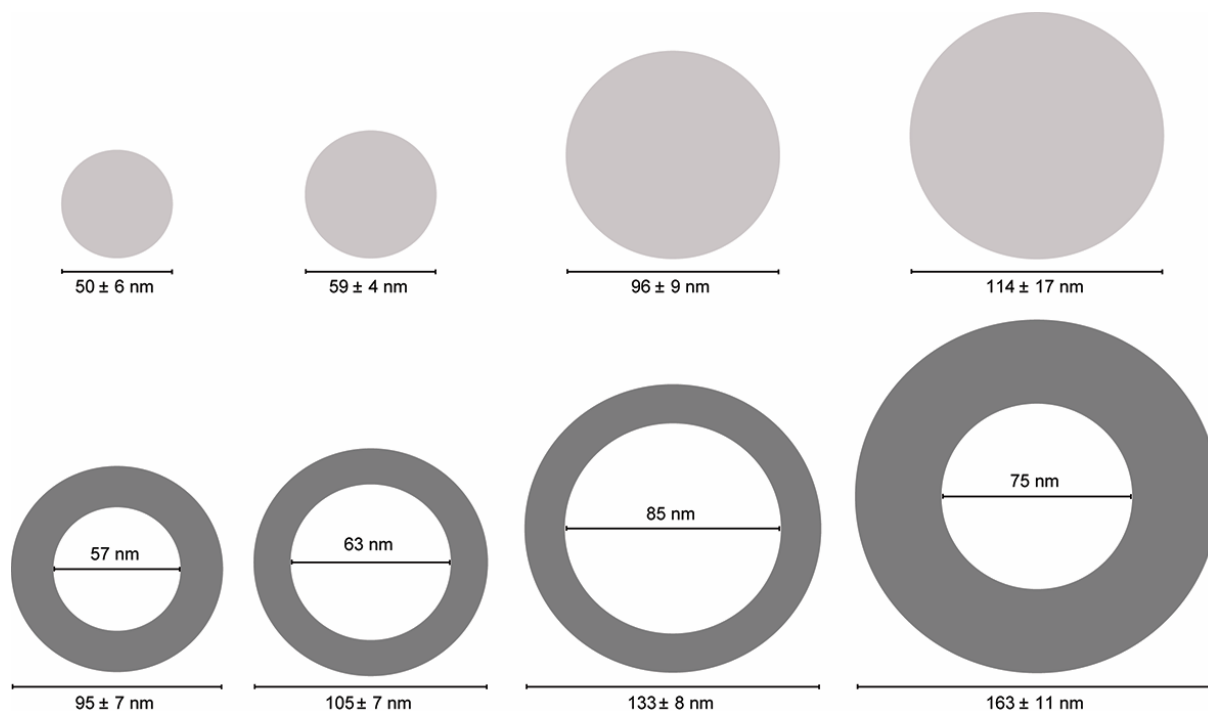


Figure 6.5. Scheme showing the average outer diameters for Ag nanoparticles with controlled sizes (top row) and average outer and inner diameters for the AgPt nanoshells (bottom row).

The Pt at. % in the AgPt nanoshells, as determined by ICP-OES analyses (Table 6.1), corresponded to 32, 53, 57, and 58 % for AgPt 95, AgPt 105, AgPt 133, and AgPt 163 nm, respectively.

Table 6.1. Containing of Ag and Pt in the AgPt nanoparticles obtained by ICP-OES.

Sample	Ag (mol %)	Pt (mol%)
AgPt 95 nm	68	32
AgPt 105 nm	47	53
AgPt 133 nm	43	57
AgPt 163 nm	42	58

Interestingly, it was observed that the AgPt 95 nm nanoshells presented lower Pt (%) relative to the larger AgPt materials. Theoretically, similar nanoparticle compositions would be expected when the Ag:PtCl₆²⁻_(aq) molar ratio was kept the same. It is plausible that the smaller Pt (%) in the AgPt 95 nm nanoshells could be explained as a result of the alloying process between Ag and Pt atoms, which is strongly dependent on the particle size. In this case, a higher the rate of alloying could lead to an increase in the stability of Ag atoms at the nanoparticle, preventing their oxidation and sub-sequential removal by the galvanic replacement with PtCl₆²⁻_(aq) ions.^{169–171}

In order to gain further insights into the morphological features of the AgPt nanoshells, the AgPt 95 and 163 nm nanoshells (nanoshells having the smaller and the larger outer diameters) were analyzed by HRTEM as shown in Figure 6.6. It can be observed that the AgPt 95 nm nanoshells displayed hollow interiors and a rough surface comprised of several NPs islands that were ~ 10 nm in size uniformly deposited over the surface of the material (Figure 6.6A and 6.6B). While the hollow interiors and rough surfaces comprised of small nanoparticle island were also detected for the AgPt 163 nm nanoshells, the size of the nanoparticle islands at the surface corresponded to 4 nm (Figure 6.6D and 6.6E). This indicates that, despite their large overall diameters, the larger AgPt nanoshells were comprised of smaller nanoparticles islands at their surface. Phase-contrast HRTEM images for the AgPt 95 and 163 nm nanoshells (Figure 6.6B and 6.6E, respectively) indicate that the individual nanoparticle islands are single-crystalline, while the entire material is polycrystalline. In this case, the ~0.22 nm lattice spacing assigned to the Pt {111} could be detected. As the same concentration of Ag seeds was employed in the synthesis of all AgPt nanoshells, larger Ag NPs seeds enable the exposure of a larger number of nucleation sites for Pt deposition relative to smaller seeds, contributing to the formation smaller Pt NPs islands at the surface of the nanoshells. Moreover, as the Ag:hydroquinone:Pt molar ratios were kept constant during the syntheses, Ag seeds having

larger sizes required increased amounts of Pt, which led to the detected increase in wall thickness with the size of Ag NPs employed as seeds.

Figure 6.6C and 6.6F depict the EDX spectra for nanoshells 95 and 163 nm, respectively, registered from the regions highlighted by the red dashed rectangles in Figure 6.6A and 6.6D, respectively. Interestingly, the Pt at. % at the surface of the nanoshells corresponded to 31 and 58 %, which are in agreement with the ICP-OES data. This also demonstrates that Ag is present at the surface of the nanoshells, indicating that Ag can migrate/diffuse along the Pt lattice in agreement to what has been reported by our group in both AgPt and AgAu systems.^{1,104,116,172}

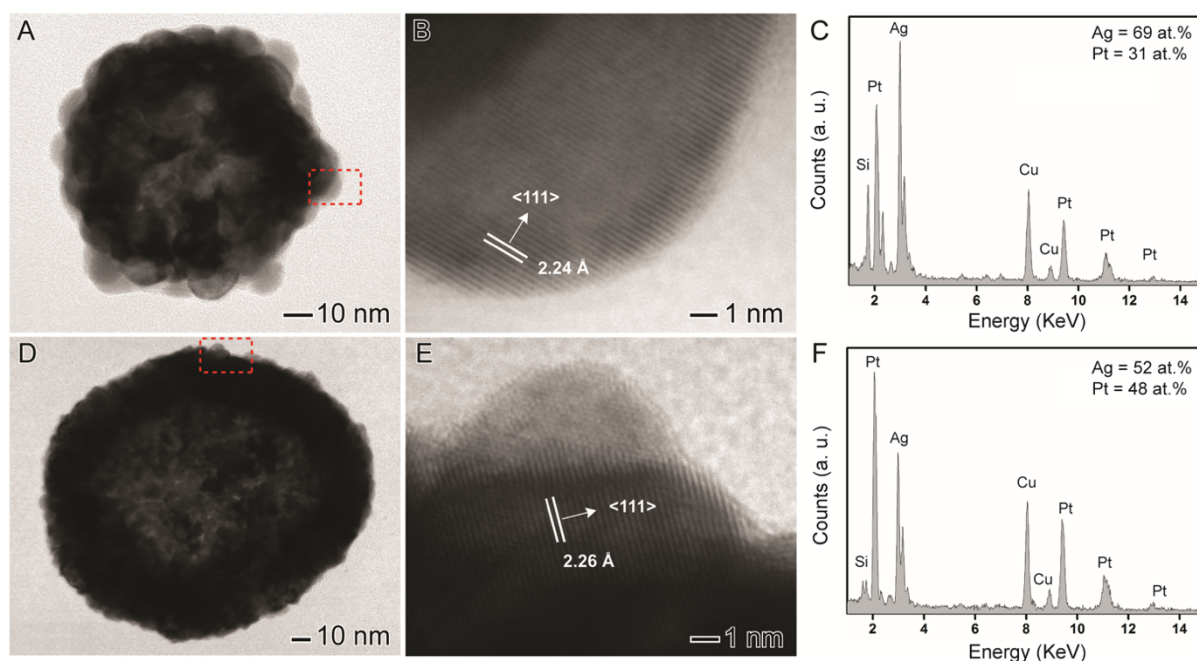


Figure 6.6. HRTEM images for the AgPt-95 (A and B) and AgPt-163 (D and E) AgPt nanoshells obtained after 1 h following the addition of $\text{PtCl}_6^{2-}(\text{aq})$ to a suspension containing Ag NPs, PVP, and hydroquinone. While (A and D) depicts individual nanoparticles, (B and E) show zoom-in images of the areas highlighted in red. (C and F) Depict the EDX spectra for the AgPt nanoshells showed in A and D, respectively.

In order to evaluate the role played by hydroquinone over the formation of the nanoshells, we performed control experiments in the absence of hydroquinone (conventional galvanic replacement reaction) as shown in Figure 6.7.

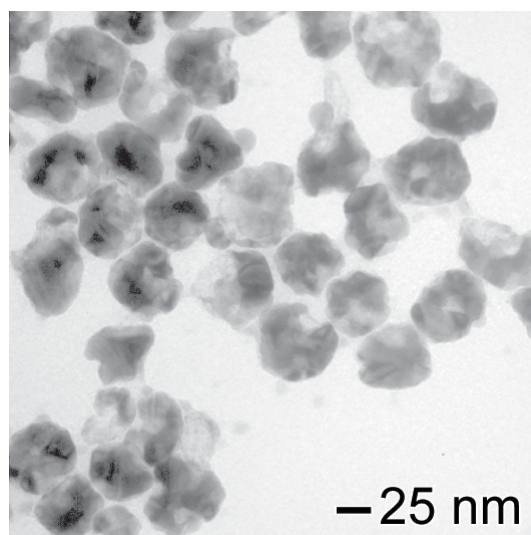


Figure 6.7. TEM image for AgPt nanoshells obtained by the addition of $\text{PtCl}_6^{2-}(\text{aq})$ to a suspension containing the Ag 50 nm nanoparticle and PVP under absence of hydroquinone.

In this case, we employed Ag NPs 50 nm as the starting material. The presence of smoother surfaces as compared to those obtained in the presence of hydroquinone (Figure 6.3E) could be detected. Moreover, in the absence of hydroquinone, the formation of AgPt nanoshells 53 ± 6 nm in outer diameter took place. Thus, the AgPt nanoshells obtained by the conventional galvanic reaction in the absence of hydroquinone presented similar sizes (overall diameter) compared to the starting Ag NPs. This observation further confirms that the increase in size and change of morphology for the formation of AgPt nanoshells in the presence of hydroquinone took place by a combination of two processes: *i*) galvanic replacement reaction between the Ag nanoparticle and $\text{PtCl}_6^{2-}(\text{aq})$ that lead to the dissolution of Ag from the cores and together with Pt deposition; and *ii*) $\text{PtCl}_6^{2-}(\text{aq})$ to Pt reduction by hydroquinone that leads to further deposition of Pt at the surface leading to increased outer diameters and the formation of nanoparticle islands at the surface.^{10,116,173}

The formation of AgPt nanoshells displaying controlled sizes was also monitored by UV-VIS spectroscopy and XRD analyses as shown in Figure 6.8. Figure 6.8A shows the extinction spectra for the Ag NPs. The Ag 50 nm NPs displayed an extinction peak centered at ~ 428 nm assigned to the dipolar mode of the surface plasmon resonance excitation (SPR).¹⁷⁴

This peak gradually red-shifted to longer wavelengths with the increase in size, which is in agreement with the increased charge separation during plasmon oscillation at larger sizes.^{175,176} Specifically, the Ag 59, 96, and 114 nm NPs displayed SPR peaks centered at 436, 448, and 453 nm, respectively. On the other hand, no SPR extinction signals assigned to Ag were detected in all AgPt nanoshells (Figure 6.8B), which is agreement with the Ag dissolution from the cores to yield hollow interiors as well as Pt deposition at the surface of the nanostructures.¹¹⁶

The XRD diffractograms for Ag NPs is shown in Figure 6.8C. It can be observed that the main peaks assigned to Ag become sharper with the increase in size, indicating that the size of the crystallites increase as a function of the outer diameter. Upon the formation of AgPt nanoshells (Figure 6.8D), a decrease in all crystallite sizes could be observed which manifested itself by the presence of broader diffraction peaks as compared to each corresponding initial Ag NPs, in agreement with the formation of AgPt nanoshells. As the Pt lattice has a 3.9 % mismatch with Ag (both have *fcc* lattice), the XRD diffraction peaks for these two species could not be resolved under our experimental conditions.¹⁷⁷

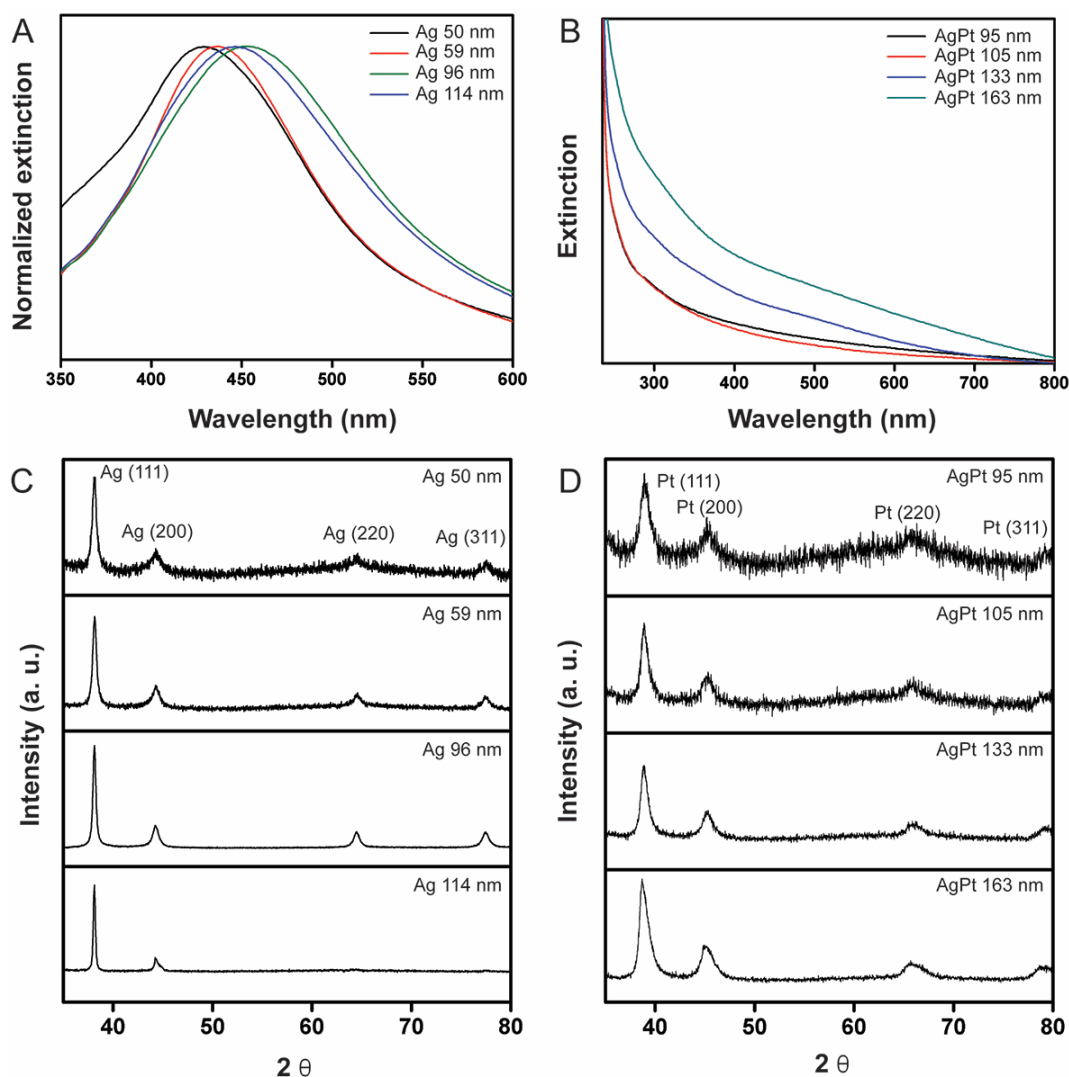


Figure 6.8. UV–VIS extinction spectra recorded from aqueous suspensions containing the obtained Ag nanoparticles (A) and AgPt nanoshells (B) with controlled sizes. X-ray diffraction patterns for the obtained Ag nanoparticles (C) and AgPt nanoshells (D) with controlled sizes.

After the synthesis of AgPt nanoshells with controlled sizes, we investigated their catalytic properties as a function of their size and surface morphology. In particular, we were interested in the catalytic activities towards the gas phase oxidation of volatile organic compounds (to benzene, toluene, and *o*-xylene). To this end, the produced AgPt nanoshells were supported onto commercial SiO₂ by wet impregnation to yield AgPt/SiO₂ solid catalysts. We focused on commercial SiO₂ because this support is inert towards BTX oxidation. Therefore, it enables us to isolate and probe the effect of size and surface morphology of the AgPt nanoshells over their catalytic performance, which is the main goal of this study. It is

important to note that all the supported catalysts (AgPt/SiO_2) were prepared so that they had the same Pt loading, which corresponded to 0.25 wt. %. This enabled us to exclude the effect of the compositional variations in the nanoshells over the performance. Figure 6.9 shows SEM images for the produced AgPt/SiO_2 catalysts. In all cases, the Pt loading corresponding to only 0.25 wt. %. It can be observed that all AgPt nanoshells (AgPt 95, 105, 133, and 163 nm) could be uniformly incorporated and distributed over the entire SiO_2 surface without any agglomeration. The solid catalysts were denoted $\text{AgPt 95 nm}/\text{SiO}_2$ (Figure 6.9A), $\text{AgPt 105 nm}/\text{SiO}_2$ (Figure 6.9B), $\text{AgPt 133 nm}/\text{SiO}_2$ (Figure 6.9C), and $\text{AgPt 163 nm}/\text{SiO}_2$ (Figure 6.9D) according to the size of the supported AgPt nanoshells.

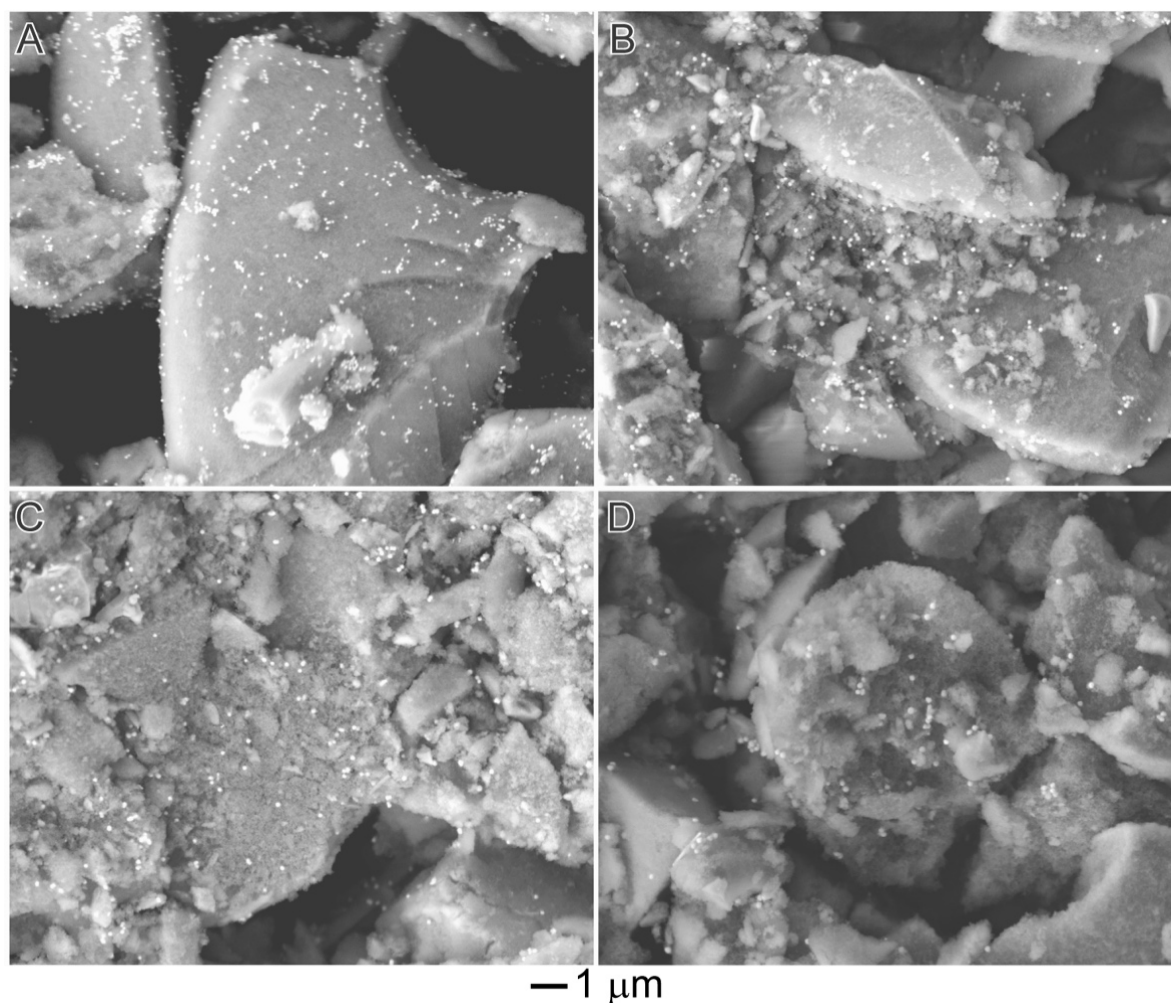


Figure 6.9. SEM images of (A) $\text{AgPt 95 nm}/\text{SiO}_2$, (B) $\text{AgPt 105 nm}/\text{SiO}_2$, (C) $\text{AgPt 133 nm}/\text{SiO}_2$, and (D) $\text{AgPt 163 nm}/\text{SiO}_2$ catalysts obtained by the wet impregnation of the AgPt nanoshells onto commercial SiO_2 . The Pt loading in all catalysts corresponded to 0.25 wt. %.

The AgPt/SiO₂ catalysts materials were further characterized XRD, H₂-TPR, N₂ physisorption, and H₂ chemisorption. The XRD analyses (Figure 6.10) indicated that the silica support was partially crystalline due the presence of well-defined peaks assigned to α -cristobalite and tridimite phases. After the deposition of AgPt, the XRD profiles for AgPt/SiO₂ were comprised of a mixture of SiO₂ and AgPt signals, suggesting that no destruction of both the SiO₂ and AgPt structures were observed after the impregnation process, which is in agreement with the SEM data (Figure 6.9).

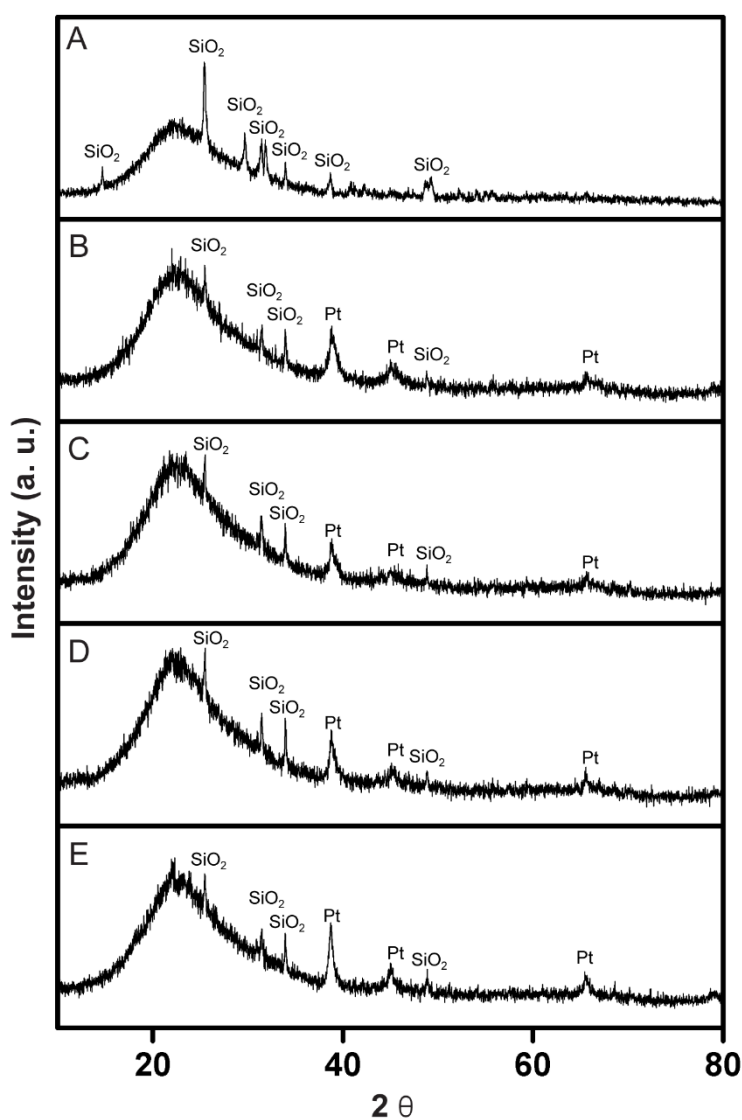


Figure 6.10. X-ray diffraction patterns for the (A) pure commercial SiO₂, (B) AgPt 95 nm/SiO₂, (C) AgPt 105 nm/SiO₂, (D) AgPt 133 nm/SiO₂, and (E) AgPt 163 nm/SiO₂ catalysts.

Table 6.1 shows the values of the textural features for the SiO₂ support and the AgPt/SiO₂ catalysts. The specific surface area for all materials measured by N₂ physisorption was between 145 - 155 m².g⁻¹. Also, the total volume of pores was in the 0.68 – 0.70 cm³.g⁻¹ range and average pore diameter was in the 17.5 – 18.8 nm range. These results indicated that no significant modification in SiO₂ support took place after AgPt incorporation, illustrating the robustness of our employed approach for the synthesis of supported catalysts. H₂ chemisorption was employed to estimate the Pt surface area in all catalysts, which corresponded to 6.29, 6.92, 7.44, and 7.96 μmol per gram for AgPt 95/SiO₂, AgPt 105/SiO₂, AgPt 133/SiO₂ and AgPt 163 nm/SiO₂, respectively. It is noteworthy that the same Pt loading was employed in these measurements, suggesting an increase in the Pt surface area with outer diameters. Moreover, relatively high values of metallic dispersion were observed in all cases, which corresponded to 49, 54, 58, and 63 % for AgPt 95, 105, 133 and 163 nm, respectively. This result illustrates that our employed approach leads to high Pt exposition (> 49 %), potentially enabling the optimization of catalytic performances.^{116,135,136} As demonstrated in Figure 6.6, it is plausible that the increase in the surface area for the nanoshells presenting larger outer diameters may be related to the fact that the larger nanoshells are comprised of smaller NPs islands deposited at their surface (4 and 10 nm in the AgPt 163 and 95 nanoshells, respectively).

Table 6.1. Surface properties of AgPt/SiO₂ catalysts obtained by N₂ physisorption and H₂ chemisorption.

Sample	Surface area (m²/g)	Total volume of pores (cm³/g)	Average pore diameter (nm)	Metallic area (μmol/g catalyst)	Metallic dispersion (%)
SiO₂	155	0.70	18.1	-	-
AgPt-95/SiO₂	156	0.68	17.5	6.29	49
AgPt-105/SiO₂	149	0.70	18.8	6.92	54
AgPt-133/SiO₂	153	0.70	18.2	7.44	58
AgPt-163/SiO₂	145	0.68	18.3	7.96	63

Figure 6.11 shows the N₂-adsorption–desorption isotherms for all AgPt/SiO₂ catalysts, which corresponded to type IV profiles and hysteresis loop type H1 (in the IUPAC classification), which are typical of mesoporous materials (SiO₂). All isotherms presented a similar behavior in agreement with the fact that no structural modifications were detected after AgPt deposition over the SiO₂ support.

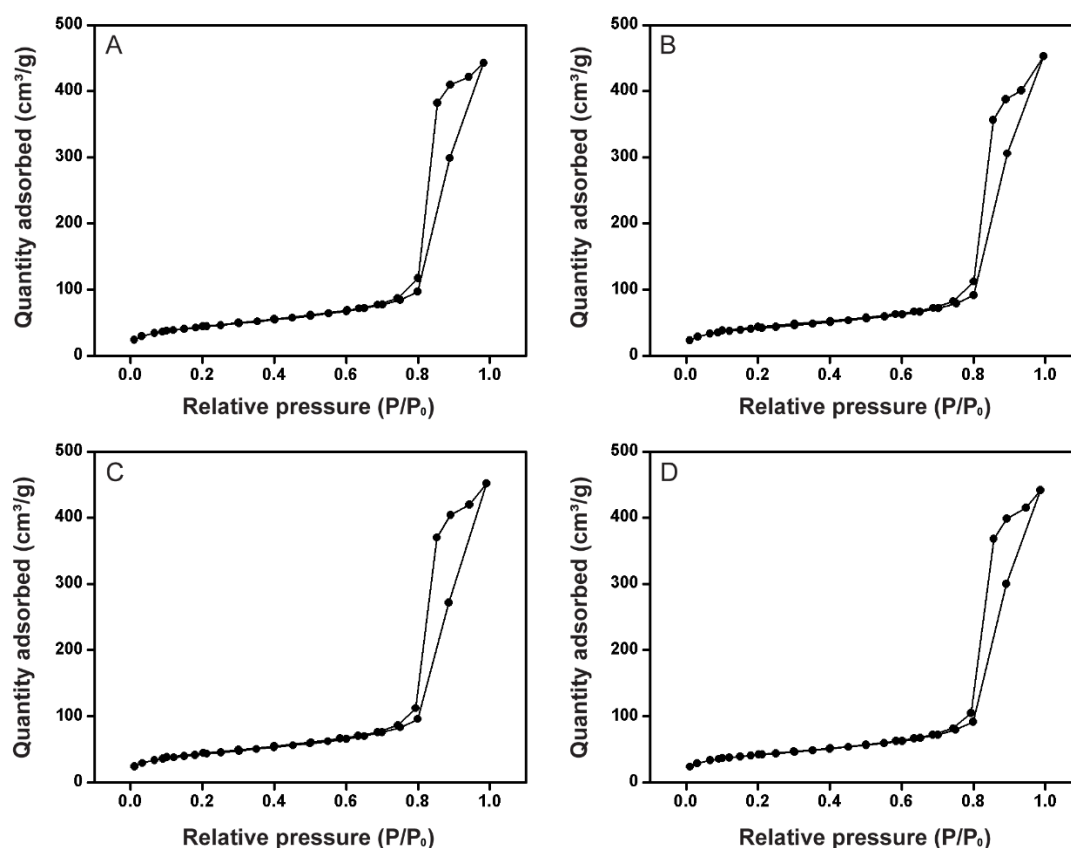


Figure 6.11. Adsorption/desorption N₂ isotherms for (A) AgPt 95 nm/SiO₂, (B) AgPt 105 nm/SiO₂, (C) AgPt 133 nm/SiO₂, and (D) AgPt 163 nm/SiO₂ catalysts.

The H₂-TPR analyses (Figure 6.12) showed an intense peak of H₂ consumption centered 907 °C for pure SiO₂ attributed to the reduction of SiO₂ phases.¹⁷⁸ After AgPt incorporation, this peak completely disappeared indicating an effective interaction between AgPt nanostructures and the SiO₂ support. This behavior is extremely important in catalysis, as several examples have been reported on the enhancement of catalytic activities due to metal support interactions.^{94,179–181}

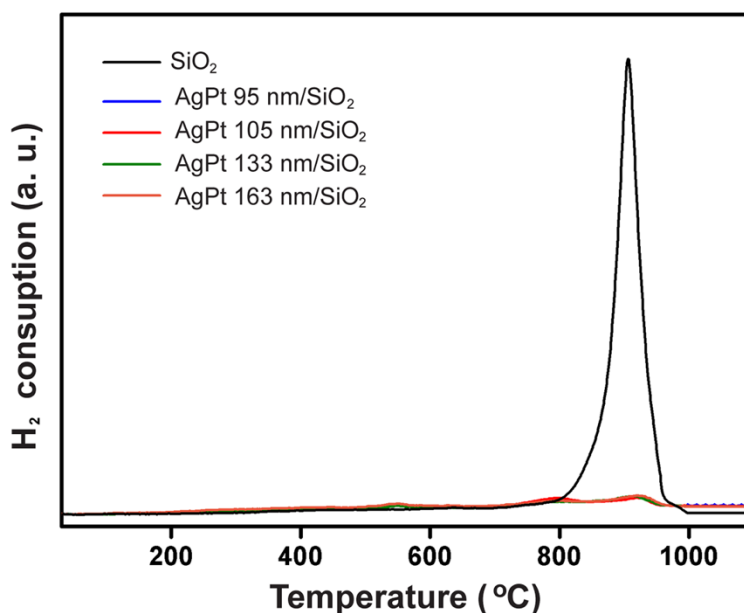


Figure 6.12. (A) TPR profiles for pure SiO₂ (black trace), AgPt 95 nm/SiO₂ (blue trace), AgPt 105 nm/SiO₂ (red trace), AgPt 133 nm/SiO₂ (green trace), and AgPt 163 nm/SiO₂ (orange trace).

Figure 6.13 shows the conversion percentages (%) for BTX oxidation as a function of temperature employing the AgPt/SiO₂ as solid catalysts. Only H₂O and CO₂ were detected as products from BTX oxidation in all cases. As expected, the BTX % conversion increased with reaction temperature, and the reactivity of the substrates followed the order: benzene > toluene > o-xylene in agreement with previous reports on BTX oxidation.^{116,152,161} It can be observed that the conversion % for the AgPt/SiO₂ catalysts increased with size in all temperatures. For instance, at 450 °C, the conversion % for benzene oxidation corresponded to 54, 57, 62, and 79 % for AgPt 95 nm/SiO₂, AgPt 105 nm/SiO₂, AgPt 133 nm/SiO₂, and AgPt 163 nm/SiO₂, respectively. This is in agreement with the H₂ chemisorption results, and can be assigned to the increase in the Pt surface area with size due to the presence of smaller NPs islands at the surface of the nanoshells having larger outer diameters. It is plausible that other factors, in addition to the increased surface areas, could also be involved in the catalytic performances. For instance, taking the AgPt 95/SiO₂ catalyst as a reference, an increase in surface area of 10, 18, and 27% was observed for AgPt 105/SiO₂, AgPt 133/SiO₂, and AgPt 163 nm/SiO₂, respectively.

According to the BTX conversion results, an increase in the benzene conversion of 6, 14, and 42 % was detected for AgPt 105/SiO₂, AgPt 133/SiO₂ and AgPt 163 nm/SiO₂, respectively, relative to AgPt 95/SiO₂. Although this demonstrates a relatively good correlation/proportionality between Pt surface area and percentages of BTX conversion, it is expected that smaller Pt NPs islands would display increased surface energy/reactivity as well as a larger exposure of defect sites and high index faces relative to their larger counterparts, which could further enhance their catalytic performances. These results indicate that, in addition to the overall diameters, the control over the surface morphology may play an important role over the optimization of catalytic activities in metal-based nanocatalysts, which can be even more pronounced than the size effect.³¹ This is in agreement with our previous report that showed that the surface morphology was relevant to the optimization of catalytic activities in AgPt nanoshells having similar sizes, in which nanoshells having smooth surfaces displayed increased performances relative to nanoshells with rough surfaces.³¹ Here, all catalysts presented similar crystallinities. Thus, we believe that the crystallinity of the NPs should not affect the observed variations in the catalytic performances.

We also investigated the catalytic stabilities of the AgPt/SiO₂ catalysts towards benzene oxidation, at 450 °C, for 40 h as illustrated in Figure 6.13E. It can be observed that no significant loss of catalytic activity was detected even after 40 h. For instance, a drop from 80 to only 71 % in benzene conversion was detected for the AgPt 163 nm/SiO₂ catalyst (11 % drop in activity). For AgPt 95 nm/SiO₂, AgPt 105 nm/SiO₂, and AgPt 133 nm/SiO₂, the drop in catalytic activity after 40 h corresponded to 17, 20, and 21 %, respectively.

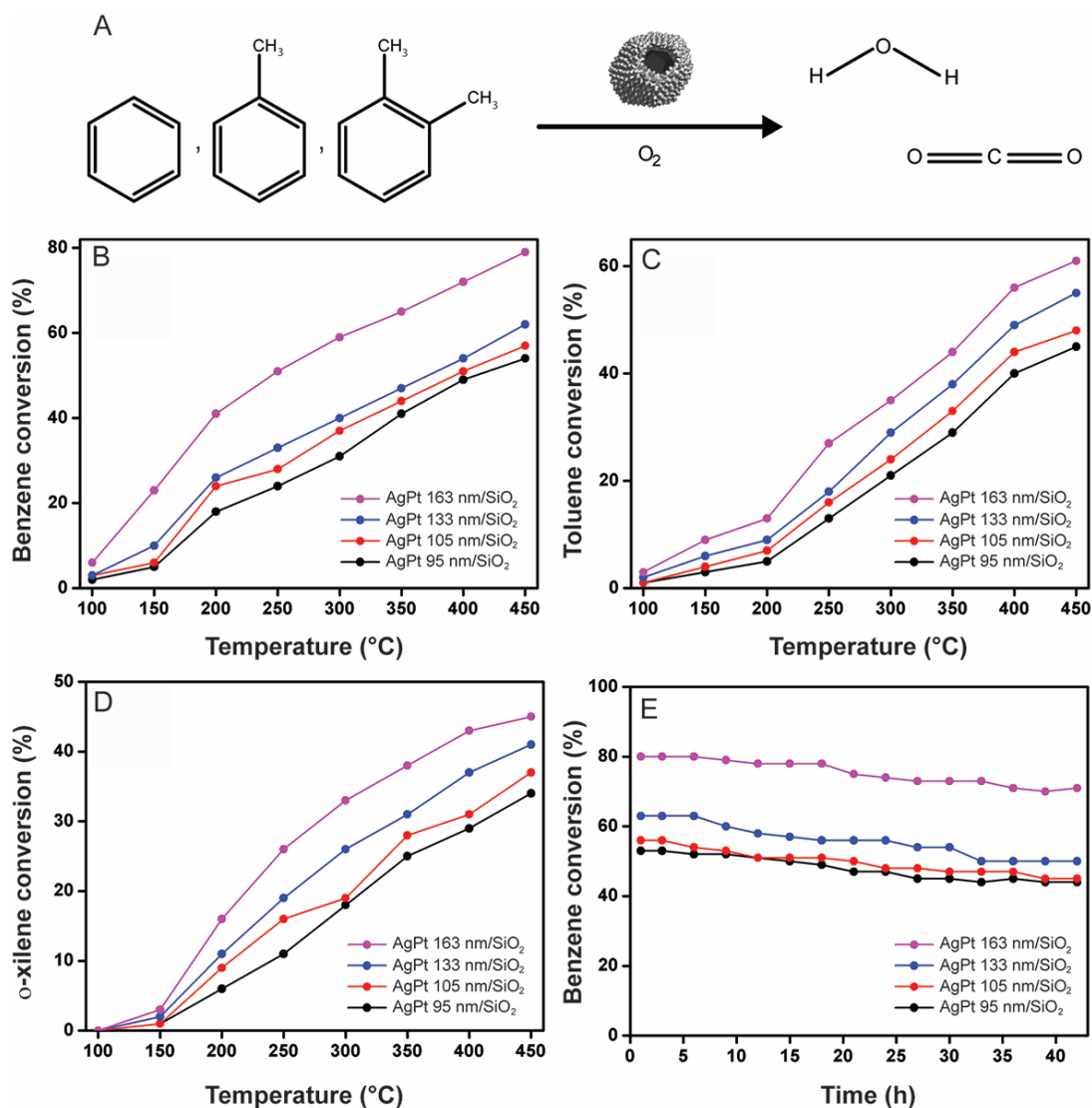


Figure 6.13. (A) Scheme for benzene, toluene, and *o*-xylene oxidation employing AgPt/SiO₂ as catalysts. Conversion percentages of benzene (B), toluene (C), and *o*-xylene oxidation (D) as a function of temperature catalyzed by AgPt/SiO₂. (E) Stability experiments for all AgPt/SiO₂ catalysts over benzene oxidation at 450 °C.

Furthermore, as depicted in Figure 6.14, the overall morphology of all AgPt catalysts remained unchanged even after 40 h of reaction at 450 °C, showing that these materials may represent promising candidates for gas-phase catalytic applications. It is noteworthy that all AgPt/SiO₂ catalysts displayed no loss of catalytic activity and remained stable and well-dispersed over the surface of the commercial silica support without any agglomeration even after 40 h of reaction at 450 °C. At this point, if any significant morphological changes took place, a decrease in activity would be expected.

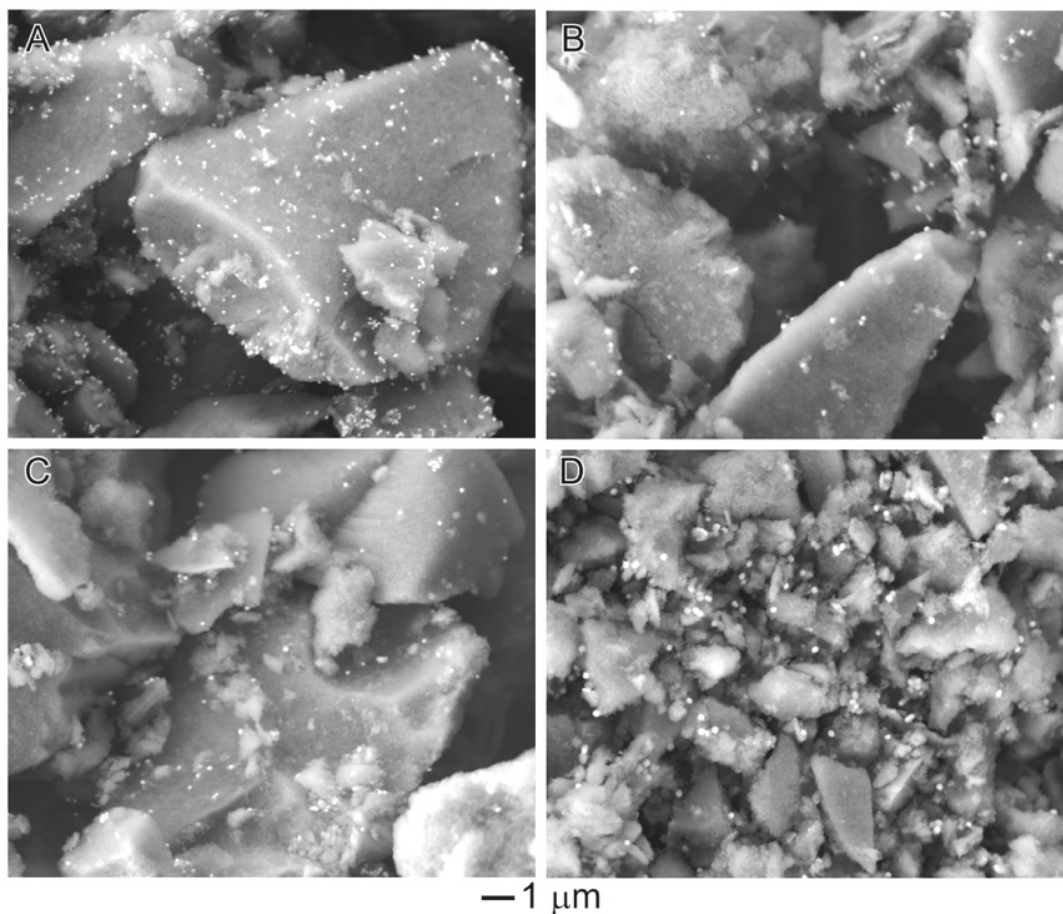


Figure 6.14. SEM images of (A) AgPt 95 nm/SiO₂, (B) AgPt 105 nm/SiO₂, (C) AgPt 133 nm/SiO₂, and (D) AgPt 163 nm/SiO₂ catalysts after the stability experiments at 5000x magnification.

6.4. Conclusion

We described herein a systematic investigation on the catalytic properties of solid catalysts comprised of AgPt nanoshells supported onto commercial SiO₂ as a function of the size of the Ag nanoparticles employed as starting materials for the synthesis of the nanoshells. The AgPt nanoshells were obtained by a galvanic replacement reaction between Ag and PtCl₆²⁻ coupled with Pt reduction by hydroquinone. By varying the size of the starting Ag NPs, AgPt nanoshells having different outer diameters, shells thicknesses, and nanoparticle-sized islands at the surface were obtained. The use of larger Ag nanoparticles as starting materials led to larger and thicker nanoshells, but that were comprised of smaller nanoparticles islands at the

surface. The catalytic activities towards BTX oxidation revealed that the catalytic activities increased with the nanoshells outer diameter, indicating that the presence of smaller nanoparticle islands at the surface surpassed the increase in outer diameter and shell thickness towards the enhancement of Pt surface area and thus catalytic activities. This result indicates that the control over surface morphology play a very important role relative to the effect of size to the optimization of catalytic performances in catalysts based on noble-metal nanostructures.

6.5. References

- (1) Hennessy, J. Catalysis: Pinpointing Platinum. *Nat Mater* **2015**, *14* (11), 1075.
- (2) Meister, T. K.; Riener, K.; Gigler, P.; Stohrer, J.; Herrmann, W. A.; Kühn, F. E. Platinum Catalysis Revisited—Unraveling Principles of Catalytic Olefin Hydrosilylation. *ACS Catal.* **2016**, *6* (2), 1274–1284.
- (3) Du, M.; Cui, L.; Cao, Y.; Bard, A. J. Mechanoelectrochemical Catalysis of the Effect of Elastic Strain on a Platinum Nanofilm for the ORR Exerted by a Shape Memory Alloy Substrate. *J. Am. Chem. Soc.* **2015**, *137* (23), 7397–7403.
- (4) Hu, Y.; Liu, Y.; Sun, Y. Mesoporous Colloidal Superparticles of Platinum-Group Nanocrystals with Surfactant-Free Surfaces and Enhanced Heterogeneous Catalysis. *Adv. Funct. Mater.* **2015**, *25* (11), 1638–1647.
- (5) Chen, A.; Holt-Hindle, P. Platinum-Based Nanostructured Materials: Synthesis, Properties, and Applications. *Chem. Rev.* **2010**, *110* (6), 3767–3804.
- (6) Hatanaka, M.; Takahashi, N.; Tanabe, T.; Nagai, Y.; Dohmae, K.; Aoki, Y.; Yoshida, T.; Shinjoh, H. Ideal Pt Loading for a Pt/CeO₂-Based Catalyst Stabilized by a Pt–O–Ce Bond. *Appl. Catal. B Environ.* **2010**, *99* (1–2), 336–342.
- (7) Martin, S.; Garcia-Ybarra, P. L.; Castillo, J. L. High Platinum Utilization in Ultra-Low Pt Loaded PEM Fuel Cell Cathodes Prepared by Electrospraying. *Int. J. Hydrogen Energy* **2010**, *35* (19), 10446–10451.
- (8) Rodrigues, T. S.; da Silva, A. G. M.; Gonçalves, M. C.; Fajardo, H. V.; Balzer, R.; Probst, L. F. D.; Camargo, P. H. C. AgPt Hollow Nanodendrites: Synthesis and Uniform Dispersion over SiO₂ Support for Catalytic Applications. *ChemNanoMat* **2015**, *1* (1), 46–51.
- (9) Park, J.; Zhang, L.; Choi, S.-I.; Roling, L. T.; Lu, N.; Herron, J. A.; Xie, S.; Wang, J.; Kim, M. J.; Mavrikakis, M.; et al. Atomic Layer-by-Layer Deposition of Platinum on Palladium Octahedra for Enhanced Catalysts toward the Oxygen Reduction Reaction. *ACS Nano* **2015**, *9* (3), 2635–2647.
- (10) Ma, L.; Wang, C.; Xia, B. Y.; Mao, K.; He, J.; Wu, X.; Xiong, Y.; Lou, X. W. (David). Platinum Multicubes Prepared by Ni²⁺-Mediated Shape Evolution Exhibit High Electrocatalytic Activity for Oxygen Reduction. *Angew. Chemie* **2015**, *127* (19), 5758–5763.
- (11) Zhang, L.; Roling, L. T.; Wang, X.; Vara, M.; Chi, M.; Liu, J.; Choi, S.-I.; Park, J.; Herron, J. A.; Xie, Z.; et al. Platinum-Based Nanocages with Subnanometer-Thick Walls and Well-Defined, Controllable Facets. *Science*. **2015**, *349* (6246), 412–416.
- (12) Rodrigues, T. S.; Silva, A. G. M.; Macedo, A.; Farini, B. W.; Alves, R. da S.; Camargo,

- P. H. C. Probing the Catalytic Activity of Bimetallic versus Trimetallic Nanoshells. *J. Mater. Sci.* **2015**, *50* (16), 5620–5629.
- (13) Silva, A. G. M.; Rodrigues, T. S.; Taguchi, L. S. K.; Fajardo, H. V.; Balzer, R.; Probst, L. F. D.; Camargo, P. H. C. Pd-Based Nanoflowers Catalysts: Controlling Size, Composition, and Structures for the 4-Nitrophenol Reduction and BTX Oxidation Reactions. *J. Mater. Sci.* **2015**, *51* (1), 603–614.
 - (14) Cao, Y.; Yang, Y.; Shan, Y.; Fu, C.; Viet Long, N.; Huang, Z.; Guo, X.; Nogami, M. Large-Scale Template-Free Synthesis of Ordered Mesoporous Platinum Nanocubes and Their Electrocatalytic Properties. *Nanoscale* **2015**, *7* (46), 19461–19467.
 - (15) Liu, Q.; Xu, Y.-R.; Wang, A.-J.; Feng, J.-J. A Single-Step Route for Large-Scale Synthesis of Core-shell Palladium@platinum Dendritic Nanocrystals/reduced Graphene Oxide with Enhanced Electrocatalytic Properties. *J. Power Sources* **2016**, *302*, 394–401.
 - (16) Vines, F.; Gomes, J. R. B.; Illas, F. Understanding the Reactivity of Metallic Nanoparticles: Beyond the Extended Surface Model for Catalysis. *Chem. Soc. Rev.* **2014**, *43* (14), 4922–4939.
 - (17) Corma, A. Heterogeneous Catalysis: Understanding for Designing, and Designing for Applications. *Angew. Chemie Int. Ed.* **2016**, n/a – n/a.
 - (18) Mellouki, A.; Wallington, T. J.; Chen, J. Atmospheric Chemistry of Oxygenated Volatile Organic Compounds: Impacts on Air Quality and Climate. *Chem. Rev.* **2015**, *115* (10), 3984–4014.
 - (19) Silvert, P.-Y.; Herrera-Urbina, R.; Duvauchelle, N.; Vijayakrishnan, V.; Elhsissen, K. T. Preparation of Colloidal Silver Dispersions by the Polyol Process. Part 1-Synthesis and Characterization. *J. Mater. Chem.* **1996**, *6* (4), 573–577.
 - (20) Petri, M. V.; Ando, R. A.; Camargo, P. H. C. Tailoring the Structure, Composition, Optical Properties and Catalytic Activity of Ag–Au Nanoparticles by the Galvanic Replacement Reaction. *Chem. Phys. Lett.* **2012**, *531*, 188–192.
 - (21) Jiang, S. P. A Review of Wet impregnation—An Alternative Method for the Fabrication of High Performance and Nano-Structured Electrodes of Solid Oxide Fuel Cells. *Mater. Sci. Eng. A* **2006**, *418* (1–2), 199–210.
 - (22) Wiley, B.; Sun, Y.; Mayers, B.; Xia, Y. Shape-Controlled Synthesis of Metal Nanostructures: The Case of Silver. *Chem. – A Eur. J.* **2005**, *11* (2), 454–463.
 - (23) Lee, Y.-J.; Schade, N. B.; Sun, L.; Fan, J. A.; Bae, D. R.; Mariscal, M. M.; Lee, G.; Capasso, F.; Sacanna, S.; Manoharan, V. N.; et al. Ultrasmooth, Highly Spherical Monocrystalline Gold Particles for Precision Plasmonics. *ACS Nano* **2013**, *7* (12), 11064–11070.
 - (24) Langille, M. R.; Zhang, J.; Personick, M. L.; Li, S.; Mirkin, C. A. Stepwise Evolution of Spherical Seeds into 20-Fold Twinned Icosahedra. *Science*. **2012**, *337* (6097), 954–957.
 - (25) Ruan, Q.; Shao, L.; Shu, Y.; Wang, J.; Wu, H. Growth of Monodisperse Gold Nanospheres with Diameters from 20 Nm to 220 Nm and Their Core/Satellite Nanostructures. *Adv. Opt. Mater.* **2014**, *2* (1), 65–73.
 - (26) Mori, H.; Komatsu, M.; Takeda, K.; Fujita, H. Spontaneous Alloying of Copper into Gold Atom Clusters. *Philos. Mag. Lett.* **1991**, *63* (3), 173–178.
 - (27) Shibata, T.; Bunker, B. A.; Zhang, Z.; Meisel, D.; Vardeman, C. F.; Gezelter, J. D. Size-Dependent Spontaneous Alloying of Au–Ag Nanoparticles. *J. Am. Chem. Soc.* **2002**, *124* (40), 11989–11996.
 - (28) Lu, X.; Tuan, H.-Y.; Chen, J.; Li, Z.-Y.; Korgel, B. A.; Xia, Y. Mechanistic Studies on the Galvanic Replacement Reaction between Multiply Twinned Particles of Ag and HAuCl₄ in an Organic Medium. *J. Am. Chem. Soc.* **2007**, *129* (6), 1733–1742.

- (29) Slater, T. J. A.; Macedo, A.; Schroeder, S. L. M.; Burke, M. G.; O'Brien, P.; Camargo, P. H. C.; Haigh, S. J. Correlating Catalytic Activity of Ag–Au Nanoparticles with 3D Compositional Variations. *Nano Lett.* **2014**, *14* (4), 1921–1926.
- (30) Lewis, E. A.; Slater, T. J. A.; Prestat, E.; Macedo, A.; O'Brien, P.; Camargo, P. H. C.; Haigh, S. J. Real-Time Imaging and Elemental Mapping of AgAu Nanoparticle Transformations. *Nanoscale* **2014**, *6* (22), 13598–13605.
- (31) Rodrigues, T. S.; da Silva, A. H. M.; da Silva, A. G. M.; Ceara, D. G.; Gomes, J. F.; Assaf, J. M.; Camargo, P. H. C. Hollow AgPt/SiO₂ Nanomaterials with Controlled Surface Morphologies: Is the Number of Pt Surface Atoms Imperative to Optimize Catalytic Performances? *Catal. Sci. Technol.* **2016**, *6* (7), 2162–2170.
- (32) Xia, X.; Wang, Y.; Ruditskiy, A.; Xia, Y. 25th Anniversary Article: Galvanic Replacement: A Simple and Versatile Route to Hollow Nanostructures with Tunable and Well-Controlled Properties. *Adv. Mater.* **2013**, *25* (44), 6313–6333.
- (33) da Silva, A. G. M.; Rodrigues, T. S.; Slater, T. J. A.; Lewis, E. A.; Alves, R. S.; Fajardo, H. V.; Balzer, R.; da Silva, A. H. M.; de Freitas, I. C.; Oliveira, D. C.; et al. Controlling Size, Morphology, and Surface Composition of AgAu Nanodendrites in 15 S for Improved Environmental Catalysis under Low Metal Loadings. *ACS Appl. Mater. Interfaces* **2015**, *7* (46), 25624–25632.
- (34) Sun, Y.; Mayers, B.; Xia, Y. Transformation of Silver Nanospheres into Nanobelts and Triangular Nanoplates through a Thermal Process. *Nano Lett.* **2003**, *3* (5), 675–679.
- (35) Dadosh, T. Synthesis of Uniform Silver Nanoparticles with a Controllable Size. *Mater. Lett.* **2009**, *63* (26), 2236–2238.
- (36) Bastús, N. G.; Merkoçi, F.; Piella, J.; Puentes, V. Synthesis of Highly Monodisperse Citrate-Stabilized Silver Nanoparticles of up to 200 Nm: Kinetic Control and Catalytic Properties. *Chem. Mater.* **2014**, *26* (9), 2836–2846.
- (37) Zhu, C.; Guo, S.; Dong, S. Rapid, General Synthesis of PdPt Bimetallic Alloy Nanosponges and Their Enhanced Catalytic Performance for Ethanol/Methanol Electrooxidation in an Alkaline Medium. *Chem. – A Eur. J.* **2013**, *19* (3), 1104–1111.
- (38) Steen, E. van; Sewell, G. S.; Makhoshe, R. A.; Micklethwaite, C.; Manstein, H.; de Lange, M.; O'Connor, C. T. TPR Study on the Preparation of Impregnated Co/SiO₂ Catalysts. *J. Catal.* **1996**, *162* (2), 220–229.
- (39) Perini, L.; Durante, C.; Favaro, M.; Perazzolo, V.; Agnoli, S.; Schneider, O.; Granozzi, G.; Gennaro, A. Metal–Support Interaction in Platinum and Palladium Nanoparticles Loaded on Nitrogen-Doped Mesoporous Carbon for Oxygen Reduction Reaction. *ACS Appl. Mater. Interfaces* **2015**, *7* (2), 1170–1179.
- (40) Lunkenbein, T.; Schumann, J.; Behrens, M.; Schlögl, R.; Willinger, M. G. Formation of a ZnO Overlay in Industrial Cu/ZnO/Al₂O₃ Catalysts Induced by Strong Metal–Support Interactions. *Angew. Chemie* **2015**, *127* (15), 4627–4631.
- (41) Carrasco, J.; López-Durán, D.; Liu, Z.; Duchoň, T.; Evans, J.; Senanayake, S. D.; Crumlin, E. J.; Matolín, V.; Rodríguez, J. A.; Ganduglia-Pirovano, M. V. In Situ and Theoretical Studies for the Dissociation of Water on an Active Ni/CeO₂ Catalyst: Importance of Strong Metal–Support Interactions for the Cleavage of O–H Bonds. *Angew. Chemie Int. Ed.* **2015**, *54* (13), 3917–3921.
- (42) Fang, J.; Li, J.; Zhang, B.; Yuan, X.; Asakura, H.; Tanaka, T.; Teramura, K.; Xie, J.; Yan, N. The Support Effect on the Size and Catalytic Activity of Thiolated Au₂₅ Nanoclusters as Precatalysts. *Nanoscale* **2015**, *7* (14), 6325–6333.
- (43) Liotta, L. F. Catalytic Oxidation of Volatile Organic Compounds on Supported Noble Metals. *Appl. Catal. B Environ.* **2010**, *100* (3–4), 403–412.

Chapter 7

Hollow AgPt/SiO₂ Nanomaterials with Controlled Surface Morphologies: Is the Number of Pt Surface Atoms Imperative to Optimized Catalytic Performances?

7.1. Introduction

Platinum (Pt) based nanomaterials display remarkable catalytic activities towards several transformations that include hydrogenation,^{127,182} oxidation,^{183,184} dehydrogenation,^{185,186} reforming of fuels,^{187–189} and electrocatalytic reductions and oxidations.^{141,190–194} Regarding their applications in catalysis, strategies that enable the optimization of performances are imperative not only because Pt is an expensive material, but also to allow for the utilization of milder or more environmentally friendly conditions.^{195,196}

The understanding on how catalytic performances are affected by composition (in bimetallic systems), structure (solid versus hollow interiors), number of surface atoms, and nature of exposed surface facets is crucial to enable the rational design of highly active catalysts.^{17,197–200} In this context, the synthesis of nanomaterials with controlled surface morphologies as well as hollow interiors represent an intuitive approach to optimize performances.^{92,116,201,202} Firstly, atoms in the interior of Pt nanocrystals are “wasted”, i.e., do not play any role over catalytic properties. Secondly, while controlled surface morphologies may dictate the nature of the exposed surface facets and number of surface atoms, hollow interiors provide larger surface-to-volume ratios than their solid counterparts. Finally, although the morphology and shape controlled synthesis of Pt nanocrystals represents a promising

strategy to tune catalytic performances, it remains challenging in terms of large-scale production, widespread use, and uniform incorporation of the Pt-based material over solid supports such as silica^{143,203,204} and other metal oxides (which is crucial for applications in gas-phase reactions).^{17,205–207}

In this paper, we describe a systematic investigation on how the number of Pt surface atoms and nature of exposed surface facets affect the catalytic performances of AgPt nanomaterials displaying controlled surface morphologies (smooth or rough surfaces), shapes (spherical or one-dimensional), and hollow interiors towards the CO oxidation. More specifically, we focused on AgPt nanoshells (smooth surfaces), assembled nanoparticles (rough surfaces), nanotubes with smooth surfaces, and nanotubes with rough surfaces, which could be incorporated into commercial SiO₂ to produce AgPt/SiO₂ catalysts. Their catalytic performances were then investigated towards the CO_(g) oxidation, which was chosen as a model reaction due to its importance in the purification of hydrogen streams from organic compounds reforming and environmental remediation.^{208–211} We were particularly interested in studying how effects associated with different surface morphologies would influence the catalytic performances of the investigated nanomaterials. Would the catalytic performances depend only on the number of surface atoms available in each case as enabled by the different surface morphologies?

7.2. Experimental

Materials and Instrumentation

Analytical grade chemicals silver nitrate (AgNO₃, 99%, Sigma-Aldrich), polyvinylpyrrolidone (PVP, Sigma-Aldrich, M.W. 55,000 g/mol), polyvinylpyrrolidone (PVP, Sigma-Aldrich, M.W. 10,000 g/mol), ethylene glycol (EG, 99.8%, Sigma-Aldrich), chloroplatinic acid hexahydrate (H₂PtCl₆·6H₂O, ≥37.50% Pt basis, Sigma-Aldrich),

hydroquinone (C₆H₆O₂, 99%, Vetec), hydrochloric acid (HCl, 37%, Sigma-Aldrich), silica (pore size 22 Å, 800 m²/g, Sigma-Aldrich), were used as received.

Transmission electron microscopy (TEM) images were obtained with a JEOL 1010 microscope operating at 80 kV or a JEOL JEM2100 microscope operated at 200 kV. High angle annular dark field (HAADF) scanning transmission electron microscope (STEM) images and energy dispersive X-ray (EDX) spectrum images were acquired using a FEI TECNAI G2 F20 operated at 200 kV. Samples for TEM were prepared by drop-casting an aqueous suspension of the nanostructures over a carbon-coated copper grid, followed by drying under ambient conditions. The scanning electron microscopy (SEM) images were obtained using a JEOL field emission gun electron microscope JSM6330F operated at 5 kV. The samples were prepared by drop-casting an aqueous suspension containing the nanostructures over a silicon wafer, followed by drying under ambient conditions. UV-VIS spectra were obtained from aqueous suspensions containing the nanostructures with a Shimadzu UV-1700 spectrophotometer. The Ag and Pt atomic percentages were measured by inductively coupled plasma optical emission spectrometry (ICP-OES) using a Spectro Arcos equipment at the IQ-USP analytical center facilities. The determination of the number of Pt surface atoms was carried out in a Micrometrics Chemisorb 2705. Typically, 0.1 g of catalysts was dried with N₂ flow at 125 °C for 1h. The system was then heated at 500 °C for 1 h under O₂ flow to remove remaining organic compounds. Afterwards, the samples were cooled down to room temperature, subsequently reduced at 550 °C under H₂ flow for 80 min, and allowed to cool down to room temperature under N₂ flow. Finally, H₂ pulses were provided to the samples until the H₂ consumption ceased. The amount of H₂ adsorbed on the catalyst was estimated considering the following reaction: $\text{H}_2 + 2\text{Pt} \rightarrow 2\text{PtH}$, in which 1 H atom is quimisorbed in 1 Pt atom. The value of 0.08 nm²/atom Pt surface area and 21.45 g.cm⁻³ as the Pt density was considered.

The catalytic oxidation of CO over AgPt/SiO₂ catalysts was carried out in a fixed-bed quartz tubular reactor with 5 mm in intern diameter. The reactions products were analyzed by an in-line chromatograph (GC 3800-VARIAN), with two thermal conductivity detectors (Porapak N and 13X molecular sieve packed columns).

Synthesis of Ag spheres

In a typical procedure,¹³ 5 g of polyvinylpyrrolidone (PVP) was dissolved in 37.5 mL of ethylene glycol (EG). Then, AgNO₃ (200 mg, 1.2 mmol) was added and mixed until the complete dissolution. The resulting solution was heated to 125 °C for 2.5 hours, leading to the appearance of a greenish-yellow color, allowed to cool down to room temperature, and diluted to 125 mL of water.

Synthesis of Ag wires

In a typical procedure,²¹² 5 mL of EG was pre-heated for 1 hour at 140 °C with vigorous stirring, followed by the addition of 0.2 mL of 3 mM HCl (in EG). After 10 min, 3 mL of 94 mM AgNO₃ and 3 mL of 147 mM PVP (both in EG) were simultaneously added dropwise to this mixture (at a speed of 45 mL/h) and left overnight, yielding a beige suspension. The reaction flask was then allowed to cool down to room temperature.

Synthesis of AgPt nanoshells

In a typical synthesis, a mixture containing 5 mL of PVP aqueous solution (0.1 wt %) and 1 mL of as-prepared suspension containing the Ag nanospheres was stirred at 100 °C for 10 min in a 25 mL round-bottom flask. Then, 2 mL of a 5 mM PtCl₆²⁻_(aq) solution was added dropwise and the reaction allowed to proceed at 100 °C for 1 h.

Synthesis of AgPt assembled nanoparticles

In a typical synthesis, a mixture containing 9.4 mL of PVP aqueous solution (0.3 wt %) and 60 μL of the as-prepared Ag nanospheres suspension was stirred at 100 °C for 10 min in a 25 mL round-bottom flask. Then, 0.1 mL of hydroquinone aqueous solution (30 mM) was added. After 30 s, 47.8 μL of $\text{PtCl}_6^{2-}(\text{aq})$ (12 mM) was added and the reaction was quenched by cooling the reaction flask in ice water after 1 h.

Synthesis of AgPt nanotubes with smooth or rough surfaces

For the synthesis of smooth nanotubes, a mixture containing 5 mL of PVP aqueous solution (0.1 wt %) and 1 mL of as-prepared suspension containing the Ag wires was stirred at 100 °C for 10 min in a 25 mL round-bottom flask. Then, 2 mL of a 1 mM $\text{PtCl}_6^{2-}(\text{aq})$ solution was added dropwise and the reaction allowed to proceed at 100 °C for 1 h. The procedure for the synthesis of nanotubes with rough surfaces followed a similar protocol, except that it was carried out at room temperature. After their synthesis, all AgPt nanomaterials were washed twice with a supersaturated $\text{NaCl}_{(\text{aq})}$ solution and three times with water by successive rounds of centrifugation at 12000 rpm and removal of the supernatant. After washing, the AgPt nanomaterials were suspended in 10 mL of PVP aqueous solution (0.3 wt %).

Synthesis of 1 wt. % AgPt supported onto SiO_2 (AgPt/ SiO_2)

The incorporation of AgPt nanostructures onto the silica support (1 % wt, Pt basis) was performed using a wet impregnation approach.¹⁴⁹ Typically, a suspension containing the AgPt nanostructures was added to a beaker containing commercial silica. The resulting mixture was stirred at room temperature for 24h. Then, the resulting solid was washed twice with water and twice with ethanol by successive rounds of centrifugation at 7000 rpm and removal of the

supernatant. After washing, the catalysts were dried at 120 °C for 2 h under air in order to produce the AgPt/SiO₂ catalysts.

Catalytic activity towards CO oxidation

The catalytic oxidation of CO over AgPt/SiO₂ catalysts was carried out under atmospheric pressure. The catalysts (0.1 g) were pretreated *in situ* at 500 °C under an O₂ flow of 30 cm³ min⁻¹ for 1h, followed by a H₂ flow of 30 cm³ min⁻¹ for 1h. Then the catalysts were cooled down to 200 °C and exposed to the reactant gases mixture, composed by 4 % CO, 12 % O₂, and 84 % N₂. The total flow was 50 cm³ min⁻¹. The catalytic tests were performed at a temperature range from 200 to 330 °C.

The CO conversion (X_{CO}) for all the reactions was calculated as follows:

$$X_{CO} (\%) = [(CO_{in} - CO_{out})] / CO_{in} \times 100 \quad (1)$$

where $X_{CO} (\%)$ = percentage of CO conversion; CO_{in} = input quantity and CO_{out} = output quantity.

7.3. Results and discussion

Our studies started with the synthesis of Ag spheres and wires displaying well-defined sizes and shapes as depicted in Figure 7.1.

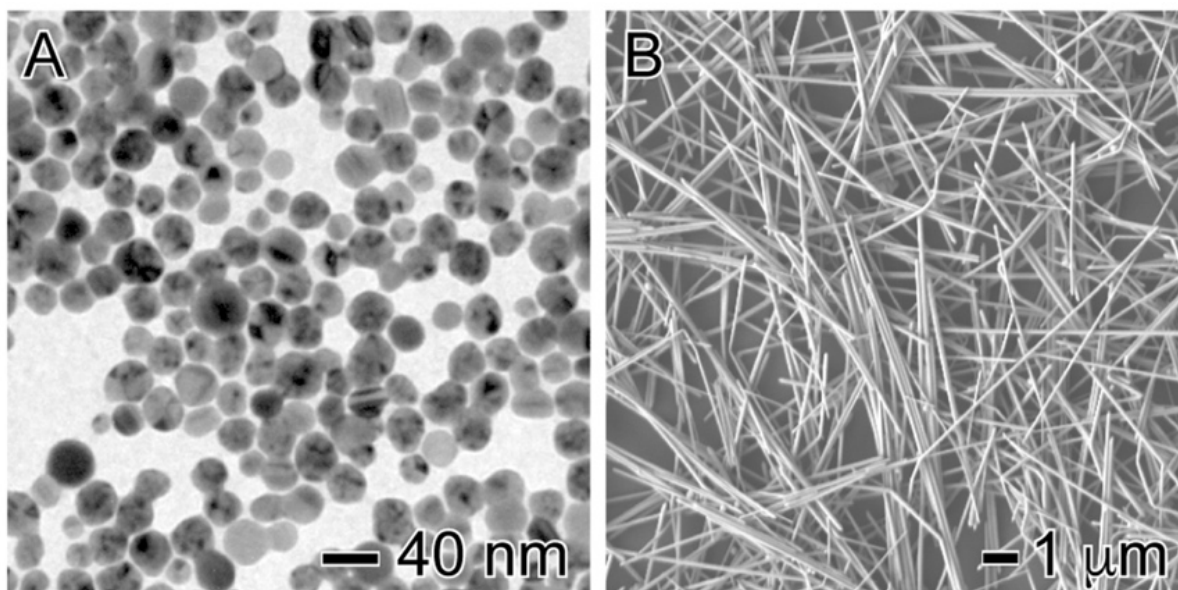


Figure 7.1. TEM image for Ag spheres (A) and SEM image for Ag wires (B) employed as templates for the synthesis of the AgPt hollow nanostructures.

The Ag spheres were 34 ± 3 nm in diameter and the wires were 153 ± 15 nm in width and > 1 μm in length.^{13,212} The Ag spheres and wires were employed as chemical templates to the synthesis of AgPt nanomaterials displaying hollow interiors as well as controlled surface morphologies as illustrated in Figure 7.2. While the Ag spheres could be employed as templates to the synthesis of AgPt nanoshells and assembled nanoparticles, the Ag wires could be employed to produce AgPt nanotubes with smooth or rough surfaces. Our experimental strategy for controlling the Pt surface morphologies by employing the Ag spheres as templates was based on the galvanic replacement reaction between Ag and $\text{PtCl}_6^{2-}(\text{aq})$ (Figure 7.2A). In this case, when the galvanic replacement reaction was carried out in the presence of PVP at 100 °C, the formation of nanoshells was observed.^{1,10} Conversely, the addition of hydroquinone to this galvanic replacement recipe led to AgPt assembled nanoparticles.¹¹⁶ The synthesis of AgPt tubes with controlled surface morphologies could be achieved by simply changing the reaction temperature during the galvanic replacement reaction in the presence of PVP (Figure 7.2B): nanotubes with smooth surfaces were obtained at 100 °C, while nanotubes with rough surfaces were produced at room temperature.²¹³

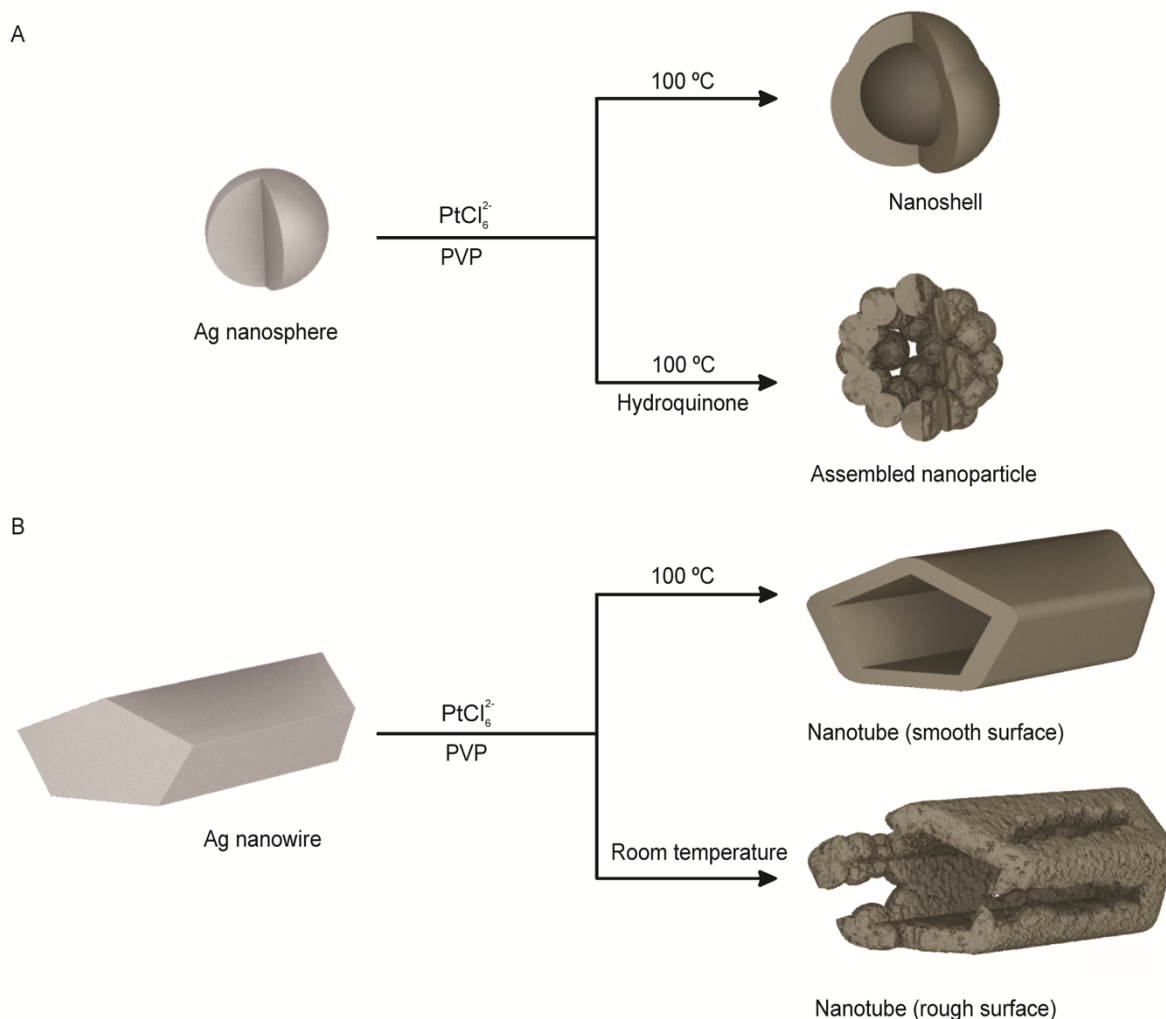


Figure 7.2. Synthesis of AgPt nanoshells, assembled nanoparticles and nanotubes having smooth or rough surfaces by galvanic replacement reaction employing Ag nanospheres or wires as templates.

Figure 7.3A-D show TEM and SEM images for AgPt nanoshells (Figure 7.3A), assembled nanoparticles (Figure 7.3B), and nanotubes displaying smooth or rough surfaces (Figure 7.3C and 7.3D, respectively). It can be observed that all the AgPt nanostructures displayed well-defined shapes and relatively monodisperse sizes. The AgPt nanoshells and assembled nanoparticles (Figure 7.3A and 7.3B, respectively) were 36 ± 2 and 48 ± 3 nm in diameter, respectively (their shell thickness corresponded to 7 and 10 nm, respectively). It is important to note that the AgPt assembled nanoparticles were comprised by several Pt islands with ~ 6 nm in diameter. The hollow interiors in the nanoshells and assembled nanoparticles

can be clearly visualized from the TEM images due to differences in mass-thickness contrast (brighter regions at the center of each particle). The AgPt nanotubes displaying smooth and rough surfaces (Figure 7.3C and 7.3D, respectively) were 198 ± 15 and 186 ± 18 nm in diameter, respectively, and presented wall thickness of 45 and 47 nm, respectively.

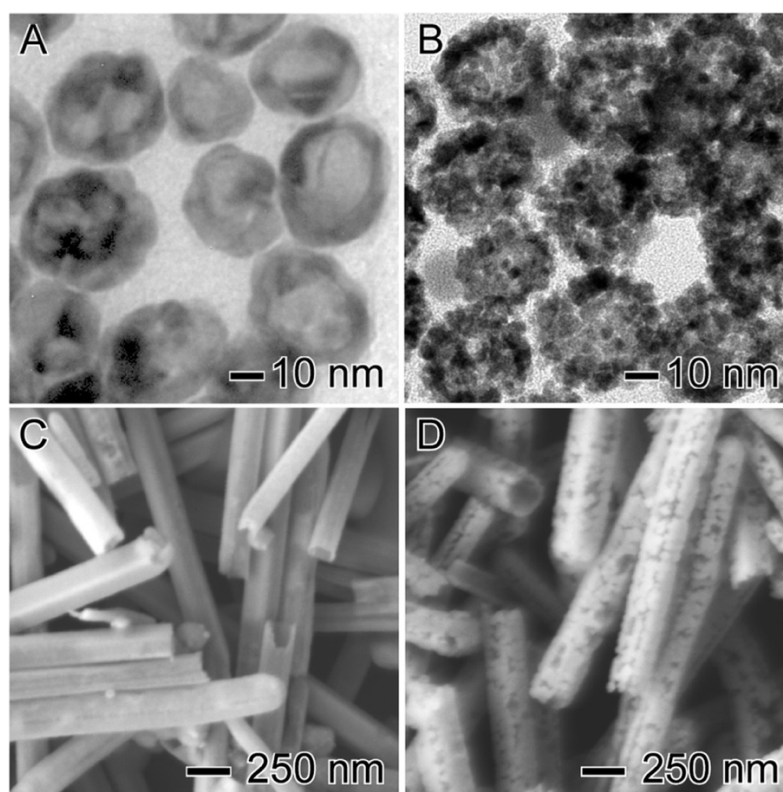


Figure 7.3. TEM (A and B) and SEM (C and D) images for AgPt nanoshells (A), assembled nanoparticles (B), nanotubes with smooth surfaces (C), and nanotubes with rough surfaces (D).

The Pt at. % in all these AgPt nanostructures was determined by ICP-OES analyses and is depicted in Table 7.1. For both nanoshells and assembled nanoparticles, the Pt at. % corresponded to 51, while for the nanotubes the Pt at. % corresponded to 26 and 25 for smooth and rough surfaces, respectively. Therefore, the nanoshells and assembled nanoparticles had similar compositions, differing only on their surface morphologies. The same can be stated regarding the nanotubes with smooth and rough surfaces, thus enabling us to isolate the effect of surface morphology in each of these classes of AgPt nanomaterials over their catalytic activities.

Table 7.1. Ag and Pt Atomic percentages obtained by ICP-OES.

Sample	Ag (mol %)	Pt (mol%)
nanoshells	49	51
assembled nanoparticles	49	51
nanotubes (smooth surface)	74	26
nanotubes (rough surface)	75	25

Figure 7.4 depicts high-resolution transmission electron microscopy (HRTEM), high angle annular dark field (HAADF) scanning transmission electron microscopy (STEM), and energy dispersive X-ray (EDX) spectrum images for AgPt nanoshells (Figure 7.4A-E), assembled nanoparticles (Figure 7.4F-J), nanotubes with smooth surfaces (Figure 7.4K-O), and nanotubes with rough surfaces (Figure 7.4P-T). HRTEM results for the AgPt nanoshells and assembled nanoparticles indicated that, in addition to their hollow interiors (Figure 7.4A and 7.4F), both materials displayed a polycrystalline surface (Figure 7.4B and 7.4G). This can be assigned to the polycrystalline nature of the Ag spheres employed as seeds for their synthesis. The 2.27 Å lattice spacings due to {111} lattice fringes in *fcc* Pt can be clearly visualized from the images. Interestingly, the directions of the lattice fringes in HRTEM image for the AgPt assembled nanoparticles (Figure 7.4G) may suggest a preferential exposure of {111} surface facets relative to {100} in the individual Pt islands that comprise its surface.

HRTEM images for AgPt nanotubes displaying smooth (Figure 7.4K and 7.4L) or rough (Figure 7.4P and 7.4Q) surfaces also confirmed the formation of hollow interiors (Figure 7.4K and 7.4P). Moreover, it can be inferred that the smooth nanotubes displayed a single-crystalline surface enclosed by {100} side facets as a result of the Pt epitaxial deposition over the surface of the Ag nanowires (their side surfaces are enclosed by {100} facets). Conversely, the rough nanotubes were polycrystalline (Figure 7.4Q), and this can be assigned to the island-

mode deposition of Pt over its surface at room temperature. HAADF STEM images for all AgPt nanostructures (Figure 7.4C, 7.4H, 7.4M and 7.4R) supported the formation of hollow interiors and revealed some structural details such as porous walls for nanotubes with rough surfaces and assembled nanoparticles. EDX elemental maps for Ag (green) and Pt (red) (Figure 7.4D, 7.4E, 7.4I, 7.4J, 7.4N, 7.4O, 7.4S, and 7.4T) showed that both Ag and Pt were uniformly distributed in all AgPt nanostructures.

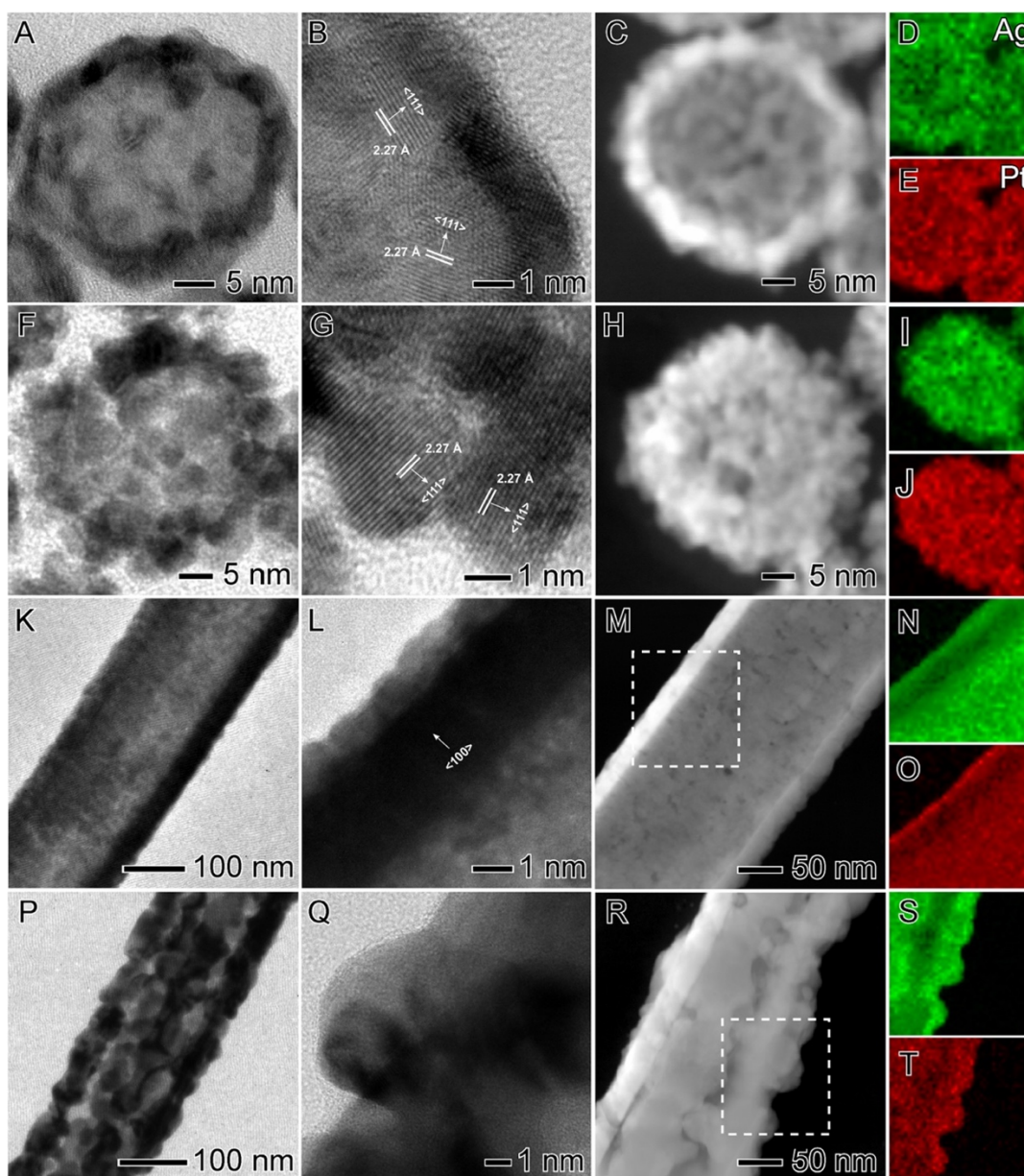


Figure 7.4. HRTEM (first and second columns), HAADF STEM (third column), and EDX spectrum (fourth column) images for AgPt nanoshells (A-E), assembled nanoparticles (F-J), nanotubes with smooth surfaces (K-O), and nanotubes with rough surfaces (P-T). In the EDX spectrum images, the green and red maps corresponded to Ag and Pt, respectively.

The formation of hollow AgPt nanomaterials was also supported by UV-VIS spectroscopy (Figure 7.5A-B). The UV-VIS spectra registered from aqueous suspensions containing the nanoshells, assembled nanoparticles, and nanotubes relative to their corresponding Ag nanocrystals employed as templates show the disappearance of the band associated with the dipolar mode of the localized surface plasmon resonance (LSPR) excitation from Ag as a result of Pt deposition (Pt does not display SPR extinction in the visible range) and the formation of hollow interiors.^{214,215} The XRD patterns (Figure 7.5C-D) confirmed the formation of AgPt nanostructures without any impurities in all cases.

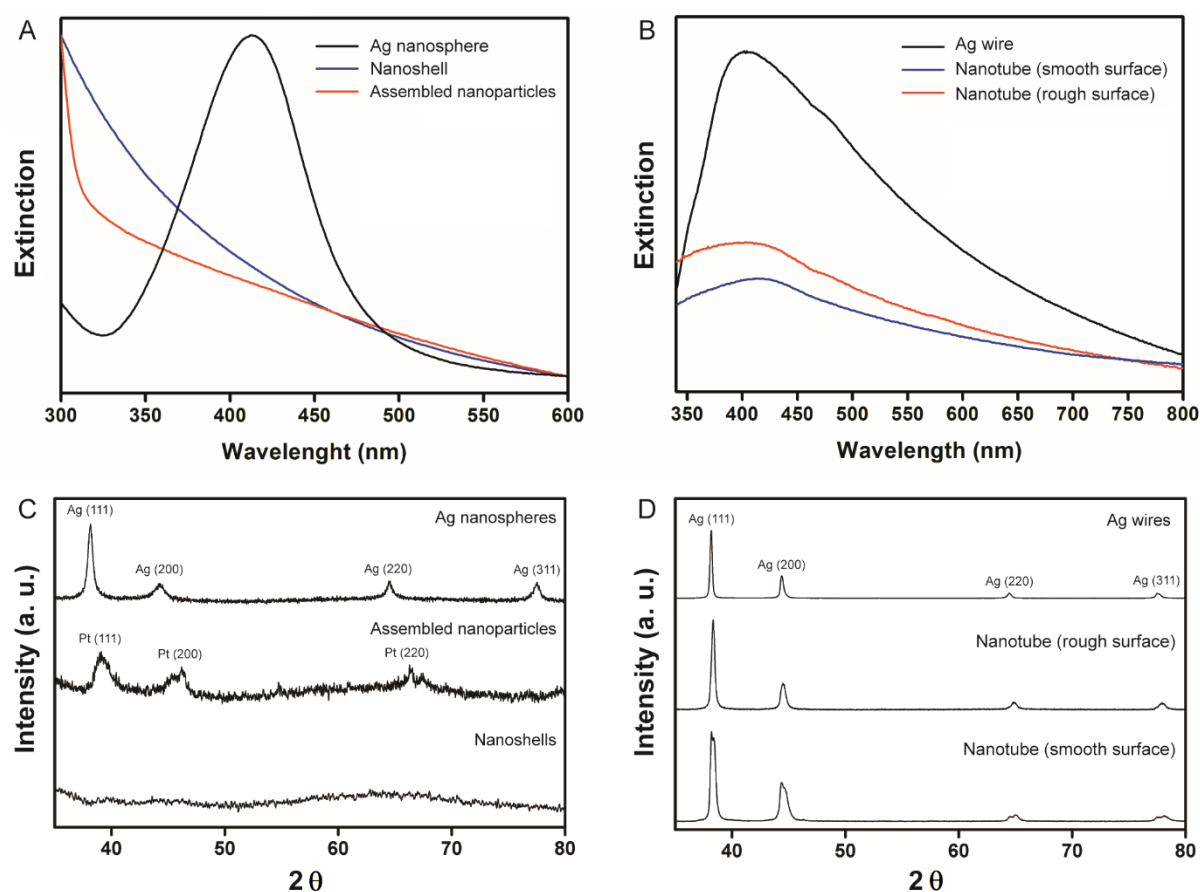


Figure 7.5. UV–VIS extinction spectra recorded from aqueous suspensions containing Ag nanospheres, nanoshells, and assembled nanoparticles (A) and wires, nanotubes with smooth surfaces, and nanotubes with rough surfaces (B).

In addition to the fact that AgPt nanoshells, assembled nanoparticles, and nanotubes represent attractive materials for catalytic applications, we were particularly interested in investigating how shape (spherical vs one-dimensional) and surface morphologies (smooth vs rough) affected their catalytic performances. To this end, we employed the CO oxidation as a model reaction due to its relevance in the field of fuel production, as it represents an efficient way to purify hydrogen streams from organic compounds reforming.^{208,209} Also, this reaction plays an important role in environmental remediation owing to the high toxicity of CO.^{210,211} It is important to note that the utilization of metal nanoparticles as catalysts for gas-phase transformations requires the utilization of solid supports to avoid nanoparticle agglomeration (that leads to decreased catalytic performances) during the catalytic reactions that are often carried out at relatively high temperatures (up to ~350 °C in this paper). However, the generation of supported catalysts in which the noble-metal component is uniformly dispersed over the entire surface of the support (without agglomeration) remains very challenging. We could circumvent this limitation by employing a wet impregnation approach, which enabled the uniform deposition of the obtained AgPt nanoshells, assembled nanoparticles, and nanotubes over the entire surface of the SiO₂ support to generate AgPt/SiO₂ materials as shown in Figure 7.6A-D. The low-magnification SEM images clearly demonstrate that no agglomeration took place and the nanoshells, assembled nanoparticles, and nanotubes were uniformly distributed over the SiO₂ surface. It is noteworthy that, in order to generate the AgPt/SiO₂ catalysts, the synthesis of the AgPt nanoshells, assembled nanoparticles and nanotubes were firstly scaled-up by 100 folds as compared to the synthesis described in the experimental section (Figure 7.3). The Pt loading in the AgPt/SiO₂ materials shown in Figure 7.6A-D corresponded to 1 % in weight as determined by ICP-OES.

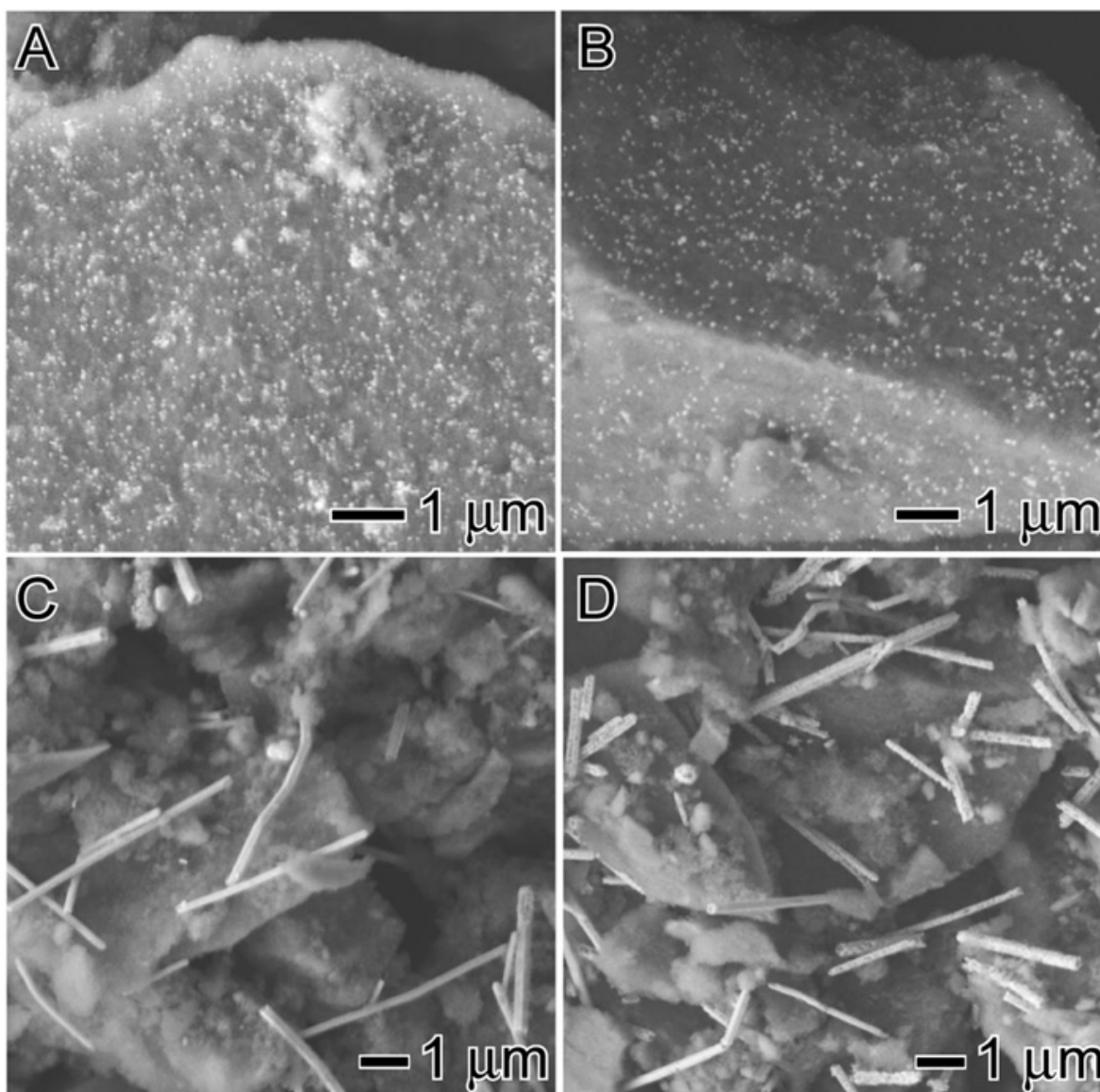


Figure 7.6. SEM images of AgPt/SiO₂ catalysts obtained by the wet impregnation of AgPt nanoshells (A), assembled nanoparticles (B), nanotubes with smooth surfaces (C), and nanotubes with rough surfaces (D) onto commercial SiO₂. The Pt content in all samples corresponded to 1 wt. %.

As shown in Figure 7.7, no changes in morphology were observed after scaling up the synthesis, indicating that our approach was robust. This represents a significant progress relative to the literature concerning the large-scale production of morphology and shape controlled Pt nanocrystals.

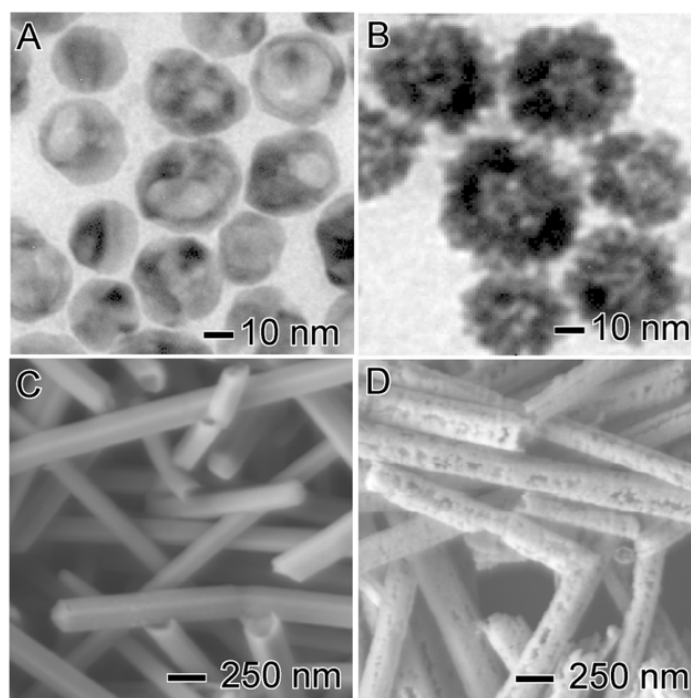


Figure 7.7. (A and B) TEM and (C and D) SEM images for AgPt nanoshells (A), assembled nanoparticles (B), nanotube with smooth surfaces (C), and nanotubes with rough surfaces (D) obtained after 1 h employing the scaled-up approach performed in the same conditions described in Scheme 1.

The number of Pt surface atoms in the AgPt/SiO₂ materials was determined by hydrogen chemisorption (Table 7.2) and corresponded to 4.25, 1.70, 4.10, and 4.56 μmol per gram of catalysts for nanoshells (Figure 7.6A), assembled nanoparticles (Figure 7.6B), nanotubes with smooth surfaces (Figure 7.6C), and nanotubes with rough surfaces (Figure 7.6D), respectively. With the exception of the AgPt assembled nanoparticles, all the other AgPt materials presented similar surface areas as revealed by the chemisorption results. Interestingly, while all other AgPt catalysts were synthesized by a galvanic replacement reaction between PtCl₆²⁻ and Ag, the AgPt assembled nanoparticles was obtained by a combination of the galvanic replacement reaction between PtCl₆²⁻ and Ag as well as PtCl₆²⁻ to Pt reduction by hydroquinone, which led to the deposition of dense Pt islands at the surface of the assembled nanoparticles. Therefore, it is plausible that the presence of hydroquinone at the particle's

surface, together with its distinct surface morphologies, contributed to its lower surface areas relative to the other samples.

Table 7.2. Number of Pt surface atoms in the AgPt/SiO₂ catalysts obtained by H₂ chemisorption.

Sample	Pt surface atoms (μmol/g catalyst)
nanoshells	4.25
assembled nanoparticles	1.70
nanotubes (smooth surface)	4.10
nanotubes (rough surface)	4.56

The AgPt/SiO₂ materials were then investigated as catalyst towards the gas-phase CO oxidation reaction according to Equation 1:



Figure 7.8A shows the CO conversion percentages as a function of temperature for nanoshells (blue trace), assembled nanoparticles (green trace), nanotubes with smooth surfaces (black trace), and nanotubes with rough surfaces (red trace). Control experiments employing pure SiO₂ (without any catalyst) and Ag nanospheres and wires supported on SiO₂ were also included for comparison.

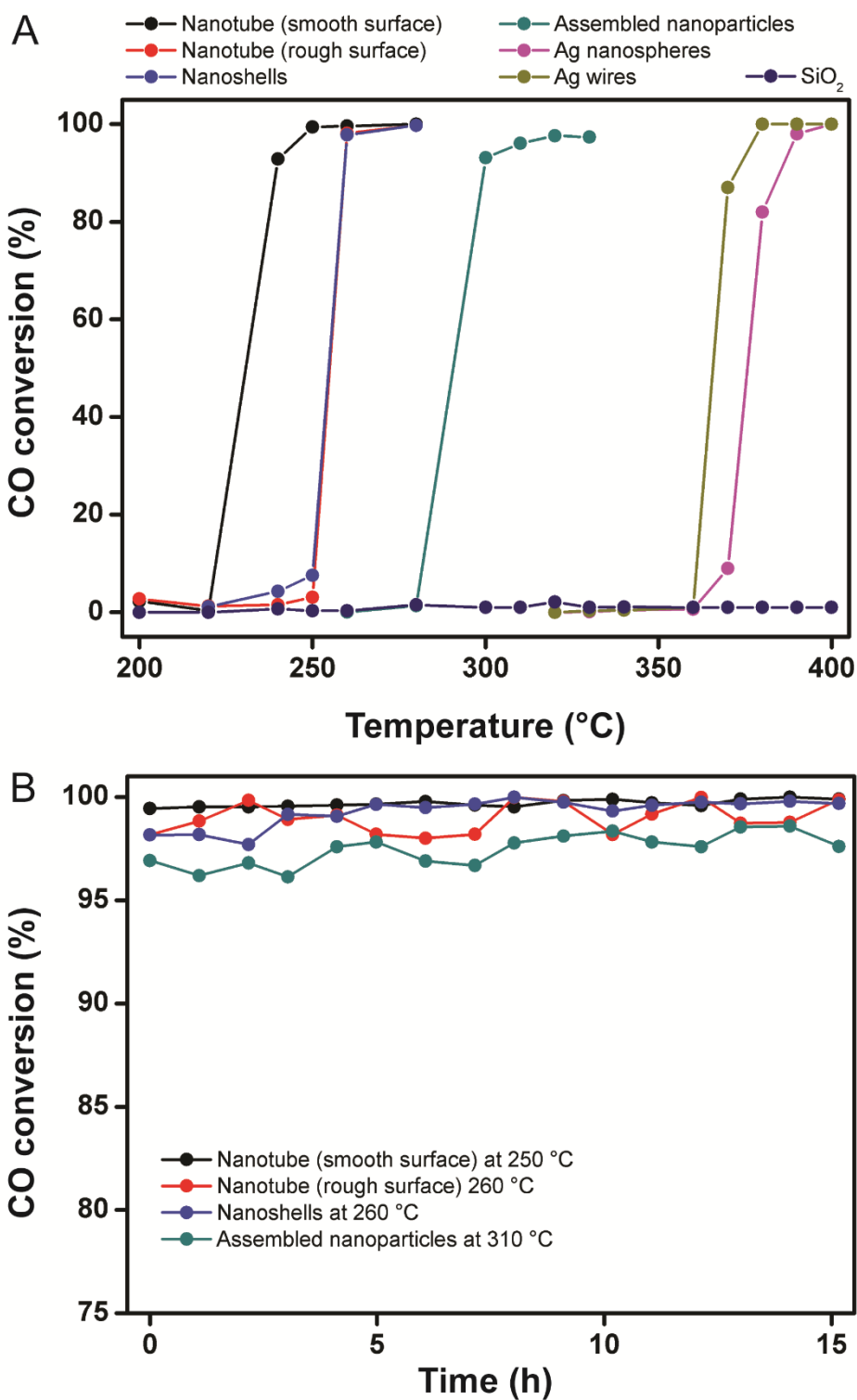


Figure 7.8. CO conversion percentages as a function of temperature (A) and time (B) employing AgPt/SiO₂ nanoshells (blue trace), assembled nanoparticles (green trace), nanotubes with smooth surfaces (black trace), and nanotubes with rough surfaces (red trace) as catalysts. The catalytic activities towards CO oxidation followed the order: nanotubes with smooth surfaces > nanoshells, nanotubes with rough surfaces > assembled nanoparticles.

In the presence of pure SiO₂, no significant CO conversion was observed in the employed temperature range. When Ag nanospheres and wires were used as catalysts, the CO conversion was observed only at high temperatures (> 390 °C), showing that pure SiO₂ and the Ag nanostructures have poor activities towards CO oxidation under our employed conditions (below 300 °C). For all AgPt catalysts, the CO conversion percentages increased with the reaction temperature,^{210,211} but nanotubes with smooth surfaces begin to oxidize CO and reach 100% CO conversion at lower temperatures relative to nanoshells and nanotubes with rough surfaces, which in turn start to oxidize CO and achieve its total conversion at lower temperatures than the assembled nanoparticles. At 250 °C, for example, 100% CO conversion was observed for nanotubes with smooth surfaces, around 50% CO conversion for nanoshells and nanotubes with rough surfaces, and 0% CO conversion for assembled nanoparticles. 100% conversion was achieved at 250, 280, 280, and 330 °C for nanotubes with smooth surfaces, nanoshells, nanotubes with rough surfaces, and assembled nanoparticles, respectively. Thus, the catalytic performance of the AgPt/SiO₂ materials as a function of the temperature decreased in the following order: nanotubes with smooth surfaces > nanoshells, nanotubes with rough surfaces > assembled nanoparticles.

When the CO conversion percentages catalyzed by nanoshells and assembled nanoparticles are compared, the better catalytic performance observed for the nanoshells can be associated with the higher number of Pt surface atoms relative to the assembled nanoparticles. Specifically, the nanoshells had an increase of 150% in the number of Pt surface atoms relative to the assembled nanoparticles, and this higher number of Pt surface atoms may be associated with their smaller particle size and shell thickness, and the consequent increased number of AgPt particles per mass of catalyst, relative to the assembled nanoparticles (Figures 7.3 and 7.4). On the other hand, nanotubes with rough surfaces had a higher number of Pt surface atoms than the nanotubes with smooth surfaces (the number of Pt surface atoms was

10 % higher relative to the nanotubes with smooth surfaces), but they displayed inferior catalytic performances. These variations can be explained based on the differences in surface morphologies that enable the exposure of distinct surface facets in each sample. For instance, while the nanotubes with rough surfaces were polycrystalline (enclosed by a mix of {111} and {100} surface facets), the nanotubes with smooth surfaces were enclosed by {100} surface facets at their side walls as a result of the epitaxial Pt deposition over the surface of the Ag nanowires employed as templates. In this context, it has been reported that the CO and formic acid oxidation catalyzed by noble metal nanoparticles display a facet-dependent behavior, in which {100} facets shows enhanced catalytic activities towards the CO and formic acid oxidation.²¹⁶⁻²²⁰ Thus, it is plausible that the preferential exposition of {100} facets on the AgPt nanotubes with smooth surfaces enabled better catalytic performances not only relative to nanotubes with rough surfaces, but also relative to the nanoshells and assembled nanoparticles, even though the number of Pt surface atoms for the nanoshells and nanotubes with rough surfaces were higher than that for nanotubes with smooth surfaces. Therefore, our results indicate that the increase number of Pt surface atoms of nanoshells relative to the assembled nanoparticles may have contributed higher catalytic performances of the nanoshells as compared to the assembled nanoparticles. However, the preferential exposure of {100} side facets in the nanotubes with smooth surfaces compensated the decrease in the number of Pt surface atoms relative to both the nanotubes with rough surfaces and nanoshells. This observation is in agreement with the apparent preferential exposure of {111} facets in the assembled nanoparticles, which could also contribute to their lower performance relative to the other catalysts. It is possible that presence of hydroquinone at the surface of the assembled nanoparticles may also have contributed to their lower surface areas, and thus lower catalytic activities, relative to the other samples.

It is important to note that the differences in size among the samples are related to the detected variation in the Pt surface areas, and we focused on this parameter, rather than size, to explain the catalytic results. In fact, although the observed catalytic activities did not correlated directly with size (this comparison is difficult as the assembled nanoparticles and nanotubes with rough surfaces display complex surface morphologies), they could be explained based both on the detected variations of Pt surface area and preferential exposure of {100} facets in the nanotubes with smooth surfaces.

Figure 7.8B shows the catalytic stability for the nanoshells (blue trace), assembled nanoparticles (green trace), nanotubes with smooth surfaces (black trace), and nanotubes with rough surfaces (red trace) expressed as a function of CO % conversion as a function of time. It can be observed that no significant loss of catalytic activity was detected even after 15 h in these materials. Figure 7.9A-D show SEM images for AgPt/SiO₂ nanoshells, assembled nanoparticles, nanotubes with smooth surfaces, and nanotubes with rough surfaces, respectively, that were obtained after the catalytic experiments described in Figure 7.7. All catalysts displayed identical morphological features as compared to the samples before the catalytic studies (Figure 7.6). As a matter of fact, the shape and uniform dispersion over the SiO₂ support remained unchanged, in agreement with the results shown in Figure 7.6 and indicating their good stability towards aggregation or morphology loss under the experimental conditions employed during the catalytic investigations, showing that these materials may represent promising candidates for gas-phase catalytic applications.

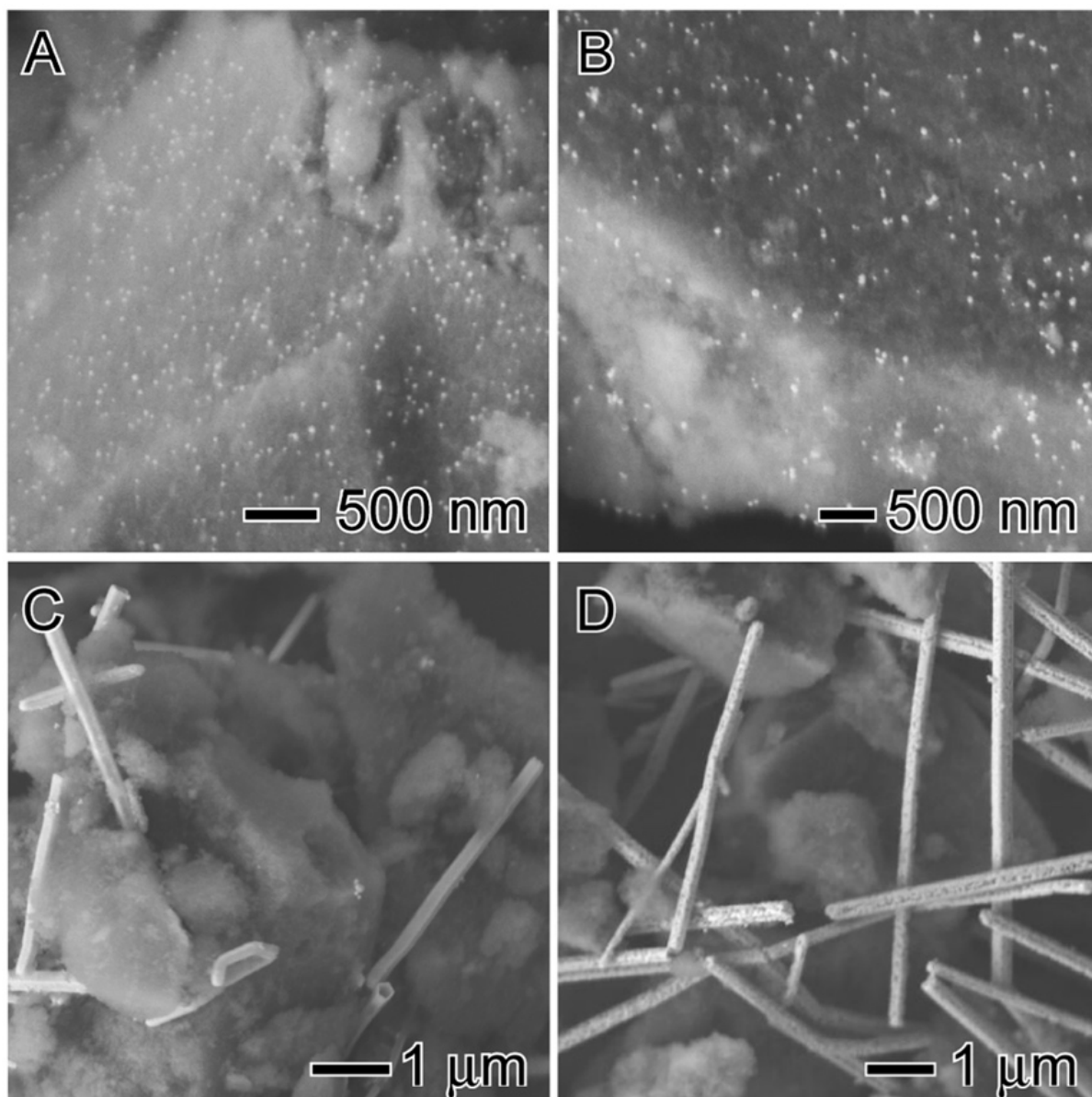


Figure 7.9. SEM images of the AgPt/SiO₂ nanoshells (A), assembled nanoparticles (B), nanotubes with smooth surfaces (C), and nanotubes with rough surfaces (D) catalysts after the catalytic studies. No changes in morphology or dispersion were detected (see Figure 7.6).

7.4. Conclusion

In summary, we investigated the effect of the number of Pt surface atoms and the nature of exposed surface facets over the catalytic performances of AgPt nanomaterials displaying controlled surface morphologies (smooth or rough surfaces), shapes (spherical or one-dimensional), and hollow interiors towards the CO oxidation reaction. To this end, we focused

of AgPt nanoshells (smooth surfaces), assembled nanoparticles (rough surfaces), and nanotubes with smooth or rough surfaces. All these materials could be synthesized by the galvanic replacement reaction between Ag spheres or wires and PtCl_6^{2-} (aq), and were supported onto SiO_2 to generate the AgPt/ SiO_2 catalysts in which the AgPt component was uniformly dispersed over the entire surface of the support without agglomeration. Catalytic performances towards the CO oxidation followed the order: nanotube with smooth surfaces > nanoshells, nanotubes with rough surfaces > assembled nanoparticles. The better catalytic performance observed for the nanoshells relative to the assembled nanoparticles could be assigned to their higher number of Pt surface atoms. Conversely, while nanotubes with smooth surfaces presented a lower number of Pt surface atoms relative to the nanotubes with rough surfaces, they displayed superior catalytic performances as a result of the preferential exposure of {100} facets (which are the most active towards CO oxidation relative to {111} and {110}). Interestingly, the nanotubes with smooth surfaces also displayed higher catalytic activities when compared to the nanoshells, showing that the preferential exposure of {100} side facets in the nanotubes with smooth surfaces compensated the decrease in the number of Pt surface atoms relative to the nanoshells for improved catalytic performances. The data presented herein show that the optimization of catalytic performances of AgPt materials depend not only on the number of Pt surface atoms, but also (and more importantly) on the preferential exposure of active surface facets. We believe these results can have important implications for the design of highly active Pt-based catalysts towards gas-phase transformations.

7.5. References

- (1) Li, Y.; Gao, W.; Ci, L.; Wang, C.; Ajayan, P. M. Catalytic Performance of Pt Nanoparticles on Reduced Graphene Oxide for Methanol Electro-Oxidation. *Carbon N. Y.* **2010**, *48* (4), 1124–1130.
- (2) Du, W.; Xia, S.; Nie, R.; Hou, Z. Magnetic Pt Catalyst for Selective Hydrogenation of Halonitrobenzenes. *Ind. Eng. Chem. Res.* **2014**, *53* (12), 4589–4594.
- (3) Sanz, O.; Delgado, J. J.; Navarro, P.; Arzamendi, G.; Gandía, L. M.; Montes, M. VOCs

- Combustion Catalysed by Platinum Supported on Manganese Octahedral Molecular Sieves. *Appl. Catal. B Environ.* **2011**, *110* (0), 231–237.
- (4) An, K.; Alayoglu, S.; Musselwhite, N.; Plamthottam, S.; Melaet, G.; Lindeman, A. E.; Somorjai, G. A. Enhanced CO Oxidation Rates at the Interface of Mesoporous Oxides and Pt Nanoparticles. *J. Am. Chem. Soc.* **2013**, *135* (44), 16689–16696.
 - (5) Chen, W.; Ji, J.; Duan, X.; Qian, G.; Li, P.; Zhou, X.; Chen, D.; Yuan, W. Unique Reactivity in Pt/CNT Catalyzed Hydrolytic Dehydrogenation of Ammonia Borane. *Chem. Commun.* **2014**, *50* (17), 2142–2144.
 - (6) Wu, J.; Peng, Z.; Sun, P.; Bell, A. T. N-Butane Dehydrogenation over Pt/Mg(In)(Al)O. *Appl. Catal. A Gen.* **2014**, *470* (0), 208–214.
 - (7) Panagiotopoulou, P.; Verykios, X. E. Mechanistic Aspects of the Low Temperature Steam Reforming of Ethanol over Supported Pt Catalysts. *Int. J. Hydrogen Energy* **2012**, *37* (21), 16333–16345.
 - (8) Arroyo-Ramirez, L.; Chen, C.; Cargnello, M.; Murray, C. B.; Fornasiero, P.; Gorte, R. J. Supported Platinum-Zinc Oxide Core-Shell Nanoparticle Catalysts for Methanol Steam Reforming. *J. Mater. Chem. A* **2014**, *2* (45), 19509–19514.
 - (9) Nomikos, G. N.; Panagiotopoulou, P.; Kondarides, D. I.; Verykios, X. E. Kinetic and Mechanistic Study of the Photocatalytic Reforming of Methanol over Pt/TiO₂ Catalyst. *Appl. Catal. B Environ.* **2014**, *146* (0), 249–257.
 - (10) Guo, D.-J.; You, J.-M. Highly Catalytic Activity of Pt Electrocatalyst Supported on Sulphated SnO₂/multi-Walled Carbon Nanotube Composites for Methanol Electro-Oxidation. *J. Power Sources* **2012**, *198* (0), 127–131.
 - (11) Li, Y.; Li, Y.; Zhu, E.; McLouth, T.; Chiu, C.-Y.; Huang, X.; Huang, Y. Stabilization of High-Performance Oxygen Reduction Reaction Pt Electrocatalyst Supported on Reduced Graphene Oxide/Carbon Black Composite. *J. Am. Chem. Soc.* **2012**, *134* (30), 12326–12329.
 - (12) Guo, X.; Ye, W.; Zhu, R.; Wang, W.; Xie, F.; Sun, H.; Zhao, Q.; Ding, Y.; Yang, J. Gold Nanorod-Templated Synthesis of Polymetallic Hollow Nanostructures with Enhanced Electrocatalytic Performance. *Nanoscale* **2014**, *6* (20), 11732–11737.
 - (13) Xue, M.; Tan, Y. Hollow Alloy Nanostructures Templated by Au Nanorods: Synthesis, Mechanistic Insights, and Electrocatalytic Activity. *Nanoscale* **2014**, *6* (21), 12500–12514.
 - (14) Kang, Y.; Pyo, J. B.; Ye, X.; Diaz, R. E.; Gordon, T. R.; Stach, E. A.; Murray, C. B. Shape-Controlled Synthesis of Pt Nanocrystals: The Role of Metal Carbonyls. *ACS Nano* **2012**, *7* (1), 645–653.
 - (15) Chen, J.; Lim, B.; Lee, E. P.; Xia, Y. Shape-Controlled Synthesis of Platinum Nanocrystals for Catalytic and Electrocatalytic Applications. *Nano Today* **2009**, *4* (1), 81–95.
 - (16) Xia, Y.; Xiong, Y.; Lim, B.; Skrabalak, S. E. Shape-Controlled Synthesis of Metal Nanocrystals: Simple Chemistry Meets Complex Physics? *Angew. Chemie Int. Ed.* **2009**, *48* (1), 60–103.
 - (17) Cheong, S.; Watt, J. D.; Tilley, R. D. Shape Control of Platinum and Palladium Nanoparticles for Catalysis. *Nanoscale* **2010**, *2* (10), 2045–2053.
 - (18) Yu, W.; Porosoff, M. D.; Chen, J. G. Review of Pt-Based Bimetallic Catalysis: From Model Surfaces to Supported Catalysts. *Chem. Rev.* **2012**, *112* (11), 5780–5817.
 - (19) Mahmoud, M. A.; O’Neil, D.; El-Sayed, M. A. Hollow and Solid Metallic Nanoparticles in Sensing and in Nanocatalysis. *Chem. Mater.* **2014**, *26* (1), 44–58.
 - (20) Norskov, J. K.; Bligaard, T.; Hvolbaek, B.; Abild-Pedersen, F.; Chorkendorff, I.; Christensen, C. H. The Nature of the Active Site in Heterogeneous Metal Catalysis. *Chem. Soc. Rev.* **2008**, *37* (10), 2163–2171.

- (21) Wu, B.; Zheng, N. Surface and Interface Control of Noble Metal Nanocrystals for Catalytic and Electrocatalytic Applications. *Nano Today* **2013**, *8* (2), 168–197.
- (22) da Silva, A. G. M.; Fajardo, H. V.; Balzer, R.; Probst, L. F. D.; Lovón, A. S. P.; Lovón-Quintana, J. J.; Valença, G. P.; Schreine, W. H.; Robles-Dutenhefner, P. A. Versatile and Efficient Catalysts for Energy and Environmental Processes: Mesoporous Silica Containing Au, Pd and Au-Pd. *J. Power Sources* **2015**, *285*, 460–468.
- (23) Rodrigues, T. S.; da Silva, A. G. M.; Gonçalves, M. C.; Fajardo, H. V.; Balzer, R.; Probst, L. F. D.; Camargo, P. H. C. AgPt Hollow Nanodendrites: Synthesis and Uniform Dispersion over SiO₂ Support for Catalytic Applications. *ChemNanoMat* **2015**, n/a-n/a.
- (24) Rodrigues, T.; da Silva, A. M.; Macedo, A.; Farini, B.; Alves, R.; Camargo, P. C. Probing the Catalytic Activity of Bimetallic versus Trimetallic Nanoshells. *J. Mater. Sci.* **2015**, *50* (16), 5620–5629.
- (25) Silva, A. G. M.; Rodrigues, T. S.; Dias, A.; Fajardo, H. V.; Gonçalves, R. F.; Godinho, M.; Robles-Dutenhefner, P. A. Ce_{1-x}Sm_xO_{1.9}-[Small Delta] Nanoparticles Obtained by Microwave-Assisted Hydrothermal Processing: An Efficient Application for Catalytic Oxidation of [Small Alpha]-Bisabolol. *Catal. Sci. Technol.* **2014**, *4* (3), 814–821.
- (26) da Silva, A. M.; Rodrigues, T.; Taguchi, L. K.; Fajardo, H.; Balzer, R.; Probst, L. D.; Camargo, P. C. Pd-Based Nanoflowers Catalysts: Controlling Size, Composition, and Structures for the 4-Nitrophenol Reduction and BTX Oxidation Reactions. *J. Mater. Sci.* **2015**, 1–12.
- (27) Astruc, D.; Lu, F.; Aranzaes, J. R. Nanoparticles as Recyclable Catalysts: The Frontier between Homogeneous and Heterogeneous Catalysis. *Angew. Chemie Int. Ed.* **2005**, *44* (48), 7852–7872.
- (28) Mizuno, N.; Misono, M. Heterogeneous Catalysis. *Chem. Rev.* **1998**, *98* (1), 199–218.
- (29) Zaera, F. Nanostructured Materials for Applications in Heterogeneous Catalysis. *Chem. Soc. Rev.* **2013**, *42* (7), 2746–2762.
- (30) Zhang, S.; Gai, S.; He, F.; Dai, Y.; Gao, P.; Li, L.; Chen, Y.; Yang, P. Uniform Ni/SiO₂@Au Magnetic Hollow Microspheres: Rational Design and Excellent Catalytic Performance in 4-Nitrophenol Reduction. *Nanoscale* **2014**, *6* (12), 7025–7032.
- (31) An, K.; Zhang, Q.; Alayoglu, S.; Musselwhite, N.; Shin, J.-Y.; Somorjai, G. A. High-Temperature Catalytic Reforming of N-Hexane over Supported and Core–Shell Pt Nanoparticle Catalysts: Role of Oxide–Metal Interface and Thermal Stability. *Nano Lett.* **2014**, *14* (8), 4907–4912.
- (32) Asadirad, A. M.; Branda, N. R. Two Colors of Light Are Needed to Break Bonds and Release Small Molecules from the Surface of SiO₂–Au Core–Shell Nanoparticles. *J. Am. Chem. Soc.* **2015**, *137* (8), 2824–2827.
- (33) Choudhary, T. V.; Goodman, D. W. Stepwise Methane Steam Reforming: A Route to CO-Free Hydrogen. *Catal. Letters* **1999**, *59* (2–4), 93–94.
- (34) Faur Ghenciu, A. Review of Fuel Processing Catalysts for Hydrogen Production in PEM Fuel Cell Systems. *Curr. Opin. Solid State Mater. Sci.* **2002**, *6* (5), 389–399.
- (35) Moura, J. S.; Fonseca, J. da S. L.; Bion, N.; Epron, F.; Silva, T. de F.; Maciel, C. G.; Assaf, J. M.; Rangel, M. do C. Effect of Lanthanum on the Properties of Copper, Cerium and Zirconium Catalysts for Preferential Oxidation of Carbon Monoxide. *Catal. Today* **2014**, *228* (0), 40–50.
- (36) Maciel, C. G.; Silva, T. de F.; Profeti, L. P. R.; Assaf, E. M.; Assaf, J. M. Study of CuO/CeO₂ Catalyst with for Preferential CO Oxidation Reaction in Hydrogen-Rich Feed (PROX-CO). *Appl. Catal. A Gen.* **2012**, *431–432* (0), 25–32.
- (37) da Silva, A. G. M.; de Souza, M. L.; Rodrigues, T. S.; Alves, R. S.; Temperini, M. L.

- A.; Camargo, P. H. C. Rapid Synthesis of Hollow Ag–Au Nanodendrites in 15 Seconds by Combining Galvanic Replacement and Precursor Reduction Reactions. *Chem. – A Eur. J.* **2014**, *20* (46), 15040–15046.
- (38) de Oliveira, C. C. S.; Ando, R. A.; Camargo, P. H. C. Size-Controlled Synthesis of Silver Micro/nanowires as Enabled by HCL Oxidative Etching. *Phys. Chem. Chem. Phys.* **2013**, *15* (6), 1887–1893.
- (39) Jiang, S. P. A Review of Wet impregnation—An Alternative Method for the Fabrication of High Performance and Nano-Structured Electrodes of Solid Oxide Fuel Cells. *Mater. Sci. Eng. A* **2006**, *418* (1–2), 199–210.
- (40) Xia, X.; Wang, Y.; Ruditskiy, A.; Xia, Y. 25th Anniversary Article: Galvanic Replacement: A Simple and Versatile Route to Hollow Nanostructures with Tunable and Well-Controlled Properties. *Adv. Mater.* **2013**, *25* (44), 6313–6333.
- (41) Slater, T. J. A.; Macedo, A.; Schroeder, S. L. M.; Burke, M. G.; O'Brien, P.; Camargo, P. H. C.; Haigh, S. J. Correlating Catalytic Activity of Ag–Au Nanoparticles with 3D Compositional Variations. *Nano Lett.* **2014**, *14* (4), 1921–1926.
- (42) Sun, Y.; Xia, Y. Multiple-Walled Nanotubes Made of Metals. *Adv. Mater.* **2004**, *16* (3), 264–268.
- (43) Zhang, W.; Yang, J.; Lu, X. Tailoring Galvanic Replacement Reaction for the Preparation of Pt/Ag Bimetallic Hollow Nanostructures with Controlled Number of Voids. *ACS Nano* **2012**, *6* (8), 7397–7405.
- (44) Chen, L.; Chabu, J. M.; Liu, Y. Bimetallic AgM (M = Pt, Pd, Au) Nanostructures: Synthesis and Applications for Surface-Enhanced Raman Scattering. *RSC Adv.* **2013**, *3* (13), 4391–4399.
- (45) Zhang, H.; Jin, M.; Liu, H.; Wang, J.; Kim, M. J.; Yang, D.; Xie, Z.; Liu, J.; Xia, Y. Facile Synthesis of Pd–Pt Alloy Nanocages and Their Enhanced Performance for Preferential Oxidation of CO in Excess Hydrogen. *ACS Nano* **2011**, *5* (10), 8212–8222.
- (46) Jin, M.; Zhang, H.; Xie, Z.; Xia, Y. Palladium Nanocrystals Enclosed by {100} and {111} Facets in Controlled Proportions and Their Catalytic Activities for Formic Acid Oxidation. *Energy Environ. Sci.* **2012**, *5* (4), 6352–6357.
- (47) Wang, R.; He, H.; Wang, J.; Liu, L.; Dai, H. Shape-Regulation: An Effective Way to Control CO Oxidation Activity over Noble Metal Catalysts. *Catal. Today* **2013**, *201* (0), 68–78.
- (48) Chen, G.; Tan, Y.; Wu, B.; Fu, G.; Zheng, N. Carbon Monoxide-Controlled Synthesis of Surface-Clean Pt Nanocubes with High Electrocatalytic Activity. *Chem. Commun.* **2012**, *48* (22), 2758–2760.
- (49) Jin, M.; Liu, H.; Zhang, H.; Xie, Z.; Liu, J.; Xia, Y. Synthesis of Pd Nanocrystals Enclosed by {100} Facets and with Sizes <10 Nm for Application in CO Oxidation. *Nano Res.* **2011**, *4* (1), 83–91.

Chapter 8

Cu₂O Spheres as an Efficient Source of Catalytic Cu(I) Species for Performing Azide-Alkyne Click Reactions

8.1. Introduction

The copper(I)-catalyzed azide–alkyne cycloaddition (CuAAC) corresponds to one of the best clic examples of click reactions. This transformation enables the connection of two molecular fragments in a facile, selective, and high-yield approach under mild conditions, being not sensitive to aqueous conditions, and with little or no by-product formation.^{221–224} Therefore, it represents a transformation of great interest in many fields such as organic synthesis,^{225,226} pharmaceuticals,^{227,228} polymers,^{229,230} and chemical biology²³¹ due to the possibility of generate relatively complex products under mild conditions.

Conventionally, this click reaction is performed using a water soluble catalyst comprised of Cu(I) salts, Cu(I) complexes, or Cu(II) salts combined with a reducing agent such as sodium ascorbate or hydrazine.^{226,232–237} However, the low efficiency of conversion of Cu(II) into Cu(I) species associated with the high toxicity of the reducing agents as well as the demand for improved and greener processes has driven the development of several new catalytic systems towards click transformations.^{226,238–241}

In this context, the employment of cuprous oxide (Cu₂O) as the source of highly active Cu(I) species for catalyzing CuAAC reactions represents a promising strategy. This can be performed by two general approaches: by adding pre-synthesized Cu₂O based structures as catalysts in the reaction mixture or by synthesizing them *in-situ* before the substrate addition by using Cu(II) salts combined with reducing agents.^{105,106,233,242} The latter approach, albeit is more widely employed, has several drawbacks that include: *i*) limited amounts of produced

Cu(I) based species; *ii*) poor control over their physicochemical properties (size and shape) that usually lead to low substrate conversions and poor yields; and *iii*) formation a more complex and toxic reaction mixture, which makes the product purification more troublesome and also decrease environmentally friendliness of the process.²³⁸

In this paper, we report the high yield synthesis of Cu₂O spheres displaying well-defined shapes and monodisperse sizes by a facile and robust polyol approach. The Cu₂O spheres were then employed as source of highly catalytic active Cu(I) species towards click reactions between a variety of alkynes and azides under ligand-free and mild conditions (in an open reactor). More specifically, the utilization of Cu₂O spheres enabled superior performances as compared to a conventional protocol in which CuSO₄ is employed in combination with sodium ascorbate as the catalyst system. In addition, good yields for a variety of click products was achieved, which enabled the synthesis of seven unpublished, novel molecules.

8.2. Experimental

Material and Instrumentation

Analytical grade copper(II) nitrate trihydrate (Cu(NO₃)₂·3H₂O, 99%, Sigma-Aldrich), polyvinylpyrrolidone (PVP, Sigma-Aldrich, M.W. 55,000 g/mol), ethylene glycol (EG, 99.8%, Sigma-Aldrich), solvents (dimethyl formamide, C₃H₇NO, 99.8%; methanol, CH₄O, 99.8%; diethyl ether, C₄H₁₀O, 99.5%; anhydrous ethanol, C₂H₆O, 99.8%; acetonitrile, CH₃CN, 99.8%; hexane, C₆H₁₄ – mixture of isomers; ethyl acetate, C₄H₈O₂, 99.5%; dichloromethane, CH₂Cl₂, 99.5%; acetone, C₃H₆O, 99.5%; all of them were purchased from Vetec, Brazil), anhydrous sodium sulphate (Na₂SO₄, 99%, Vetec, Brazil), potassium carbonate (K₂CO₃, 99.0%, Vetec, Brazil), sodium carbonate (Na₂CO₃, 99.5%, Vetec, Brazil), Benzyl alcohols (benzyl alcohol, C₇H₈O, 99.8%; 4-methoxy benzyl alcohol, 98% ; 4-(trifluoromethyl)benzyl alcohol, 98%; all of them purchased from Sigma-Aldrich), pent-4-yn-1-ol (C₅H₈O, 97%, Sigma-Aldrich),

methanesulfonyl chloride ($\text{CH}_3\text{SO}_2\text{Cl}$, 98%, Sigma-Aldrich), sodium azide (NaN_3 , 99%, Vetec, Brazil), triethylamine ($\text{C}_6\text{H}_{15}\text{N}$, 99% Sigma-Aldrich), propargyl bromide solution ($\text{C}_3\text{H}_3\text{Br}$, 80% wt. in toluene, contains 0.3% of magnesium as stabilizer, Sigma-Aldrich), vaniline ($\text{C}_8\text{H}_8\text{O}_3$, 99%, Sigma-Aldrich), (phthalimide, $\text{C}_8\text{H}_5\text{NO}_2$, 99%, Sigma-Aldrich), cinnamic acid ($\text{C}_9\text{H}_8\text{O}_2$, 97%, Sigma-Aldrich), 4-(dimethylamino)pyridine (DMAP, $\text{C}_7\text{H}_{10}\text{N}_2$, 99%, Sigma-Aldrich), *N,N*-dicyclohexylcarbodiimide (DCC, 99%, Sigma-Aldrich) and phenol ($\text{C}_6\text{H}_5\text{OH}$, 99%, Vetec, Brazil) were used as received. Eugenol was extracted via hydrodistillation from cloves purchased from local market. Subsequently, eugenol was purified by column chromatography.

The scanning electron microscopy (SEM) images were obtained using a JEOL field emission gun electron microscope JSM6330F operated at 5 kV. The samples were prepared by drop-casting an aqueous suspension containing the structure over a silicon wafer, followed by drying under ambient conditions. UV-VIS spectrum were obtained from aqueous suspension containing the structure with a Shimadzu UV-1700 spectrophotometer. The Cu content was measured by inductively coupled plasma optical emission spectrometry (ICP-OES) using a Spectro Arcos equipment. X-ray diffractometry (XRD) measurement was performed on a Rigaku model Miniflex equipment using a $\text{CuK}\alpha$ radiation (30 kV, 15 mA, $\lambda = 0.15418$ nm). The diffraction pattern was measured between 10° and $90^\circ 2\theta$ with a step size of $0.02^\circ 2\theta$. ^1H - and ^{13}C -NMR spectra were recorded on a Varian Mercury 300 instrument at 300 MHz and 75 MHz, respectively using CDCl_3 as solvents. NMR data are presented as follows: chemical shift (δ) in ppm, multiplicity, number of protons, *J* values in Hertz (Hz), and proton assignment. Multiplicities are shown as the following abbreviations: s (singlet), d (doublet), dd (doublet of doublets), ddt_{ap} (apparent doublet of doublets of triplets) t (triplet), td (triplet of doublets), q (quartet), quint (quintet), m (multiplet). IR spectra were obtained using Varian 660-IR equipped with GladiATR scanning from 4000 to 500 cm^{-1} . Analytical thin layer chromatography

analysis was conducted on aluminum backed precoated silica gel plates using different solvent systems and were visualized using potassium permanganate solution, phosphomolybdic acid solution and/or UV light. Flash column chromatography was performed using silica gel 60 (60–230 mesh).

Synthesis of Cu₂O spheres

Cu₂O spheres were prepared by the polyol process. In a typical experiment, 3.3 g of polyvinylpyrrolidone (PVP) was dissolved in 25 mL of ethyleneglycol. The resulting solution was heated at 172 °C for 10 minutes and then 200 mg of Cu(NO₃)₂·3H₂O was quickly added. The reaction mixture was kept for 10 more minutes under vigorous stirring leading to the appearance of a light yellow color. Then, the mixture was allowed to cool down to room temperature. After their synthesis, the Cu₂O spheres were washed twice with ethanol and once with ethyleneglycol by successive rounds of centrifugation at 7,000 rpm and removal of the supernatant. After washing, the Cu₂O spheres were suspended in 25 mL of ethyleneglycol.

Click reactions – general procedure

In a 10 mL round bottom flask, it was added 0.5 mmol of azide, 0.6 mmol of terminal alkyne, 310 µL of Cu₂O spheres suspended in ethylene glycol, 1 mL of distilled water and 1 mL of dichloromethane. The resulting mixture was stirred at 40 °C until reaction completion, which was monitored by TLC analysis. Then, the mixture was extracted with ethyl acetate (three times with portions of 15 mL). The organic extracts were combined and the resulting organic layer was dried over sodium sulphate, filtered and concentrated under reduced pressure. The residue was purified by column chromatography eluted with hexane-ethyl acetate-dichloromethane (3:1:3 v/v).

8.3. Results and discussion

Our studies started with the synthesis of Cu₂O spheres by a polyol approach employing Cu(NO₃)₂·3H₂O as the precursor, ethylene glycol as the solvent and source of reducing agents, PVP as the stabilizer/reducing agent, and 172 °C as the reaction temperature (Figure 8.1).²⁴³

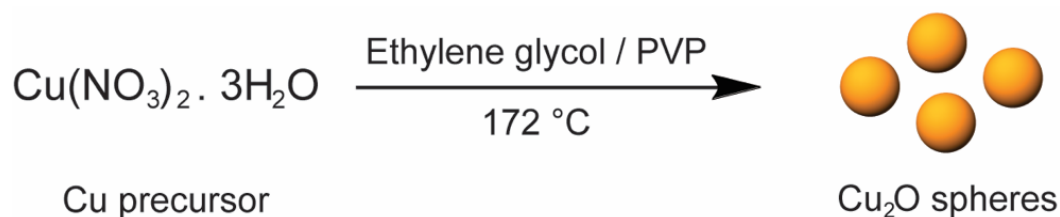


Figure 8.1. Synthesis of Cu₂O spheres by a polyol approach employing Cu(NO₃)₂·3H₂O as the precursor, ethylene glycol as the solvent and source of reducing agents PVP as the stabilizer/reducing agent at 172 °C.

As we were interested in the application of Cu₂O spheres as a source of catalytic active Cu(I) species towards click reactions, the development of a synthetic procedure that enabled narrow size distribution in high yields was crucial to achieve reproducible and efficient click protocols, which represents one of the bottlenecks in the field.²⁴⁴ In fact, SEM images (Figure 8.2A and 8.2B) for the product obtained after only 10 minutes following the addition of Cu(NO₃)₂·3H₂O to a solution containing ethylene glycol and PVP, revealed the formation of Cu₂O spheres displaying well-defined shapes and monodisperse sizes, having 346 ± 13 nm in diameter (histogram of size distribution is shown in Figure 8.2C).

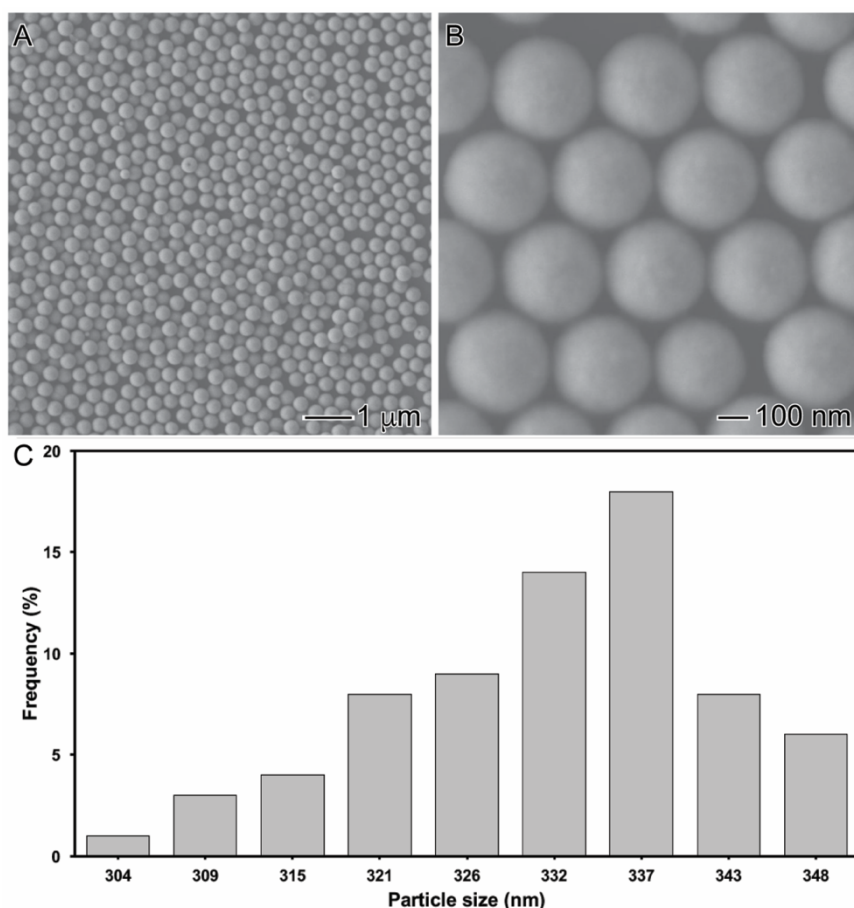


Figure 8.2. (A-B) SEM images for Cu_2O spheres obtained after only 10 minutes following the addition of $\text{Cu}(\text{NO}_3)_2 \cdot 3\text{H}_2\text{O}$ to a solution containing EG and PVP (C) Histogram showing the particle size distribution for the obtained Cu_2O spheres.

The formation of Cu_2O spheres was supported by XRD results (Figure 8.3), in which only the presence of peaks assigned to Cu_2O was detected (cuprite, with lattice constant of 4.26 Å, JCPDS card no. 77-0199) without any crystalline impurities or by-products.²⁴⁵ The UV-VIS spectrum also supports the formation of Cu_2O (Figure 8.4). In this case, the UV-vis spectrum for the obtained Cu_2O spheres displayed a broad band centered at ~ 570 nm with a shoulder centered at ~ 650 nm attributed to weak d^{10} - d^{10} interactions in the cuprite structure (*bbc* Cu_2O array), which also explain the origin of the intense yellow color for this material.²⁴⁶ In addition, the bands centered at ~ 570 and at ~ 650 nm are in agreement with the absorption of Cu_2O structures with particle average size of 300 – 600 nm and their calculated band gap energies corresponded to 2.18 and 1.91 eV, respectively.^{247,248} The Cu content from the synthesis, as

determined by ICP-OES analyses, corresponded to 0.77 mmol, indicating a yield of 93% for the formation of the spheres under our employed conditions.

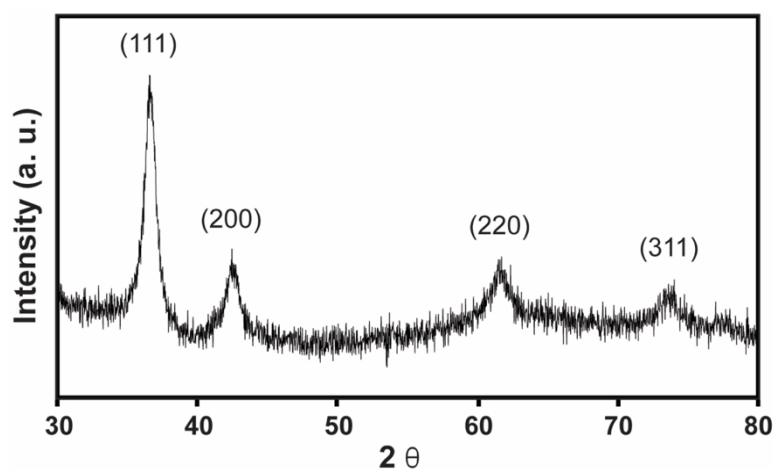


Figure 8.3. (A) X-ray diffraction pattern recorded from the obtained Cu₂O spheres.

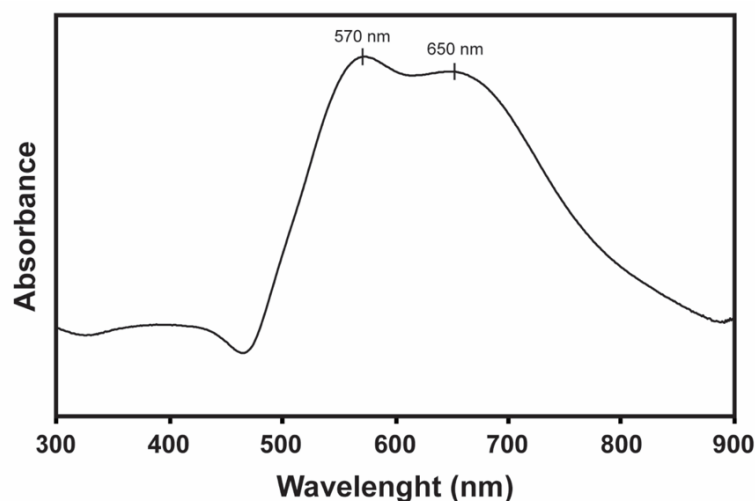


Figure 8.4. (A) UV–VIS spectra recorded from aqueous suspensions containing the obtained Cu₂O spheres.

After the synthesis of Cu₂O spheres in high yields, having monodisperse sizes, and controlled shapes, we turned our attention to their application as source of highly catalytic active Cu(I) species towards click transformations employing terminal alkynes and benzyl azides as substrates under mild conditions, without additional ligands, and in an open reactor (ambient atmosphere). The alkynes were prepared via standard alkylation procedures of phenols, phthalimide, indan-1,3-dione and cinnamic acid. The synthesis of azides were achieved

according previous reports.²⁴⁹ For the characterization of the compounds, spectroscopic (IR and NMR) and spectrometric (mass spectrometry) techniques were utilized.

Our catalytic investigation started with a control experiment without the utilization of any catalyst (Table 8.1, entry 1), in which no significant substrate conversion was observed after 10 h of reaction at room temperature, demonstrating the need of Cu(I) species to achieve the target transformation, as demonstrated by previous reports.^{221–224} This hypothesis was probed when CuSO₄ combined with sodium ascorbate (a traditional catalyst system in click reactions) was added to the system under the same experimental conditions (Table 8.1, entry 2), in which a yield of (46%) for click product (12) was observed after 10 h at room temperature. However, when Cu₂O spheres were employed as source of Cu(I) species (Table 8.1, entry 3) a significant increase in yield for the click product was achieved (85%) under the same Cu loading after 10 h, illustrating their superior catalytic activity which can be associated with limited amount of Cu(I) species formed in situ using CuSO₄ and sodium ascorbate.

Table 8.1. Effect of the nature of the catalyst over the click reaction yield ^a

Reaction scheme: Alkyne (1) + Azide (9) $\xrightarrow[\text{Cu}_2\text{O}]{\text{water/CH}_2\text{Cl}_2 (1:1 \text{ v/v})}$ Product (12)

Entry	Source of Cu(I)	Yield (%) ^b
1	-	(-) ^c
2	CuSO ₄ /Sodium ascorbate	46
3	Cu ₂ O spheres	85

^a All the reactions were run using 1.0 equivalent of alkyne (1) and 1.2 equivalent of azide (9), 20 mol% of catalyst (Cu basis), at room temperature for 10h.

^b Isolated yields.

^c Reaction performed without any catalyst; no product detected.

After demonstrating the superior activity of Cu₂O spheres as catalysts (source of Cu(I) species), we performed a series of experiments in order to optimize the efficiency of our click process as a function of the temperature (Table 8.2) using the alkyne **1** and benzylazide **9** as model substrates to afford the triazolic compound **12** as depicted in the first row of Table 8.2. Herein, when the reaction was performed at room temperature (Table 8.2, entry 1), a yield of 85 % for compound **12** was obtained after 10 h of reaction. However, when the reaction temperature was increased to 40 °C (Table 8.2, entry 2), almost the same yield (87 %) was achieved after only 2 h of reaction. Finally, at 60 °C (Table 8.2, entry 3), the total conversion of alkyne was observed but a lower yield for the compound **12** (63%) was achieved, indicating a lower selectivity for the click product at this temperature. Thus, 40 °C corresponded to lowest temperature in which good yields and maximum selectivity were achieved, and it was chosen as the temperature for our further studies.

Table 8.2. Optimization of the temperature parameter for the click reaction in the presence of Cu₂O spheres as catalysts^a

Reaction scheme: Alkyne **1** (4-ethynylphenyl ether) + Benzylazide **9** (benzene ring with -CH₂N₃) → Triazolic compound **12** (1-(4-phenoxyphenyl)-1H-1,2,3-triazole-4-ylmethane). Conditions: water/CH₂Cl₂ (1:1 v/v), Cu₂O catalyst.

Entry	Temperature	Reaction Time (h)	Yield (%) ^b
1	Room temperature	10	85
2	40 °C	2	87
3	60 °C	1	63

^a All the reactions were run using 1.0 equivalent of alkyne (**1**) and 1.2 equivalent of azide (**9**), 20 mol% of catalyst (Cu basis, 310 μL of Cu₂O suspension).

^b Isolated yields.

Thus, by using the optimized conditions, several alkynes and azides were employed as substrates in the click reactions to afford the corresponding 1,2,3-triazols as shown in Table 8.3. Herein, we performed several experiments in order to evaluate the influence of substrate structures over the click reaction and probe the robustness of our system for the synthesis of 1,2,3-triazols compounds with a large variety of chemical skeleton. Firstly, we employed azides containing electron-donating 10 and electron-withdrawing 11 groups in reactions with alkyne 1 (Table 8.3, entries 1 and 2, respectively). When the azide contained an electron-donating group (Table 8.3, entry 1), the triazole product (13) was obtained in 41 % yield after 5 h of reaction. However, when an azide containing an electron-withdrawing group was employed (Table 8.3, entry 2) a yield of 75 % for the triazole product (14) was observed after 3 h of reaction, indicating a higher reaction rate and selectivity for the click compound in agreement with previous reports.^{250,251} Then, we probed the influence of the size of the chain linked to the triazole group over the yield for the respective click product. To this end, we employed as substrates two alkynes derived from eugenol, a natural product found in several aromatic plants and corresponding to the main component of essential oil from cloves. More specifically, we employed alkynes with three (Table 8.3, entry 3) and five (Table 8.3, entry 4) carbon atoms in the aliphatic chain. In both cases, high yields were observed after 3 h of reaction. When the eugenol derivative (2) (containing a three carbon atom aliphatic chain) was employed as substrate, 90 % yield for the unpublished, novel click product 15 was observed. On the other hand, the utilization of a substrate with a five carbon aliphatic chain (3) led to a drop in the yield to 71 % for 16, which is also novel/unpublished. We also performed click reactions employing as substrates alkynes derived from two other natural products, denoted compound 5, which was obtained from cinnamic acid, and compound 6, which is derived from vaniline (Table 8.3, entries 6 and 7). In both cases, the reaction of compounds 5 and 6 with benzyl azide 9 afforded the unpublished click compounds 18 and 19 in synthetically useful

yields (61 and 57 %, respectively). This results indicate that the utilization of Cu₂O spheres as source of Cu(I) species under our reported conditions can represent a promising strategy for the synthesis of novel click products derived from natural raw-materials, generating complex molecules with high aggregated-value using natural products as starting material. In order to demonstrate the versatility of our Cu₂O spheres for this target application, satisfactory yields were obtained for a variety of alkynes (4, 7 and 9) as substrates for the reaction with benzilazide 9 (Table 8.3, entries 5, 8 and 9), which produced three novel, unpublished compounds (17, 20, and 21, respectively).

Table 8.3 - Click reactions using different alkynes and azides in the presence of Cu₂O spheres as catalyst^a

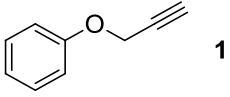
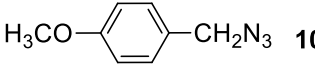
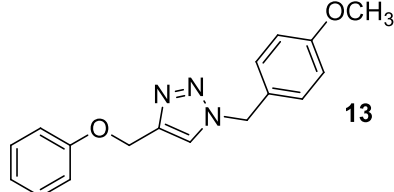
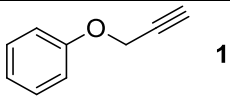
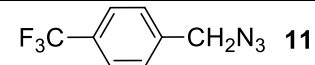
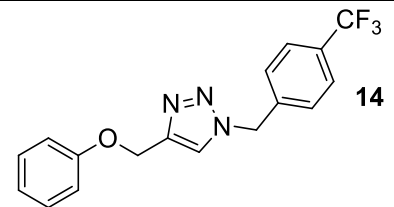
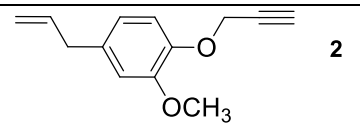
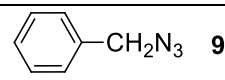
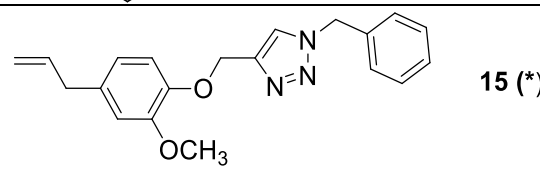
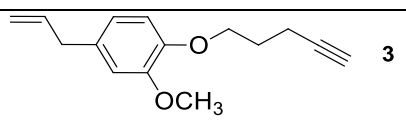
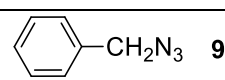
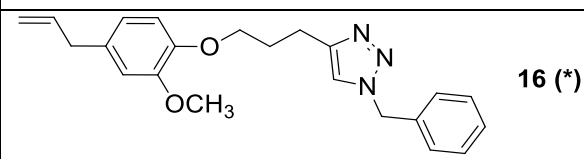
Entry	Alkyne	Azide	Product	Reaction Time (h)	Yield (%) ^b
1	 1	 10	 13	5	41
2	 1	 11	 14	3	75
3	 2	 9	 15 (*)	3	90
4	 3	 9	 16 (*)	3	71

Table 8.3 – continued

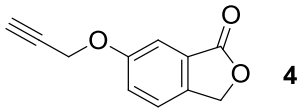
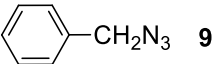
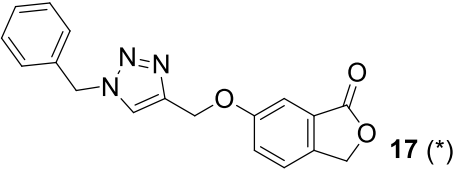
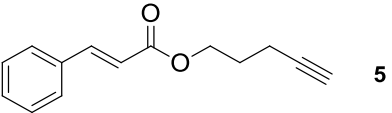
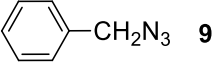
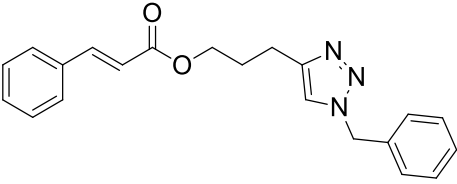
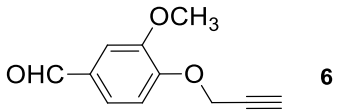
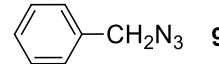
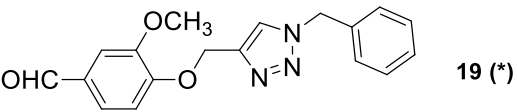
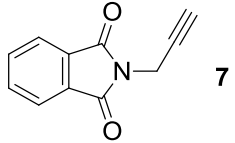
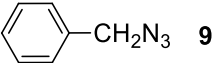
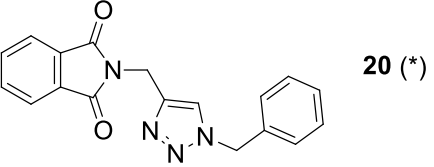
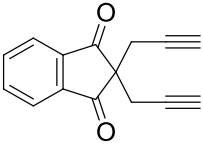
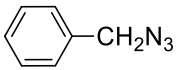
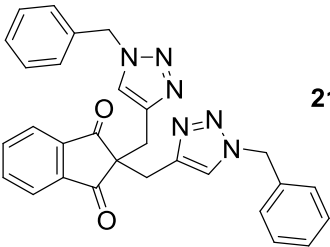
5	 <p>4</p>	 <p>9</p>	 <p>17 (*)</p>	2	65
6	 <p>5</p>	 <p>9</p>	 <p>18 (*)</p>	2	61
7	 <p>6</p>	 <p>9</p>	 <p>19 (*)</p>	2	57
8	 <p>7</p>	 <p>9</p>	 <p>20 (*)</p>	2	76

Table 8.3 – continued

<p>9</p>	 <p>8</p> <p>(4)</p>	 <p>9</p>	 <p>21 (*)</p>	<p>17</p>	<p>11</p>
-----------------	---	---	--	-----------	-----------

^a All the reactions were performed using 1.0 equivalent of alkyne (**1**) and 1.2 equivalent of azide (**2**), 20 mol% of catalyst (Cu basis, 310 μ L of Cu_2O suspension).

^b Isolated yields.

* novel/unpublished molecules

A general proposed mechanism for the cycloaddition reaction between terminal alkynes and benzyl azides in the presence of Cu_2O spheres as the source of Cu(I) catalytic species is shown in Figure 8.5.²⁵² As we employed a suspension containing solid copper(I) species (Cu_2O), it is intuitive that the CuAAC reaction would occur at the particle surface.^{253,254} In this context, the proposed reaction mechanism would involve the following steps: *i*) alkyne coordination onto the Cu_2O surface; *ii*) its deprotonation to form the alkynyl-copper(I) intermediate, *iii*) nucleophilic attack from alkynyl-copper(I) intermediate to the azide followed by its coordination onto the Cu_2O surface; (iv) the cycloaddition reaction, (v) protonation of C–Cu bond followed by *iv*) desorption of 1,2,3-triazole product to the reaction medium.

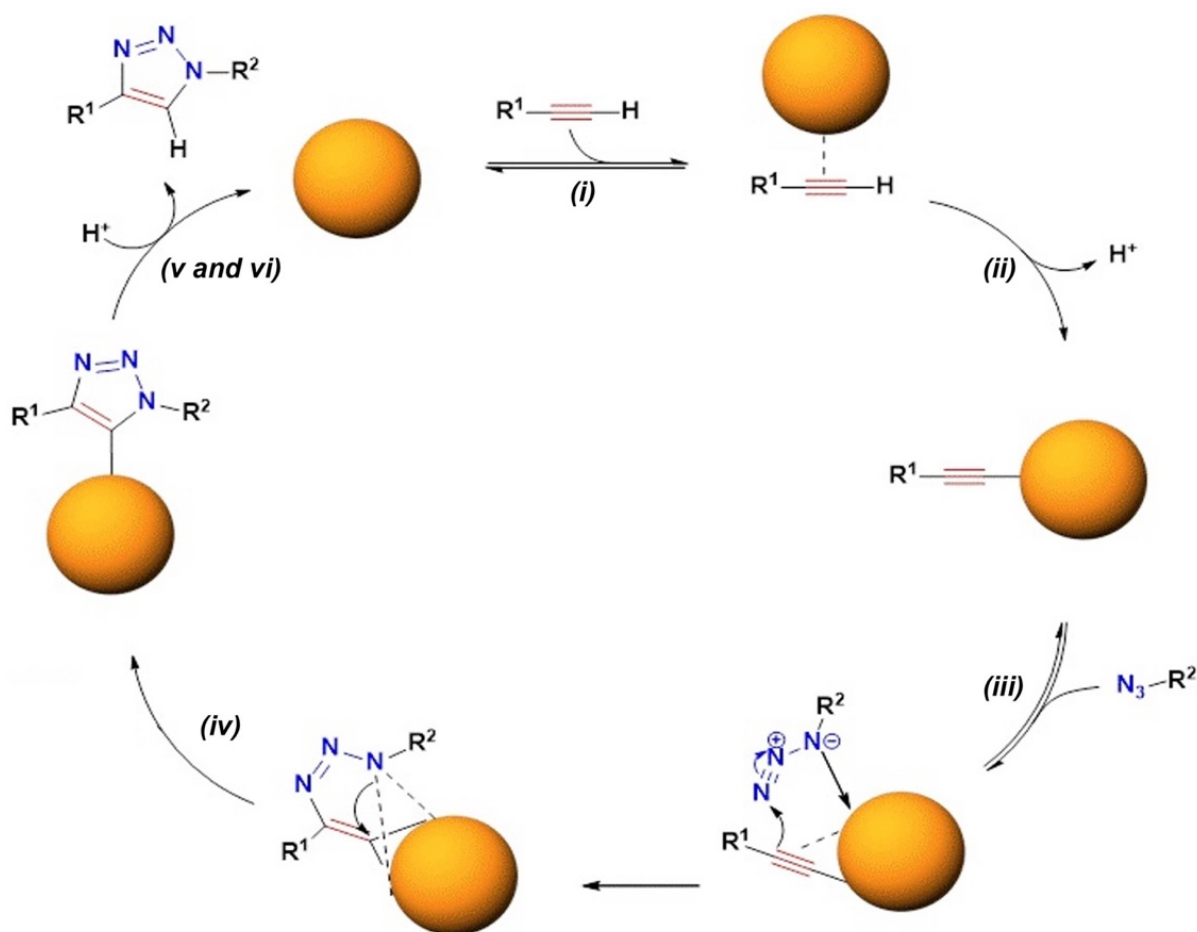


Figure 8.5. Proposed mechanism for the click reaction in the presence of Cu_2O spheres as catalysts (source of Cu(I) active species).

8.4. Conclusion

We described herein the utilization of monodisperse Cu₂O spheres as an efficient source of Cu(I) catalytic species for the synthesis of 1,2,3-triazoles via the Copper(I)-catalyzed azide–alkyne cycloaddition (CuAAC) reaction (also known as click reaction) between terminal alkynes and benzyl azides. The Cu₂O spheres were successfully obtained in high yields (93 %) in only 10 minutes by a simple and robust polyol approach using ethyleneglycol as solvent and PVP as stabilizer at 172 °C. The utilization of Cu₂O spheres as catalysts (source of Cu(I) species) led superior performance in the click reaction as compared to conventional methods employing CuSO₄ and sodium ascorbate as the catalyst system under the same experimental conditions (time, temperature, and Cu loading). Interestingly, using Cu₂O spheres as source of Cu(I) species, satisfactory yields, for a wealth of substrates with different chemical skeletons under mild conditions, ligand-free, and in an open reactor (without inert atmosphere), were obtained demonstrating the promising application of Cu₂O spheres towards click reactions. Moreover, the reported approach enabled the synthesis of seven unpublished/novel molecules including derivate compounds from natural raw-material, showing the applicability of our reported approach for the synthesis of new structures by click chemistry. We believe the results reported herein shed new insights into the optimization of activity and versatility of click reactions towards the synthesis of target molecules in environmentally friendly conditions.

8.5. References

- (1) Kolb, H. C.; Finn, M. G.; Sharpless, K. B. Click Chemistry: Diverse Chemical Function from a Few Good Reactions. *Angew. Chemie Int. Ed.* **2001**, *40* (11), 2004–2021.
- (2) Gothelf, K. V; Jørgensen, K. A. Asymmetric 1,3-Dipolar Cycloaddition Reactions. *Chem. Rev.* **1998**, *98* (2), 863–910.
- (3) Padwa, A. 4.9 - Intermolecular 1,3-Dipolar Cycloadditions A2 - Trost, Barry M.; Fleming, I. B. T.-C. O. S., Ed.; Pergamon: Oxford, 1991; pp 1069–1109.
- (4) Rostovtsev, V. V; Green, L. G.; Fokin, V. V; Sharpless, K. B. A Stepwise Huisgen Cycloaddition Process: Copper(I)-Catalyzed Regioselective “Ligation” of Azides and

- Terminal Alkynes. *Angew. Chemie* **2002**, *114* (14), 2708–2711.
- (5) Moses, J. E.; Moorhouse, A. D. The Growing Applications of Click Chemistry. *Chem. Soc. Rev.* **2007**, *36* (8), 1249–1262.
 - (6) Simon, M.-O.; Li, C.-J. Green Chemistry Oriented Organic Synthesis in Water. *Chem. Soc. Rev.* **2012**, *41* (4), 1415–1427.
 - (7) Kolb, H. C.; Sharpless, K. B. The Growing Impact of Click Chemistry on Drug Discovery. *Drug Discov. Today* **2003**, *8* (24), 1128–1137.
 - (8) Thirumurugan, P.; Matosiuk, D.; Jozwiak, K. Click Chemistry for Drug Development and Diverse Chemical–Biology Applications. *Chem. Rev.* **2013**, *113* (7), 4905–4979.
 - (9) Golas, P. L.; Matyjaszewski, K. Marrying Click Chemistry with Polymerization: Expanding the Scope of Polymeric Materials. *Chem. Soc. Rev.* **2010**, *39* (4), 1338–1354.
 - (10) Yao, B.; Sun, J. Z.; Qin, A.; Tang, B. Z. Click Chemistry: A Powerful and Versatile Methodology for Preparation of Ferrocene-Containing Polymers. *J. Inorg. Organomet. Polym. Mater.* **2015**, *25* (1), 37–46.
 - (11) Rosner, D.; Schneider, T.; Schneider, D.; Scheffner, M.; Marx, A. Click Chemistry for Targeted Protein Ubiquitylation and Ubiquitin Chain Formation. *Nat. Protoc.* **2015**, *10* (10), 1594–1611.
 - (12) Baron, A.; Bleriot, Y.; Sollogoub, M.; Vauzeilles, B. Phenylenediamine Catalysis Of “click Glycosylations” in Water: Practical and Direct Access to Unprotected Neoglycoconjugates. *Org. Biomol. Chem.* **2008**, *6* (11), 1898–1901.
 - (13) Jiang, Y.; Kong, D.; Zhao, J.; Qi, Q.; Li, W.; Xu, G. Cu(OAc)₂H₂O/NH₂NH₂H₂O: An Efficient Catalyst System That in Situ Generates Cu₂O Nanoparticles and HOAc for Huisgen Click Reactions. *RSC Adv.* **2014**, *4* (2), 1010–1014.
 - (14) Díez-González, S.; Nolan, S. P. [(NHC)₂Cu]X Complexes as Efficient Catalysts for Azide–Alkyne Click Chemistry at Low Catalyst Loadings. *Angew. Chemie Int. Ed.* **2008**, *47* (46), 8881–8884.
 - (15) Özçubukçu, S.; Ozkal, E.; Jimeno, C.; Pericàs, M. A. A Highly Active Catalyst for Huisgen 1,3-Dipolar Cycloadditions Based on the Tris(triazolyl)methanol–Cu(I) Structure. *Org. Lett.* **2009**, *11* (20), 4680–4683.
 - (16) Garcia-Alvarez, J.; Diez, J.; Gimeno, J. A Highly Efficient Copper(i) Catalyst for the 1,3-Dipolar Cycloaddition of Azides with Terminal and 1-Iodoalkynes in Water: Regioselective Synthesis of 1,4-Disubstituted and 1,4,5-Trisubstituted 1,2,3-Triazoles. *Green Chem.* **2010**, *12* (12), 2127–2130.
 - (17) Pathigoolla, A.; Pola, R. P.; Sureshan, K. M. A Versatile Solvent-Free Azide–alkyne Click Reaction Catalyzed by in Situ Generated Copper Nanoparticles. *Appl. Catal. A Gen.* **2013**, *453*, 151–158.
 - (18) Alonso, F.; Moglie, Y.; Radivoy, G. Copper Nanoparticles in Click Chemistry. *Acc. Chem. Res.* **2015**, *48* (9), 2516–2528.
 - (19) Jin, T.; Yan, M.; Yamamoto, Y. Click Chemistry of Alkyne–Azide Cycloaddition Using Nanostructured Copper Catalysts. *ChemCatChem* **2012**, *4* (9), 1217–1229.
 - (20) Deraedt, C.; Pinaud, N.; Astruc, D. Recyclable Catalytic Dendrimer Nanoreactor for Part-Per-Million CuI Catalysis of “Click” Chemistry in Water. *J. Am. Chem. Soc.* **2014**, *136* (34), 12092–12098.
 - (21) Totobenazara, J.; Burke, A. J. New Click-Chemistry Methods for 1,2,3-Triazoles Synthesis: Recent Advances and Applications. *Tetrahedron Lett.* **2015**, *56* (22), 2853–2859.
 - (22) Chanda, K.; Rej, S.; Huang, M. H. Facet-Dependent Catalytic Activity of Cu₂O Nanocrystals in the One-Pot Synthesis of 1,2,3-Triazoles by Multicomponent Click Reactions. *Chem. – A Eur. J.* **2013**, *19* (47), 16036–16043.
 - (23) Chanda, K.; Rej, S.; Huang, M. H. Investigation of Facet Effects on the Catalytic Activity

- of Cu₂O Nanocrystals for Efficient Regioselective Synthesis of 3,5-Disubstituted Isoxazoles. *Nanoscale* **2013**, 5 (24), 12494–12501.
- (24) Tsai, Y.-H.; Chanda, K.; Chu, Y.-T.; Chiu, C.-Y.; Huang, M. H. Direct Formation of Small Cu₂O Nanocubes, Octahedra, and Octapods for Efficient Synthesis of Triazoles. *Nanoscale* **2014**, 6 (15), 8704–8709.
- (25) Chen, W.; Li, L.; Peng, Q.; Li, Y. Polyol Synthesis and Chemical Conversion of Cu₂O Nanospheres. *Nano Res.* **2012**, 5 (5), 320–326.
- (26) Nandivada, H.; Jiang, X.; Lahann, J. Click Chemistry: Versatility and Control in the Hands of Materials Scientists. *Adv. Mater.* **2007**, 19 (17), 2197–2208.
- (27) Park, J. C.; Kim, J.; Kwon, H.; Song, H. Gram-Scale Synthesis of Cu₂O Nanocubes and Subsequent Oxidation to CuO Hollow Nanostructures for Lithium-Ion Battery Anode Materials. *Adv. Mater.* **2009**, 21 (7), 803–807.
- (28) Buljan, A.; Llundell, M.; Ruiz, E.; Alemany, P. Color and Conductivity in Cu₂O and CuAlO₂: A Theoretical Analysis of d₁₀–d₁₀ Interactions in Solid-State Compounds. *Chem. Mater.* **2001**, 13 (2), 338–344.
- (29) Yang, M.; Zhu, J.-J. Spherical Hollow Assembly Composed of Cu₂O Nanoparticles. *J. Cryst. Growth* **2003**, 256 (1–2), 134–138.
- (30) Wang, L. X. and X. C. and Y. W. and C. C. and W. L. and W. P. and Y. Solution-Phase Synthesis of Single-Crystal Hollow Cu₂O Spheres with Nanoholes. *Nanotechnology* **2006**, 17 (5), 1501.
- (31) Borgati, T. F.; Alves, R. B.; Teixeira, R. R.; Freitas, R. P. de; Perdigão, T. G.; Silva, S. F. da; Santos, A. A. dos; Bastidas, A. de J. O. Synthesis and Phytotoxic Activity of 1,2,3-Triazole Derivatives. *Journal of the Brazilian Chemical Society*. scielo 2013, pp 953–961.
- (32) Demko, Z. P.; Sharpless, K. B. A Click Chemistry Approach to Tetrazoles by Huisgen 1,3-Dipolar Cycloaddition: Synthesis of 5-Acyltetrazoles from Azides and Acyl Cyanides. *Angew. Chemie Int. Ed.* **2002**, 41 (12), 2113–2116.
- (33) Demko, Z. P.; Sharpless, K. B. Preparation of 5-Substituted 1H-Tetrazoles from Nitriles in Water. *J. Org. Chem.* **2001**, 66 (24), 7945–7950.
- (34) Balcioglu, N.; Uraz(Ünalán), I.; Bozkurt, C.; Sevin, F. Reaction Mechanism of copper(I) Catalysed Head-to-Head Dimerization of 1-Alkynes: An Experimental and Theoretical Study. *Polyhedron* **1997**, 16 (2), 327–334.
- (35) Paxton, W. F.; Spruell, J. M.; Stoddart, J. F. Heterogeneous Catalysis of a Copper-Coated Atomic Force Microscopy Tip for Direct-Write Click Chemistry. *J. Am. Chem. Soc.* **2009**, 131 (19), 6692–6694.
- (36) Veerakumar, P.; Velayudham, M.; Lu, K.-L.; Rajagopal, S. Highly Dispersed Silica-Supported Nanocopper as an Efficient Heterogeneous Catalyst: Application in the Synthesis of 1,2,3-Triazoles and Thioethers. *Catal. Sci. Technol.* **2011**, 1 (8), 1512–1525.

Chapter 9

Kinetic Understanding of Galvanic Replacement Reactions in Cu₂O Under Aerobic Conditions: Elucidating the Formation of Bowls, Rattles, and Dendrites

9.1. Introduction

Galvanic replacement has been established as an efficient and versatile approach for the one-step and relatively fast synthesis of hollow nanostructures displaying controllable sizes, shapes, compositions, and interiors.¹⁻⁷ This strategy has been extensively investigated for the synthesis of bi- and trimetallic nanoparticles based on (Ag, Pd, Pt, Au, Rh, and Ru).¹⁻⁹ In addition, it has been demonstrated that this approach can be extended to metal oxides to generate both oxide/oxide and metal/oxide systems. In these systems, oxides in low oxidation states such as Mn₃O₄, Co₃O₄, and Cu₂O are employed as sacrificial templates. This is because these species are susceptible to oxidation and dissolution, under appropriate conditions, by a variety of species.¹⁰⁻¹⁵

Galvanic replacement in metal oxides opens enormous possibilities for the synthesis of hollow oxide-based systems for sensing, catalytic, and energy storage/conversion applications.^{16,17} However, despite these attractive features, a precise understanding over the formation mechanism governing galvanic replacement reactions in metal oxide systems remains limited to a few systems. Moreover, detailed explanations concerning the formation of relatively complex morphologies are scarce.^{10,16-18}

Even though it has been shown that precursor kinetics can be put to work to the controlled synthesis of various nanomaterials, its effect over galvanic replacement reactions have remained unexploited.¹⁹⁻²³ It may be expected that precursor reduction kinetics should significantly influence the morphology and composition when it becomes comparable with other oxidative processes that

may occur during galvanic replacement reactions.²⁴ Therefore, kinetic control may represent a promising strategy for the rational understanding and synthesis of metal/metal-oxides hybrids displaying novel or complex morphologies.²⁴

We report herein a systematic investigation on the effect of precursor reduction kinetics over the morphology and composition of the materials obtained by galvanic replacement reaction employing Cu₂O oxides as sacrificial templates. Cu₂O was chosen due to its susceptibility to oxidation under aerobic conditions. In this case, we were particularly interested in investigating how the relative rates of Cu₂O oxidation by O₂ relative to Cu₂O oxidation by galvanic replacement can be employed to control the morphology and composition. Specifically, we focused on three metal precursors with fast, medium, and slow reduction kinetics in the presence of Cu₂O under aerobic conditions: PdCl₄²⁻_(aq), AuCl₄⁻_(aq), and Ru³⁺_(aq), respectively. Surprisingly, we found that metal-oxide based bowls, rattles, or dendrites could be obtained by simply changing the precursor reduction kinetics, expanding on the versatility and understanding of the galvanic replacement approach in metal oxides.

9.2. Experimental

Material and Instrumentation

Analytical grade copper(II) nitrate trihydrate (Cu(NO₃)₂·3H₂O, 99%, Sigma-Aldrich), polyvinylpyrrolidone (PVP, Sigma-Aldrich, M.W. 55,000 g/mol), ethylene glycol (EG, 99.8%, Sigma-Aldrich), tetrachloroauric acid (HAuCl₄·3H₂O, ≥99.9%, Sigma-Aldrich), potassium tetrachloropalladate (K₂PdCl₄, ≥99.99%, Sigma-Aldrich), Ruthenium(III) chloride hydrate (RuCl₃·xH₂O, 38-42% Ru basis, Sigma-Aldrich), 4-nitrophenol (C₆O₃NH₅, ≥99%, Sigma-Aldrich), and sodium borohydride (NaBH₄, 98%, Sigma-Aldrich) were used as received.

The scanning electron microscopy (SEM) images were obtained using a JEOL field emission

gun electron microscope JSM6330F operated at 5 kV. The samples were prepared by drop-casting an aqueous suspension containing the structure over a silicon wafer, followed by drying under ambient conditions. Transmission electron microscopy (TEM) images were obtained using a JEOL JEM2100 microscope operated at 200 kV. High angle annular dark field (HAADF) scanning transmission electron microscopy (STEM) images and energy dispersive X-ray (EDX) spectroscopy images were acquired using a FEI TECNAI G2 F20 operated at 200 kV. Samples for TEM were prepared by drop-casting an aqueous suspension of the nanostructures over a carbon-coated copper grid, followed by drying under ambient conditions. UV-VIS spectrum were obtained from aqueous suspension containing the structure with a Shimadzu UV-1700 spectrophotometer. The metal contents were measured by inductively coupled plasma optical emission spectrometry (ICP-OES) using a Spectro Arcos equipment. X-ray diffractometry (XRD) measurement was performed on a Rigaku model Miniflex equipment using a $\text{CuK}\alpha$ radiation (30 kV, 15 mA, $\lambda = 0.15418$ nm). The diffraction pattern was measured between 10 and $90^\circ 2\theta$ with a step size of $0.02^\circ 2\theta$. X-ray photoelectron spectroscopy (XPS) data of the samples was obtained with an SPECSLAB II (Phoibos-Hsa 3500 150, 9 channeltrons) SPECS spectrometer, with Al $\text{K}\alpha$ source ($E = 1486.6$ eV) operating at 12 kV, pass energy (E_{pass}) = 40 eV, 0.1 eV energy step and acquisition time of 1 s per point. The samples were placed on stainless steel sample-holders and were transferred under inert atmosphere to the XPS prechamber and held there for a 2 h in a vacuum atmosphere. The residual pressure inside the analysis chamber was $\sim 1 \times 10^{-9}$ Torr.

Synthesis of Cu_2O spheres

Cu_2O spheres were prepared by the polyol process. In a typical experiment, 3.3 g of polyvinylpyrrolidone (PVP) was dissolved in 25 mL of ethyleneglycol. The resulting solution was heated at 172°C for 10 minutes and then 200 mg of $\text{Cu}(\text{NO}_3)_2 \cdot 3\text{H}_2\text{O}$ was quickly added. The

reaction mixture was kept for 15 more minutes under vigorous stirring leading to the appearance of a light yellow color. Then, the mixture was allowed to cool down to room temperature. After their synthesis, the Cu₂O spheres were washed twice with ethanol and once with ethyleneglycol by successive rounds of centrifugation at 7,000 rpm and removal of the supernatant. After washing, the Cu₂O spheres were suspended in 25 mL of ethyleneglycol. For the synthesis of the bimetallic nano hybrids, 1 mL of the suspension of Cu₂O spheres was washed twice with ethanol and twice with water by successive rounds of centrifugation at 7,000 rpm and removal of the supernatant. After washing, the Cu₂O spheres were suspended in 1 mL of PVP aqueous solution (0.1 wt %).

Galvanic replacement reaction between Cu₂O and PdCl₄²⁻_(aq), AuCl₄⁻_(aq), or Ru³⁺_(aq)

In a typical run, 6 mL of PVP aqueous solution (0.1 wt %) was stirred at 90 °C for 10 min in a 25 mL round-bottom flask. Then, 1 mL of as-prepared Cu₂O spheres washed and suspended in PVP aqueous solution (0.1 wt %) was added to the flask and stirred for 30 s followed by the quick addition (one shot) of 5 mL of aqueous solutions of the respective metal precursor (PdCl₄²⁻_(aq), AuCl₄⁻_(aq), or Ru³⁺_(aq)). Here, for each precursor, three parallel reactions were carried out, in which their concentrations corresponded to 0.1, 0.6, and 1.0 mM (0.5, 3.0, and 5.0 μmol). After the addition of the precursor solution, the reaction was allowed to proceed at 90 °C for another 2 h. In order to monitor the kinetic of metal reduction during the formation of the nano hybrids as a function of time, parallel reactions were performed in the same conditions and quenched by cooling the reaction flask in ice water at different intervals: 30 s, 1 min, 5 min, 10 min, 30 min, 1 h, and 2 h, followed by the immediate washing with ethanol (twice) and water (twice) by successive rounds of centrifugation at 13,000 rpm and removal of the supernatant. After washing, the resulting nanostructures were suspended in 12 mL of PVP aqueous solution (0.1 wt %). The resulting suspensions were then employed in the catalytic tests for the 4-nitrophenol reduction reaction.

Catalytic reduction of 4-nitrophenol

Typically, 1 mL of a 1.4×10^{-4} M 4-nitrophenol aqueous solution, 2 mL of 4.2×10^{-2} M sodium borohydride aqueous solution, and 50 μL of the suspension containing the synthesized nanostructures was added into a quartz cuvette. The catalytic transformation was monitored by UV–VIS spectroscopy, in which the intensity in the absorbance at 400 nm (assigned to 4-nitrophenolate ions) was monitored as a function of time (this signal decreased as the consumption of 4-nitrophenolate ions and formation of 4-aminophenol take place). In this case, the UV-VIS spectra were collected at 13 s time intervals in the 350 to 500 nm range. A calibration curve for absorbance as a function of the 4-nitrophenolate concentration was employed in order to calculate the 4-nitrophenol conversion %. The catalytic activities were expressed in terms of substrate conversion versus time.

9.3. Results and discussion

Our studies started with the synthesis of Cu_2O spheres by a polyol approach.^{25,26} As shown in Figure 9.1, they displayed uniform spherical shapes and monodisperse sizes (503 ± 23 nm in diameter).

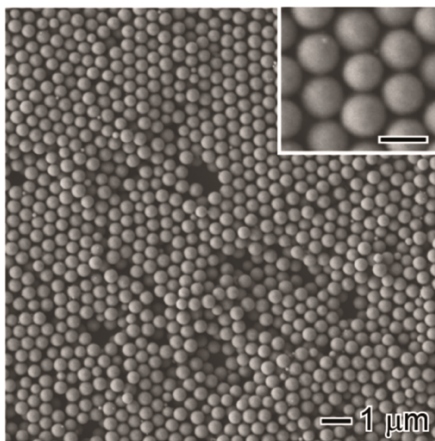


Figure 9.1. SEM image of the Cu_2O spheres synthesized by a polyol approach and employed as templates in the galvanic replacement reaction with $\text{PdCl}_4^{2-}(\text{aq})$, $\text{AuCl}_4^-(\text{aq})$, and $\text{Ru}^{3+}(\text{aq})$. The scale bar in the inset corresponds to 500 nm.

XRD (Figure 9.2A), UV-Vis (Figure 9.2B), and XPS (Figure 9.2C-E) results confirmed that the obtained spheres are composed by Cu_2O species in the structure.

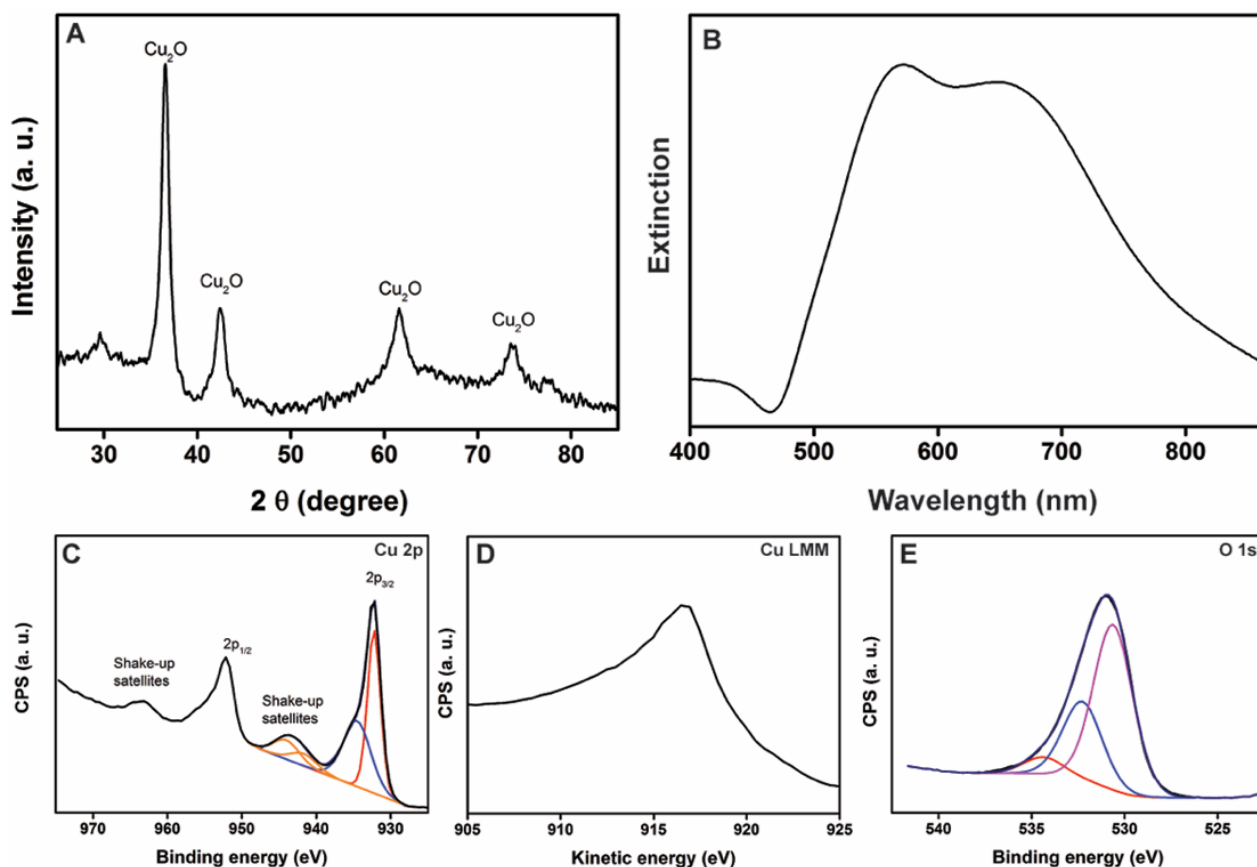


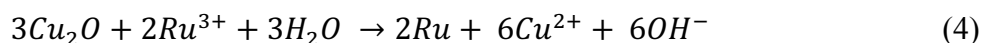
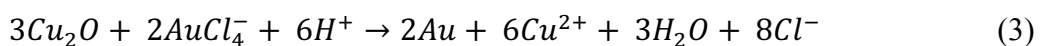
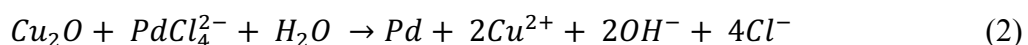
Figure 9.2. (A) XRD pattern, (B) UV-VIS spectrum, and XPS spectra of the Cu 2p (C), Cu LMM (D), and O 1s (E) core-levels for the Cu_2O spheres.

The XRD results (Figure 9.2A) showed peaks related to the presence of Cu_2O (cuprite, with lattice constant of 4.26 \AA , JCPDS card no. 77-0199). No additional peaks could be detected associated with the presence of other crystalline impurities or by-products.² The formation of Cu_2O is also supported by UV-VIS analysis (Figure 9.2B), in which the spectrum presented a broad band centered at $\sim 570 \text{ nm}$ together a shoulder centered at $\sim 650 \text{ nm}$. Both bands can be attributed to the cuprite structure (*bbc* Cu_2O array) with calculated band gap energies of 2.18 and 1.91 eV, respectively.³⁻⁵ The Cu 2p XPS spectra (Figure 9.2C) presented peaks relate to Cu_2O (932.3 eV) and $\text{Cu}(\text{OH})_2$ (934.5 eV) with their respective weak satellites also present. However, the Cu LMM

spectrum (Figure 9.2D) indicated the predominance of Cu₂O species due to presence of only one LMM peak at 916.7. The O 1s XPS spectra (Figure 9.2E) showed the presence of three surface oxygen species with binding energies in range of 525–540 eV: *i*) lattice oxygen (denoted as O_L, green trace) in the range of 529.9–529.5; *ii*) oxygen vacancies or surface oxygen ions (denoted as O_s, orange trace) in the range of 532.0–531.4 eV; and adsorbed water (denoted as O_w, blue trace) around 533.9 eV. The presence of Cu(OH)₂ species at the surface can be associated with the Cu⁺ to Cu²⁺ oxidation, which agrees with the high oxidation susceptibility of Cu⁺ in Cu₂O, as described by Equation 1.²⁷



The Cu₂O spheres were then employed as model starting materials to understand the effect of different precursors over the morphology of complex materials obtained from the galvanic replacement reaction between Cu₂O and different noble metals. Specifically, we focused on PdCl₄²⁻_(aq), AuCl₄⁻_(aq), and Ru³⁺_(aq) as precursors aiming at the generation of complex nanostructures comprised of Cu₂O or CuO and Pd, Au, and Ru nanoparticles. In these systems, the following galvanic replacement reactions are expected:²⁸



Moreover, other parallel reactions can also take place. These include the Cu₂O oxidation to CuO (or Cu(OH)₂ as shown in Equation 1) and CuO dissolution to Cu²⁺ in acidic media as shown below.²⁷



Therefore, it can be expected that the morphological and compositional features of the produced nanostructures will be strongly dependent on the relative rates of all these reactions, in which the precursor reduction kinetics is expected to play a central role and thus enable the tuning of morphological and compositional features. As a matter of fact, it has been established that kinetic control represents a powerful tool for the precise manipulation of the properties (size, structure, and shape) of metal nanoparticles.^{19–23} Thus, a change in the kinetic profile may drastically affect the final morphology and composition of a nanostructure, which represents the goal of our study.^{29,30}

To this end, we started by monitoring the PdCl₄²⁻_(aq), AuCl₄⁻_(aq), and Ru³⁺_(aq) precursor reduction kinetics during their galvanic replacement reaction with Cu₂O spheres, in which the amount of precursor reduced as a function of time was measured as described in Figure 9.3.

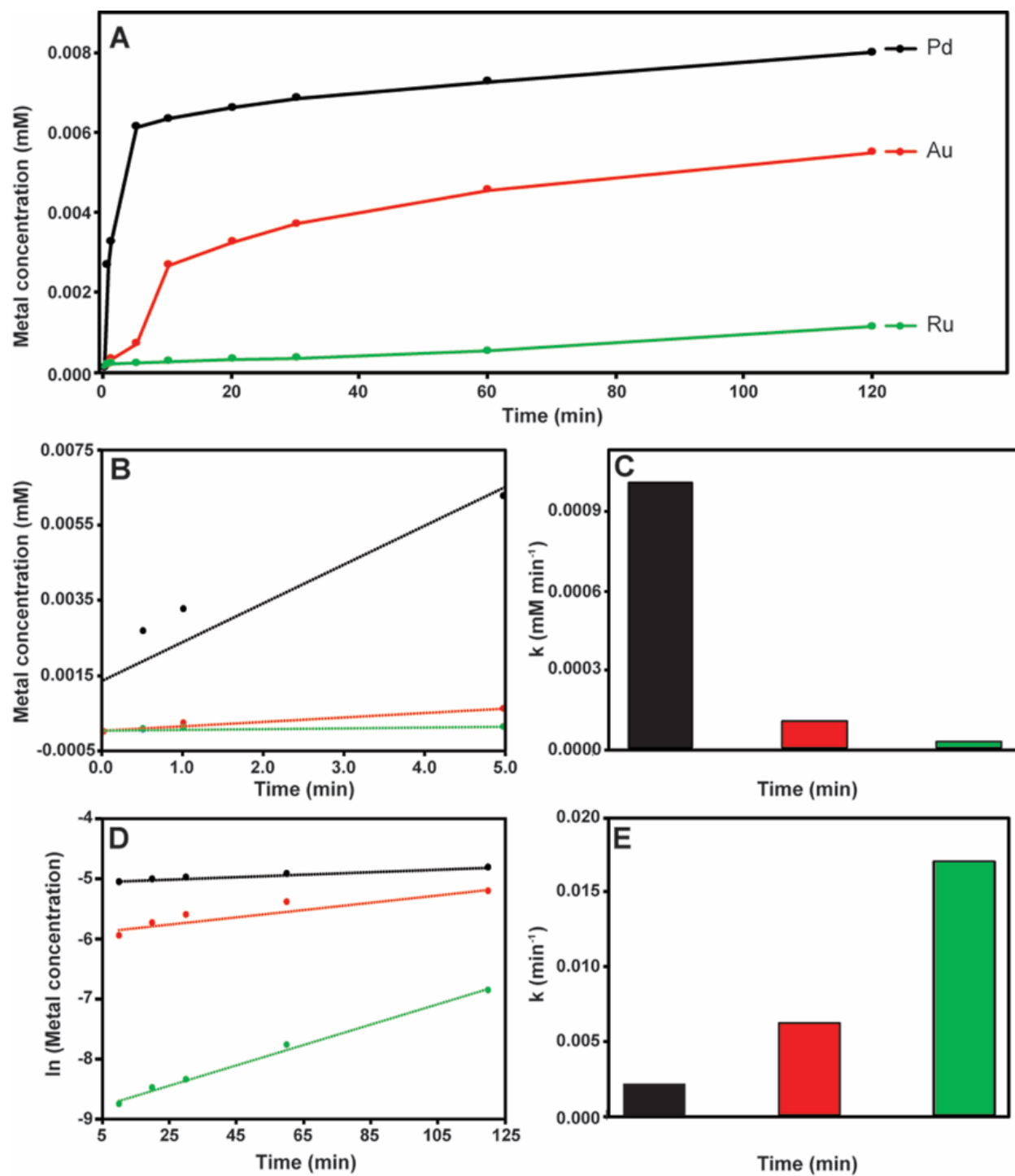


Figure 9.3. (A) Concentration of $\text{PdCl}_4^{2-}(\text{aq})$, $\text{AuCl}_4^-(\text{aq})$, or $\text{Ru}^{3+}(\text{aq})$ (black, red, and green traces, respectively) as a function of time during their galvanic replacement reaction with Cu_2O . (B) Plots of $[\text{PdCl}_4^{2-}(\text{aq})]$, $[\text{AuCl}_4^-(\text{aq})]$ or $[\text{Ru}^{3+}(\text{aq})]$ up to 5 min of reaction. (C) Zero order rate constants (k) calculated from the slopes from the curves shown in (B). (D) Plots of $\ln[\text{PdCl}_4^{2-}(\text{aq})]$, $\ln[\text{AuCl}_4^-(\text{aq})]$ or $\ln[\text{Ru}^{3+}(\text{aq})]$ as function of time after 5 min of reaction. (E) First order rate constants (k) calculated from the slopes of the curves shown in (D).

Figure 9.3A shows that the rate of reduction of the precursors was strongly dependent on the nature of the metal, and decreased in the following order: $\text{PdCl}_4^{2-} > \text{AuCl}_4^- > \text{Ru}^{3+}$. The reactions comprising the precursors consumption could not be modulated using only one kinetic model. In this case, we found that this system can be described by two regimes: *i*) an initial reaction step (up to 5 min, described for a zero-order law); and *ii*) a propagation step (after 5 min, first-order law). This data hints that competitive processes may take place together with the galvanic reaction. During the initial step (under 5 min, Figure 9.3B), while the reduction rate of PdCl_4^{2-} (black trace) was fast, AuCl_4^- (red trace) and Ru^{3+} (green trace) showed much lower reduction rates. The calculated rate constants (k) indicated that the reaction performed in the presence of the $\text{PdCl}_4^{2-}(\text{aq})$ precursor took place 10 and 50 times faster relative to the reactions in the presence of $\text{AuCl}_4^-(\text{aq})$ and $\text{Ru}^{3+}(\text{aq})$ precursors, respectively (Figure 9.3C). This result indicates that while a significant part of $\text{PdCl}_4^{2-}(\text{aq})$ was reduced in the first 5 min of the reaction, only small amounts of $\text{AuCl}_4^-(\text{aq})$ and $\text{Ru}^{3+}(\text{aq})$ precursors were consumed during this step. Figure 9.3D-E shows the plots of $\ln[M]_t$ as a function of the reaction time and k values for all metal precursors in the second reaction regime (step *ii*, after 5 min of reaction). Here, an opposite tendency in the reduction was observed, in which the reduction of PdCl_4^{2-} became significantly lower as compared to AuCl_4^- and Ru^{3+} . This agrees with the amount of precursor remaining in solution after 5 min of reaction.

In order to investigate how the nature of the metal precursors and their reduction kinetics affected the morphological features of the produced nanostructures, we performed SEM analyses for the samples obtained by galvanic replacement reaction between Cu_2O and different amounts of $\text{PdCl}_4^{2-}(\text{aq})$, $\text{AuCl}_4^-(\text{aq})$, and $\text{Ru}^{3+}(\text{aq})$ precursors as shown in Figure 9.4.

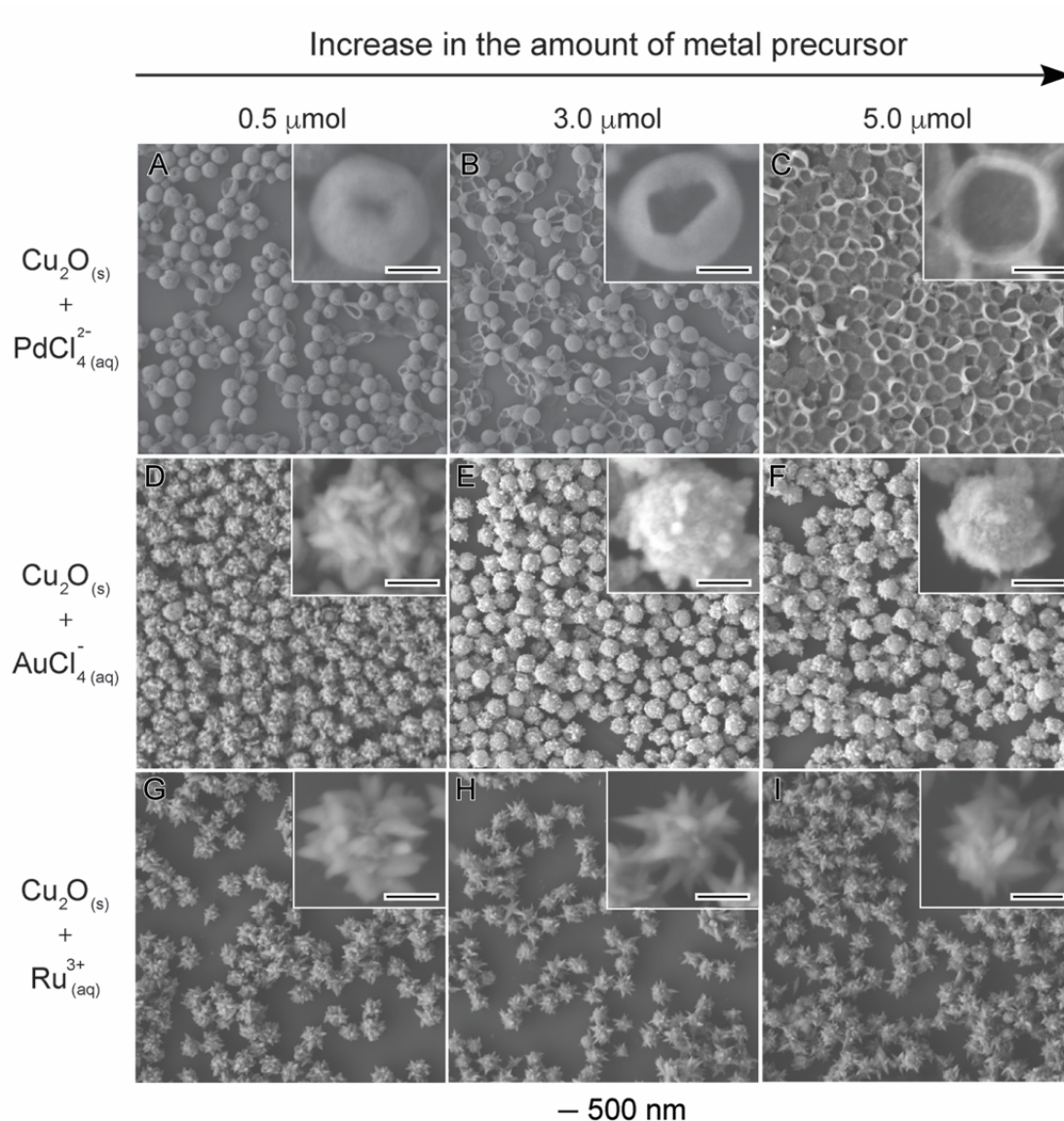


Figure 9.4. SEM images for materials obtained from the galvanic replacement reaction between 0.5, 3.0, and 5.0 μmol of different metal precursors and 10 μmol of Cu_2O spheres: (A-C) $\text{PdCl}_4^{2-}_{(aq)}$, (D-F) $\text{AuCl}_4^{-}_{(aq)}$, and (G-I) $\text{Ru}^{3+}_{(aq)}$. The scale bar in the insets correspond to 250 nm.

It can be observed that the structures (solid vs hollow interiors) and surface morphologies (smooth vs branched surfaces) were strongly dependent on the nature of the metal precursor employed during the synthesis. The rupture of the spherical shape was observed in all cases when the amount of metal precursor was higher than 5.0 μmol as depicted in Figure 9.5.

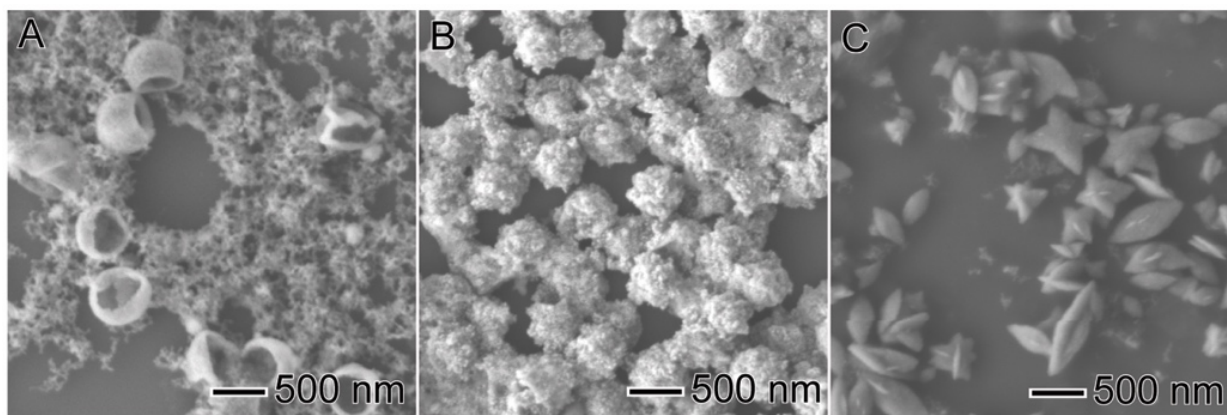


Figure 9.5. SEM images for the materials obtained from the galvanic replacement reaction between of 6.0 μmol of $\text{PdCl}_4^{2-}(\text{aq})$ (A), $\text{AuCl}_4^-(\text{aq})$ (B), and $\text{Ru}^{3+}(\text{aq})$ (C) and 10 μmol of Cu_2O spheres.

The UV-VIS spectra and XRD patterns (Figure 9.6 and 9.7, respectively) indicate the disappearance for the bands or diffraction peaks assigned to Cu_2O in all nanomaterials, in agreement with the consumption of Cu_2O during the galvanic reaction.³¹ The UV-vis spectrum of Cu_2O spheres (black trace) is also shown for comparison. The UV-VIS spectra show the disappearance of the band related to the Cu_2O spheres in all cases as a result of Cu_2O oxidation. In addition, after addition of 5 μmol of metal precursors, bands associated with the deposition of second metal could be observed for Pd (~ 270 nm) and Au (~ 690 nm) in (A) and (B), respectively. No bands due to Ru-based species could be detected in (C).

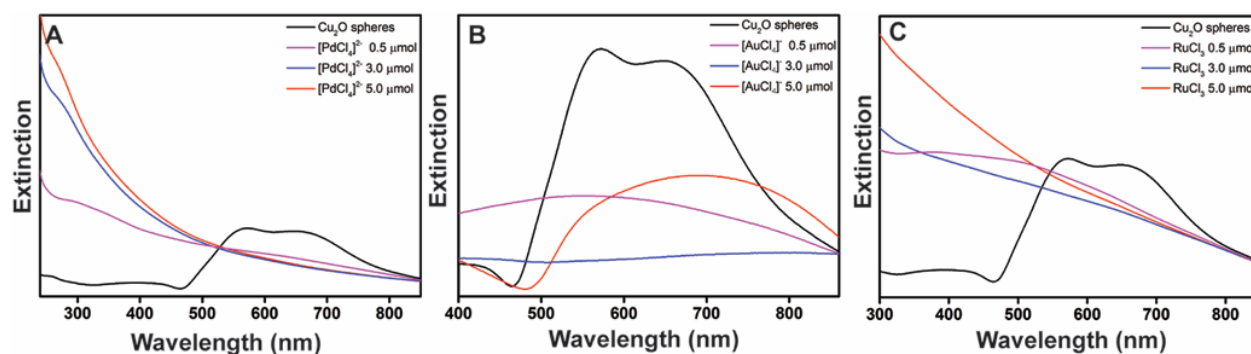


Figure 9.6. UV-VIS extinction spectra recorded from aqueous suspensions containing the materials obtained after the addition of 0.5 (violet trace), 3.0 (blue trace), and 5.0 mmol (red trace) of $\text{PdCl}_4^{2-}(\text{aq})$ (A), $\text{AuCl}_4^-(\text{aq})$ (B), and $\text{Ru}^{3+}(\text{aq})$ (C) to aqueous suspensions containing 10 μmol of Cu_2O spheres.

Only peaks assigned to *fcc* Pd and Au were detected after the reaction between Cu₂O and PdCl₄²⁻_(aq) and AuCl₄⁻_(aq), respectively. On the other hand, only peaks assigned to CuO were detected in after the reaction between Cu₂O and Ru³⁺_(aq).

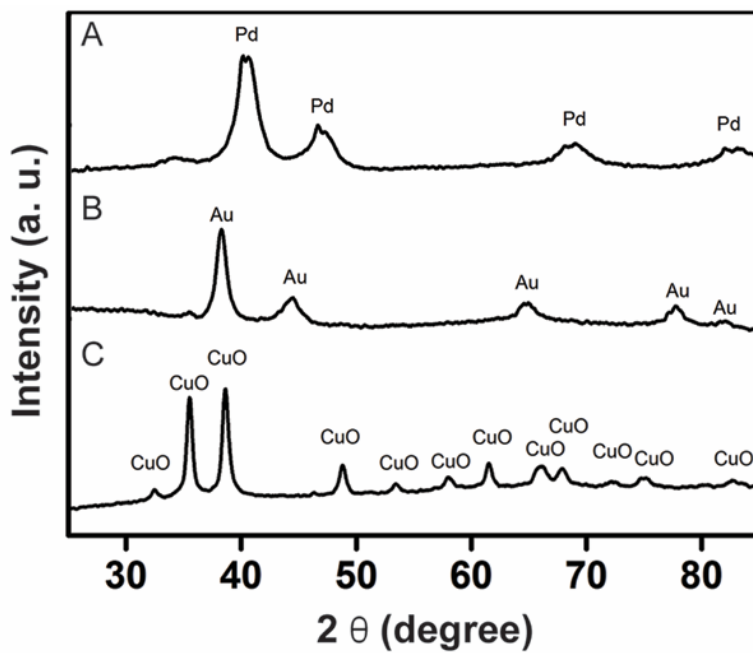


Figure 9.7. XRD patterns for the materials obtained from the reaction between 5.0 μmol of PdCl₄²⁻_(aq) (top trace), AuCl₄⁻_(aq) (middle trace), and Ru³⁺_(aq) (bottom trace) and 10 μmol of Cu₂O spheres.

In the synthesis employing PdCl₄²⁻ as precursor (Figure 9.4A-C), the formation of hollow nanoparticles displaying apparently smooth surfaces was observed. An increase in the degree of hollowing was detected when the amount of metal precursor was increased from 0.5 μmol up to 3.0 and 5.0 μmol. This observation may be explained due to the increased extension of the galvanic reaction as a function of the amount of metal precursor added into the reaction.³² More specifically, the reaction between Cu₂O and PdCl₄²⁻_(aq) led to the formation of well-defined bowls containing a single and relatively big pore at the surface of each particle. The size of the pores increased after the addition of 0.5, 3.0, and 5.0 μmol of PdCl₄²⁻_(aq), until the rupture of the structure after the addition of 6.0 μmol of PdCl₄²⁻_(aq) (Figure 9.5A).

HRTEM and STEM-HAADF images for the sample obtained after the reaction between Cu_2O with $5.0 \mu\text{mol}$ of $\text{PdCl}_4^{2-}(\text{aq})$ (Figure 9.8A-D) confirm the formation of the bowl morphology, in which the walls were comprised of small Pd NPs $\sim 8 \text{ nm}$ in size.

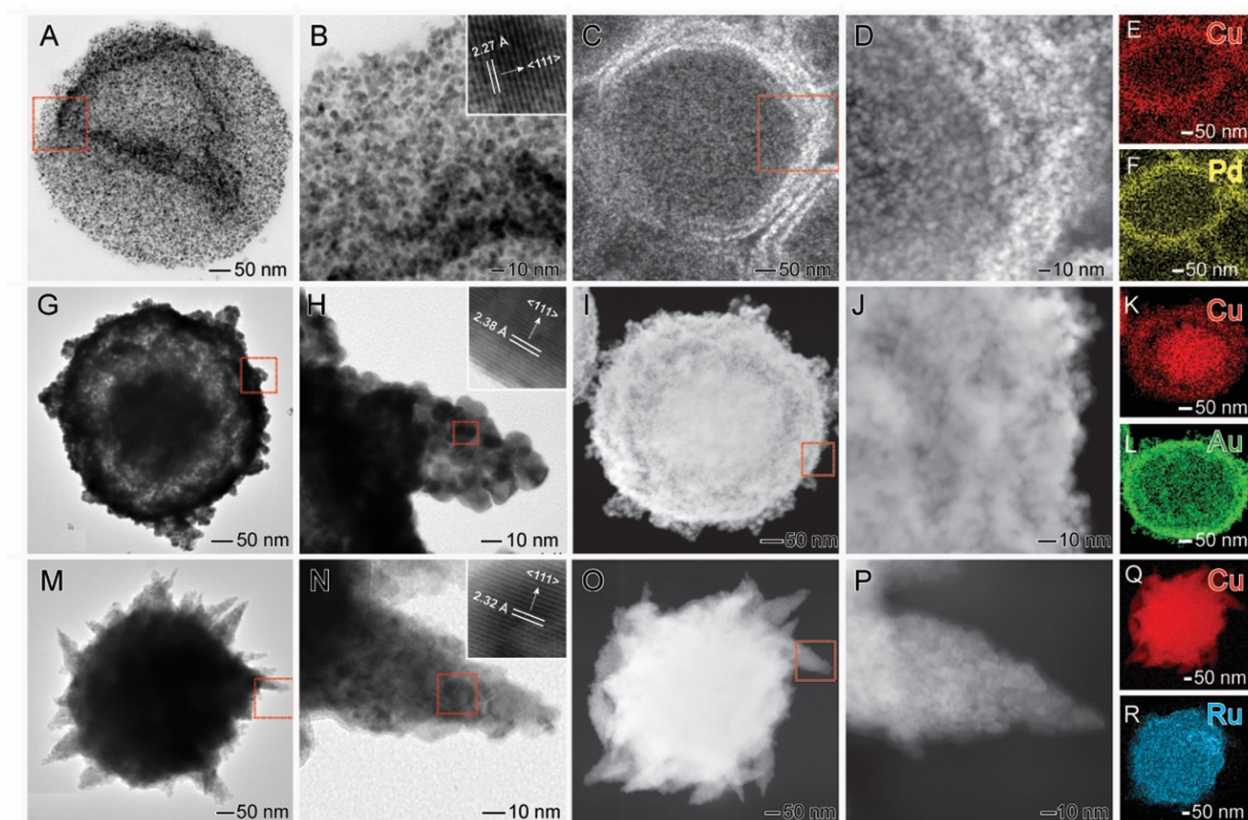


Figure 9.8. HRTEM (first and second columns), HAADF-STEM (third and fourth columns), and STEM-EDX elemental map (fifth column) images for the materials obtained from the galvanic replacement reaction between of $5.0 \mu\text{mol}$ of $\text{PdCl}_4^{2-}(\text{aq})$ (A-F), $\text{AuCl}_4^-(\text{aq})$ (G-L), or $\text{Ru}^{3+}(\text{aq})$ (M-R) and $10 \mu\text{mol}$ of Cu_2O spheres.

Furthermore, STEM-EDX mapping (Figure 9.8E-F) confirmed that both Cu and Pd are uniformly distributed over the extension of the walls. Herein, the the formation of bowls can be associated with the high rate of galvanic reaction between $\text{PdCl}_4^{2-}(\text{aq})$ and Cu_2O , which exceed the parallels oxidative reactions that compete with the galvanic process. Thus, a high degree of Cu_2O template oxidation was achieved leading to the formation of a complete hollow structure displaying high level of porosity and thinner walls.¹⁵ This result is supported by the ICP-OES analyses, which

showed a 70 at. % of Pd in the obtained nanomaterials. Here, when a Cu_2O sphere is kept in contact with small amounts of an aqueous $\text{PdCl}_4^{2-}(\text{aq})$ solution, the Cu^+ ions from the sphere surface with high surface energy (defects, stacking faults, among others) can quickly be oxidized and dissolved by $\text{PdCl}_4^{2-}(\text{aq})$ ions, producing Cu^{2+} ions into the reaction and leading to the formation of small cavities at the nanoparticle surface. Correspondingly, Pd atoms are deposited on the nanoparticle surface as a result of the reduction of the $\text{PdCl}_4^{2-}(\text{aq})$ precursor. As more Cu_2O is replaced by Pd, the formation of a hollow nanomaterial is expected.^{32,33} As Pd and CuO do not display a great miscibility at nanoscale due to their different lattices constants ($a_{\text{Pd}} = 3.61 \text{ \AA}$; $a_{\text{CuO}} = 4.68 \text{ \AA}$) of the face-centered cubic (*fcc*) and monoclinic structures of Pd and CuO, respectively, the Pd atoms do not tend to deposit as an uniform Pd layer but as islands at the Cu_2O surface, leading to the formation of the observed bowls whose shells are comprised of several Pd nanoparticles as observed by HRTEM (Figure 9.4A-C).^{34,35} XPS analysis (Figure 9.9A-D) indicate that the Cu^{2+} species were present at the walls as CuO or $\text{Cu}(\text{OH})_2$. Therefore, this material can be defined as containing a thin CuO and/or $\text{Cu}(\text{OH})_2$ shell decorated with Pd NPs ~8 nm in size. Only Pd peaks could be indexed in the XRD diffractogram (Figure 9.7A), in agreement with the probably thin thickness of the CuO/ $\text{Cu}(\text{OH})_2$ walls.

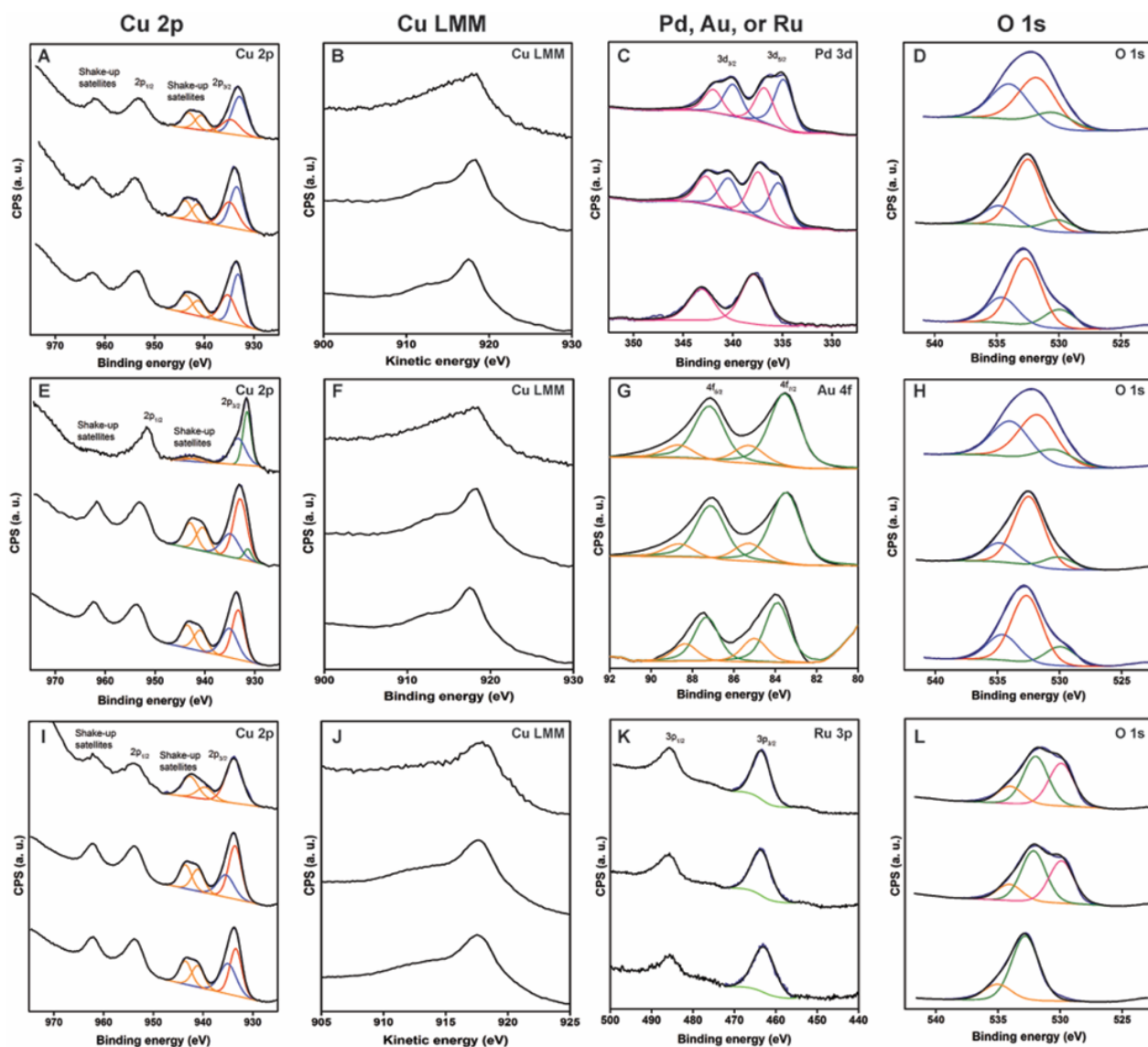


Figure 9.9. XPS spectra of the Cu 2p (first column), Cu LMM (second column), noble metals (third column), and O 1s (fourth column) levels for the materials obtained following the addition of 0.5, 3.0, and 5.0 μmol (top to bottom) of $\text{PdCl}_4^{2-}(\text{aq})$ (A-D), $\text{AuCl}_4^{-}(\text{aq})$ (E-H), and $\text{Ru}^{3+}(\text{aq})$ (I-L) precursors to an aqueous suspension containing 10 μmol of Cu_2O spheres.

Even though the formation of bowls has been previously reported for some polymer and oxide systems, we would like to extend the knowledge concerning their formation mechanism for our developed system. During the synthesis of hollow nanostructures, a stress in the structure is generated by the transformations that occurs over the entire particle such as the removal (dissolution) of components as well as the deposition/crystallization of a new phase. This generated stress is withstood by the walls. Thus, the rupture of the wall is conditioned to its mechanical

resistance, which consequently depends on the wall thickness. In our system, which involves the galvanic reaction between $\text{PdCl}_4^{2-}(\text{aq})$ and Cu_2O , as the reaction progresses, the formation of progressively thinner walls was observed. The thinner walls tend to present lower mechanical resistance to the stress generated during the process. Thus, it is plausible that this generated stress exceeds the mechanical resistance of the wall and can be relieved by the partial rupture of the structure by the formation of a single hole at its surface and thus bowls as depicted in Figure 9.10.^{36,37}

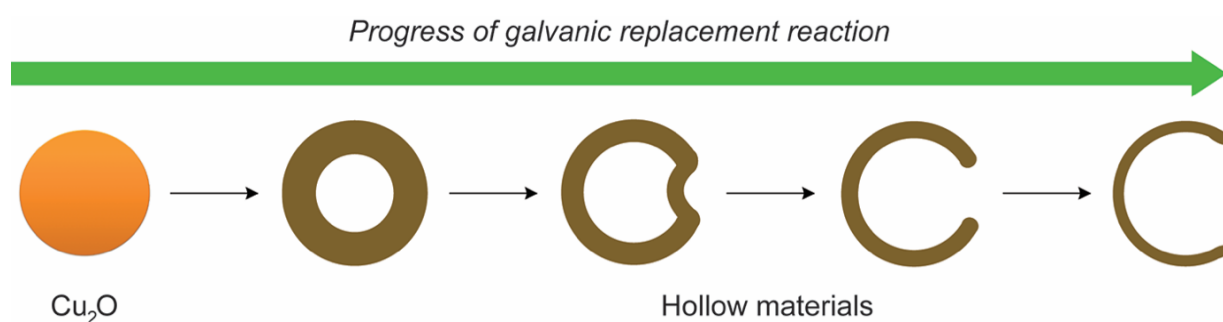


Figure 9.10. Proposed mechanism for the formation of CuO-Pd bowls by the reaction between Cu_2O spheres and $\text{PdCl}_4^{2-}(\text{aq})$ under aerobic conditions.

A markedly different result in terms of morphological evolution was observed when AuCl_4^- (aq) (Figure 9.4D-F) and Ru^{3+} (aq) (Figure 9.4G-I) were employed as the precursors in the reaction with Cu_2O . In both materials, the formation of islands or branches at the surface of the templates was observed, leading to dendritic surface morphologies. The reaction between Cu_2O and AuCl_4^- (aq) led to the deposition of branches at the surface followed by the further deposition of Au NPs as the amount of AuCl_4^- (aq) employed in the reaction increased from 0.5 to 5.0 μmol . In the reaction between Cu_2O and Ru^{3+} (aq), only the formation of branches was detected.

The atomic percentage of Au and Ru (measured by ICP-OES) detected in the materials obtained after the galvanic reaction with 5.0 μmol of precursor corresponded to 52 and 13 at%, respectively. This indicates that the galvanic replacement reaction between Cu_2O and Ru^{3+} (aq)

occurred to a lesser extent as compared to AuCl_4^- (aq) and PdCl_4^{2-} (aq). While only Au diffraction peaks were detected in the XRD diffractograms after the reaction between Cu_2O and 5.0 μmol AuCl_4^- (aq) (Figure 9.7B), only peaks assigned to CuO were detected for the Ru^{3+} (aq) counterpart (Figure 9.7C). In both materials, XPS spectra also indicated the presence of CuO/Cu(OH)₂ species at the surface (Figure 9.9E-H and 9.9I-L).

Intriguingly, HRTEM (Figure 9.8G-H) and STEM-HAADF (Figure 9.8I-J) images for the sample obtained after the reaction between Cu_2O and 5.0 μmol AuCl_4^- (aq) indicated that this material displayed a rattle-like morphology. More specifically, the rattles can be described as having an outer shell comprised of hollow branches as well as the presence of NPs islands ~ 12 nm in size at its surface (Figure 9.4H). Moreover, a solid core ~ 210 nm in diameter could be clearly visualized from the images. The STEM-EDX elemental maps (Figure 9.4K-L) revealed that, while the shells were comprised on both uniformly dispersed Cu and Au, the core did not contain any Au. Conversely, HRTEM (Figure 9.4M-N) and STEM-HAADF (Figure 9.4O-P) images of the materials obtained after the reaction between Cu_2O and 5.0 μmol Ru^{3+} (aq) indicated the formation of a solid structure (without hollow interiors or surface holes/pores). Also, the STEM-EDX maps (Figure 9.4Q-R) showed that while both Ru and Cu were present at the core of the structure, only Cu was present at the branches. The XPS data (Figure 9.9 and Tables 9.1-9.3) revealed the presence of Cu^{2+} species at the surface in both cases (from CuO and Cu(OH)₂). While Au was detected in the materials obtained from the reaction between Cu_2O and AuCl_4^- (aq), RuO_2 species were detected from the reaction between Cu_2O and Ru^{3+} (aq). Here, the formation RuO_2 species may be achieved from the oxidation of Ru under aerobic conditions as follows.^{38,39}



Table 9.1. Binding energies, surface composition, and Pd:Cu ratio as measured by XPS analyses in the CuO-Pd bowls obtained from the galvanic replacement reaction between of 0.5, 3.0, or 5.0 μmol of $\text{PdCl}_4^{2-}(\text{aq})$ and 10.0 μmol of Cu_2O spheres.

$\text{PdCl}_4^{2-}(\text{aq})$ (μmol)	BE of Cu 2p _{3/2} (eV)		KE of Cu Auger (eV)	α_{Cu} (eV)	BE of O 1s (eV)			BE of Pd 3d _{5/2} (eV)		Pd 3d _{5/2} / Cu 2p _{3/2}
	I (CuO)	II (Cu(OH) ₂)			O _L	O _S	O _W	I (Pd ⁰)	II (Pd ^{δ+})	
0.5	933.2 (3.0)	935.3 (3.6)	917.4	1850.6	529.9 (16)	532.6 (60)	534.5 (24)		337.8 (100)	0.1
3.0	933.5 (3.2)	935.1 (4.0)	917.5	1851.0	530.1 (12)	532.5 (69)	534.8 (19)	335.3 (48)	337.4 (52)	0.9
5.0	932.9 (3.6)	934.7 (4.2)	917.9	1850.8	530.4 (21)	531.9 (46)	534.1 (33)	335.0 (58)	336.8 (42)	1.3

Table 9.2. Binding energies, surface composition, and Au:Cu ratio as measured by XPS analyses in the Cu₂O@CuO-Au nanorattles obtained from the galvanic replacement reaction between of 0.5, 3.0, or 5.0 μmol of $\text{AuCl}_4^-(\text{aq})$ and 10.0 μmol of Cu_2O spheres.

$\text{AuCl}_4^-(\text{aq})$ (μmol)	BE of Cu 2p _{3/2} (eV)			KE of Cu Auger (eV)	α_{Cu} (eV)	BE of O 1s (eV)			BE of Au 4f _{7/2} (eV)		Au 4f _{7/2} / Cu 2p _{3/2}
	I (CuO)	II (Cu(OH) ₂)	III (Cu ₂ O)			O _L	O _S	O _W	I (Au ⁰)	II (Au ^{δ+})	
0.5	933.2 (3.0)	935.1 (3.8)		917.7	1849.9	529.8 (38)	532.0 (45)	534.0 (17)	83.9 (72)	85.0 (28)	0.03
3.0	933.0 (3.1)	935.0 (3.9)	931.4 (1.7)	918.0	1851.0	529.4 (37)	531.6 (42)	533.8 (21)	83.5 (78)	85.2 (22)	1.0
5.0		933.8 (3.6)	931.5 (1.9)	918.0	1849.5		531.7 (62)	533.9 (38)	83.5 (80)	85.2 (20)	8.7

Table 9.3. Binding energies, surface composition, and Ru:Cu ratio as measured by XPS analyses in the CuO-RuO₂ dendrites obtained from the galvanic replacement reaction between of 0.5, 3.0, or 5.0 μmol of Ru³⁺_(aq) and 10.0 μmol of Cu₂O spheres.

Ru ³⁺ _(aq) (μmol)	BE of Cu 2p _{3/2} (eV)		KE of Cu Auger (eV)	α _{Cu} (eV)	BE of O 1s (eV)			BE of Ru 3p _{3/2} (eV)	Ru 3p _{3/2} / Cu 2p _{3/2}
	I (CuO)	II (Cu(OH) ₂)			O _L	O _S	O _W	I (RuO)	
0.5	933.4 (2.8)	935.0 (3.9)	917.6	1851.0	529.9 (39)	532.1 (46)	534.0 (15)	462.8 (6.2)	0.03
3.0	933.6 (3.0)	935.4 (3.9)	917.7	1851.3	529.9 (39)	532.0 (45)	534.0 (16)	463.5 (5.6)	0.06
5.0	933.8 (3.8)		917.8	1851.6		532.7 (80)	535.0 (20)	463.4 (5.2)	1.0

Our results demonstrate that, although the galvanic replacement reaction may be used to explain the morphological changes in the CuO-Pd material, it can not be exclusively explain the results observed when AuCl_4^- (aq) and Ru^{3+} (aq) precursors were employed in the reactions. In fact, as the reduction rate of both AuCl_4^- (aq) and Ru^{3+} (aq) precursors are slower in the initial step of the reaction, we would like to suggest that a competitive oxidative process (Cu^+ to Cu^{2+}) may explain the differences on the morphologies and composition of the produced nanostructures.

It is well-established that Cu_2O species have low stabilities in water suspensions and can be easily oxidized to Cu^{2+} in the presence of air/dissolved oxygen.^{27,28,40,41} Moreover, the presence of ions such as Cl^- (which usually is a component in many metal precursors) can enhance several oxidative processes promoted by dissolved oxygen.⁴² In order to verify if a Cu_2O oxidative process takes place under aerobic conditions, we performed a control experiment under the same conditions described in Figure 9.4 but in the absence of any metal precursors (Figure 9.11A) and by adding different amounts of NaCl: 0.5 μmol (Figure 9.11B), 3.0 μmol (Figure 9.11C), and 5.0 μmol (Figure 9.11D), in which the morphology of the Cu_2O spheres was monitored. Our results confirmed the formation of dendritic structures, in which the number and size of the formed branches increased as the amount of Cl^- (aq) added into the reaction mixture was increased.

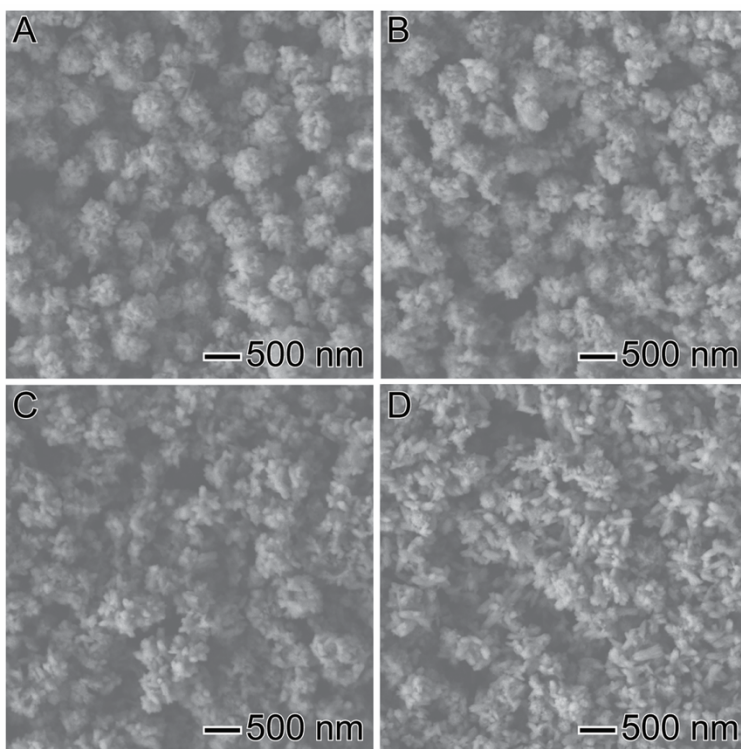


Figure 9.11. SEM images for the materials obtained from the oxidation of Cu_2O spheres in aerobic conditions in the absence of any other metal precursors (A) and in the presence of 0.5 (B), 3.0 (C), and 5.0 (D) μmol of $\text{NaCl}_{(\text{aq})}$.

Moreover, the intense yellow color of the Cu_2O suspension changed to brown, which is characteristic of the formation of CuO . UV-VIS and XRD results for these samples also confirmed the oxidation of Cu_2O to CuO due to the presence of air/dissolved oxygen and Cl^- ions (Figure 9.12).

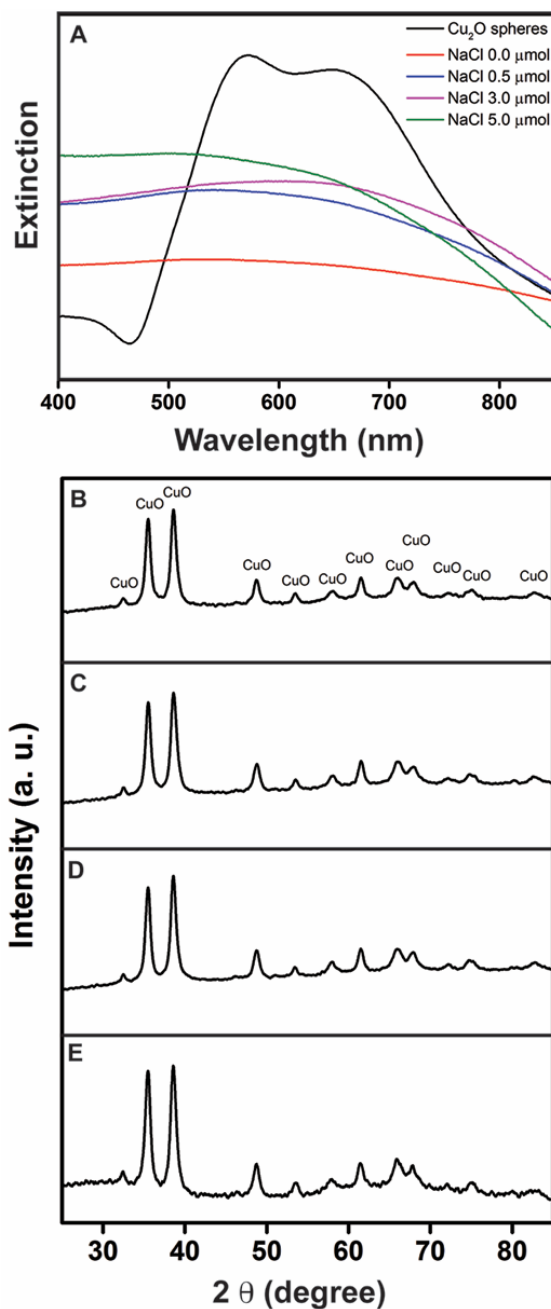


Figure 9.12. UV-VIS extinction spectra (A) and XRD patterns (B) for the structures obtained from the oxidation of Cu₂O spheres in aerobic conditions in the absence of any other metal precursors (B) and in the presence of 0.5 (C), 3.0 (D), and 5.0 (E) mmol of NaCl_(aq) under similar conditions as described in Figure 9.4.

In the presence of higher concentrations of Cl⁻ ions, the color change was even faster (less than 5 min). Therefore, the formation of the branches at the surface can be associated with the Cu₂O to CuO oxidation under aerobic conditions.⁴³ It is noteworthy that the morphological, optical

the structural properties of the Cu_2O spheres remained unaffected when the same tests were performed under a N_2 (inert) atmosphere, which confirms that O_2 oxidation plays an important role over the morphology of the obtained materials.

Based on our morphological observations, control experiments, and kinetics curves, we would like to propose a mechanism that is based on the occurrence of Cu^+ to Cu^{2+} oxidation process that competes with the galvanic replacement reaction. as illustrated in Figure 9.13, to explain the differences in the morphologies as a function of the precursor reduction kinetics.

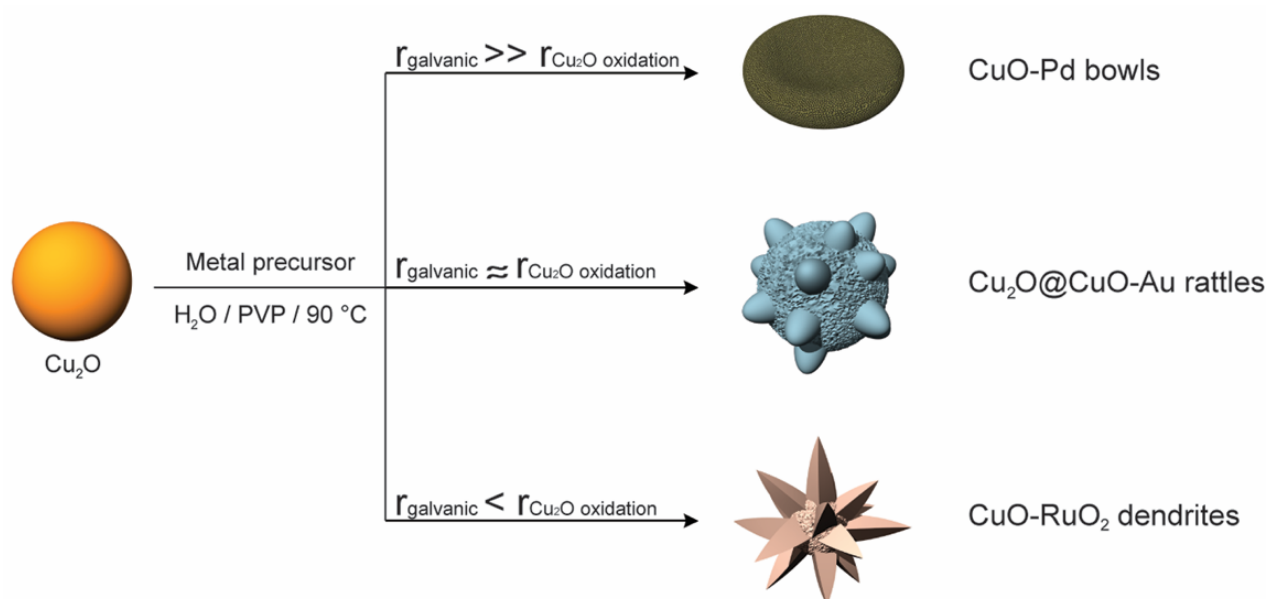


Figure 9.13. Proposed mechanism for the formation of bowls, rattles, and dendrites based on the relative initial rates of two competitive processes: *i*) galvanic replacement reaction between Cu_2O spheres and each metal precursors (r_{galvanic}) and *ii*) aerobic oxidation of Cu_2O spheres to CuO dendrites ($r_{\text{Cu}_2\text{O oxidation}}$).

In this case, the detected morphologies were strongly dependent on the initial reduction rates of each metal precursor relative to the Cu_2O oxidation by O_2 . Basically, the morphologies were determined by two competitive processes: *i*) the aerobic oxidation of Cu_2O spheres to CuO dendrites and *ii*) the galvanic replacement reaction between Cu_2O spheres and each metal precursor. In the presence of $\text{PdCl}_4^{2-}(\text{aq})$, the initial rate for galvanic reaction was faster relative to

the Cu_2O oxidation by O_2 ($r_{\text{galvanic}} > r_{\text{Cu}_2\text{O oxidation}}$). Thus, most of the metal precursor was consumed in the first minutes of the reaction, leading the formation hollow CuO -Pd bowls. When AuCl_4^- (aq) was employed as precursor, the initial rate of the galvanic reaction was slower relative to the PdCl_4^{2-} (aq) scenario, and became comparable with the Cu_2O oxidation by O_2 ($r_{\text{galvanic}} \cong r_{\text{Cu}_2\text{O oxidation}}$), which took place together with the galvanic replacement reaction and led the formation of rattles. Figure 9.14 depicts a scheme for explaining the formation of the rattles.

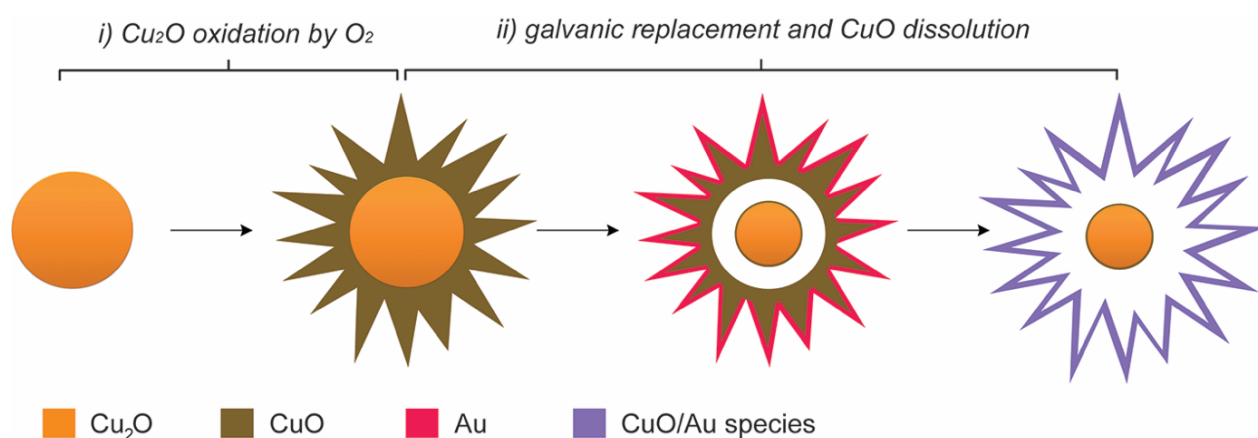


Figure 9.14. Proposed mechanism for the formation of $\text{Cu}_2\text{O}@$ CuO -Au rattles from the reaction between Cu_2O spheres and AuCl_4^- (aq) precursor under aerobic conditions.

At the early stages of the reaction, the formation of CuO from Cu_2O oxidation by O_2 occurs at the surface leading to the formation of CuO branches. This process is accompanied by the Au deposition at surface due to galvanic replacement between Cu_2O and AuCl_4^- (aq). This process also led to the consumption of Cu_2O , which is dissolved from the cores leading to hollow interiors. As the amount of AuCl_4^- (aq) reduced was increased, further Au deposition took place leading to the formation of Au NPs islands at the surface of the walls. This process was accompanied by the increased dissolution of Cu_2O from the cores by the galvanic replacement. Furthermore, the intermediate CuO layer/branches formed by the simultaneous Cu_2O oxidation to CuO can be dissolved by H^+ at high AuCl_4^- (aq) concentrations (H^+ comes from the HAuCl_4 precursor). These

processes, thus, lead to the formation of the Cu₂O@CuO-Au rattles, in which the formation of the hollow branches (Figure 9.8H) agrees with this mechanism.^{12,15,40,44,45}

Finally, when the initial rate of the galvanic reaction was slower relative to the Cu₂O oxidation by O₂ ($r_{\text{galvanic}} \leq r_{\text{Cu}_2\text{O oxidation}}$), the oxidation of Cu₂O to CuO in the presence of air/dissolved oxygen became much more significant compared to the galvanic replacement reaction. Thus, only minor deposition of Ru (which was further oxidized to RuO₂) was detected during the early stages of the reaction, after which only Cu₂O to CuO oxidation by O₂ took place. The absence of Ru at the branches as well as the presence of peaks only assigned to CuO in the XRD is in agreement with this observation.

Finally, the Pd, Au and RuO₂ could be employed as catalysts towards the 4-nitrophenol reduction as shown in Figure 9.15. While the Pd and Au-based nanomaterials presented superior performances as compared to the initial Cu₂O spheres, the performance for the RuO₂-based materials was similar. Herein, in addition to the nature of the metal and nanoparticle sizes, the differences in the catalytic performances can be associated with the higher surface to volume ratios enabled by the hollow interiors and porous walls, which increased in the same order than the catalytic activity.⁴⁶

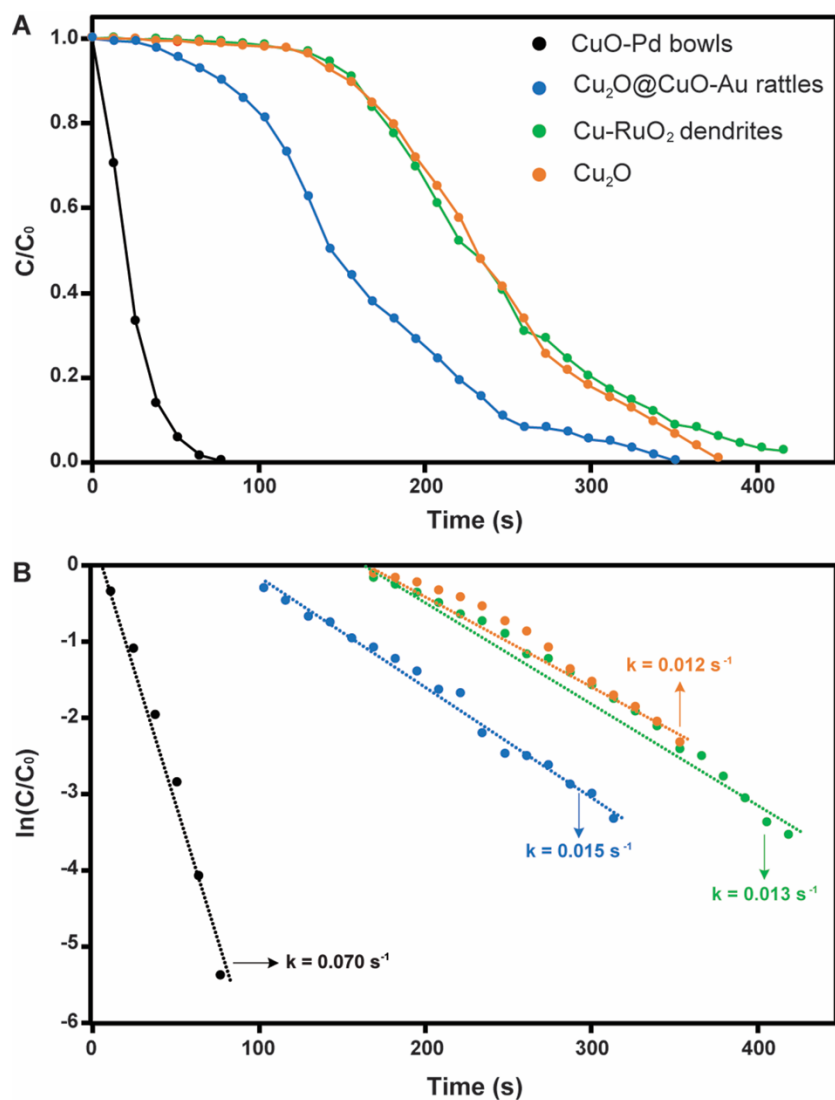


Figure 9.15. C/C_0 (A) and $\ln(C/C_0)$ (B) profiles as a function of time employing CuO-Pd bowls (black trace), $\text{Cu}_2\text{O}@Cu\text{O}$ -Au rattles, and CuO-RuO_2 dendrites as catalysts towards the 4-nitrophenol reduction reaction. A blank reaction using the pure Cu_2O spheres was also performed (orange trace).

9.4. Conclusion

We have demonstrated that the precursor reduction kinetics played a pivotal role over the morphological and compositional features in nanostructures obtained from the galvanic replacement reaction between Cu_2O spheres and $\text{PdCl}_4^{2-}(\text{aq})$, $\text{AuCl}_4^-(\text{aq})$, or $\text{Ru}^{3+}(\text{aq})$ as precursors. We

found that the final morphologies were determined by the relative initial rates of two competitive processes: *i*) the aerobic oxidation of Cu₂O spheres to CuO dendrites and *ii*) the galvanic replacement reaction between Cu₂O spheres and each metal precursors. In the presence of PdCl₄²⁻ precursor, the initial rates of the galvanic reaction were fast ($r_{\text{galvanic}} > r_{\text{Cu}_2\text{O oxidation}}$) relative to oxidation by O₂, contributing to the formation of CuO-Pd bowls containing a single and well-defined cavity on its surface and walls comprised of Pd NPs ~8 nm in diameter. When AuCl₄⁻(aq) was employed as precursor, the initial rates for galvanic replacement became comparable to the oxidation by O₂, which, in turn, led to the formation of Cu₂O@CuO-Au rattles in acidic media. Finally, when Ru³⁺(aq) was employed as the precursor, galvanic replacement became slower relative to the oxidation by O₂, leading to the formation of CuO dendrites containing RuO₂ NPs (formed from the Ru oxidation). These results demonstrate that the precursor reductions kinetics can be put to work to maneuver morphology and composition during the galvanic replacement reaction in oxide-based systems, in which the balance between galvanic replacement and parallel oxidation reactions can be tuned on order to enable the synthesis novel and/or complex nanostructures having desired compositions and morphologies. We believe the results described provide mechanistic insights on galvanic replacement processes involving metal/metal oxides systems and may inspire the development of a wealth of oxide-based hybrids with desired features and performances.

9.5. References

- (1) Xia, X.; Wang, Y.; Ruditskiy, A.; Xia, Y. 25th Anniversary Article: Galvanic Replacement: A Simple and Versatile Route to Hollow Nanostructures with Tunable and Well-Controlled Properties. *Adv. Mater.* **2013**, *25* (44), 6313–6333.
- (2) Sun, Y.; Mayers, B.; Xia, Y. Metal Nanostructures with Hollow Interiors. *Adv. Mater.* **2003**, *15* (7–8), 641–646.
- (3) Rodrigues, T. S.; Silva, A. G. M.; Macedo, A.; Farini, B. W.; Alves, R. da S.; Camargo, P. H. C. Probing the Catalytic Activity of Bimetallic versus Trimetallic Nanoshells. *J. Mater. Sci.* **2015**, *50* (16), 5620–5629.
- (4) Sun, Y.; Xia, Y. Shape-Controlled Synthesis of Gold and Silver Nanoparticles. *Science*.

- 2002**, 298 (5601), 2176 LP-2179.
- (5) Sun, Y.; Xia, Y. Mechanistic Study on the Replacement Reaction between Silver Nanostructures and Chloroauric Acid in Aqueous Medium. *J. Am. Chem. Soc.* **2004**, 126 (12), 3892–3901.
 - (6) Skrabalak, S. E.; Chen, J.; Sun, Y.; Lu, X.; Au, L.; Cobley, C. M.; Xia, Y. Gold Nanocages: Synthesis, Properties, and Applications. *Acc. Chem. Res.* **2008**, 41 (12), 1587–1595.
 - (7) Hangarter, C. M.; Lee, Y.-I.; Hernandez, S. C.; Choa, Y.; Myung, N. V. Nanopeapods by Galvanic Displacement Reaction. *Angew. Chemie Int. Ed.* **2010**, 49 (39), 7081–7085.
 - (8) da Silva, A. G. M.; Rodrigues, T. S.; Correia, V. G.; Alves, T. V.; Alves, R. S.; Ando, R. A.; Ornellas, F. R.; Wang, J.; Andrade, L. H.; Camargo, P. H. C. Plasmonic Nanorattles as Next-Generation Catalysts for Surface Plasmon Resonance-Mediated Oxidations Promoted by Activated Oxygen. *Angew. Chemie Int. Ed.* **2016**, 55 (25), 7111–7115.
 - (9) da Silva, A. G. M.; Lewis, E. A.; Rodrigues, T. S.; Slater, T. J. A.; Alves, R. S.; Haigh, S. J.; Camargo, P. H. C. Surface Segregated AgAu Tadpole-Shaped Nanoparticles Synthesized Via a Single Step Combined Galvanic and Citrate Reduction Reaction. *Chem. – A Eur. J.* **2015**, 21 (35), 12314–12320.
 - (10) Oh, M. H.; Yu, T.; Yu, S.-H.; Lim, B.; Ko, K.-T.; Willinger, M.-G.; Seo, D.-H.; Kim, B. H.; Cho, M. G.; Park, J.-H.; et al. Galvanic Replacement Reactions in Metal Oxide Nanocrystals. *Science*. **2013**, 340 (6135), 964 LP-968.
 - (11) Diab, M.; Mokari, T. Role of the Counteranions on the Formation of Different Crystal Structures of Iron Oxyhydroxides via Redox Reaction. *Cryst. Growth Des.* **2017**.
 - (12) Wang, Z.; Luan, D.; Li, C. M.; Su, F.; Madhavi, S.; Boey, F. Y. C.; Lou, X. W. Engineering Nonspherical Hollow Structures with Complex Interiors by Template-Engaged Redox Etching. *J. Am. Chem. Soc.* **2010**, 132 (45), 16271–16277.
 - (13) Gao, G.; Yu, L.; Wu, H. Bin; (David) Lou, X. W. Hierarchical Tubular Structures Constructed by Carbon-Coated α -Fe₂O₃ Nanorods for Highly Reversible Lithium Storage. *Small* **2014**, 10 (9), 1741–1745.
 - (14) Gu, Y.; Cai, J.; He, M.; Kang, L.; Lei, Z.; Liu, Z.-H. Preparation and Capacitance Behavior of Manganese Oxide Hollow Structures with Different Morphologies via Template-Engaged Redox Etching. *J. Power Sources* **2013**, 239, 347–355.
 - (15) Pang, M.; Wang, Q.; Zeng, H. C. Self-Generated Etchant for Synthetic Sculpturing of Cu₂O-Au, Cu₂O@Au, Au/Cu₂O, and 3D-Au Nanostructures. *Chem. – A Eur. J.* **2012**, 18 (46), 14605–14609.
 - (16) Yu, L.; Wu, H. Bin; Lou, X. W. D. Self-Templated Formation of Hollow Structures for Electrochemical Energy Applications. *Acc. Chem. Res.* **2017**.
 - (17) Trogadas, P.; Ramani, V.; Strasser, P.; Fuller, T. F.; Coppens, M.-O. Hierarchically Structured Nanomaterials for Electrochemical Energy Conversion. *Angew. Chemie Int. Ed.* **2016**, 55 (1), 122–148.
 - (18) Sohn, J. H.; Cha, H. G.; Kim, C. W.; Kim, D. K.; Kang, Y. S. Fabrication of Hollow Metal Oxide Nanocrystals by Etching Cuprous Oxide with Metal(ii) Ions: Approach to the Essential Driving Force. *Nanoscale* **2013**, 5 (22), 11227–11233.
 - (19) Biacchi, A. J.; Schaak, R. E. The Solvent Matters: Kinetic versus Thermodynamic Shape Control in the Polyol Synthesis of Rhodium Nanoparticles. *ACS Nano* **2011**, 5 (10), 8089–8099.
 - (20) Xia, Y.; Xiong, Y.; Lim, B.; Skrabalak, S. E. Shape-Controlled Synthesis of Metal Nanocrystals: Simple Chemistry Meets Complex Physics? *Angew. Chemie Int. Ed.* **2009**, 48 (1), 60–103.
 - (21) Zhang, H.; Jin, M.; Xia, Y. Noble-Metal Nanocrystals with Concave Surfaces: Synthesis and Applications. *Angew. Chemie Int. Ed.* **2012**, 51 (31), 7656–7673.

- (22) Wang, Y.; He, J.; Liu, C.; Chong, W. H.; Chen, H. Thermodynamics versus Kinetics in Nanosynthesis. *Angew. Chemie Int. Ed.* **2015**, *54* (7), 2022–2051.
- (23) Xia, Y.; Gilroy, K. D.; Peng, H.-C.; Xia, X. Seed-Mediated Growth of Colloidal Metal Nanocrystals. *Angew. Chemie Int. Ed.* **2017**, *56* (1), 60–95.
- (24) López-Ortega, A.; Roca, A. G.; Torruella, P.; Petrecca, M.; Estradé, S.; Peiró, F.; Puentes, V.; Nogués, J. Galvanic Replacement onto Complex Metal-Oxide Nanoparticles: Impact of Water or Other Oxidizers in the Formation of Either Fully Dense Onion-like or Multicomponent Hollow MnOx/FeOx Structures. *Chem. Mater.* **2016**, *28* (21), 8025–8031.
- (25) Chen, W.; Li, L.; Peng, Q.; Li, Y. Polyol Synthesis and Chemical Conversion of Cu₂O Nanospheres. *Nano Res.* **2012**, *5* (5), 320–326.
- (26) Rodrigues, T. S.; da Silva, A. G. M.; de Oliveira, L. C.; da Silva, A. M.; Teixeira, R. R.; Camargo, P. H. C. Cu₂O Spheres as an Efficient Source of Catalytic Cu(I) Species for Performing Azide-Alkyne Click Reactions. *Tetrahedron Lett.* **2017**, *58* (6), 590–595.
- (27) Marcus, P. *Corrosion Mechanisms in Theory and Practice*; CRC Press, 2011.
- (28) Sun, S.; Yang, Z. Cu₂O-Templated Strategy for Synthesis of Definable Hollow Architectures. *Chem. Commun.* **2014**, *50* (56), 7403–7415.
- (29) Wang, Y.; Peng, H.-C.; Liu, J.; Huang, C. Z.; Xia, Y. Use of Reduction Rate as a Quantitative Knob for Controlling the Twin Structure and Shape of Palladium Nanocrystals. *Nano Lett.* **2015**, *15* (2), 1445–1450.
- (30) Zhou, M.; Wang, H.; Vara, M.; Hood, Z. D.; Luo, M.; Yang, T.-H.; Bao, S.; Chi, M.; Xiao, P.; Zhang, Y.; et al. Quantitative Analysis of the Reduction Kinetics Responsible for the One-Pot Synthesis of Pd–Pt Bimetallic Nanocrystals with Different Structures. *J. Am. Chem. Soc.* **2016**, *138* (37), 12263–12270.
- (31) Zhang, J.; Liu, J.; Peng, Q.; Wang, X.; Li, Y. Nearly Monodisperse Cu₂O and CuO Nanospheres: Preparation and Applications for Sensitive Gas Sensors. *Chem. Mater.* **2006**, *18* (4), 867–871.
- (32) Lu, X.; Tuan, H.-Y.; Chen, J.; Li, Z.-Y.; Korgel, B. A.; Xia, Y. Mechanistic Studies on the Galvanic Replacement Reaction between Multiply Twinned Particles of Ag and HAuCl₄ in an Organic Medium. *J. Am. Chem. Soc.* **2007**, *129* (6), 1733–1742.
- (33) Gilroy, K. D.; Ruditskiy, A.; Peng, H.-C.; Qin, D.; Xia, Y. Bimetallic Nanocrystals: Syntheses, Properties, and Applications. *Chem. Rev.* **2016**, *116* (18), 10414–10472.
- (34) Cao, M.; Hu, C.; Wang, Y.; Guo, Y.; Guo, C.; Wang, E. A Controllable Synthetic Route to Cu, Cu₂O, and CuO Nanotubes and Nanorods. *Chem. Commun.* **2003**, No. 15, 1884–1885.
- (35) Lamber, R.; Wetjen, S.; Jaeger, N. I. Size Dependence of the Lattice Parameter of Small Palladium Particles. *Phys. Rev. B* **1995**, *51* (16), 10968–10971.
- (36) Jagadeesan, D.; Mansoori, U.; Mandal, P.; Sundaresan, A.; Eswaramoorthy, M. Hollow Spheres to Nanocups: Tuning the Morphology and Magnetic Properties of Single-Crystalline α -Fe₂O₃ Nanostructures. *Angew. Chemie Int. Ed.* **2008**, *47* (40), 7685–7688.
- (37) Klein, Y.; Efrati, E.; Sharon, E. Shaping of Elastic Sheets by Prescription of Non-Euclidean Metrics. *Science*. **2007**, *315* (5815), 1116 LP-1120.
- (38) Kötz, R.; Lewerenz, H. J.; Stucki, S. XPS Studies of Oxygen Evolution on Ru and RuO₂ Anodes. *J. Electrochem. Soc.* **1983**, *130* (4), 825–829.
- (39) Suzuki, M. K. and T. N. and M. H. and Y. N. and I. A. and T. Ruthenium Films Prepared by Liquid Source Metalorganic Chemical Vapor Deposition Using Ru(dpm)₃ Dissolved with Tetrahydrofuran Solvent. *Jpn. J. Appl. Phys.* **2002**, *41* (3B), L347.
- (40) Park, J. C.; Kim, J.; Kwon, H.; Song, H. Gram-Scale Synthesis of Cu₂O Nanocubes and Subsequent Oxidation to CuO Hollow Nanostructures for Lithium-Ion Battery Anode Materials. *Adv. Mater.* **2009**, *21* (7), 803–807.
- (41) Surface-Modified CuO Layer in Size-Stabilized Single-Phase Cu₂O Nanoparticles. *Appl.*

- Phys. Lett.* **2001**, *79* (19), 3176–3178.
- (42) Xiong, Y.; Chen, J.; Wiley, B.; Xia, Y.; Aloni, S.; Yin, Y. Understanding the Role of Oxidative Etching in the Polyol Synthesis of Pd Nanoparticles with Uniform Shape and Size. *J. Am. Chem. Soc.* **2005**, *127* (20), 7332–7333.
- (43) Park, J. C.; Kim, A. Y.; Kim, J. Y.; Park, S.; Park, K. H.; Song, H. ZnO-CuO Core-Branch Nanocatalysts for Ultrasound-Assisted Azide-Alkyne Cycloaddition Reactions. *Chem. Commun.* **2012**, *48* (68), 8484–8486.
- (44) Bao, H.; Zhang, Z.; Hua, Q.; Huang, W. Compositions, Structures, and Catalytic Activities of CeO₂@Cu₂O Nanocomposites Prepared by the Template-Assisted Method. *Langmuir* **2014**, *30* (22), 6427–6436.
- (45) Yao, W.; Li, F.-L.; Li, H.-X.; Lang, J.-P. Fabrication of Hollow Cu₂O@CuO-Supported Au-Pd Alloy Nanoparticles with High Catalytic Activity through the Galvanic Replacement Reaction. *J. Mater. Chem. A* **2015**, *3* (8), 4578–4585.
- (46) Rodrigues, T. S.; da Silva, A. G. M.; Gonçalves, M. C.; Fajardo, H. V.; Balzer, R.; Probst, L. F. D.; Camargo, P. H. C. AgPt Hollow Nanodendrites: Synthesis and Uniform Dispersion over SiO₂ Support for Catalytic Applications. *ChemNanoMat* **2015**, *1* (1), 46–51.

Chapter 10

Final Remarks and Perspectives

In summary, this dissertation described the synthesis of variety of well-defined metal-based nanoparticles displaying hollow interiors for applications in catalysis and plasmonic catalysis. Herein, by the use of the galvanic replacement reaction approach between preformed nanoparticles (spheres and wires) and different noble metal precursors combined metal deposition assisted by hydroquinone, a variety of very important properties of the nanoparticles could be precisely controlled and systematically correlated with the catalytic or photocatalytic performances. We highlighted the control over size, composition, structure, surface morphology, and optical properties, which are imperative for the synthesis of nanoparticles displaying increasingly enhanced performances. Interestingly, some synthetic routes developed herein could be successfully scale-up and the resulting nanoparticles were supported onto SiO₂ support without agglomeration, which represents a bottleneck for application of well-defined nanoparticles in catalysis. Thus, we believe our data show that the optimization of catalytic performances of metal-based nanomaterials by the precise control over their properties represents a powerful tool and may inspire the design of new advanced catalysts for a variety of transformations.

CURRICULUM VITAE

Thenner Silva Rodrigues

58 6th Street NE, Midtown
Atlanta, GA, US – Zip Code: 30308
thenner@usp.com

EDUCATION

Georgia Institute of Technology, Atlanta, GA, United States

Visiting Ph.D. graduate in Chemistry, 2016

Advisor: Professor Younan Xia

University of São Paulo, SP, Brazil

PhD. in Chemistry, expected defense in March 2017

Advisor: Professor Pedro H. C. Carmago

Federal University of Ouro Preto, Ouro Preto, MG, Brazil

M.S. in Materials Engineering, Chemistry, February 2013

Thesis: Synthesis of transition metals-containing matrices: study of catalytic activity in fine chemistry reactions

Advisor: Professor Patricia A. Robles-Dutenhefner

Federal University of Ouro Preto, Ouro Preto, MG (Brazil)

B.S. in Industrial Chemistry, April 2011.

RESEARCH EXPERIENCE

2016: Georgia Institute of Technology

Visiting Ph.D. Graduate Research Fellow

(Advisor: Younan Xia)

- Working on the synthesis controlled nanocages with complex morphologies based on noble-metal (gold, palladium, and platinum) for catalytic and electrocatalytic applications.

2013-2016: University of São Paulo, SP, Brazil

PhD. Graduate Research Fellow

(Advisor: Pedro H. C. Camargo)

- Worked on the synthesis of hollow nanoparticles based on noble-metal (silver, gold, palladium, platinum) displaying controlled properties (size, shape, composition, architectures) for applications in heterogeneous catalysis (liquid and gas-phase transformations).

2011-2013: Federal University of Ouro Preto, Ouro Preto, MG (Brazil)

M.S. Graduate Research Fellow

(Advisor: Patricia A. Robles-Dutenhefner)

- Worked on the synthesis of matrices based on SiO₂, TiO₂ and SiO₂-TiO₂ containing Chromium, molybdenum, and cerium for application as heterogeneous catalysts for desulfurization of liquid fuels.
- Developed analytical methods for determination of sulfur compounds in liquids fuels via GC-FID.

2009-2011: Federal University of Ouro Preto, Ouro Preto, MG (Brazil)

*Undergraduate Research Fellow, Department of Chemistry
(Advisor: Gilmar Pereira de Souza)*

- Worked on the synthesis and purification of complexes based on Ni, Pd, Cu, and Mg for magnetic and catalytic applications.

2007-2008: Federal University of Ouro Preto, Ouro Preto, MG (Brazil)

*Undergraduate Research Fellow, Department of Chemistry
(Advisors: Robson José de C. Franco Afonso and Mauricio Xavier Coutrim)*

- Developed analytical methods for analyses of alcoholic beverages.

TEACHING EXPERIENCE

2013-2015: University of São Paulo, São Paulo, SP (Brazil)

Graduate monitor, Institute of Chemistry

- General Chemistry
- Inorganic Chemistry

Activities included: preparing, teaching and coordinating lab sections as well as correcting exams/homework. Received excellent teaching evaluations from students and from the professors.

2012-2013: Federal University of Ouro Preto, Ouro Preto, MG (Brazil)

Substitute professor, Department of Chemistry

- General Chemistry
- Chemistry applied to nutrition

COMPLEMENTARY EXPERIENCE

Electron Microcopy: Experience in the operation (Zeiss Ultra60, and JEOL JSM-7401F) and TEM (Hitachi HT7700) microscopes, including sample preparation and analyses of results.

Catalysis: Experience in the operation of different characterization techniques widely employed in catalysis field such as surface area and chemisorption measurements (Quantachrome Autosorb IQ BET), Temperature programmed reduction (TPR Quantachrome ChemBET-300) X-ray diffraction (Rigaku Geigerflex-3034 diffractometer), UV-VIS spectroscopy (Shimadzu UV-1700 spectrophotometer), and gas chromatography (GC-2014, and GC-2010AF). Experience in analyzing results by BET, gas chemisorption, TPR, XRD, XPS, UV-VIS, Raman, and gas chromatography.

HONORS AND AWARDS

- Awarded Best poster award within the 18th Brazilian Catalysis Congress, Brazilian Catalysis Society, **2015**.
- Awarded Best student poster award (Shared First Place) within the MRS Fall 2014 Symposium FF: Materials as Tools for Sustainability, MRS Fall 2014 Symposium in **2014**.
- Awarded Best poster nominee, MRS Fall 2014 Symposium in **2014**.
- Awarded Idea to Product Latin America, Center for Entrepreneurship and New Business of the Getulio Vargas Foundation FGVcenn in **2012**.
- Awarded Best Outstanding Presentation - Idea to Product Latin America, Center for Entrepreneurship and New Business of the Getulio Vargas Foundation FGVcenn in **2012**.
- Awarded Santander Entrepreneurship - Biotechnology and Health category, Banco Santander in **2011**.
- Awarded with Honorable Mention, Department of Mining Engineering at the Federal University of Ouro Preto in **2010**.

PUBLICATIONS

1. **RODRIGUES, THENNER S.**; DA SILVA, ANDERSON G.M.; DE OLIVEIRA, LUCAS C.; DA SILVA, ADALBERTO M.; TEIXEIRA, RÓBSON R.; CAMARGO, PEDRO H.C. Cu₂O Spheres as an Efficient Source of Catalytic Cu(I) Species for Performing Azide-Alkyne Click Reactions. *Tetrahedron Letters*, v. 58, p. 590-595, **2017**.
2. **RODRIGUES, THENNER**; DA SILVA, ANDERSON; DE MOURA, ARTHUR; GEONMONOND, RAFAEL; CAMARGO, PEDRO. AgAu Nanotubes: Investigating the Effect of Surface Morphologies and Optical Properties over Applications in Catalysis and Photocatalysis. *Journal of the Brazilian Chemical Society*, **2017**.
3. DA SILVA, ANDERSON G. M.; **RODRIGUES, THENNER S.**; TAGUCHI, LAÍS S. K.; FAJARDO, HUMBERTO V.; BALZER, ROSANA; PROBST, LUIZ F. D.; CAMARGO, PEDRO H. C. Pd-based nanoflowers catalysts: controlling size, composition, and structures for the 4-nitrophenol reduction and BTX oxidation reactions. *Journal of Materials Science*, v. 51, p. 603-614, **2016**.
4. **RODRIGUES, THENNER S.**; DA SILVA, ALISSON H. M.; DA SILVA, ANDERSON G. M.; CEARA, DANIEL G.; GOMES, JANAINA F.; ASSAF, JOSE M.; CAMARGO, PEDRO H. C. Hollow AgPt/SiO₂ nanomaterials with controlled surface morphologies: is the number of Pt surface atoms imperative to optimize catalytic performances? *Catalysis Science & Technology*, v. 6, p. 2162-2170, **2016**.
5. DA SILVA, ANDERSON G.M.; KISUKURI, CAMILA M.; **RODRIGUES, THENNER S.**; CANDIDO, EDUARDO G.; DE FREITAS, ISABEL C.; DA SILVA, ALISSON H.M.;

ASSAF, JOSE M.; OLIVEIRA, DANIELA C.; ANDRADE, LEANDRO H.; CAMARGO, PEDRO H.C. MnO₂ nanowires decorated with Au ultrasmall nanoparticles for the green oxidation of silanes and hydrogen production under ultralow loadings. *Applied Catalysis. B, Environmental (Print)*, v. 184, p. 35-43, **2016**.

6. **RODRIGUES, THENNER S.**; FAJARDO, HUMBERTO V.; DIAS, ANDERSON; MEZALIRA, DANIELA Z.; PROBST, LUIZ F.D.; STUMPF, HUMBERTO O.; BARROS, WDESON P.; DE SOUZA, GILMAR P. Synthesis, characterization and catalytic potential of MgNiO₂ nanoparticles obtained from a novel [MgNi(opba)]_n·9nH₂O chain. *Ceramics International*, v. 42, p. 13635-13641, **2016**.

7. YAMADA, LILIAM; DA SILVA, ANDERSON; **RODRIGUES, THENNER**; HAIGH, SARAH J; CAMARGO, PEDRO. Bimetallic Au@Pd-Au Tadpole-Shaped Asymmetric Nanostructures by a Combination of Precursor Reduction and Ostwald Ripening. *ChemNanoMat*, v. 2, p. 509-514, **2016**.

8. **RODRIGUES, THENNER SILVA**; DA SILVA, ANDERSON; DE MOURA, ARTHUR; FREITAS, ISABELLA; CAMARGO, PEDRO. Rational Design of Plasmonic Catalysts: Matching the Surface Plasmon Resonance with the Lamp Emission Spectra for Improved Performances in AgAu Nanorings. *RSC Advances: an international journal to further the chemical sciences*, v. 6, p. 62286-62290, **2016**.

9. **RODRIGUES, THENNER S.**; DA SILVA, ANDERSON G.M.; GONÇALVES, MARIANA C.; FAJARDO, HUMBERTO V.; BALZER, ROSANA; PROBST, LUIZ FERNANDO DIAS; DA SILVA, ALISSON H.M.; ASSAF, JOSE M.; CAMARGO, PEDRO HC. On the Catalytic Properties of Apt Nanoshells as a Function of Size: Larger Outer Diameters Lead to Improved Performances. *Langmuir*, **2016**.

10. KISUKURI, CAMILA M.; REIS, JOÃO L. M. S.; **RODRIGUES, THENNER S.**; CAMARGO, PEDRO H. C.; ANDRADE, LEANDRO H. Evaluation of AgPd Nanoshells in Dual Catalysis: One-Pot Silane Oxidation and Reduction of Organic Compounds. *ChemCatChem*, v. 8, p. 3657-3662, **2016**.

11. DA SILVA, ANDERSON G. M.; **RODRIGUES, THENNER S.**; CORREIA, VALQUÍRIO G.; ALVES, TIAGO V.; ALVES, RAFAEL S.; ANDO, RÔMULO A.; ORNELLAS, FERNANDO R.; WANG, JIALE; ANDRADE, LEANDRO H.; CAMARGO, PEDRO H. C. Plasmonic Nanorattles as Next-Generation Catalysts for Surface Plasmon Resonance-Mediated Oxidations Promoted by Activated Oxygen. *Angewandte Chemie (International ed. Print)*, v. 55, p. 7111-7115, **2016**.

12. **RODRIGUES, THENNER S.**; DA SILVA, ANDERSON G. M.; GONÇALVES, MARIANA C.; FAJARDO, HUMBERTO V.; BALZER, ROSANA; PROBST, LUIZ F. D.; CAMARGO, PEDRO H. C. AgPt Hollow Nanodendrites: Synthesis and Uniform Dispersion over SiO₂ Support for Catalytic Applications. *ChemNanoMat*, v. 1, p. 46-51, **2015**.

13. **RODRIGUES, THENNER S.**; DA SILVA, ANDERSON G. M.; MACEDO, ALEXANDRA; FARINI, BRUNA W.; ALVES, RAFAEL DA S.; CAMARGO, PEDRO H. C. Probing the catalytic activity of bimetallic versus trimetallic nanoshells. *Journal of Materials Science*, v. 50, p. 5620-5629, **2015**.

14. KISUKURI, CAMILA M.; PALMEIRA, DAYVSON J.; **RODRIGUES, THENNER S.**; CAMARGO, PEDRO H. C.; ANDRADE, LEANDRO H. Bimetallic Nanoshells as Platforms for Metallo- and Biometallo-Catalytic Applications. *ChemCatChem*, v. 8, p. 171-179, **2015**.
15. DA SILVA, ANDERSON G. M.; **RODRIGUES, THENNER S.**; WANG, JIALE; YAMADA, LILIAM K.; ALVES, TIAGO V.; ORNELLAS, FERNANDO R.; ANDO, RÔMULO A.; CAMARGO, PEDRO H. C. The Fault in Their Shapes: Investigating the Surface-Plasmon-Resonance-Mediated Catalytic Activities of Silver Quasi-Spheres, Cubes, Triangular Prisms, and Wires. *Langmuir*, v. 31, p. 10272-10278, **2015**.
16. DA SILVA, ANDERSON G.M.; **RODRIGUES, THENNER S.**; SLATER, THOMAS J.A.; LEWIS, EDWARD A; ALVES, RAFAEL S.; FAJARDO, HUMBERTO V.; BALZER, ROSANA; DA SILVA, ALISSON H.M.; DE FREITAS, ISABEL; OLIVEIRA, DANIELA COELHO DE; ASSAF, JOSE M.; PROBST, LUIZ F. D.; HAIGH, SARAH J.; CAMARGO, PEDRO HC. Controlling Size, Morphology, and Surface Composition of AgAu Nanodendrites in 15 s for Improved Environmental Catalysis under Low Metal Loadings. *ACS Applied Materials & Interfaces (Print)*, v. 7, p. 25624-25632, **2015**.
17. DA'SILVA, ANDERSON G. M.; LEWIS, EDWARD A.; **RODRIGUES, THENNER S.**; SLATER, THOMAS J. A.; ALVES, RAFAEL S.; HAIGH, SARAH J.; CAMARGO, PEDRO H. C. Surface Segregated AgAu Tadpole-Shaped Nanoparticles Synthesized Via a Single Step Combined Galvanic and Citrate Reduction Reaction. *Chemistry - A European Journal*, v. 21, p. 12314-12320, **2015**.
18. SILVA, A. G. M.; **RODRIGUES, T. S.**; DIAS, A.; Fajardo, H. V.; GONÇALVES, R. F.; GODINHO, M.; ROBLES-DUTENHEFNER, P. A. Ce_{1-x}Sm_xO_{1.9-δ} nanoparticles obtained by microwave-assisted hydrothermal processing: an efficient application for catalytic oxidation of α-bisabolol. *Catalysis Science & Technology*, v. 4, p. 814, **2014**.
19. DA'SILVA, ANDERSON G. M.; DE'SOUZA, MICHELE L.; **RODRIGUES, THENNER S.**; ALVES, RAFAEL S.; TEMPERINI, MARCIA L. A.; CAMARGO, PEDRO H. C.. Rapid Synthesis of Hollow Ag-Au Nanodendrites in 15 Seconds by Combining Galvanic Replacement and Precursor Reduction Reactions. *Chemistry - A European Journal*, v. 20, p. 15040-15046, **2014**.
20. SILVA, ANDERSON G. M. DA; **RODRIGUES, THENNER S.**; MACEDO, ALEXANDRA; SILVA, RAFAEL T. P. DA; CAMARGO, PEDRO H. C. AN UNDERGRADUATE LEVEL EXPERIMENT ON THE SYNTHESIS OF Au NANOPARTICLES AND THEIR SIZE-DEPENDENT OPTICAL AND CATALYTIC PROPERTIES. *Química Nova*, v. 37, p. 1716, **2014**.
21. DA SILVA, ANDERSON GABRIEL MARQUES; **RODRIGUES, THENNER SILVA**; GURGEL, LEANDRO VINÍCIUS ALVES; DE ASSIS, PATRÍCIA APARECIDA; GIL, LAURENT FRÉDÉRIC; ROBLES-DUTENHEFNER, PATRICIA ALEJANDRA. A new use for modified sugarcane bagasse containing adsorbed Co²⁺ and Cr³⁺: Catalytic oxidation of terpenes. *Industrial Crops and Products (Print)*, v. 50, p. 288-296, **2013**.
22. LOVÓN, ADRIANA S.P.; LOVÓN-QUINTANA, JUAN J.; ALMERINDO, GIZELLE I.; VALENÇA, GUSTAVO P.; BERNARDI, MARIA I.B.; ARAÚJO, VINÍCIUS D.;

RODRIGUES, THENNER S.; ROBLES-DUTENHEFNER, PATRÍCIA A.; FAJARDO, HUMBERTO V. Preparation, structural characterization and catalytic properties of Co/CeO₂ catalysts for the steam reforming of ethanol and hydrogen production. Journal of Power Sources (Print), v. 216, p. 281-289, **2012**.

PATENTS

2. ROBLES-DUTENHEFNER, P.A.; **RODRIGUES, T. S.**; SILVA, A. G. M.. Obtaining bisabolol oxides by catalytic oxidation of alpha-bisabolol using solid metal oxides. **2011**. Brazil. Registration number: PI221105495250.

3. ROBLES-DUTENHEFNER, P.A.; **RODRIGUES, T. S.**; Isabela Barreto da Costa Janeiro. oxidative desulfurization process liquid fuel catalysada by metal oxides supported on silica-titania matrix. **2013**. Brazil. Registration number: PI0430000153.

LANGUAGES

- Advanced in English and fluent in Portuguese (native language)